



HAL
open science

Interaction of plant cell wall building blocks: towards a bioinspired model system

Yotam Navon

► **To cite this version:**

Yotam Navon. Interaction of plant cell wall building blocks: towards a bioinspired model system. Other. Université Grenoble Alpes [2020-..]; Ben-Gurion university of the Negev, 2020. English. NNT: 2020GRALV006 . tel-03122761

HAL Id: tel-03122761

<https://theses.hal.science/tel-03122761>

Submitted on 27 Jan 2021

HAL is a multi-disciplinary open access archive for the deposit and dissemination of scientific research documents, whether they are published or not. The documents may come from teaching and research institutions in France or abroad, or from public or private research centers.

L'archive ouverte pluridisciplinaire **HAL**, est destinée au dépôt et à la diffusion de documents scientifiques de niveau recherche, publiés ou non, émanant des établissements d'enseignement et de recherche français ou étrangers, des laboratoires publics ou privés.



THESIS

Pour obtenir le grade de

DOCTEUR DE L'UNIVERSITE GRENOBLE ALPES

préparée dans le cadre d'une cotutelle *entre la Communauté Université Grenoble Alpes et Ben-Gurion University of the Negev*

Spécialité : **Chimie Physique Moléculaire et Structurale**

Arrêté ministériel : le 6 janvier 2005 – 25 mai 2016

Présentée par

Yotam NAVON

Thèse dirigée par **Laurent HEUX** et **Anne BERNHEIM**

préparée au sein du **Centre de Recherche sur les Macromolécules Végétales** dans les **Écoles Doctorales: Chimie et Science du Vivant et Kreitmann School for Advanced Graduate Studies**

Interaction of plant cell wall building blocks: towards a bio-inspired model system

Thèse soutenue publiquement le **29 Avril 2020**

Devant le jury composé de :

M. Eric MARECHAL Directeur de recherche, Grenoble, Examineur, Président
M. Jean-François BERRET Directeur de recherche, Paris, Rapporteur
M^{me} Karine GLINEL Prof./Maître de recherche FNRS Lauvain-la Neuve, Rapporteur
M. Alexis PEAUCELLE Directeur de Recherche, Paris, Examineur

M Laurent HEUX Directeur de recherche, Grenoble, Directeur de thèse
M^{me} Anne BERNHEIM Professeure, Ben-Gurion University of the Negev, Israël, Directrice de thèse



Table of contents

Chapter 1. Introduction	1
1.1. The primary plant cell wall (PCW): composition structure and function.....	1
1.2. Plant cell wall building blocks	3
1.2.1. From cellulose fibers to cellulose nano crystals.....	3
1.2.2. From Hemicellulose to Xyloglucan (XG).....	11
1.2.3. From Pectin to Homogalacturonan	14
1.2.4. From lipids to membranes to vesicles.....	17
1.2.4.1. Chemical structure of lipids.....	17
1.2.4.2. Self-assembly of lipids.....	18
1.2.4.3. Physical states of lipid membranes	19
1.2.4.4. Permeability.....	20
1.2.4.5. Lipids of the plant plasma membrane	22
1.2.4.6. Lipid membrane model systems.....	24
1.3. Plant cell wall architecture	27
1.4. Growth and expansion	32
1.5. Cell wall mechanical properties.....	33
1.6. Biomimetic models in 3D and 2D.....	40
1.6.1. General aspects of layer by layer (LbL)	40
1.6.2. Multilayer biomimetic films – plant cell wall analogues.....	42
1.6.3. Biomimetic capsules.....	44
1.6.3.1. Solid core systems	44
1.6.3.2. Liquid core systems-emulsions.....	46
Chapter 2. Characterization techniques.....	51
2.1. Dynamic light scattering (DLS).....	51
2.2. ξ -potential.....	53
2.3. Isothermal titration calorimetry (ITC)	54
2.4. Quartz Crystal Microbalance with Dissipation monitoring (QCM-D).....	55
2.5. Optical microscopy	56
2.6. Atomic-force microscopy (AFM).....	61
Chapter 3. Preparation of building blocks	63
3.1. Building blocks characterization.....	63
3.1.1. Lipids and lipid vesicles	63
3.1.2. CNCs.....	66
3.1.3. Xyloglucan (XG).....	69
3.1.4. Pectin.....	71
3.1.5. Grafting of Fluorophores on CNC, XG and Pectin	72
3.2. Summary.....	76

Chapter 4. Interaction studies	77
4.1. Theoretical background- intermolecular forces	78
4.1.1. Intermolecular forces.....	78
4.1.2. Derjaguin, Landau, Verwey, and Overbeek (DLVO) theory	79
4.1.3. The electrical double layer (DL)	82
4.1.4. Adsorption of polymers on surfaces	84
4.2. CNC-Lipids.....	85
4.2.1. Interaction of CNCs with lipid vesicles.....	85
4.2.1.1. Materials and methods	86
Dynamic Light Scattering (DLS) and ζ -potential.....	87
Isothermal Titration Calorimetry (ITC)	88
Transmission Electron Microscopy (TEM)	88
4.2.1.2. Size and Morphology of CNC-lipid Complexes.....	89
Characterization of the Individual Constituents	89
Addition of CNCs to DOPC vesicle suspensions	91
4.2.1.3. Electron microscopy observations of CNC-liposome complexes	94
4.2.1.4. Thermodynamic characterization of CNC-liposome interaction.....	96
Heat flow measurements using ITC	96
Interaction Modeling and Thermodynamic Parameters.....	99
4.2.1.5. Summary- CNC-liposome interaction.	107
4.2.2. Interaction of CNCs with supported lipid membranes- 2D.....	107
4.2.2.1. Materials and Methods	108
Materials	108
CNCs preparation	109
Dynamic Light Scattering (DLS) and ζ -Potential.....	109
Quartz crystal microbalance with dissipation monitoring (QCM-D).....	110
Substrate preparation	110
QCM-D data analysis	111
Scanning Force Microscopy (SFM).....	112
Total Internal Reflection Fluorescence microscopy (TIRF)	113
TIRF observation flow cell preparation.....	113
4.2.2.2. Formation of the CNCs/SLBs construct.....	114
4.2.2.3. QCM-D monitoring of film deposition.....	115
4.2.2.4. CNCs water content using D ₂ O/H ₂ O solvent exchange	119
4.2.2.5. Microscopic visualization of the constructs using TIRF	121
4.2.2.6. Constructs probed at the nanoscale by SFM	124
4.2.2.8. Summary	131
4.3. CNC-XG study.....	132
4.3.1. CNC-XG interaction in (3D)	133
4.3.1.1. Materials and methods	133
4.3.1.2. Addition of XG into a CNC suspension by ITC	134
4.3.1.3. Adsorption isotherm studied by liquid state NMR	138
4.3.1.4. Light scattering experiments on CNC-XG complexes.....	141
4.3.1.5. TEM enables the visualization of the formed complexes	145

4.3.1.6.	Surface covered by XG at $R = 0.05$ from atomistic modeling	146
4.3.1.7.	CNC-XG complexes -steric stabilization	148
4.3.1.8.	Summary and conclusions.....	150
4.3.2.	CNC-XG interaction in 2D	151
4.4.	Pectin-CNC interaction.....	154
4.4.1.	Screening experiments.....	155
4.4.2.	DLS and ζ -potential measurements.....	157
4.4.3.	Summary.....	159
4.5.	Summary of the interaction studies.....	161
Chapter 5. Biomimetic constructs: assembly and characterization.....		162
5.1.	2D configuration.....	163
5.1.1.	2D assemblies: multilayered films.....	163
5.1.2.	Characterization of layer thickness using AFM.....	164
5.2.	3D assemblies: bare and decorated vesicles.....	174
5.2.1.	GUV preparation	174
5.2.2.	Observation of GUVs in optical microscopy	175
5.2.3.	Decoration protocol.....	177
5.2.4.	Bare vesicles	178
5.2.5.	Decorated vesicles.....	179
5.3.	Vesicles under osmotic Shocks	182
5.3.1.	Observation of GUVs for osmotic shocks.....	182
5.3.2.	Bare vesicles	183
5.3.2.1.	Glucose shocks	183
5.3.2.2.	NaCl and CaCl ₂ shocks	186
5.3.3.	GUV-(CNC).....	188
5.3.4.	GUV-(CNC/XG) _{1.5}	191
5.3.5.	GUV-(CNC/) _{5.5} and GUV (CNC/XG) _{10.5}	193
5.3.7.	Decorated vesicles under CaCl ₂ shocks.....	197
5.4.	Permeability analysis.....	198
5.5.	Conclusions.....	201
Chapter 6. Mechanical properties of biomimetic constructs.....		202
6.1.	Mechanical properties of 3D constructs.....	204
6.2.	Mechanical properties of 2D constructs.....	206
Chapter 7. Summary and outlook.....		213
References		218
ANNEX I		231
ANNEX II.....		232
Abstract.....		235
General abstract		236

Acknowledgments

Many people took part in this journey yet, I would like to begin by thanking the plant cell wall for offering a perfect landscape for me to observe nature in a deeper level.

ooo

My sincere gratitude to the jury for accepting to evaluate this work: Jean-François Berret, Karine Glinel, Alexis Peaucelle and Eric Marechal. Additional appreciations to Emily Cranston, Liliane Guerente, Raz Jelinek and Dganit Danino for accepting to participate in the following committee and evaluate this work in its early stages.

To my thesis supervisor, Dr. Laurent Heux, thank you for including me in your biomimetic quest towards an artificial cell wall. For your support, guidance and ideas during these years. It is thanks to you that I could have this enriching experience.

My BGU thesis director, Prof. Anne Bernheim, overcoming the distance challenge, you have supported me scientifically and morally from the beginning to the end and I thank you for that.

I wish to express my sincere gratitude to Bruno Jean for the fruitful exchanges, manuscript corrections and the encouragement along the way, always more than just a colleague. A special gratitude to Mr. Henri Chanzy for the proof reading of my manuscripts. His wise advices and kind generosity truly enlightened this path.

I would like to express my gratitude to the cermav lab for the warm hospitality and pleasant atmosphere. Particularly the team 'structure and properties of glycomaterials': Pierre Sailer, Stephanie Pardeau and Christine Lancelon-Pin for the technical support, Jean-Luc Putaux, for the contribution to the TEM experiments and the active participation in the proof reading of my manuscripts. Karim Mazeau for the modelling and insights on CNC-XG interaction. Franck Dahlem, for the numerous great moments of scientific joy around the AFM and for the friendly advices.

I would like to acknowledge the following people for their direct and indirect contributions to this work: Isabelle Caldera and Sandrine Coindet from cermav, Magali Pourtier from UGA and Sima Korem from BGU for the administrative aspects.

Oren Regev, Moshe Gottlieb and Rachel Yerushalmi-Rozen from the chemical engineering department at BGU, for their encouragement through numerous discussions and exchanges over the years, both scientific and beyond.

Anne Imberty and Émilie Gillon for their formation and advices with the ITC, Christophe Travelet for the DLS experiments and the good humour, Liliane Guerente for her professional guidance through the QCMD analysis and Hugues Bonnet for the technical part of the trials. Giovanna Fragneto and Yuri Gerelli for their support with the neutron reflectometry studies at ILL. Sébastien Mongrand and Adiilah Mamod-Kassim for the work around the plant lipids, Thomas Podgorski from LiPhy for the EF cells, Simone Bovio from the team of Arezki Boudaoud for the AFM analysis and great adventure at ENS Lyon. Anna Szarpak and Sonia Ortega for the nice exchanges around the optical microscope and Walaa El-Mokdad for her contribution on pectin CNC interaction.

The friends from cermav: Julien, Lauric, Marlène, Lea, Robin, Harisoa, Agustin, Maëva, Françoise, Axel, Emilie, Maud, Marie-Alix and Fabien; thank you guys for the super moments at the lab, in the nature and down-town.

The folks from BGU, particularly Sam, Shachar and Dina for their friendly welcome when I came to work in Israel. Special thanks to Guy for the random walks and to the Negev desert for the great moments of inspiration.

Big thank you to my family from the French and Israeli sides for their endless support and thoughtfulness over these years and a special thought to my grandfather Sason.

ooo

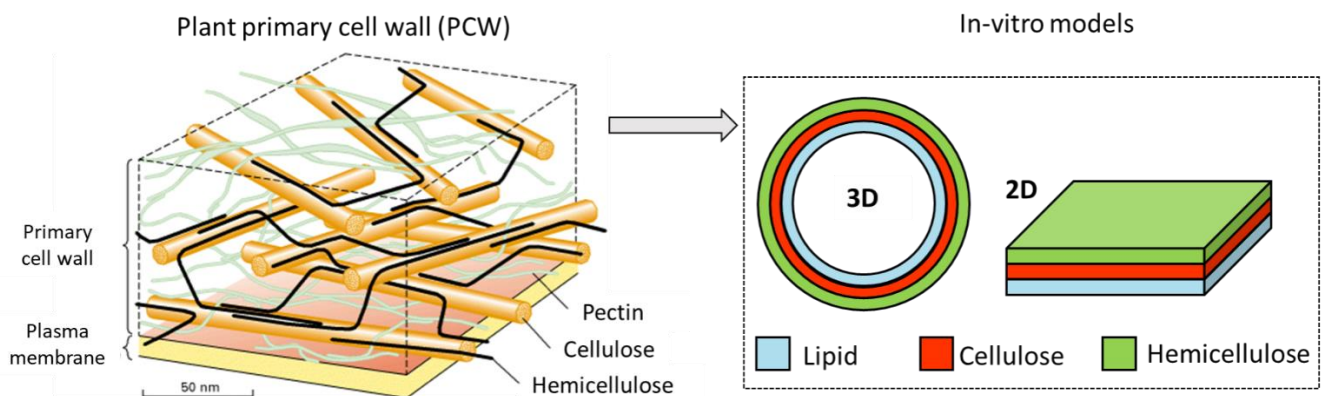
Finally, merci Eléna, this thesis is dedicated to you.

Outline

Our increasing environmental awareness brought to light the importance of plant cell wall (PCW) based materials as a renewable ecological source. It is therefore essential to understand the structure and function of the cell wall from two aspects: (i) Fundamental understanding and (ii) Utilizing the PCW for the design of novel ecofriendly materials.

Since the living cell is a complex environment, constantly changed and remodeled in response to external forces, a simple in vitro model can help to better establish the structure-property relationships of this material.

However, the model systems existing up to date are lacking the basic elements and architecture of the primary PCW, thus, it is crucial to develop a relevant model which will contain all the basic elements, organized in a manner that resembles the natural structure. Therefore, this work aims to create and characterize a simple bioinspired model of the PCW as demonstrated in the following illustration:



Following an introduction (**Chapter 1**) and a review of the characterization techniques used (**Chapter 2**), we will:

1. Define and characterize the individual elements used in this work (**Chapter 3**).
2. Study the molecular interactions between the individual elements in order to optimize the conditions for bottom-up assemblies in 2D and 3D configurations (**chapter 4**).
3. Characterize the physical properties of the resulting composite structures in 2D and 3D (**chapter 5 and 6**).

Chapter 7 will be devoted to a general summary and outlook.

Chapter 1

Introduction

1.1. The primary plant cell wall (PCW): composition structure and function

Composed of a complex network of polysaccharides and proteins, the plant cell wall (PCW) is the layer encapsulating the plant cell, designed to provide structural support, defense and protection, while enabling cell growth and expansion.

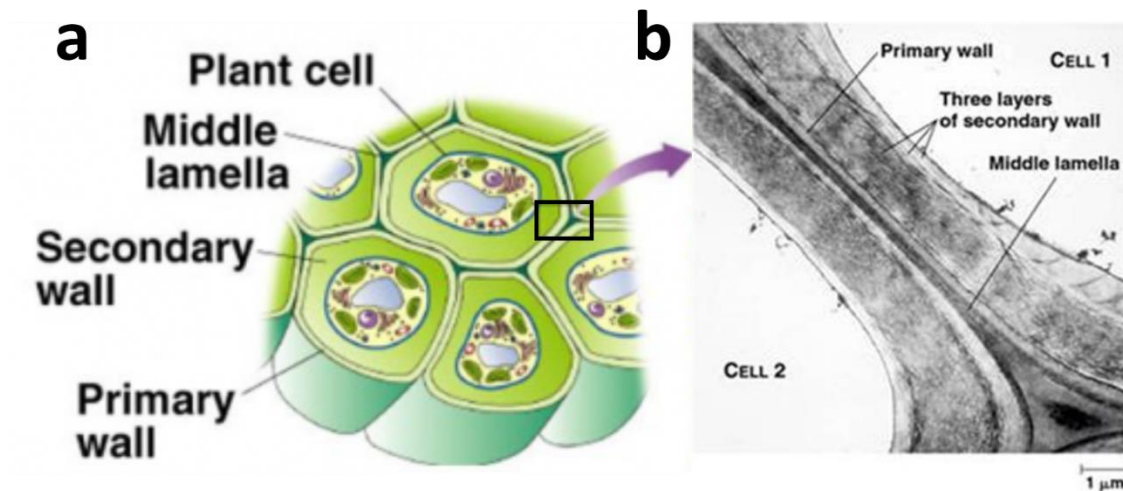


Figure 1. (a) a cartoon of a plant tissue showing the different parts of the cell wall (b) a micrograph of a junction between two plant cells. Adapted from Glycopedia.

While the constituents of the plant cell walls may vary depending on the stage of development and the type of tissue, most cell walls from land plant consist of three distinct anatomical regions (Figure 1 a and b): a *primary wall*, a thin layer which is the first to be deposited on the plasma membrane and develops during cell growth; a *secondary wall* which is laid down against the primary wall after the cell ceases growing and made of additional sub-layers; and *the middle lamella*, which forms the interface

between the primary walls of neighboring cells. While all plant cells do not have a secondary wall, all have a primary wall and middle lamella.(Albersheim, et al. 2011, Cosgrove 2005, Somerville, et al. 2004)

The primary cell wall, which is the focus and inspiration of this study, is deposited while the cell is still growing, providing both the rigid structural support of plant cells and the adjustable elasticity needed for cell expansion. In order to perform these seemingly contradictory tasks, the primary cell wall displays a composite-like structure with cellulose microfibrils embedded in a matrix of soluble polysaccharides called hemicelluloses and pectins.

Table 1. Composition of a typical primary cell wall (% dry mass) (Albersheim, et al. 2011)

Macromolecule	Dicots and monocots (Excluding grasses)	Grasses
Cellulose	25-30	20-30
Hemicellulose	30	10-15
Pectin	20-30	40-50
Structural proteins	1-10	1-5

The relative amounts of polysaccharides may vary between species (Table 1), but generally for primary walls of flowering plants it is composed of cellulose (20-30%) hemicellulose (10-30%) and pectin (35%) with structural proteins being up to 10% of the total dry mass. (Cosgrove 2005)

Different structural elements are synthesized in different locations of the cell. Cellulose is synthesized by large trans membrane complexes while hemicellulose and pectin originate from the Golgi apparatus: they are packaged into membrane bound vesicles that fuse into the plasma membrane and deliver their cargo to the wall by exocytosis. (Carpita and Gibeaut 1993, Cosgrove 2005)

Overall, the biomechanical properties of the PCW are mainly defined by the composition of the polymers, namely cellulose, hemicelluloses, and pectins and their interactions. (Ochoa-Villarreal, et al. 2012). The first step of the constitution of the cell wall is the deposition of cellulose microfibrils on the outer layer of the plasma membrane by cellulose synthase. Further cross-linked by hemicellulose and pectin,

cellulose is the main bear loading component of the cell wall, while proteins perform enzymatic, defensive signaling, and structural functions.

In the following sections, we will describe in more detail the basic elements of the PCW and the way they are represented in a bottom-up approach for PCW model systems.

1.2. Plant cell wall building blocks

1.2.1. From cellulose fibers to cellulose nano crystals

Cellulose (Figure 2), the poly β -(1 \rightarrow 4) anhydro D glucopyranose (AGU), is a natural homo-polysaccharide that is produced by a wide variety of living creatures: from higher and lower plants, to some sea animals, bacteria, fungi, and amoebas.

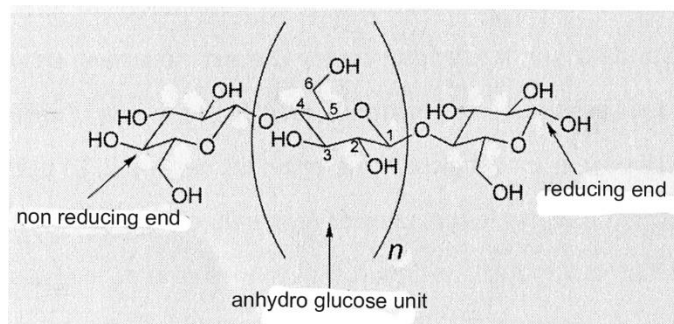


Figure 2. Molecular structure of cellulose with the numbering of carbons.

In the cellulose producing bacteria, the mechanism of cellulose biosynthesis has been recently deciphered at the molecular level (McNamara, et al. 2015, Morgan, et al. 2013, Morgan, et al. 2016).

Even if the biosynthetic mechanism of cellulose synthesis in plant cell has not been resolved with a precision similar to that in bacteria, a detailed 3D atomistic model of the plant cellulose synthase, has been established, using a molecular modeling approach (Sethaphong, et al. 2013). This model presents a close agreement with the core region of bacterial cellulose synthesis complex, implying that the molecular mechanism of cellulose biosynthesis is very similar in plants and in bacteria.

In the native state, cellulose systematically occurs as microfibrils, this particularity being due to its mode of biosynthesis (Nishiyama 2009). Indeed, in the plant plasma membrane, the cellulose biosynthesis takes place within a cluster of a well-defined number of cellulose synthases, organized into a tridimensional architecture commonly called terminal complex (TC). Within a TC, all the cellulose synthases produce cellulose chains simultaneously (figure 3). These chains, which are insoluble in the surrounding medium, readily coalesce and cluster together with precise Van der Waals (VdW) and hydrogen bonding interactions. In higher plants, TCs, observed by freeze-fracture electron microscopy, consist of 6-lobed rosettes tightly packed in a ring of outside diameter of the order of 20 to 30 nm depending on the species. (Giddings, et al. 1980, Mueller and Brown 1980, Nixon, et al. 2016)

The crystalline cellulose microfibril is extruded from a hole located at the center of the rosette. It has a diameter ~ 2 to 3nm (modeled in Figure 3A), and contains ~ 20 to 50 chains depending on the sample origin. In other plants, such as the well-studied green alga *Valonia*, the cellulose synthases are organized in elongated TCs (modeled in Figure 3B) of more than 300 nm in length (Itoh and Brown 1984) yielding micron-sized cellulose microfibrils of ~ 20 nm in diameter, presenting a high crystalline perfection (Chanzy 1990).

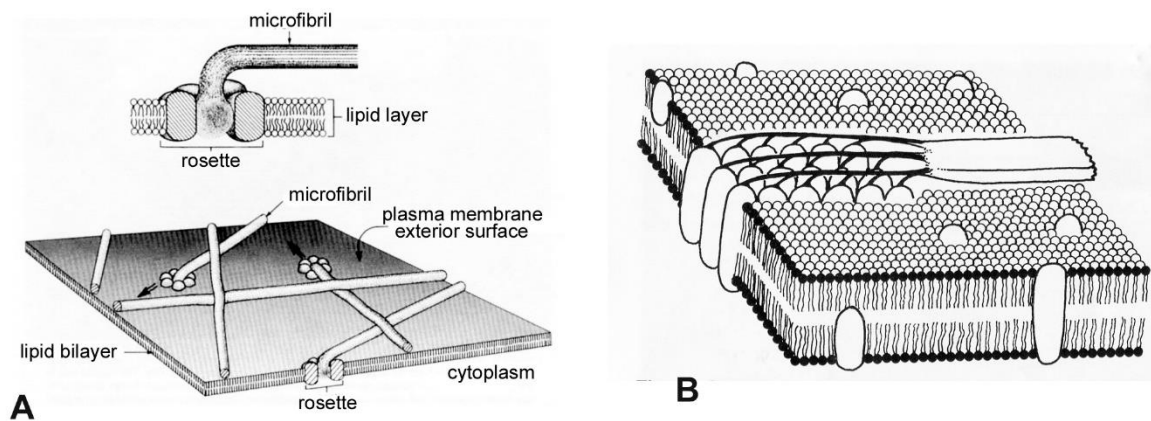


Figure 3. A: Model of microfibril deposition during primary wall formation in *Micrasterias*. Above: side view. Below: surface view. Single rosettes give rise to randomly oriented microfibrils (Giddings, et al. 1980). B: Model of assembly of a *Valonia* microfibril from an elongated TC (Itoh and Brown 1984).

Examples of the diversity of the cellulose microfibril dimensions are presented in Figures 4A and 4B. In both micrographs, the microfibrils have lengths of many microns, but in 4A those from primary wall cellulose have no more than 2-3 nm in diameter as opposed to those in Figure 4B, which have diameters 10 times wider.

Obviously, the number of cellulose chains within one microfibril is substantially different, ranging from about 20 to 30 in the primary wall cellulose such as observed in Figure 4A as opposed to more than 1000 in the sample shown in Figure 4B.

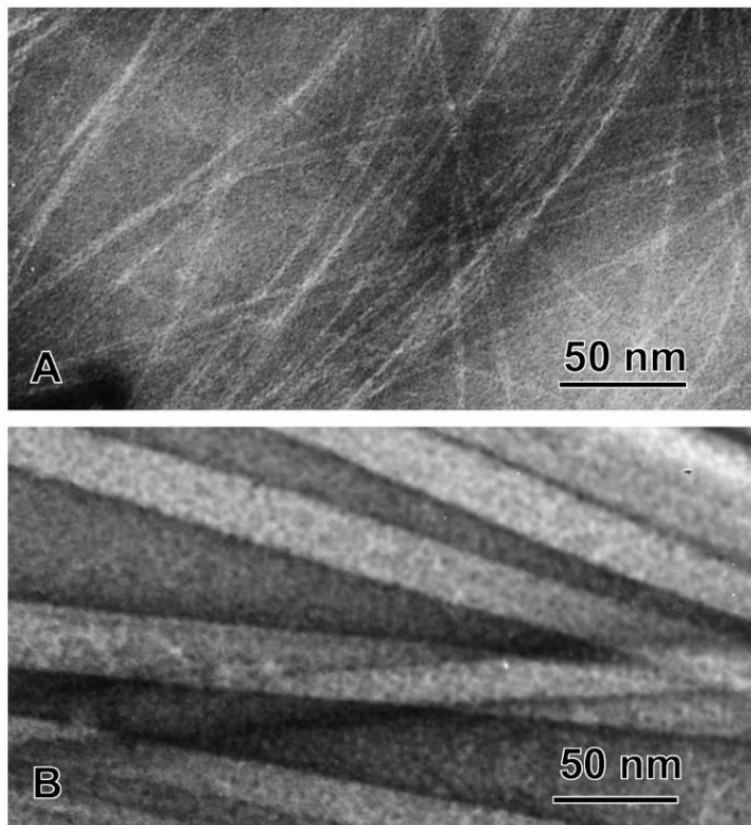


Figure 4. Negatively stained electron micrographs of: A. Thin microfibrils from protoplast cell wall, typical of primary wall cellulose. B. Wide microfibrils from *Valonia* cell wall. Taken from the CERMAV images collection.

Between these two extremes, one finds a variety of microfibril sizes, depending on the sample origin, exemplified in Figure 5.

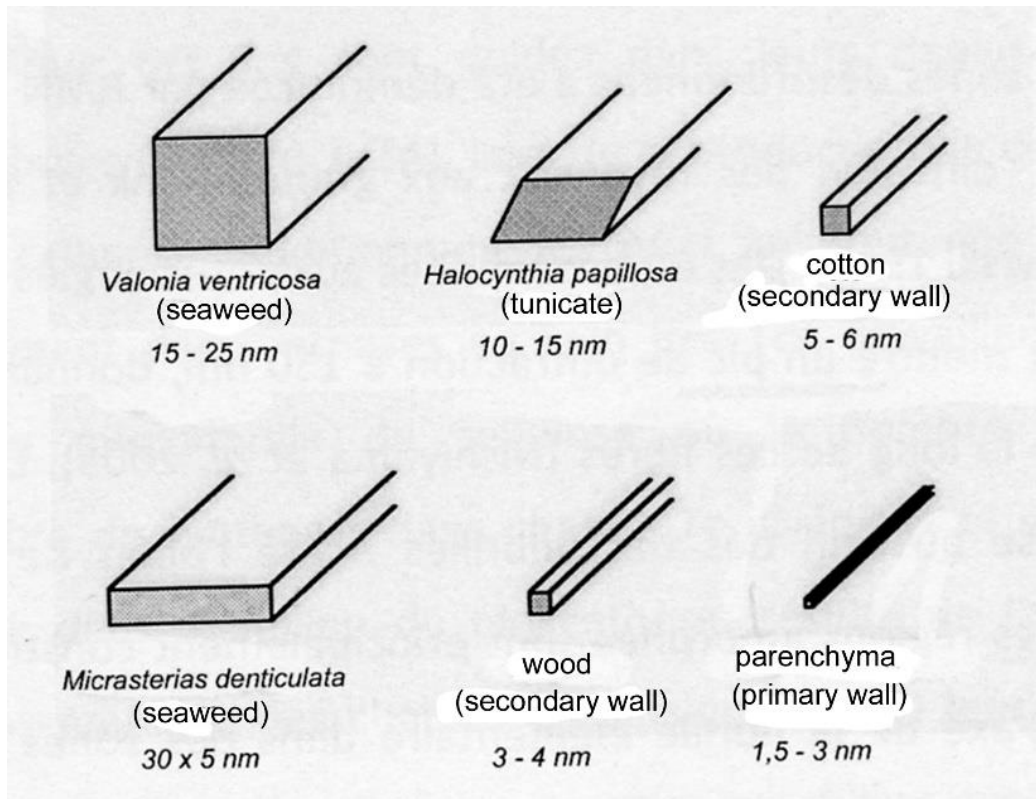


Figure 5. Typical sizes of cellulose microfibrils depending on the sample origin. For *Valonia*, *Halocynthia* and *Micrasterias*, the sections were observed by cross-sectioning and electron microscopy. For cotton, wood and parenchyma, the shape of the cross-section is hypothetical.

The association of cellulose microfibrils in PCW shows two type of organization, illustrated in Figures 6A and 6B. Figure 6A is typical of the cellulose organization in primary wall, where the microfibrils as in Figure 5 are organized in a loose net, without any preferred orientation allowing the expansion of the living cell, while maintaining its strength. On the other hand, in the thicker secondary wall, occurring when the cells have stopped their growth, the microfibrils are organized in thick sheets where the microfibrils point roughly to the same direction (Figure 6B). This wall is not extensible, but provides strength and rigidity to the plant (Cosgrove 2012).

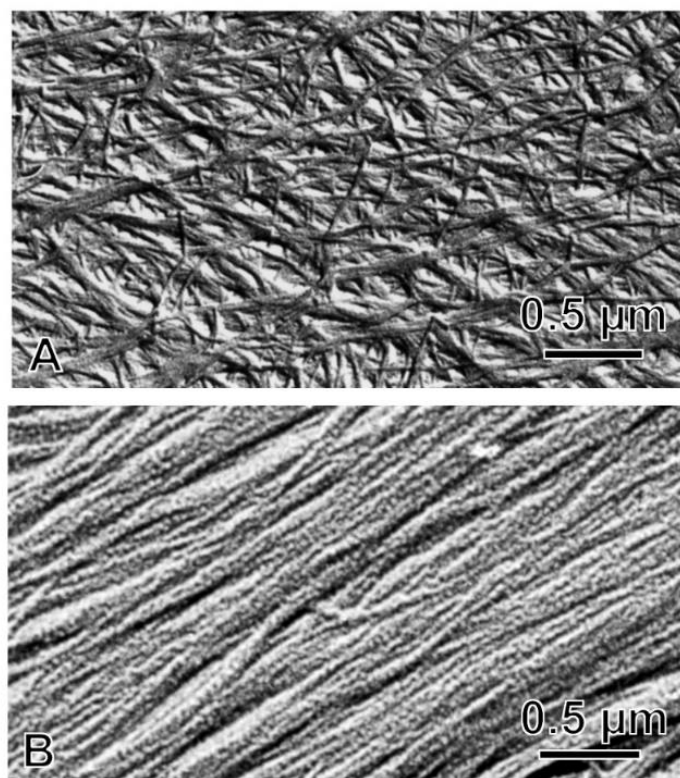


Figure 6. A Cellulose microfibrillar network in the primary wall of a *Rubus fruticosus* cell. B. Cellulose microfibrillar network in the secondary wall of wood. Taken from the CERMAV images collection.

Cellulose Nano Crystals (CNCs)

When observing the ultrastructure of cellulose in the cell wall (Figures 6A and 6B), one notices that the microfibrils are straight only over small distances. Indeed, within the cell wall, the microfibrils are intertwined and thus display a substantial number of twists and kinks alternating with the straight domains. These defects, which correspond to some amorphous phase, likely originate from the difficulty of the nascent microfibrils to find their way during their biogenesis within the crowded environment of the cell wall.

The presence of such defects in cell wall cellulose is quite interesting since they can be solubilized by a strong acid hydrolysis, thus resulting in periodical cuttings of the microfibrils, leaving intact the unperturbed straight crystalline domains. This leads to the so called “cellulose nanocrystals” (CNCs), which have the same diameter as the original microfibril, but shorter in their lengths, which correspond to the inter-defect

distances of the parent microfibrils. Remarkably, cellulose microfibrils grown in vitro in dilute suspension cannot be cut in similar acid treatment as they are free to grow without defects, being not perturbed by their neighbors (Lai-Kee-Him, et al. 2002).

The acid hydrolytic conversion of cellulose fibers into CNCs was already reported in the early 40s at Freiburg in Germany (Husemann 1943) and developed further at Uppsala in Sweden, as illustrated by improved electron micrographs (Rånby 1949, Rånby and Ribi 1950).

When celluloses are hydrolyzed by concentrated hydrochloric acid, their aqueous suspensions flocculate. On the other hand, when their hydrolysis is performed with sulfuric acid, the CNCs are surface sulfated (Figure 7). These surface charges are quite important as they promote stable CNC dispersions in aqueous suspensions. Upon concentration, these suspensions self-organize into a chiral-nematic order (Marchessault, et al. 1959, Revol, et al. 1992).

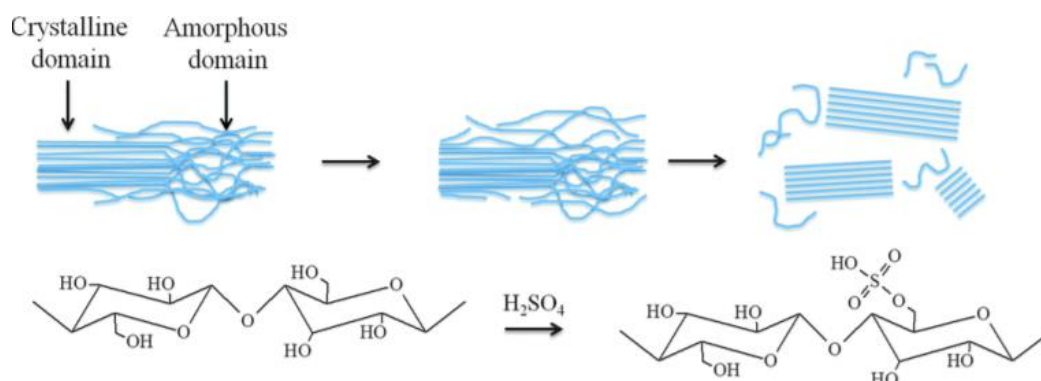


Figure 7. Sulfuric acid hydrolysis of cellulose resulting in the elimination of amorphous part located in the microfibrils defects, leaving only the crystalline parts. This process imparts a colloidal stability to the CNCs thanks to the sulfate ester group grafted on their surface.(Ehmann, et al. 2014)

The CNC dimensions range from 3 to 20 nm in cross-section and 100 to 3000 nm in length, depending on their biological origin and hydrolysis conditions (Figure 8). Some of the CNCs are organized in packets of 2 to 3 (Figure 8 a-d) whereas others remain separated as individual objects (Figure 8e,f). For each CNC, its length is directly related to the degree of polymerization (DP) of the constituting cellulose molecules. After acid hydrolysis, one obtains the so-called level-off DP (LODP), i.e., the average

inter-defect DP in the initial microfibrils. Since each AGU has a length of ~ 0.5 nm and since the cellulose chains are perfectly aligned along the CNC, the cellulose LODP can be easily deduced from the CNC length. Overall, the LODP is a constant for each cellulose origin (Battista, et al. 1956, Nishiyama, et al. 2003).

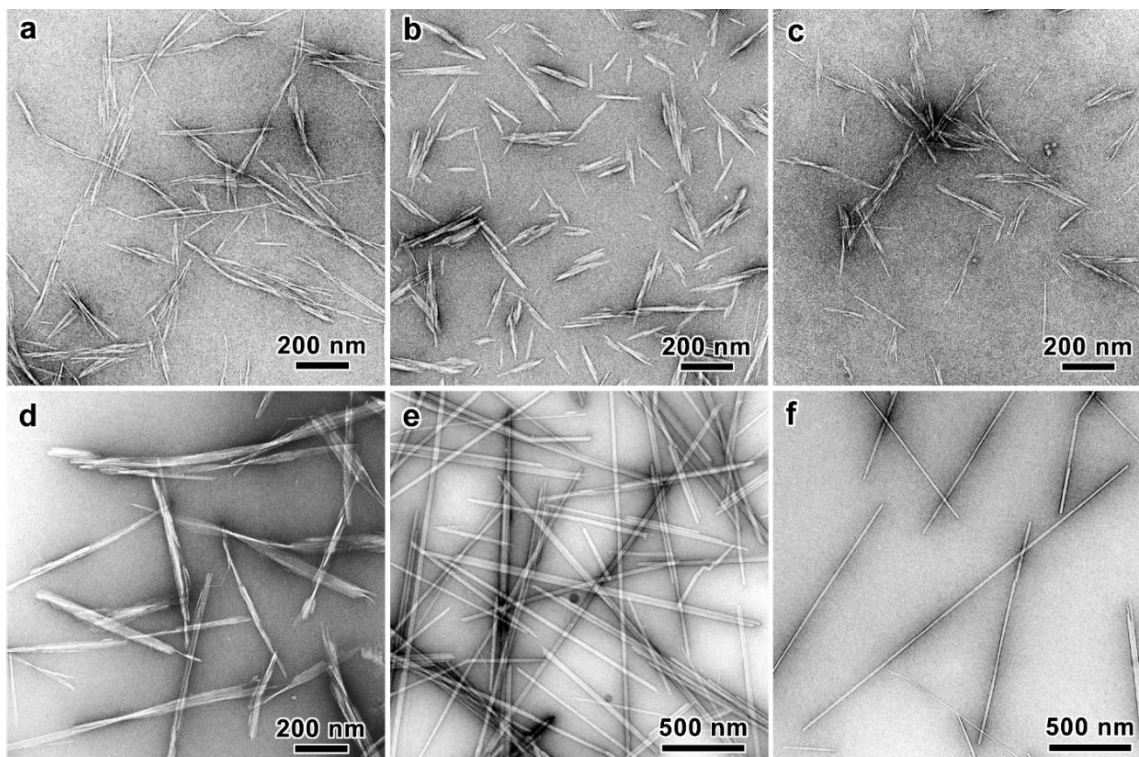


Figure 8. TEM images of negatively stained preparations of CNCs of various origins: a) wood b) cotton c) bamboo d) *Gluconacetobacter xylinus* e) *Glaucocystis* f) *Halocynthia papillosa* (Kaushik, et al. 2015). From the CERMAV image collection.

Like the overall morphology of cellulose microfibrils, the cross-section dimensions of the individual CNCs also depend on the cellulose origin (Elazzouzi-Hafraoui, et al. 2007). Figure 9a shows the cross-section dimensions of cellulose from wood, cotton, and tunicin (the cellulose from tunicate mantle), corresponding to Figures 8a, b, and f, respectively. Figure 9b shows a two-dimensional histogram obtained for the width length and height of CNCs prepared by acid hydrolysis of cotton linters (Elazzouzi-Hafraoui, et al. 2007).

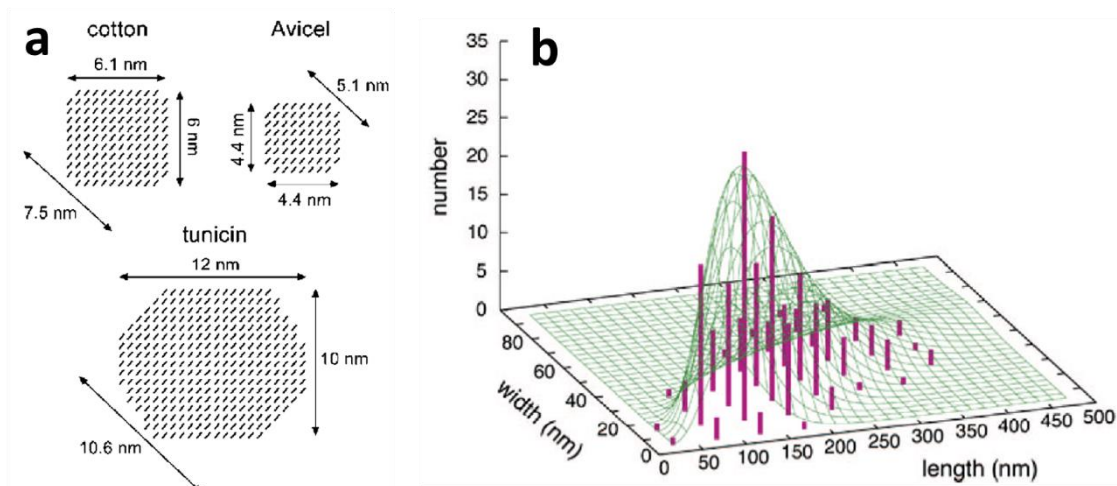


Figure 9. (a) Cross-sections of elementary crystallites of cotton, Avicel (wood origin) and tunicate cellulose

The discovery of CNCs has led to a significant amount of research and development since they possess very interesting properties: they are colloidally stable, originate from renewable resources, are readily available, non-toxic and biodegradable. In addition to their aforementioned ability to form liquid-crystalline self-organized phases, CNCs have also been reported to stabilize oil-in-water (O/W) emulsions (Kalashnikova, et al. 2011), and can be used as reinforcing agents to enhance the mechanical properties of nanocomposites (Bledzki and Gassan 1999, Favier, et al. 1995). CNCs have also been used as natural building blocks for the design of functional multilayered films (Jean, et al. 2008, Jean, et al. 2009, Kolakovic, et al. 2013, Martin and Jean 2014) or to create polymer-particle complexes (Kolakovic, et al. 2013, Wang and Roman 2011).

In addition to being colloidally stable, CNCs present crystalline structure and mechanical properties similar to the natural cellulose microfibrils (Mukherjee and Woods 1953, Tashiro and Kobayashi 1991). Thus, CNCs have been tentatively used as building blocks for the design of PCW mimicking materials (Bailly 2012, Cerclier, et al. 2010, Niinivaara, et al. 2015, Radavidson 2016, Teeri, et al. 2007).

From the above-mentioned reasons, in the present work we intend to use cellulose nanocrystals in order to mimic the role of cellulose microfibrils in the cell wall.

1.2.2. From Hemicellulose to Xyloglucan (XG)

Hemicelluloses are a group of heterogeneous polysaccharides, including Xyloglucans (XG), Glucuronoxylans, Glucomannans, Galactoglucomannans that are synthesized in the Golgi apparatus and secreted to the PCW by endocytosis (Cosgrove 1997, Fry 1989, Hayashi 1989). They bind to the surface of cellulose and have a backbone made up of (1→4)- β -D-glycans that resembles cellulose (Fry 1989, Scheller and Ulvskov 2010). Unlike cellulose, hemicelluloses contain branches and other modifications in their structure, preventing them from crystallizing by themselves into microfibrils, but increasing their water solubility. In the PCW, hemicellulose play a major role in the mechanical properties by cross linking cellulose microfibrils (Hayashi, et al. 1987, Park and Cosgrove 2015). This interaction will be discussed in more detail in chapter 4.3.

Xyloglucan (XG) is the most abundant hemicellulose in primary cell walls and had been found in almost every land plant species. Unlike other hemicelluloses, XG has a backbone of (1→4)-linked β -D-glucopyranosyl units, similar to those of cellulose, but decorated with xylose branches on 3 out of 4 glucose residues, representing the repeat unit of XG (Figure 10).

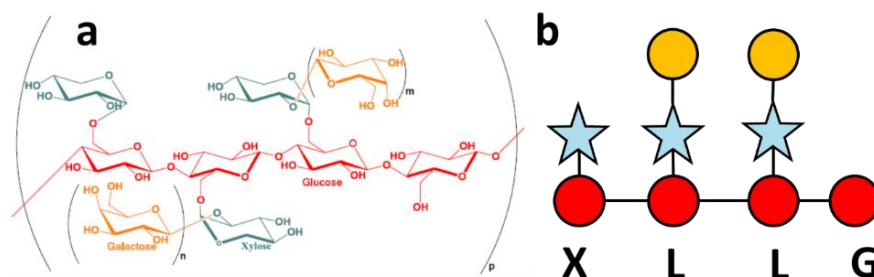


Figure 10. (a) An example of a repeating unit of xyloglucan when n and m can be 0 or 1. (b) the corresponding one letter notation where G is the unbranched glucose residue, X is a glucose linked to a xylose and L is a glucose linked to a xylose with a link to a galactose.

A common one letter notation is used to code the different side chains, (Fry, et al. 1993) where G denotes unbranched glucose residue, X denotes α -D-Xylp-(1 \rightarrow 6)- β -D-Glcp segment and L denotes a β -D-Galp-(1 \rightarrow 2)- α -D-Xylp-(1 \rightarrow 6)- β -D-Glcp segment (figure 10b). The side chains of XG can vary depending on its source. In several species, an additional Fucose (F) residue is connected to the Galactose unit. (Fry, et al. 1993, Scheller and Ulvskov 2010)

Sugar analysis on xyloglucan from tamarind seeds revealed that the majority of oligosaccharides repeat units are XLLG (50.6%) where XXLG, XXXG and XLXG represent 28, 13 and 9% respectively (Faïk, et al. 1997).

Being a hydro-soluble polymer, XG adopts a semiflexible conformation in solution. Muller et al. characterized the solution properties of XG using SEC-MALLS and small angle neutron scattering (SANS). They found that XG behaved as a semiflexible polymer, with a Mark-Houwink-Sakurada parameter of 0.67 and a Flory exponent $\nu=0.588$ in water, describing a polymer in a good solvent with excluded volume interactions as demonstrated in figure 11. (Muller, et al. 2011) The persistence length (l_p), which quantify the bending rigidity of the polymer, was found to be 80Å.

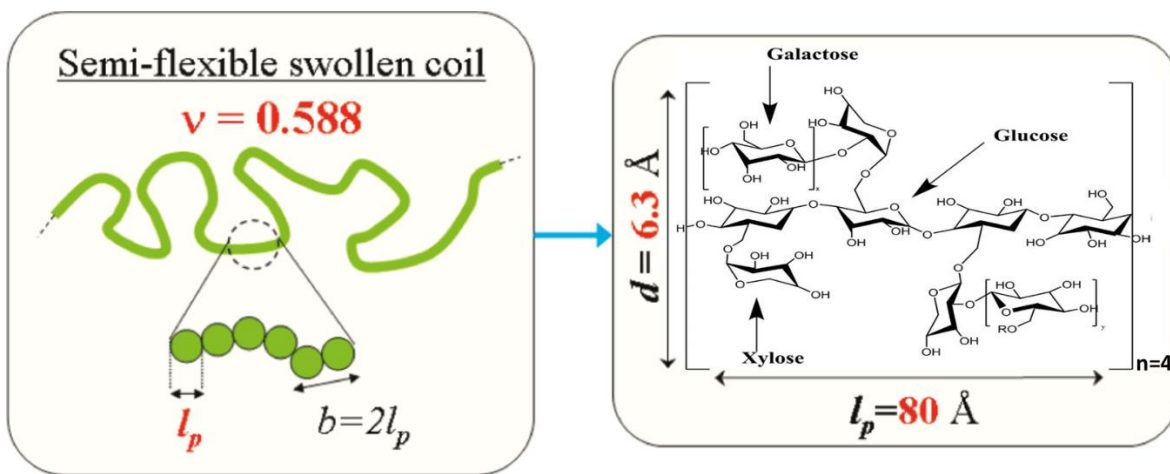


Figure 11. Schematic representation of an isolated XG chain in water, showing a self-avoiding chain with a persistence length of $l_p=80\text{\AA}$ (Muller, et al. 2011).

The behavior of XG in solution depends greatly on its molecular weight and concentration. In another work, Muller et al. (Muller, et al. 2013) used SLS, DLS and

viscosity measurements to study aqueous solutions of neutral xyloglucan extracted from tamarind seed. They found out that even at very low concentration, XG chains became associated to form swollen aggregates. (Figure 12)

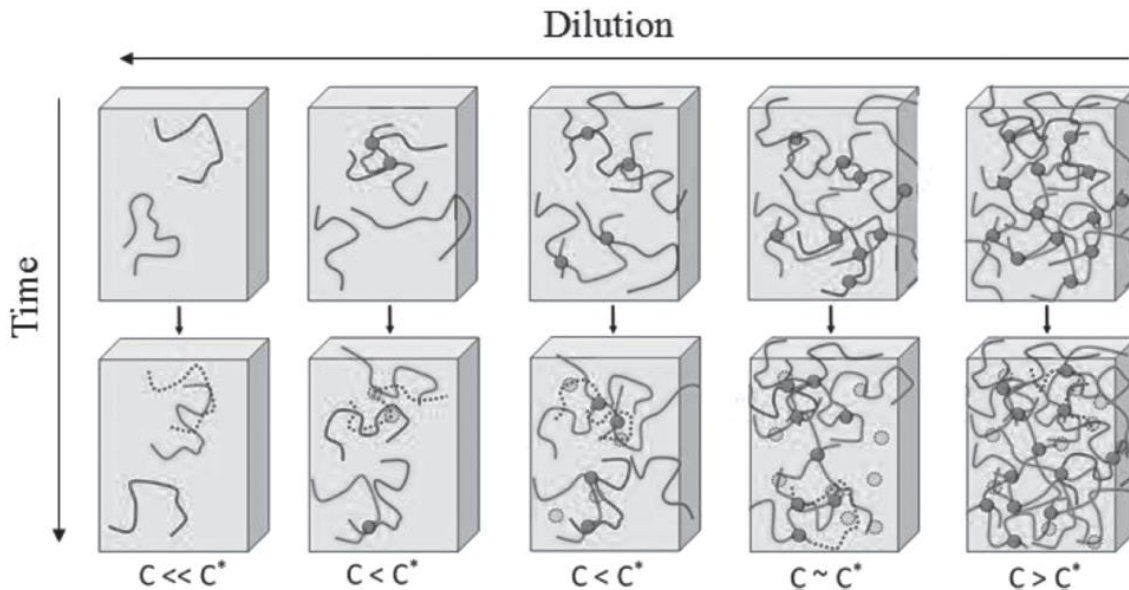


Figure 12. Schematic picture of the behavior of XG chains from tamarind seeds upon dilution (Muller, et al. 2013).

These associations, inherent to the nature of XG chains, are forming and reforming, tending towards larger structures with time. It is therefore essential to take into account not only the structural parameters, but also the physical characteristics of XG when studying its interactions with other components or incorporating it into biomimetic constructs (Kishani, et al. 2019, Park and Cosgrove 2015).

XG have been widely used to represent the role of hemicellulose with in silico (Hanus and Mazeau 2006, Zhao, et al. 2014) and in vitro models (Chambat, et al. 2005, Hayashi and Maclachlan 1984, Hayashi, et al. 1994, Jean, et al. 2009, Villares, et al. 2017).

In this work XG will be used as a representative hemicellulose in the biomimetic constructs.

1.2.3. From Pectin to Homogalacturonan

Pectins represent another diverse family of linear and branched polysaccharides, found throughout the primary wall. They are present in high concentration in the middle lamella and act as cell adhesion agent and a matrix embedding the CNC-XG network (Sharma, et al. 2006). Pectin has functions in plant growth, morphology, development, cell-cell adhesion, wall structure, and expansion (Caffall and Mohnen 2009, Mohnen 2008).

Within the plant walls pectins, several groups can be distinguished, as shown in figure 13: Homogalacturonans (HG), linear polymers of galacturonic acid; Xylogalacturonans (XGA); Rhamnogalacturonanes type I and II (RGI and RGII).

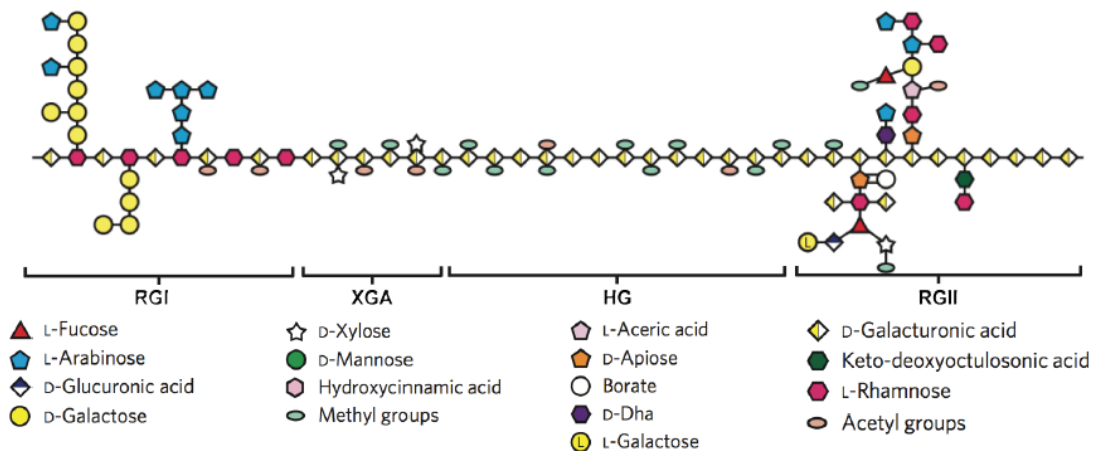


Figure 13. Pectin general structure (Burton, et al. 2010).

The linear part of pectin, homogalacturonan or HG, is the simplest and most abundant pectic structural domain, usually accounting for approximately 65% of the pectin macromolecule. It consists of a linear backbone of 85–320 (1→4) linked α -d-GalA residues, partly methyl-esterified at C-6 position. It may also be O-acetylated at O-2 or O-3 position (Figure 14a). (Burton, et al. 2010) In solution, the non-methylated carboxyl groups will dissociate depending on the pH, leaving a negative charge on the GalA monomers, resulting in typical features of an anionic polyelectrolyte. The degree of

methyl esterification (DE, in %) of the glucuronic acid backbone, have a profound impact on pectin interaction and properties in vitro and in planta. (O'Neill, et al. 1990)

In this work we focus on HG since it the most abundant pectin, believed to play a major role in the interaction and properties, and therefore its physical chemistry has been relatively well studied.

Isolated HG rich pectins exhibits two different gelation mechanisms that are influenced by the degree of methyl esterification. High methoxylated pectin (HM pectin) can form a gel in acidic medium ($\text{pH} < 3.5$) in presence of a co-solute, typically sucrose at high concentrations (Thakur, et al. 1997, Thibault and Ralet 2003). Such gels are often referred to as “acid gels”. The high sugar concentration decreases the water activity, promoting hydrophobic interactions between methoxyl groups, while the low pH is required to reduce dissociation of carboxyl groups, thus diminish electrostatic repulsions.

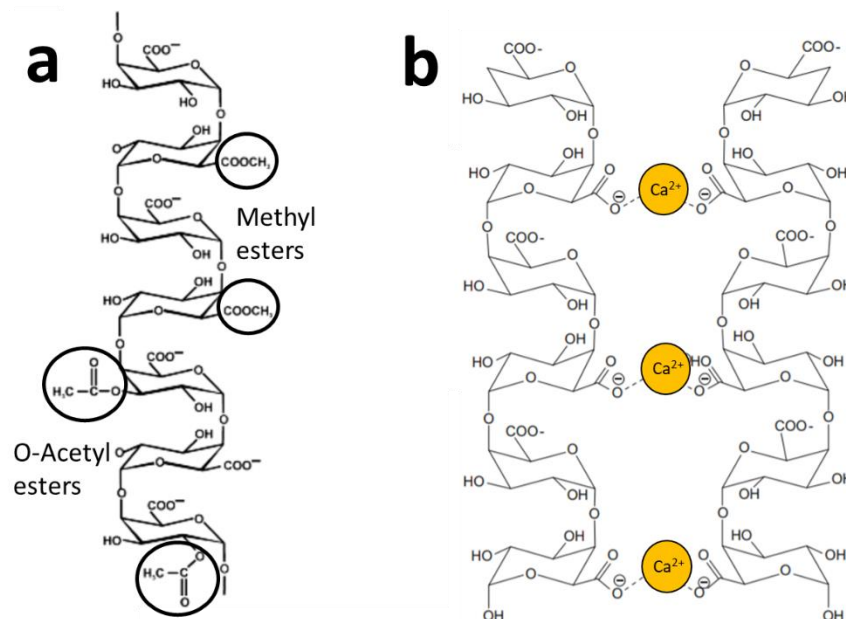


Figure 14. (a) Structure of HG showing the methyl esterified- and the O-acetyl esterified groups. (b) A suggested egg-box model of calcium crosslinking in HG.

Low methoxylated pectin (LM pectin) forms a gel in the presence of divalent metal ions such as calcium (Figure 14b). In this case, ionic linkages are formed via calcium bridges between dissociated carboxyl groups (Thibault and Ralet 2003). However, in case of pectin, the most favorable association is better described as a “shifted” egg-box, since one of the chains is slightly shifted with respect to the other (Braccini and Pérez 2001). Egg-boxes formed between two neighboring chains are stabilized by VdW interactions and hydrogen bonds in addition to electrostatic interactions (Braccini and Pérez 2001, Thibault and Rinaudo 1986).

Furthermore, it was found that a minimum number of 6-14 non-methyl esterified GalA units residues is required for the formation of egg-box pattern (Fraeye, et al. 2010).

Gelation of LM pectins has been found to be influenced by several parameters which can be denoted as intrinsic and extrinsic parameters. Intrinsic parameters refer to pectin structural characteristics, such as the amount and distribution of methyl esters (also called degree of blockiness), chain length, pectin side chains, and substitution with acetyl groups. The term extrinsic parameters refer to environmental conditions, such as Ca^{2+} and pectin concentration, pH, and temperature (Fraeye, et al. 2010, Mohnen 2008).

In addition, the biosynthesis and modification of homogalacturonan have recently emerged as key determinants of plant growth, controlling cell adhesion and organ development (Pelloux, et al. 2007). De-methyl-esterification of homogalacturonan occurs through the action of the ubiquitous enzyme ‘pectin methyl-esterase’ and have an important effect on the mechanical properties of the growing plant (Wolf, et al. 2009).

1.2.4. From lipids to membranes to vesicles

1.2.4.1. Chemical structure of lipids

Lipids are part of the large family of amphiphilic molecules which consist of a hydrocarbon chain (tail) and a polar group (head). Several groups of lipids exist in plants and they are classified by their chemical structure: glycerophospholipids, cholesterol, and sphingolipids. In this study, we focus mainly on glycerophospholipids which contain two hydrophobic tails connected by a glycerol to a hydrophilic head composed of a phosphate group and a polar group. (Figure 15)

The chemical nature of the polar group determines the net charge of the lipid. Phosphatidylcholine (PC) and phosphatidylethanolamine (PE) carry both positive and negative charges on the hydrophilic head while phosphatidic acid (PA), phosphatidylglycerol (PG), and phosphatidylserine (PS) are negatively charged.

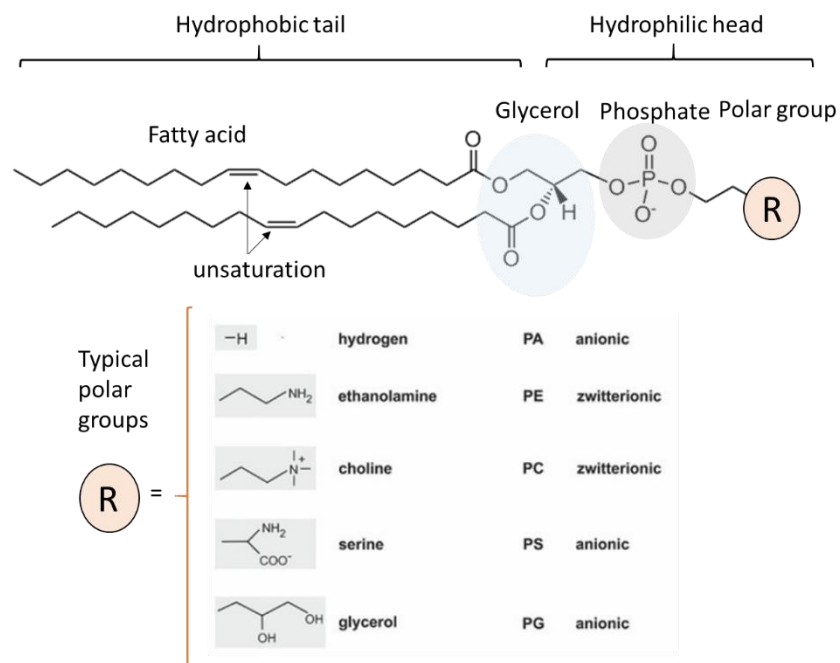


Figure 15. General chemical structure of phospholipids, showing the hydrophobic tail region connected with a glycerol group (light blue) to the hydrophilic head, a phosphate group (grey) and a polar group (R), which determine the net charge of the lipid.

1.2.4.2. Self-assembly of lipids

Due to their amphiphilic nature, lipids self-assemble into various structures above a critical micellar concentration (CMC) in aqueous medium, in order to minimize the contact of the hydrophobic tail with the surrounding water. The types of formed structures depend on the geometry of the lipid head and the hydrophobic tail, which is expressed as a dimensionless packing parameter CPP , given by $CPP = \frac{V}{a_0 l_c}$, where V is the hydrophobic tail volume, l_c is the fully extended hydrophobic chain length, and a_0 is the optimal cross-section area of the polar head group (Eeman and Deleu 2010, Israelachvili, et al. 1977).

Single-chained lipids with large head-group ($CPP < 1/3$) form spherical micelles, those with $CPP < 1/2$ form cylindrical micelles while phospholipids, which are usually doubled tailed and have a packing parameter of 0.5-1, form planar or flexible bilayer structures, the latter termed vesicles (Figure 16).

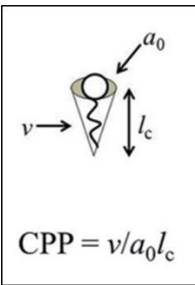
	Critical Packing Parameter ($v/a_0 l_c$)	Critical Packing Shape	Structures Formed
 $CPP = v/a_0 l_c$	$< 1/3$	Cone	Spherical micelles
	$1/3 - 1/2$	Truncated cone	Cylindrical micelles
Double-chained lipids with large head-group areas, fluid chains: <i>PC, PS, PG</i>	$1/2 - 1$	Truncated cone	Flexible bilayers, vesicles
Double-chained lipids with small head-group areas, anionic lipids in high salt, saturated frozen chains: <i>PE, PS+Ca</i>	~ 1	Cylinder	Planar bilayers
	> 1	Inverted truncated cone or wedge	Inverted micelles

Figure 16. Self-assembled structures of amphiphilic molecules and their packing parameter (Israelachvili, et al. 1977, Israelachvili 2015). Double chained phospholipids have a packing shape of a truncated cone or a cylinder and self-assemble to form bilayers.

In the present study, we will mainly focus on bilayers (yellow frame in figure 16), which are the main form of biological membranes.

1.2.4.3. Physical states of lipid membranes

In aqueous medium, lipid bilayers can occur under different physical states, characterized by the lateral organization, the molecular order and the mobility of the lipid molecules within the bilayer. Physicochemical parameters such as ionic strength, pH and temperature, among other factors such as the chemical nature of the lipid components and the presence of sterols, can strongly affect the nature of the phases and the transitions between them. Differential scanning calorimetry (DSC) and X-ray diffraction (XRD) studies have shown that several main phases of lipid membrane exists (Eeman and Deleu 2010, Janiak, et al. 1979) as well as characteristic phase transitions between them. Figure 17 shows the different phases and transitions that can be observed for lipid bilayers.

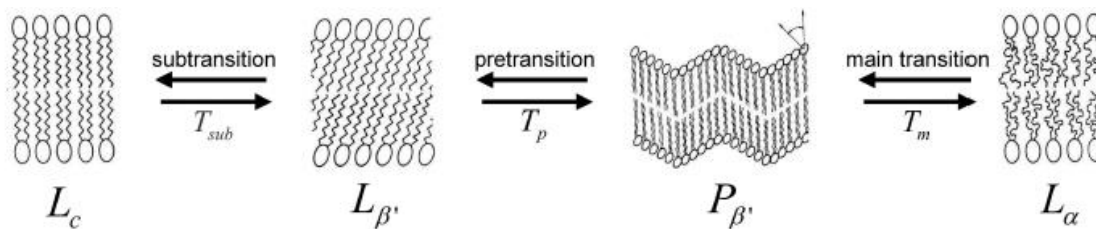


Figure 17. Main phases and transitions of lipid membranes showing the crystalline phase (L_c), the tilted gel phase ($L_{\beta'}$), the ripple gel phase ($P_{\beta'}$) and the fluid phase (L_{α}).

In the crystalline phase (L_c), the lipids are arranged on a two-dimensional lattice in the plane of the membrane, characterized by an extended frozen chain with very low lateral and rotational diffusion. The transition between the crystalline phase and the gel phase is termed T_{sub} . In the gel phase, two ordered phases exist: referred to as $P_{\beta'}$ (rippled gel phase) and $L_{\beta'}$ (tilted gel phase). The lateral diffusion of lipids is increased and the surface area decreases compared to the crystalline phase. The transition between the gel and fluid phases occurs at a specific temperature called thermotropic phase transition (T_m). The phase transition temperature of a membrane lipid depends

on the nature of its hydrophobic moiety such as chain length and degree of unsaturation. In the fluid phase, also called liquid-disordered phase (L_α , sometimes noted as L_d), the hydrophobic chains are less extended and are free to move.

The lateral and the rotational diffusion modes are more common in fluid lipid bilayers than in the crystalline or gel phase. In the presence of cholesterol, the fluid phase can increase its order and transform to liquid ordered phase (L_o) which shares the characteristics of both gel and fluid phases.

1.2.4.4. Permeability

The transport of substances across a lipid membrane can be classified into two categories: active and passive transport. While active transport requires input of energy that transports the target molecules in the direction opposed to the concentration gradient, passive transport occurs via an entropy-driven, nonspecific diffusion process of the molecule across the membrane.

The lipidic membrane is semipermeable, meaning that certain species of molecules can passively pass through the membrane. The physical property characterizing this process is termed permeability, and it represents the flux of molecules through a surface unit of the membrane. Figure 18 shows typical permeability values of several molecules through a typical lipid membrane.

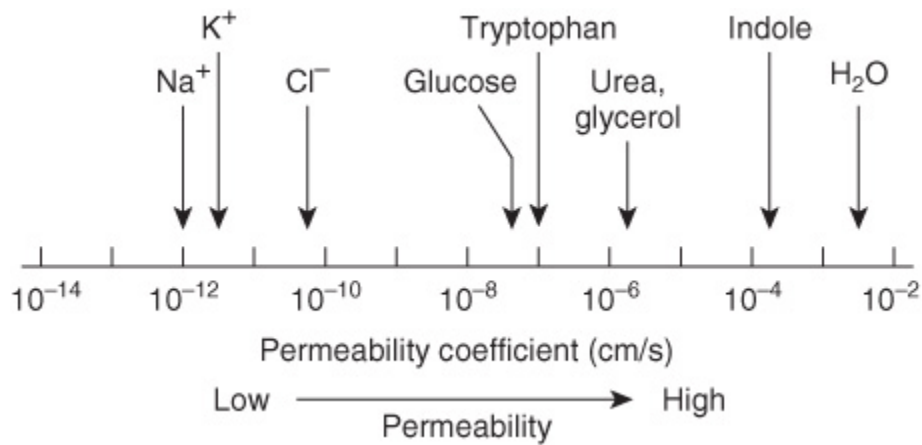


Figure 18. Typical membrane permeability values of various molecules.

In addition to the type of molecule, membrane permeability to a given substance can be influenced by several parameters such as temperature, lipid type, and physical state (liquid or gel) as well as the presence of cholesterol. Permeability can be determined using osmotic shock experiments (Bernard, et al. 2002, Boroske, et al. 1981, Mathai, et al. 2008).

Since large solute molecules such as glucose and sucrose cannot passively cross the membrane, a difference in the solute concentration creates a difference in the osmotic pressure, Π , between the interior and exterior of the membrane, according to the following equation:

$$(Eq. 1) \quad \Pi = RT \ln \frac{C_{in}}{C_{out}}$$

Where C_{in} and C_{out} are the solute concentration in and out of the membrane respectively, R is the ideal gas constant, and T is the temperature. Due to the difference in concentration, water molecules will migrate, in (hypotonic solution) or out (hypertonic solution) of the membrane until a new equilibrium is reached, a process that is called osmotic shock.

Table 2. Permeability values from osmotic shock experiments

Lipid	Permeability, $\mu\text{m s}^{-1}$	Reference
Egg lecithin	17-47	(Boroske, et al. 1981)
Egg lechithin +cholesterol 10 %	5-10	(Bernard, et al. 2002)
DOPC	150	(Mathai, et al.
DOPC+Chol 10 %	145	2008)
DOPC +Chol 20%	115	
DOPC + chol 40%	68	

This property can be exploited to study the transport of water across the lipidic membrane by applying a difference in the solute concentration between the interior and exterior of the membrane. Permeability can be thus determined experimentally using osmotic shock experiments, by directly measuring the radius, or by using fluorescence of encapsulated molecules, or chromatography (Taupin, et al. 1975). Table 2 shows typical permeability values for water across different membranes obtained with osmotic shocks experiments.

The reported permeability values were evaluated from osmotic shock experiments by directly measuring changes in vesicle diameter (Bernard, et al. 2002, Boroske, et al. 1981) or by measuring the self-quenching of entrapped carboxyfluorescein.(Mathai, et al. 2008) The variation in the reported values may emerge from the variation in experimental methods used to quantitatively determine the permeability.

1.2.4.5. Lipids of the plant plasma membrane

The plant plasma membranes display a very complex composition in terms of lipids. In plants, three major classes of plasma membrane components are the glycerophospholipids, (30-60 mol % of the total lipids) the sphingolipids (6-30%) and sterols (20-50%) depending on plant species and organs. (Cacas, et al. 2016, Gronnier, et al. 2016, Grosjean, et al. 2015) Figure 19 shows the structure of three major classes of lipids found in plant cell membranes.

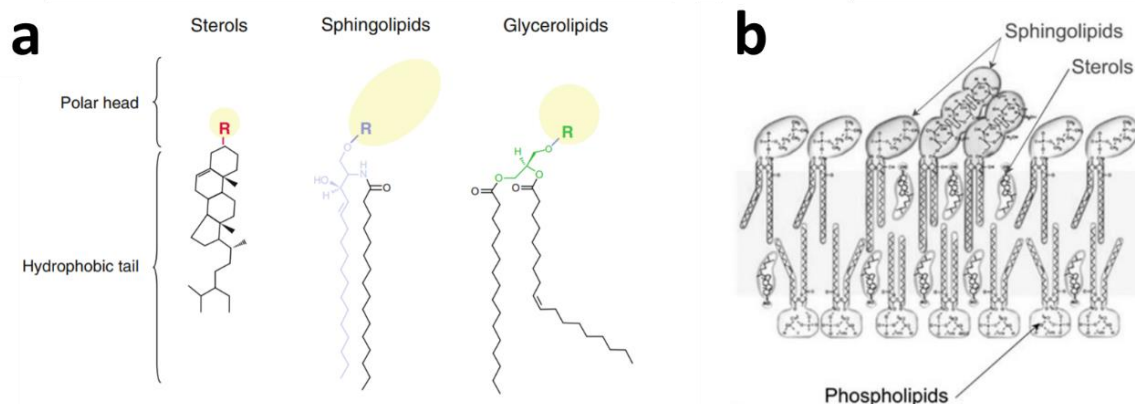


Figure 19. (a) Chemical features of the three major classes of plant plasma membrane lipids. The polar heads are highlighted in yellow. (b) A drawing of the plasma membrane composition.

Glycerophospholipids are composed of a glycerol backbone on which two fatty acid chains are esterified. The third carbon atom of the glycerol backbone supports the phospholipid polar head group, which is composed of an alcohol molecule (choline, ethanolamine, serine, glycerol or inositol) linked to a negatively charged phosphate group. Sphingolipids are composed of a sphingosine (or phytosphingosine) base, on which is linked a relatively long (up to 24 carbon atoms) saturated fatty acid chain. Acylated sphingosines are referred to as ceramides. Sphingomyelin and glycosphingolipids result from the attachment of a choline molecule and an oligosaccharide to the hydroxyl group of ceramides, respectively. Sterols are a particular class of membrane components. While the hydrophobic moiety of most membrane lipids is constituted of relatively long aliphatic chains, the one of sterols is composed of polycyclic structures (Eeman and Deleu 2010).

To overcome the complexity of the biological membranes, 2D and 3D model membranes, containing both natural and synthetic lipids, offer a good *in vitro* model for the study and potential use of the plant plasma membranes (Castellana and Cremer 2006, Eeman and Deleu 2010, Fenz and Sengupta 2012). Let us revise the main characteristics of such models.

1.2.4.6. Lipid membrane model systems

Supported lipid bilayers

Supported Lipid Bilayers (SLBs) are lipid bilayers supported onto a solid surface which can be curved (beads)(Mornet, et al. 2005) or flat (mica, glass, or silicon oxide wafers) (Richter and Brisson 2005, Richter, et al. 2006), depending on the desired geometry. Supported lipid membranes confined to the surface of a flat solid support can be characterized using a variety of surface sensitive techniques such as atomic force microscopy (AFM), optical ellipsometry, quartz-crystal microbalance (QCM-D), and neutron reflectivity (NR) (Castellana and Cremer 2006, Richter, et al. 2003, Richter and Brisson 2005, Richter, et al. 2006).

Several methods for flat SLB preparation exist as shown in Figure 20. One common method is the Langmuir-Blodgett technique (Rubinger, et al. 2006). Following the transfer of a lipid monolayer spread at the air-water interface of a Langmuir trough onto a solid support, the same support is brought into contact with the interface a second time, either vertically (Langmuir-Blodgett) or horizontally (Langmuir-Schaefer), resulting in a supported lipid bilayer (Figure 20a and b). Another method for preparing flat SLBs is the fusion of small unilamellar vesicles (SUVs) onto a hydrophilic solid support (Figure 20c). The fusion process involves the adsorption of the SUVs on the surface, followed by their deformation, flattening, and rupture. The fusion of the edges of the bilayer patches through hydrophobic interactions gives rise in final to a continuous supported lipid bilayer.

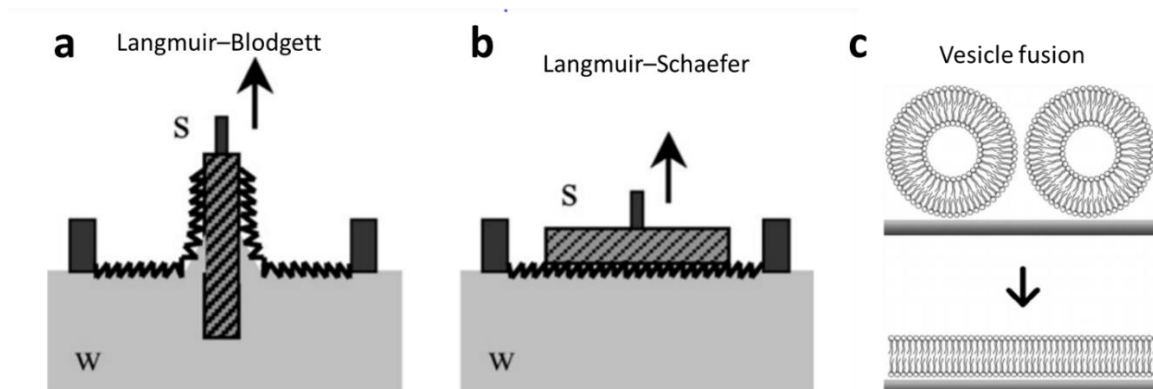


Figure 20. (a) Scheme of Langmuir-Blodgett (b) Langmuir-Schaefer experimental setups, showing the water lower phase (w), the lipids on the air/water interface (bold line) and the substrates during the transfers. (c) Vesicle fusion scheme.

Due to their versatile properties and relative ease of preparation and characterization, SLBs are commonly used as biomimetic models to study biological phenomena (Castellana and Cremer 2006, Migliorini, et al. 2014, Sandrin, et al. 2010).

Lipid vesicles

Lipid vesicles or "Liposomes" are formed when thin lipid films (single lipid component or mixture of different types of lipids) are hydrated at temperatures above the melting temperature of the lipids which compose them, and stacks of bilayers become fluid and swell. During agitation, the hydrated lipid sheets detach from the surface they were deposited on and spontaneously close to form multilamellar vesicles (MLVs) (Figure 21).

These vesicles are composed of several concentric lipid bilayers, each separated by water. The size of these MLVs can range from one to several microns and can be reduced and homogenized by performing several freeze-thaw cycles (Lasic 1988, Lichtenberg and Barenholz 1988). In the case of one bilayer separating the internal and external solvent these structures are called, with respect to their size, small, large, and giant unilamellar vesicles (SUV, LUV, and GUV respectively).

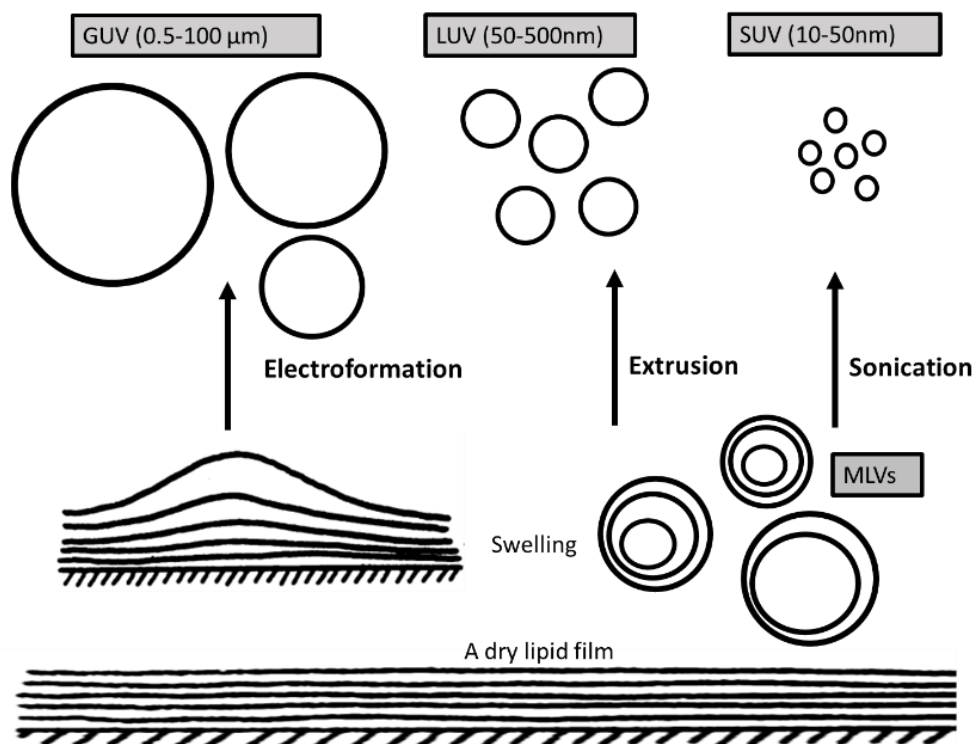


Figure 21. General scheme showing the main methods of vesicle preparation starting from a dry lipid film. Following the spontaneous or induced swelling, different types of vesicles can be formed. They are defined by the number of bilayers separating the interior and the exterior of the vesicle (multi or unilamellar), and their size (Giant, Large, and Small Unilamellar vesicles, referred to as GUV, LUV, and SUV, respectively).

According to the method of preparation, different types of vesicles can be obtained (Reeves and Dowben 1969, Szoka Jr and Papahadjopoulos 1980, Walde, et al. 2010)(Figure 21). The homogenization and extrusion of MLVs through an extruder equipped with a polycarbonate membrane with nano-sized pores gives rise to the formation of large unilamellar vesicles (LUVs) with a mean diameter of 50-500 nm, corresponding to the mesh size of the polycarbonate membrane. Small unilamellar vesicles (SUVs) are formed by sonicating the MLVs or LUVs in a classical bath sonicator or using a probe sonicator. The SUVs usually exhibit a mean diameter of 10 to 50 nm and due to their high membrane tension, they are not stable and generally tend to fuse to create larger vesicles.

GUVs can be obtained by hydrating a dried lipid film at temperatures above the crystalline to liquid-like lipid phase transition either for a long period of time (up to 36

h) (*i.e.* gentle hydration method) or in presence of an external electrical field (*i.e.* electroformation technique) (Rodriguez, et al. 2005, Walde, et al. 2010). The size of the GUVs allows their visualization by optical microscopy such as fluorescence and phase contrast microscopy, as well as their micromanipulation.

Besides their application in the fields of drug delivery (Peetla, et al. 2009) and gene therapy (Lasic and Templeton 1996), lipid vesicles are versatile biomimetic model of membranes and they commonly used for studying biological environments at the nanometric and micrometric scales (Eeman and Deleu 2010, Szoka Jr and Papahadjopoulos 1980).

After revising the main building blocks of the PCW and some typical analogues used in biomimetic models, we will now focus on the way these building blocks organize to form the multinetwork architecture of the PCW.

1.3. Plant cell wall architecture

Plant cell walls have been in use for thousands of years by humans for food, construction, and tools. Nevertheless, understanding of how polysaccharides and structural proteins are organized into plant cell walls is important for elucidating the structure-property relationships of such a complex system. It is only in the last few decades, with the improvement of characterization techniques, such as microscopy and spectroscopy, that the PCW structure and composition could be investigated. From these studies, different models have emerged, showing how the different polysaccharides are organized in the plant cell wall.

One of the first models suggested by Albersheim and carrying his name (Keegstra, et al. 1973) was deduced from the degradation of the cell wall by enzymes, followed by the chemical analysis of the purified fragments. This model, shown in figure 22, included for the first time the basic elements namely: cellulose and xyloglucan as a stratified structure providing both support and flexibility to the growing plant.

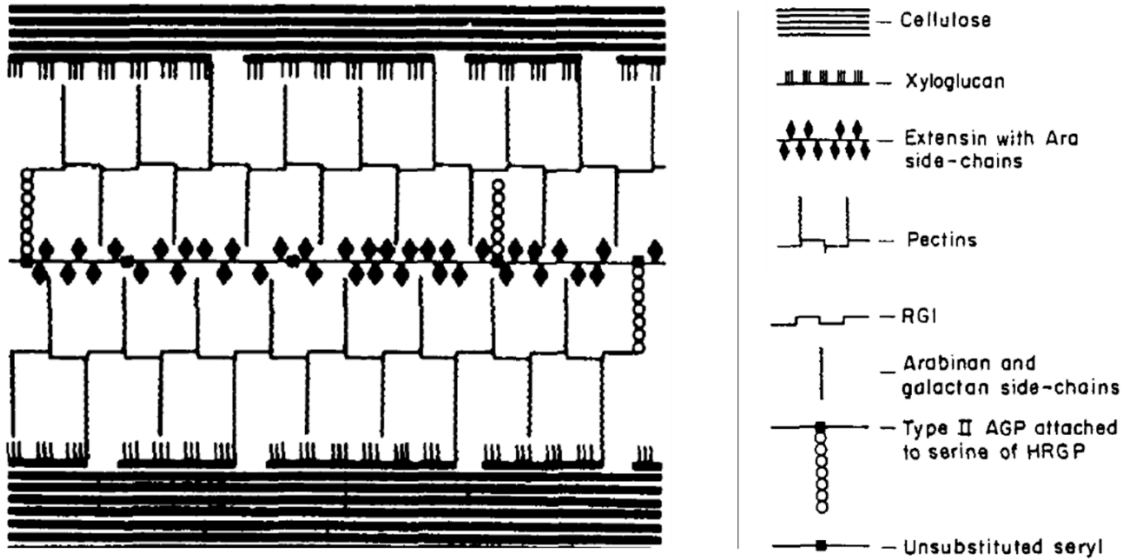


Figure 22. The Albersheim early model of primary plant cell wall. (Keegstra, et al. 1973)

In this early model, the matrix polymers were all covalently linked to one another and connected to the cellulose microfibrils. However, elaborated studies on the interactions between the basic components were still lacking. Advances in the determination of polymer structure and the preservation of its structure for electron microscopy in the following two decades led to the “tethered network” model of Hayashi (Hayashi 1989) and Fry (Fry 1989) where single xyloglucan chains spanned the gap between microfibrils and tethered them together. These models, further developed by Carpita and Gibeaut (Carpita and Gibeaut 1993) provided a more comprehensive view of how polysaccharides and structural proteins were organized within the primary PCW. This model, shown in Figure 23, illustrates the complexity of the PCW architecture.

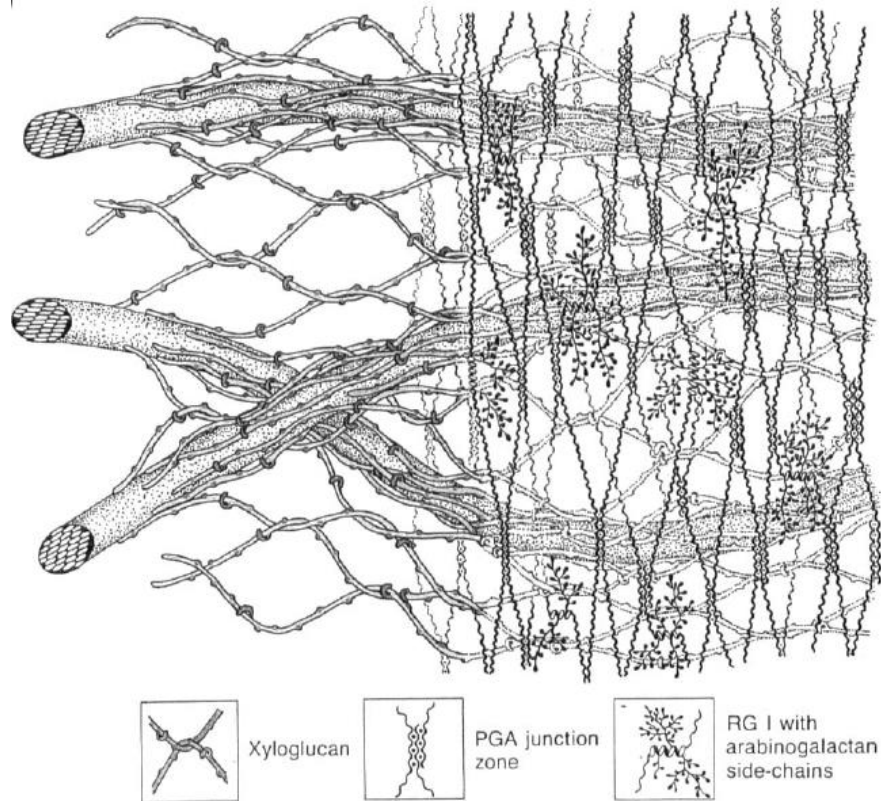


Figure 23. The model of primary plant cell wall proposed by Carpita and Gibeaut (Carpita and Gibeaut 1993).

Figure 23 shows the model proposed by Carpita and Gibeaut. According to their revised and still more elaborated model, cellulose microfibrils contain non crystalline regions that may be formed by entrapment of hemicelluloses such as xyloglucan in the early stages of cellulose synthesis. Xyloglucan can also bind to the surface of cellulose and may link two microfibrils together. Although the side chains of xyloglucan interfere with bonding of one glucan backbone to other glucans, they may twist such that short regions of the backbone form a planar configuration suitable for bonding to cellulose. In this model, pectins form a space-filled hydrophilic gel between microfibrils.

In 2001, Cosgrove published a review which describes the models obtained so far and in 2004 Somerville showed a scaled model based on NMR and electron microscopy.

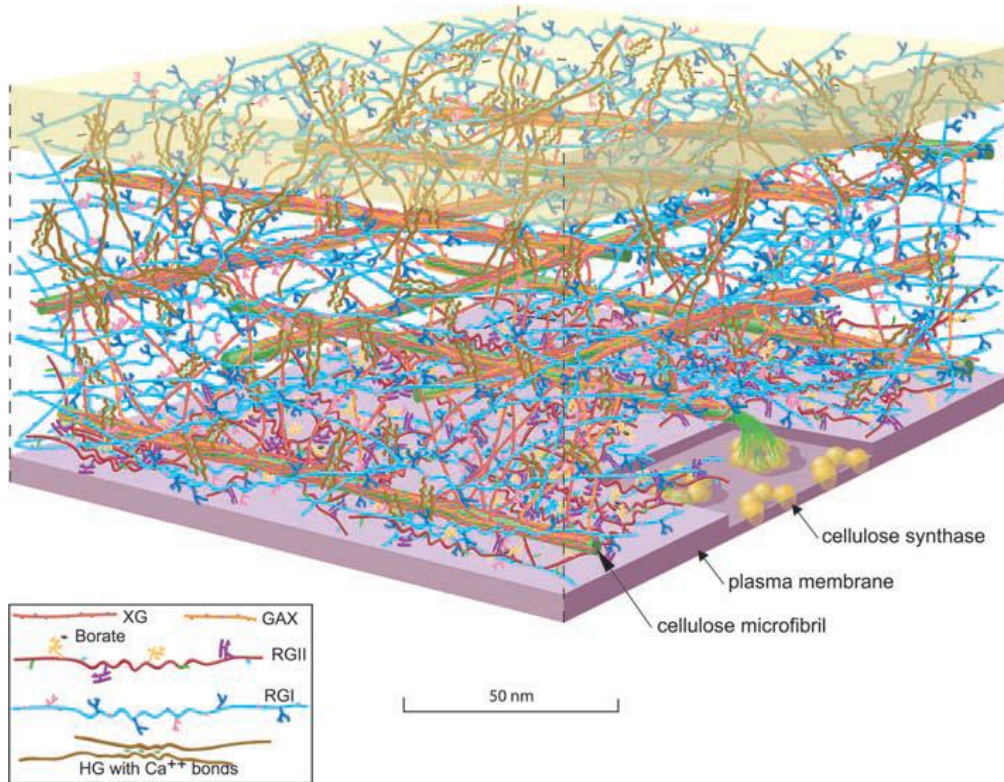


Figure 24. Scale model of the polysaccharides in an Arabidopsis leaf cell. The figure is an elaboration of a model originally presented by McCann and Roberts (Somerville, et al. 2004).

A recent paper by Cosgrove puts forward a model that introduces the concept of biomechanical hotspots (Cosgrove 2014). His model is based on recent developments in enzyme activity assays together with advanced characterization techniques such as AFM and solid-state NMR. According to this model, cellulose fibrils are linked via direct load-bearing junctions, mediated via physical bonding by xyloglucan. This idea is in accordance with common depictions of primary cell walls which show well-spaced microfibrils kept apart by matrix polysaccharides, using never-dried walls under water. Images obtained by Zhang et al. (Zhang, et al. 2014) (figure 25a) contribute to the development of the current model (figure 25b).

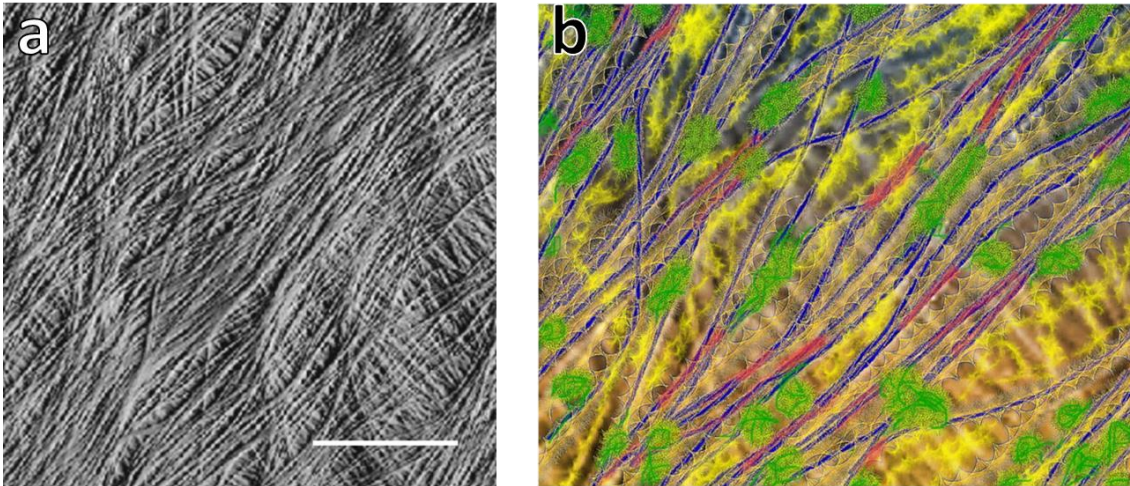


Figure 25. (a) Tapping mode AFM image of onion epidermis cell wall surface, showing microfibril and matrix detail, scale bar 500nm (Zhang, et al. 2014) (b) Artistic depiction of the cell wall, based on the microfibril arrangement shown in (a), Cellulose microfibrils in blue. Potential biomechanical hotspots in red, pectins are represented in yellow. Xyloglucans are shown as green coiled structures anchored to microfibril surfaces at limited locations.

Figure 25b shows the proposed biomechanical hotspot model in which red regions indicate potential biomechanical hotspots, where two or more microfibrils merge into close contact. Highly dispersed, mobile pectins are represented in yellow and xyloglucans are shown as green-coiled structures anchored to microfibril surfaces at limited locations.

This model was supported by enzymatic assays and multidimensional ss-NMR studies showing that only small portions of the fiber were actually in contact with XG (figure 25b – red zones). In addition, recent ss-NMR studies have shown possible proximity of cellulose and pectin in the primary wall. It is not clear whether such proximity is due to molecular crowding rather than to direct physical interactions.

In all models, a very complex picture of the primary cell wall organization is demonstrated raising the question of how is the plant able to regulate growth and expansion in such a complex and crowded environment.

Several growth regulation mechanisms exist, each targeting a different component or network, each with its own loosening enzymes. These mechanisms will be further discussed in the following section.

1.4. Growth and expansion

The growing cell wall in plants has the conflicting requirements of being strong enough to withstand the high tensile forces generated by cell turgor pressure while selectively yielding to forces inducing wall stress relaxation, leading to water uptake and polymer movements underlying cell wall expansion. The wall loosening mechanisms can be divided into three main groups, as summarized in the following table:

Table 3. Wall loosening mechanisms

Enzyme	Activity	Reference
Expansin	Break bonds between cellulose and hemicellulose	(McQueen-Mason, et al. 1992)
Endoglucanase	Hydrolyses hemicelluloses	(Levy, et al. 2002)
Pectin methyl esterase Homogalactouronase	Demethylation Shortening the HG chain	(Peaucelle, et al. 2011)

The cell wall extensibility permits an irreversible expansion of its surface area by 10 to 1000-fold between its initial state and the cessation of growth at maturity. Such expansion involves selective wall loosening to enable irreversible extension.

Summary

As can be seen from this short review, our understanding of the structure and composition of the plant cell wall did not change much since the 70s, however the structure function relationships are still not clear. This is due to the lack of a simple model for the plant cell wall, which emphasizes the advantage of in vitro model systems. These systems enable to avoid the complexity of the biological living environment, thereby allowing to study a given process, or effect, in a direct and simplified manner.

1.5. Cell wall mechanical properties

The growing plant cell wall has to adapt to two conflicting requirements: on the one hand, the wall must be strong enough to resist hydrostatic pressure exerted by the cytoplasm (turgor pressure), and on the other hand, it needs to be flexible enough to allow cell growth and expansion. As we've seen previously in this chapter, the wall accommodates these requirements through its composite and dynamic structure, presenting stiff structural elements, such as the cellulose microfibrils, embedded in a softer matrix of polysaccharides. While the main components of the cell wall are well identified (Albersheim, et al. 2011, Ochoa-Villarreal, et al. 2012), their individual contribution to its mechanical properties is not completely understood (Bidhendi and Geitmann 2015, Hamant and Mouliat 2016).

The remarkable features of plant cells and tissues have drawn interest in recent years, among biologists and biophysicists studying plant morphogenesis and development, as well as among engineers and medical scientists who regard plants as smart materials, that can be utilized as scaffold or inspire biomimetic design (Hambardzumyan, et al. 2011, Singh, et al. 2012). For all those communities a quantitative understanding of plant cell mechanical properties is essential.

Experimental techniques to study PCW mechanical properties in planta, typically involves the application of a deforming force on the cell/tissue and measuring the response to that force. The deformations can be in the form of stretching, compression, bending, or shear of the material. Depending on the studied structure and the property

one wishes to probe, different approaches have been employed to deform individual cells or cellular structures and measure their response to that deformation. The resulting deformations can be either local or global, and they can address either the properties of an individual cellular component such as the wall or the membrane, or the cell as a whole.

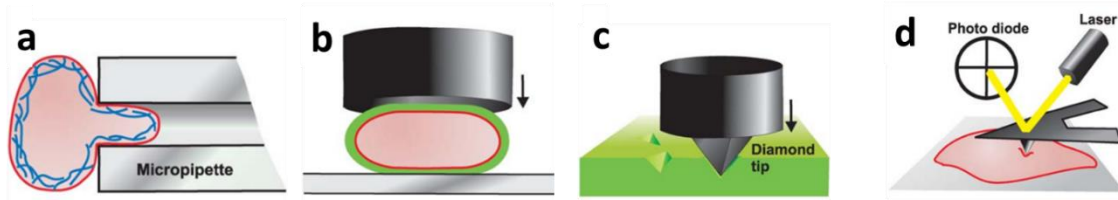


Figure 26. Schematic drawings of cell mechanical measurement techniques. The plasma membrane is shown in red, the cell cytoskeleton in blue, and the cell walls in green. (a) Micropipette aspiration- a microcapillary is placed on the cells surface, and a suction pressure is applied to force the cell into the micropipette. (b) Cell compression - a single cell is compressed between two surfaces. (c) Micro indentation - a diamond tip is used to locally deform a material with a calibrated force. (d) AFM nano-indentation - the deflection of a cantilever in contact with a sample is recorded and the mechanical properties are extracted with the help of fitting the force-deformation curve with empiric physical models. Adapted from (Geitmann 2006).

Figure 26 shows several characterization methods. In the following part, we briefly describe each of these methods.

Micropipette aspiration

This technique is based on measuring the suction pressure necessary to partially or wholly draw a single cell into a micropipette (Fig. 26a). The diameter of the pipette may range from less than 1 μm to 10 μm and the applied pressures are as small as 0.1-0.2 $\text{pN } \mu\text{m}^{-2}$ (Hochmuth 2000). While widely used to determine viscoelastic properties of mammalian cells, this technique has not been used systematically for assessing plant cells mechanics. This is due to either technical difficulties or to the inability to produce forces strong enough to act against the cell wall and the turgor pressure (Bidhendi and Geitmann 2019).

Compression of single cells

Another way to measure the mechanical properties of plant cells is to directly compress an isolated cell between two flat surfaces (Figure 26b). In cases of simple cell geometries, such as a sphere or an ellipsoid, force-deformation curves can be predicted from an analytical model and then fitted to the experimental data.

In such experiment, the deformation is global rather than local and thus includes contributions from the turgor pressure as well as from the cell wall mechanical properties. (Geitmann 2006, Routier-Kierzkowska and Smith 2013).

Indentation techniques

Indentation techniques involve indenting a sample using a tip with known geometry and recording force-indentation data, from which the mechanical properties, such as Young's modulus or stiffness, can be extracted (Figure 26c). Micro indentation is sensitive to the turgor pressure, cell wall elasticity, the tip geometry and the indentation angle. When large indenters are used, the deformation of the cell is global and modeled as an elastic shell. When smaller indenters are used, both local and global deformations influence the results (Routier-Kierzkowska and Smith 2013).

Nano indentation is used to deform cells wall locally and to determine its young's modulus in the direction normal to the surface by using an atomic force microscope (AFM) tip as a probe. Besides being a topographical imaging tool, AFM can probe local mechanical properties by applying a controlled force and measuring the deflection of a calibrated cantilever providing information on the mechanical response of the sample.

AFM-based studies of mechanical properties are performed by collecting force-indentation curves at various cell-surface points. Each curve comprises the approach and retraction of the AFM cantilever from the surface, while recording its deformation (Figure 26d). The resulting approach-retract curve is often compared to a reference curve and, following the determination of the contact point, the data is fitted to a mathematical model. Several models are available that are commonly used to extract the apparent Young's modulus, or bulk elastic modulus E , of the sample from the

loading–unloading curves. The modulus obtained using these methods is sometimes termed 'indentation modulus'.

A significant variation of probing tips exists in terms of shape and size (Fig. 27a). Knowledge of the tip geometry is crucial for data analysis as it directly determines the contact surface between the tip and the probed sample. If the indentation depth is small compared to the sample thickness, the measurement is believed to probe only the properties of the thin upper layer. In the case of the PCW, which is composed of many layers, this means that one only probes the thin upper layer composing the cell wall (figure 27d).

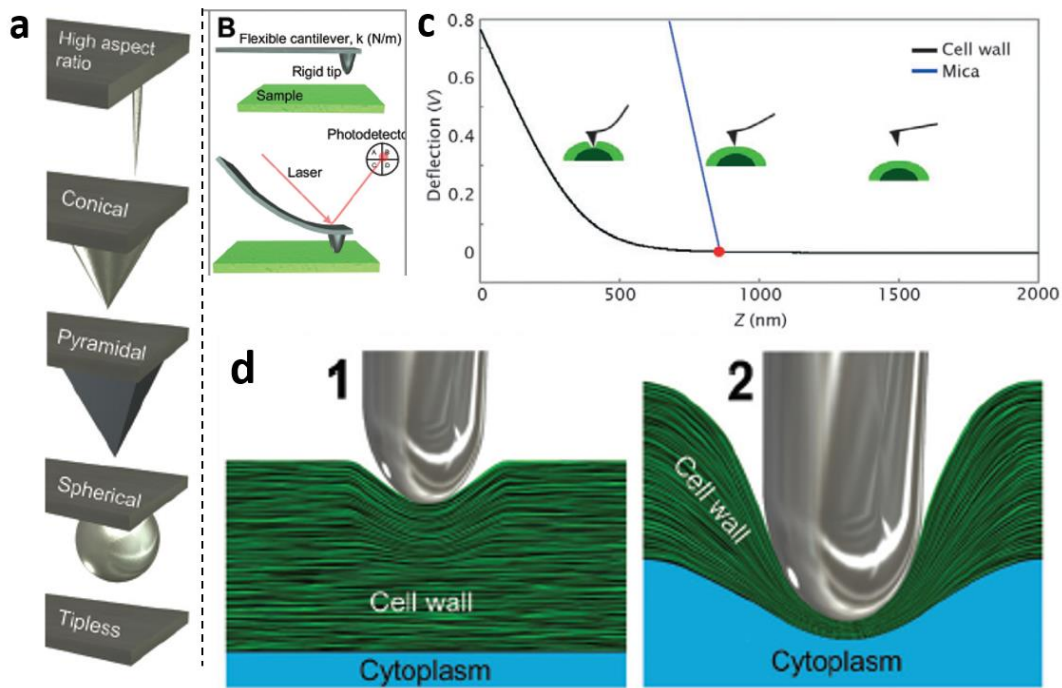


Figure 27. AFM indentation schematics. (a) Typical tip geometries used in AFM indentation experiments. (b) In a typical indentation experiment, the deflection of a flexible cantilever due to the contact with the sample is recorded. Changes in direction of the laser beam reflected off the surface of the cantilever allow measurement of applied force, and based on the measured cantilever bending spring constant (k), the mechanical properties of the sample can be extracted by fitting the data to a model. (c) A typical deflection curve obtained from primary cell wall of *A. Thaliana*. The 0 position on this axis is determined empirically by the user, and corresponds to the bending of the cantilever. In blue, a similar curve is obtained when approaching the cantilever on mica, a flat and stiff material that serves as a maximal stiffness reference (Milani, et al. 2011). (d) Nano indentation experiments of a plant cell. The depth of the indentation determines to what extent the turgor pressure (or the substrate in the case of 2D thin films) contribute to the measured forces (Bidhendi and Geitmann 2019, Geitmann 2006, Milani, et al. 2011).

Another important parameter is the cantilever spring constant, with values between $0.01\text{-}42\text{ N m}^{-1}$ being commonly used. The effect of the geometry on the data, in terms of probe dimensions, sample shape and wall thickness must be carefully considered. The modulus measured by indentation of anisotropic material is commonly thought to be an average of stiffness in different directions and often reported as the Indentation modulus or Young's modulus. Under the condition of indentation significantly smaller than the shell thickness, the Hertz or Sneddon models can be used depending on tip geometry and the depth of indentation (Figure 28).(Sneddon 1965)

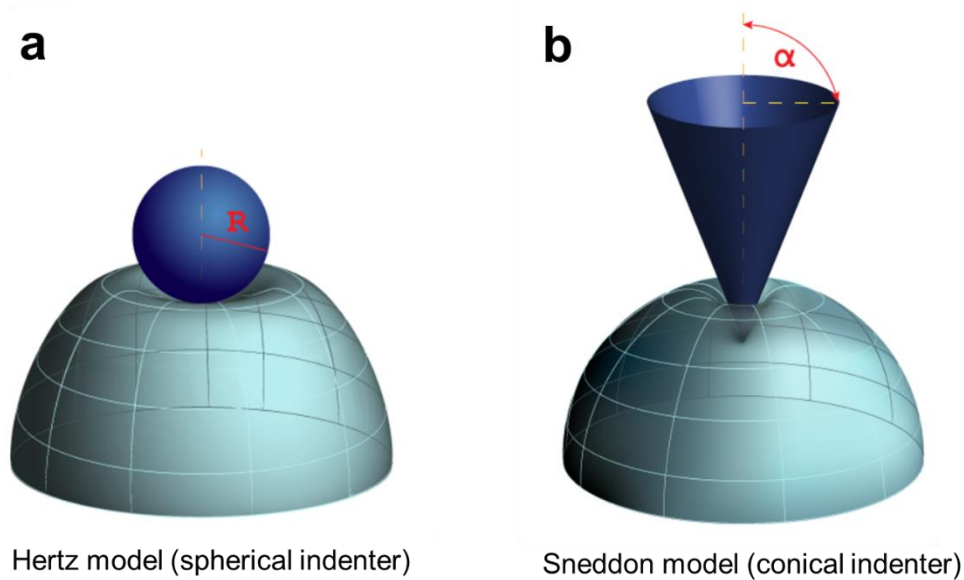


Figure 28. A scheme of Hertz (a) and Sneddon (b) mechanical models.

(Eq. 2) *Hertz model:*
$$E = \frac{4\sqrt{R}}{3(1-\nu^2)} \delta^{\frac{3}{2}}$$

(Eq. 3) *Sneddon model:*
$$E = \frac{2 \tan \alpha}{\pi(1-\nu^2)} \delta^2$$

Where R is the tip radius in the case of a spherical shaped tip, α is the opening of the cone δ is the indentation, ν is the Poisson ratio, for fully swollen hydrogel like materials, it is approximated as 0.3-0.5.

The geometry of the sample, cell, or organ can also have a significant effect on the data obtained, therefore values should preferably be reported and compared together with detailed experimental parameters.

Table 4 summarizes some main findings using nano-indentation, as well as the tip and cantilever characteristics.

Table 4. Young's modulus values of various types of plant cell walls obtained by AFM nano-indentation.

Type of cell	Modulus (MPa)	Cantilever spring constant (N/m)	Tip geometry, Radius (μm)	Reference
<i>A. thaliana</i> shoot apical meristems	1.5-5	0.16	Pyramidal, 10-40	(Milani, et al. 2011)
<i>A. thaliana</i> shoot apical meristems	0.1-0.7	0.52 for 5000 and 10-130 For 900-1100	Ball, 900-1000 5000	(Peaucelle, et al. 2011)
Epidermal cells/dark grown hypocotyl	0.1-0.4	1.5	Ball, 900-1100	(Peaucelle, et al. 2015)
cell wall of suspension-cultured <i>Arabidopsis thaliana</i>	0.1-1	0.06	unknown shape, 20	(Radotić, et al. 2012)
Suspension tomato cells	0.1 (Cone) 0.02 (Ball)	0.7 0.32	Conical, 0.02 Ball, 10	(Zdunek and Kurenda 2013)
Suspension cultured cells	0.01-10 (mean 0.7)	0.05-1	Ball, R<20 Conical	(Yakubov, et al. 2016)
Onion epidermis	~1-12	42	Ball 400	(Beauzamy, et al. 2015)
Shoot apical meristem	0.05-0.5	1.5 (nom. 10-130)	Ball, 900-1000 5000	(Braybrook and Peaucelle 2013)
Pollen tube	11 \pm 4	72	Ball, 400	(Burri, et al. 2019)

As can be seen from this summary, the Young's modulus values can span over several orders of magnitude. This is due to the diversity of experimental parameters and the different types of samples used for the different studies. In terms of probe characteristics, Zdunek et al. found different modulus for the same sample by using different cantilever spring constant and tip radius. For a ball shaped tip with a radius of 10 μm mounted on cantilever with a spring constant of 0.32 N m^{-1} the modulus was 20 kPa. This value was 5 times lower than for the modulus measured on the same sample using a cone shaped tip with diameter of 20 nm mounted on a cantilever with a spring constant of 0.7 N m^{-1} . Moreover, large variability regarding elastic properties ($>100\%$) among cells sampled from the same region in the sample was observed (Zdunek and Kurenda 2013).

In addition, different organs/cell types may have different stiffnesses. It was shown that modulus can vary even for the same type of cells during different stages of plant development (Radotić, et al. 2012).

Finally, we note several important parameters that needs to be considered when interpreting the results of an indentation experiment:

- (i) The Young's modulus is defined in the regions where the deformation is elastic and no residual deformation is observed. However, the polymeric matrix of the PCW could also contain regions where plastic deformation takes place. For example, by forcing two objects to a particle-particle separation where short range interaction takes place, the structure could collapse to a local energetic minimum, creating irreversible deformations that will not be retrieved when the force is removed.
- (ii) The cell wall is often considered mechanically as a homogenous material, when in fact it is a composite material similar to a fiber-reinforced gel. As such, varying indenter size, shape, and depth of indentation may reveal different properties of the composite. Small, shallow indentations may be more likely to reveal properties of the gel matrix, whereas larger deformations would involve the bending of cellulose fibers and cellulose-hemicellulose interactions.

- (iii) The Hertzian contact model and its variations, which are used to extract Young's moduli, is valid only for the indentation of homogenous, isotropic materials with infinite depth. This is rarely the case, in particular for plant cell walls. Moreover, due to the heterogeneity in properties within a given sample, extensive statistical data processing is required to obtain meaningful data.

Despite these limitations, indentation methods are still commonly used to qualitatively estimate the elastic modulus of plant cells wall.

These points also emphasize the need for developing in vitro model systems that can help relating the structure-property relationships in plant cells wall without the complexity of the biological environment. The next part will revise some of the existing in vitro PCW model systems.

1.6. Biomimetic models in 3D and 2D

PCW analogues can be roughly divided in two groups:

- (i) **2D constructs:** These are multilayered films of polymers, particles or their combinations, deposited in a consecutive fashion on a solid substrate.
- (ii) **3D constructs:** These are multilayered shells deposited on a spherical solid (particles) or liquid (emulsion/membrane) support.

2D constructs can provide a simple model in terms of the composition of cell wall, while 3D constructs include also the spherical geometry of real cells. In both cases, the Layer by Layer (LbL) technique is commonly used to create the structures.

1.6.1. General aspects of layer by layer (LbL)

Pioneered by Decher in the 90s, the LbL technique is used to create multilayer films on solid supports, by taking advantage of the electrostatic interactions between

oppositely charged polyelectrolytes (Decher, et al. 1992, Decher and Schlenoff 2006). Figure 29 shows a scheme of a LbL deposition of polyelectrolytes on solid substrate.

LbL has been widely used for the preparation of thin films from weakly- and strongly charged polyelectrolytes and it has been extended to other materials such as proteins, colloids, and biopolymers (Finnemore, et al. 2012, Tang, et al. 2006) where the driving force for adsorption can be other than electrostatic binding.

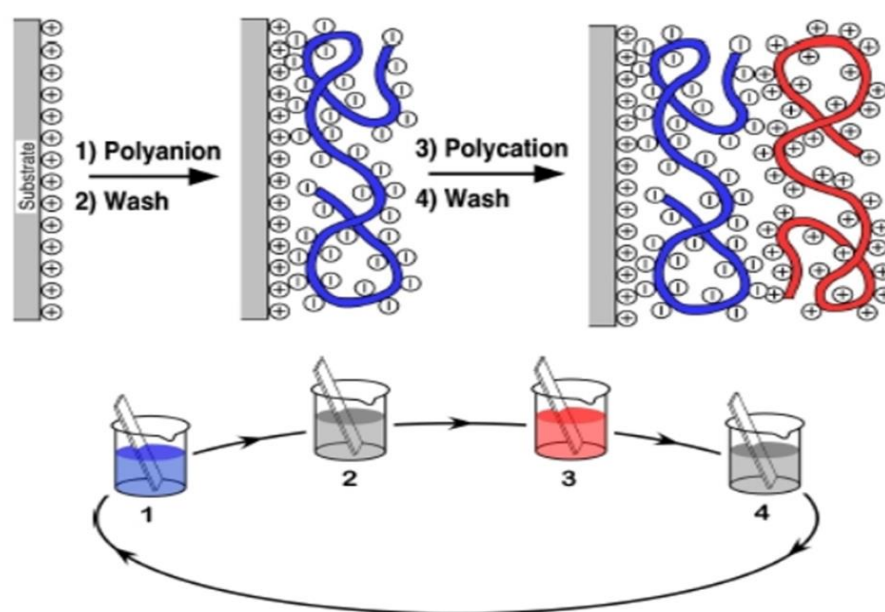


Figure 29. Schematics of a LbL deposition of polyelectrolytes on solid substrate, Steps 1 and 3 represent the adsorption of a polyanion and polycation respectively and steps 2 and 4 are washing steps. (Decher 2012)

The resulting film properties depend on numerous factors such as polyelectrolyte charge density (Glinel, et al. 2002) or conformation (Schoeler, et al. 2006), the particle or polymer concentration, or the solutions ionic strength. (Wong, et al. 2009) Moreover, the effect of the deposition method and the incorporation of intermediate drying steps can have a profound effect on the resulting structures.

The deposition can be done either from bulk solutions (dip-coating) or by induced deposition such as centrifugation (spin coating) and spraying. (Li, et al. 2012) In dip

coating, the deposition of a polymer layer involves the diffusion, adsorption and rearrangement of polymer chains, and may take up to several tens of minutes while in induced deposition such as spin coating or spraying, mechanical forces are used to accelerate the process.(Richardson, et al. 2015) The substrates for LbL deposition are typically flat, though, spherical substrates such as multilayered capsules(Gao, et al. 2001, Glinel, et al. 2007, Vinogradova 2004), or even porous substrates (Alem, et al. 2007) have also been described.

In this bibliographic review we will focus on biomimetic multilayered structures that serves as PCW analogues.

1.6.2. Multilayer biomimetic films – plant cell wall analogues

The LbL technique can be applied to create PCW mimetic films. Films including cellulosic material and synthetic polymers have been reviewed (Martin and Jean 2014). We will focus here on biomimetic systems containing two or more PCW components.

Although many LbL nanocellulose multilayered films have been built through electrostatic interactions, film growth can also be achieved using other attractive forces such as hydrogen bonding, hydrophobic interactions, or by using covalent crosslinks. Table 5 shows some examples of such constructs and the deposition method used.

Table 5. PCW analogue 2D multilayer systems.

Reference	System	Method
(Jean, et al. 2009)	CNC-XG	Dip coating
(Cerclier, et al. 2010)	CNC-XG	Spin coating
(Valentin, et al. 2010)	Pectin-Extensin	Dip coating
(Hambardzumyan, et al. 2011)	Cellulose-Lignin	Spin coating
(Mølgaard, et al. 2014)	Cellulose- Polygalacturonic acid	Dip coating

The naturally occurring affinity between cellulose and XG, was exploited in few cases to create all biobased multilayered films. Jean et al. used dip coating to deposit multilayer consisting of the periodic repetition of a single layer of CNC and a thin layer of xyloglucan, up to 5 bilayers (Jean, et al. 2009). The resulting film architecture was studied with AFM and neutron reflectivity, and a linear film growth was observed with approximately 9 nm per bilayer. This stands in agreement with the thickness value of a single crystal of 7 nm, (Elazzouzi-Hafraoui, et al. 2007) with an additional thin XG layer.

Cerclier et al. used spin coating to create multilayered CNC/XG films, up to 8 bilayers. (Cerclier, et al. 2010). The growth of the film in their case depended on XG concentration. At high XG concentrations (5 and 10 g L⁻¹) the XG chains were entangled resulting in nonlinear film growth with a plateau after 4 bilayers, where at low XG concentration the growth was linear. They attributed this difference to the conformation of XG in the different concentrations. Multilayered films reminiscent of primary wall may provide a good in vitro model to study the degradation of cell wall polymers and relaxation mechanisms linked to specific enzymes. Further studies, dealt with a single CNC/XG bilayer and the investigation of enzymatic hydrolysis and the effect of XG chain length on the adsorption onto CNCs (Villares, et al. 2015, Villares, et al. 2017).

Whereas pectins have already been used to create multilayered films with polycations such as polylysine or chitosan, very little literature covers their combination with other plant cell wall components. Valentin et al. used Extensin and de-esterified pectin from citrus to construct multilayer structures by LbL techniques taking advantage of the opposite charge of the components. The film growth was non-uniform and involved swelling/deswelling process (Valentin, et al. 2010). In another work, Mølgaard et al. (Mølgaard, et al. 2014) used cationic cellulose fibers and polygalacturonic acid to create multilayered films up to 8 bilayers. When the films were exposed to pectin degrading enzymes, they showed a significant reduction in mass.

The LbL technique can be modified and transferred to create 3D architecture. In the following sections, we will review some examples of multilayered biomimetic capsules prepared by LbL technique.

1.6.3. Biomimetic capsules

The LbL technique was successfully transferred to spherical geometries where the flat substrate is replaced by spherical objects (Donath, et al. 1998). Similar to the 2D case, these structures rely on intermolecular interactions to successively deposit alternating layers of various components. Generally, two types of systems exist (i) liquid cores, where emulsions or aqueous phase are occupying the capsule interior and (ii) solid cores, where colloidal particles are used as a template for component deposition. In the latter case, the solid core can be removed leaving a hollow polymeric shell. The rinsing step, essential for removal of non-adsorbed material, is replaced here with sedimentation of the decorated objects, removal of the supernatant and redispersion into a new solution. Let us review some examples for each system.

1.6.3.1. Solid core systems

This type of systems is based on the deposition of polymer layers on a solid colloidal template, which can be later removed to create hollow shells (Figure 30a). This method can be used to prepare synthetic polymer multilayer capsules based on electrostatic interactions. The templates include silicon dioxide (SiO_2) or carbonate (MnCO_3 , CaCO_3 , CdCO_3) microparticles, or crosslinked polymer (polystyrene). Among the shell forming polymers one can point polyelectrolytes like poly(allylamine hydrochloride) (PAH), poly(styrenesulfonate)(PSS) and polyethylenimine (PEI) (Vinogradova 2004).

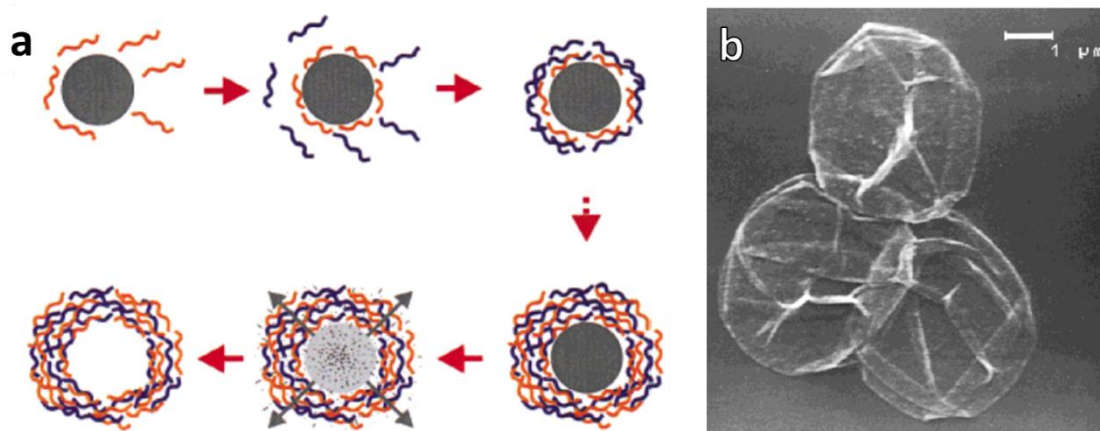


Figure 30. (a) A representative scheme for multilayer deposition on a solid core. The core can be removed by additional steps leaving hollow shells. (b) A SEM image of (PSS/PAH)₄PSS polyelectrolyte shells following core removal (Donath, et al. 1998).

In a pioneering work, Donath et al. used LbL to produce PSS/PAH polyelectrolyte shells onto melamin resin templates. The templates were subsequently removed leaving hollow shells of $\sim 8 \mu\text{m}$ in diameter and shell thickness of about 20 nm (Figure 30b).

This method has been elaborated to create biomimetic capsules containing cellulose xyloglucan and pectin. Paulraj et al. used CaCO_3 microparticles as a template for microcapsule preparation. They covered the microcapsules with alternating layers of apple pectin (AP), xyloglucan (XyG) and cationic cellulose nano fibers (CNF) to obtain $\text{CaCO}_3(\text{AP}/\text{CNF})_5/\text{AP}/\text{XG}$ particles. The modification of cellulose permits the electrostatic binding of pectin while in the case of XyG, hydrophobic and VdW forces dominates the interactions. They could control the permeability of the shells to small (~ 7 and 12 nm) molecules by exposing them to NaCl shocks. (Paulraj, et al. 2017) In that work, XG was only present in the outer layer.

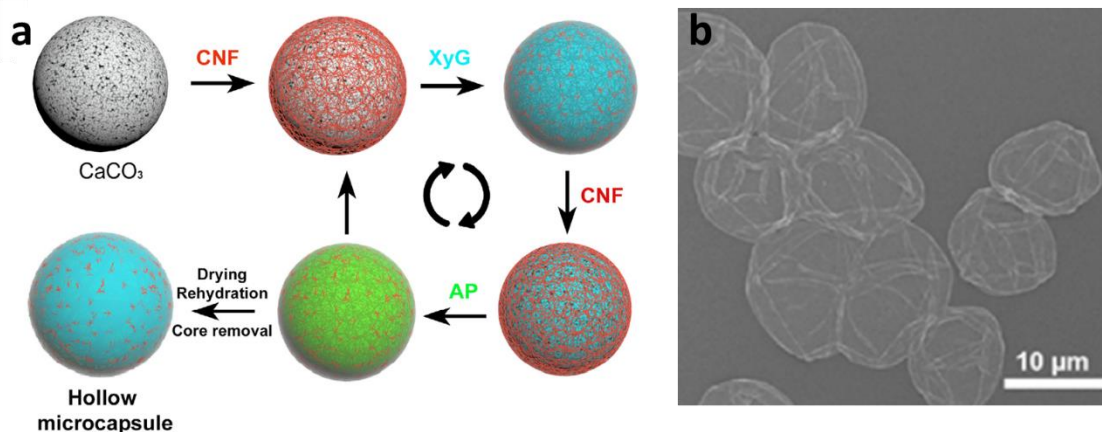


Figure 31. (a) Simplified overview of LbL microcapsule fabrication process. Between each adsorption step, a washing step was included. (b) SEM image and of $(AP/CNF)_5AP/XyG$ microcapsules after core removal. (Paulraj, et al. 2018)

They have further elaborated the system to create $(CNF/XG/CNF/AP)_2CNF/XG$ and $(CNF/XG)_5$ systems (figure 31). The capsules were partially permeable to 2000 kDa FITC dextrans (hydrodynamic diameter of ca. 54 nm) in water, but in saline conditions (250 mM NaCl), the microcapsules permeability dropped. They attributed the change in permeability to the microcapsule wall composition, i.e. the presence of XG and small amount of charged molecules such as pectins. (Paulraj, et al. 2018).

1.6.3.2. Liquid core systems-emulsions

An emulsion is a system of dispersed droplets of one immiscible liquid in another stabilized by emulsifiers. If solid colloidal particles are adsorbed at the fluid interfaces they are called “Pickering emulsions” (Pickering 1907). Kalashnikova et al. created oil in water Pickering emulsions stabilized by bacterial cellulose nanocrystals. The resulting solid particles, formed a highly stable colloidal suspension in water (Kalashnikova, et al. 2011) (Figure 32).

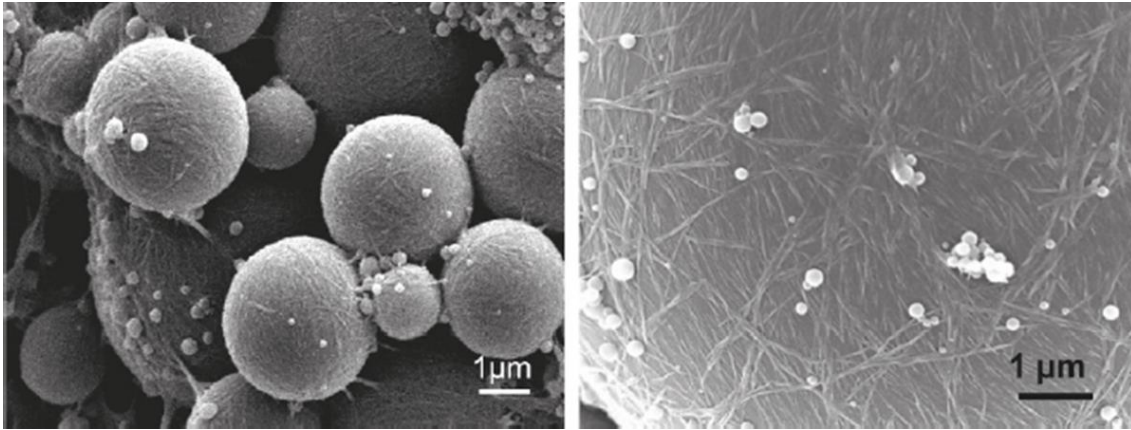


Figure 32. SEM image of the CNC stabilized emulsions (Kalashnikova, et al. 2011).

The droplet stability was attributed to the irreversible adsorption of CNC and the resulting 2D network formed at the interface. This study was further elaborated to test the effect of cellulose origin and dimensions on the stabilizing effect. It was found that the cellulose particle aspect ratio directly influenced the coverage and the morphology of the droplets. Short nanocrystals lead to a dense organization with droplet surface coverage higher than 80%. When longer nanocrystals were used, surface coverage reduced to 40% whereas the nanocrystals form an loose interconnected network (Kalashnikova, et al. 2013).

In another work, Svagan et al. prepared liquid-core capsules with a shell made of cross-linked NFC/CNC from wood pulp hydrolysis. The mechanical properties were estimated with AFM indentation and a Young's modulus of up to several GPa was found. This high modulus value were attributed to the dense nanofiber structure, present in the outer part of the capsule wall, held together by both covalent (urethane bonds) and physical bonds (hydrogen bonds) (Svagan, et al. 2014)(Figure 33).

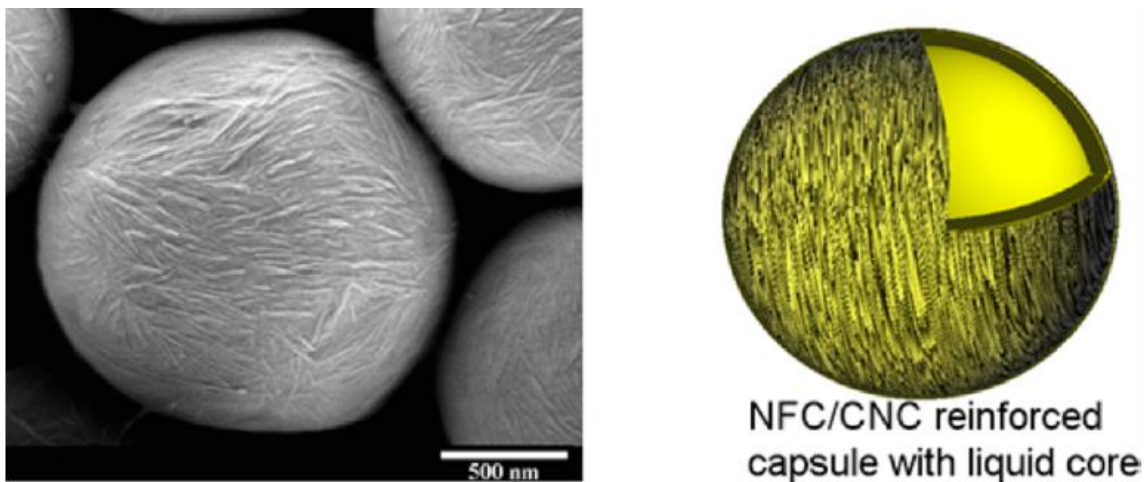


Figure 33. NFC/CNC liquid core capsules (Svagan, et al. 2014).

These studies showed the possibility of stabilizing emulsion using cellulose nano crystals, and put forward the potential use of emulsions to create biomimetic constructs. In a work done previously in the group by Bailly (Bailly 2012), oil in water emulsions were prepared and the liquid core was decorated with alternating layers of CNC and XG serving as a simplified model of plant cell wall. Octamethyl cyclotetra siloxane was used as a starting material for the emulsion and Cetylpyridinium chloride (CPC) as surfactant, up to 15 bilayers were obtained. Figure 34 shows a scheme of the preparation protocol (a) and the resulting decorated capsules (b and c).

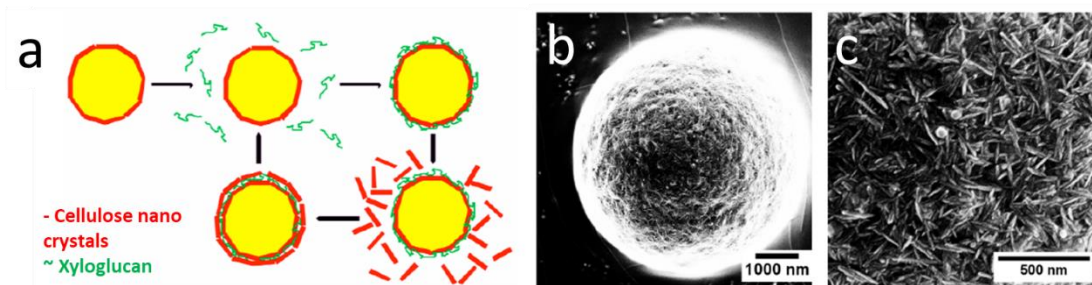


Figure 34. Biomimetic multilayered capsules from CNC and XG. (a) Deposition scheme, (b) SEM image of the covered capsule, and (c) SEM image of the capsule shell (Bailly 2012).

One drawback of emulsion systems is that they are difficult to characterize in terms of shell mechanical properties, such as bending rigidity or Young's modulus.

Osmotic shocks are not possible and indentations will be too sensitive to the incompressible oily phase supporting the shell. In addition, they do not contain an important component of the biological system, the lipid membrane.

Therefore, in a recent work in the group, biomimetic capsules with a lipid membrane as a scaffold were prepared.(Radavidson 2016) These capsules were decorated with alternating layers of CNC and XG (up to 10 bilayers, figure 35) and their mechanical properties were examined and compared to the ones obtained for plant tissues. The Young's modulus of the vesicles was found to be 6-22 MPa, close to what was found for onion epidermis.

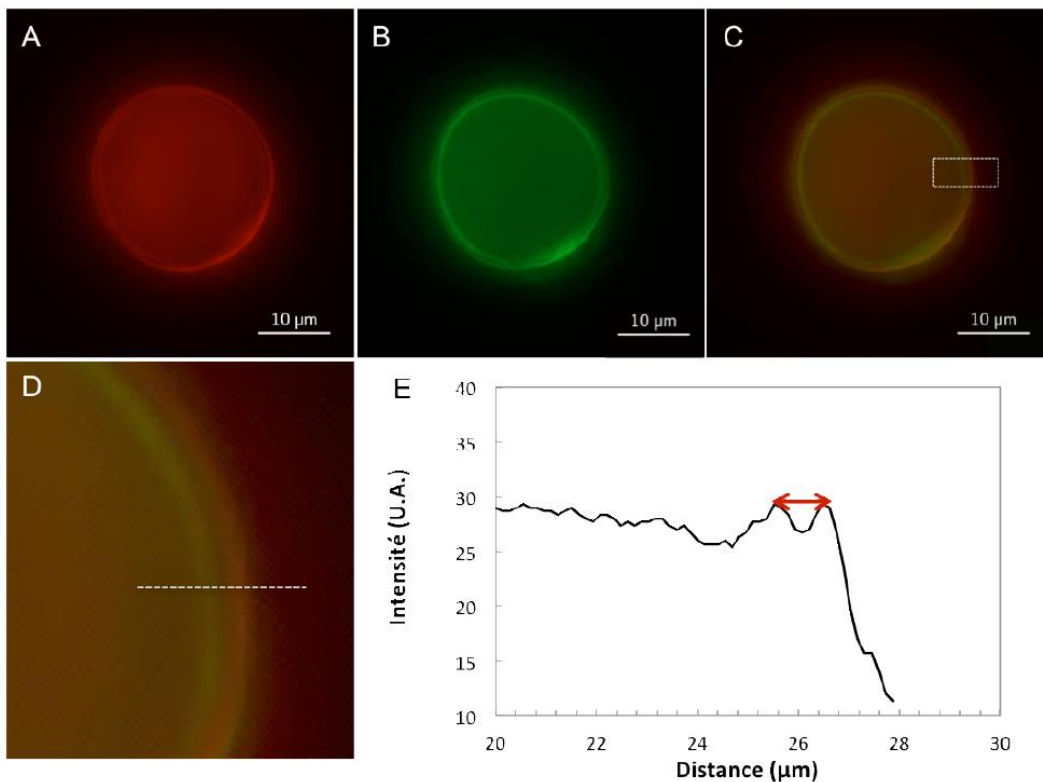


Figure 35. Fluorescence microscopy image of CNC/XG decorated lipid vesicles. (A) Red channel, CNC-RhodB, (B) green channel, NBD-PC, (C) overlay of the red and green channels, (D) magnification of the shell region, (E) fluorescence intensity profile along the dotted line shown in (D) (Radavidson 2016).

This pioneering work paved the way for the creation of new class of biomimetic constructs composed of a lipid membrane and plant polysaccharides. However, the factors governing the interaction between the building blocks were not yet studied in depth.

The proposed work aims to further elaborate the above-mentioned system, first by deciphering the underlying mechanisms governing the interactions between the different components, and second, by exploring additional bio-based building blocks.

Chapter 2

Characterization techniques

2.1. Dynamic light scattering (DLS)

Dynamic Light Scattering (sometimes named Photon Correlation Spectroscopy or Quasi-Elastic Light Scattering) is a technique used for extracting the mean hydrodynamics diameter of particles in the sub-micron scale. In dynamic light scattering, the speed at which the particles are diffusing, due to Brownian motion, is measured by determining the rate at which the intensity of the scattered light fluctuates (Rayleigh scattering). From the intensity fluctuation signals, calculated between time t and $t+\delta t$, one can determine the first order autocorrelation function (g^1):

$$(Eq. 4) \quad g^1(q, t) = \exp(-\Gamma\tau)$$

Where Γ is the decay rate, τ the delay time, and q is the wave vector given by:

$$(Eq. 5) \quad q = \frac{4\pi n_0}{\lambda} \sin(\theta/2)$$

Where n_0 is the refractive index of the sample, λ is the wavelength and θ is the angle at which the detector is located with respect to the sample cell. For a spherical object, the decay rate relates to the translational self-diffusion coefficient D using the following equation:

$$(Eq. 6) \quad \Gamma = q^2 D$$

The stocks-Einstein relationship is then used to convert the self-diffusion coefficient of a perfect sphere to its size by:

$$(Eq. 7) \quad D_h = \frac{k_B T}{3\pi\eta_s D}$$

Where k_B is the Boltzmann constant, T is the temperature, η_s is the solvent medium viscosity. Figure 36 shows the experimental setup used, typical intensity fluctuations from small and large particles and the resulting correlation function.

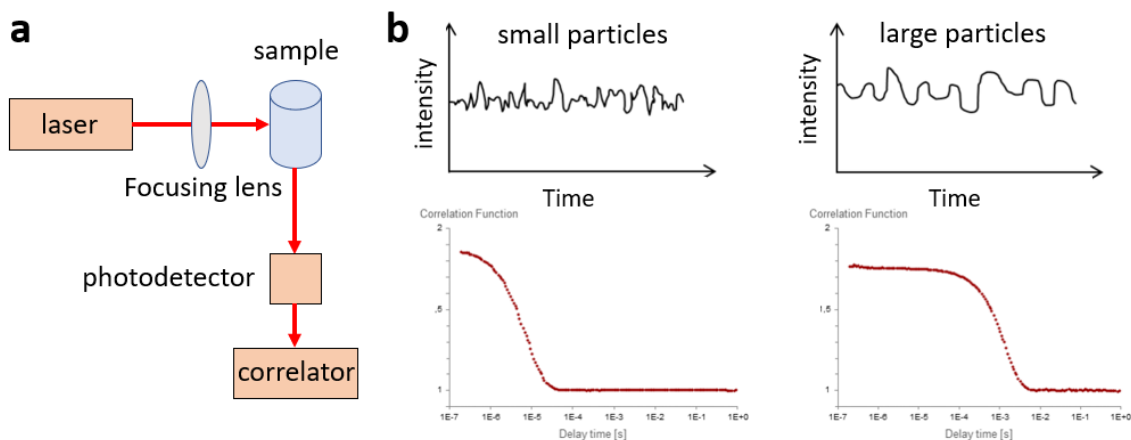


Figure 36. (a) A schematic representation of the DLS setup used. (b) Intensity fluctuations and the resulting autocorrelation function for small and large particles.

The correlation function is analyzed using either CONTIN (non-monomodal distribution) or cumulants (monomodal distribution) fitting routines. In addition to the hydrodynamic diameter, DLS provides information on the polydispersity (PDI) of the sample used to describe the degree of non-uniformity of a size distribution of particles. PDI is calculated from a two-parameter fit to the correlation data (the cumulants analysis). This index is dimensionless and scaled such that values smaller than 0.05 are mainly seen with highly monodisperse standards. PDI values bigger than 0.7 indicate that the sample has a very broad particle size distribution and is probably not suitable to be analyzed by DLS technique.

DLS was used in this work to probe the hydrodynamic diameter of individual building blocks (Liposomes, CNCs, XG and pectins) and their complexes (chapters 3 and 4).

2.2. ξ -potential

ξ -potential is a physical property which is exhibited by any charged particle in suspension. It can be used to predict the stability of colloidal suspensions and is based on the electrokinetic effect.

The development of a net charge at a particle surface affects the distribution of ions in its surrounding region. Specifically, there is an increased concentration of counter ions, namely, ions of opposite charge to that of the particle, close to the particle surface with a thickness that corresponds to the Debye screening length λ_D (see figure 53 section 4.1.3 for a more detailed description). When the particle moves, ions within this boundary move with it, while the ions beyond the boundary stay with the bulk dispersant. The net potential at this boundary (surface of hydrodynamic shear) is the ξ potential.

The ξ -potential can be estimated from electrophoresis experiments, where the movement of a charged particle relative to the liquid it is suspended in, is measured under the influence of an applied electric field E . When an electric field is applied, the charged particles are attracted to the electrode of opposite sign while viscous forces acting on the particles tend to oppose this movement. When steady state is reached between these two opposing forces, the particles move with constant velocity v . The electrophoretic mobility, U_e , defined as v/E , can be related to the ξ -potential by the Henry equation:

$$(Eq. 8) \quad U_e = \frac{2\varepsilon_r\varepsilon_0\xi}{3\eta} f(a/\lambda_D)$$

Where ε_r and ε_0 are the permittivities of the solution and the vacuum respectively, a is the particle radius, η is the viscosity of the medium and λ_D is the Debye length which refers to the thickness of the electrical double layer. The term $f(a/\lambda_D)$ is called the Henry function and it ranges for a sphere from 1 for $a/\lambda_D \ll 1$ (Huckel limit) to 3/2 for $a/\lambda_D \gg 1$ (Smoluchowski limit)(Hunter 2013). In the case where $a \gg \lambda_D$, eq. 8 then becomes the Smoluchowski relationship:

$$(Eq. 9) \quad U_e = \frac{\varepsilon_r\varepsilon_0\xi}{\eta}$$

ξ -potential was used in this work to probe the electrophoretic mobilities of the individual building blocks (liposomes, CNCs, and pectins) and their complexes (chapters 3 and 4).

2.3. Isothermal titration calorimetry (ITC)

Isothermal titration calorimetry (ITC) is used for the thermodynamic study of the interaction between different biological components such as lipids, proteins and carbohydrates. (Freyer and Lewis 2008) The measurement principle is based on injection of a molecule A into vessel containing molecule B and the measurement of applied current required in order to maintain constant temperature difference between the sample cell and a reference cell. Figure 37a shows a typical ITC experimental setup.

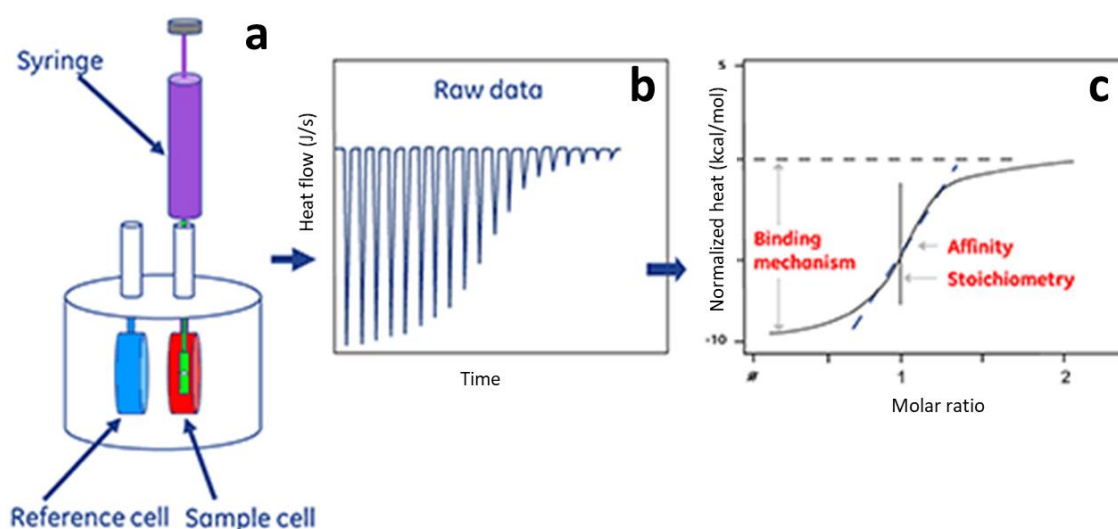


Figure 37. (a) Typical ITC experimental setup. (b) ITC raw data curve, showing the heat flow resulting from injection of substance A into a cell containing substance B as a function of time. (c) ITC data analysis curve showing the normalized heat value as a function of the molar ratio of A and B. (from www.malvernpanalytical.com)

The injection is performed in subsequent additions of small volumes of the molecule A, present in a syringe, to the vessel containing molecule B. The peaks resulting from the measurement of the heat flow (figure 37b) are integrated over time (figure 37c). From the titration curve obtained, one can extract the reaction

stoichiometry as well as valuable thermodynamic parameters such as enthalpy (ΔH) entropy (ΔS) Gibbs free energy (ΔG), and association constant (K_a) by applying an adequate model.

ITC was used in this work to probe the interaction between CNC and liposomes (chapter 4.2.1) and between CNC and XG (chapter 4.3.1).

2.4. Quartz crystal microbalance with dissipation monitoring (QCM-D)

Quartz crystal microbalance (QCM or QCM-D) is a versatile tool for investigating soft and solvated interfaces between solid surfaces and bulk liquids because it can provide a wealth of information about key structural and functional parameters of these interfaces. (Reviakine, et al. 2011) QCM is based on the inverse piezoelectric effect discovered by the Curies in the late 19th century: application of voltage results in mechanical deformation of the material (Ward and Buttry 1990). In the QCM-D method, the external driving voltage is turned off intermittently and the oscillations are left to decay freely. Given that quartz is piezoelectric, a voltage is generated during these decaying mechanical oscillations (figure 38). This signal is recorded, yielding two parameters, the resonance frequency f_n and the dissipation D_n (figure 38c) from which the adsorbed mass as well as the viscoelastic properties of the layer can be extracted. Bandwidth and dissipation are equivalent, with $D_n = 2\Gamma_n/f_n$ (figure 38d). The use of QCM-D is based on the linear relationship between changes in the resonator (crystal) mass and in the resonance frequency, derived by Sauerbrey:

$$(Eq. 10) \quad \Delta f_n = -\frac{n}{C} m_f = -\frac{n}{C} \rho_f h_f$$

where f_n is the resonance frequency, m_f is the areal mass density of the adsorbed film (mass per unit area), and ρ_f and h_f are the density and the thickness of the adsorbed film, respectively. The mass sensitivity constant C depends solely on the fundamental resonance frequency f_F and the material properties of the quartz crystal. For typically used crystals with $f_F = 5$ MHz, it is $18 \text{ ng cm}^{-2} \text{ Hz}^{-1}$. (Johannsmann 1999, Johannsmann 2008)

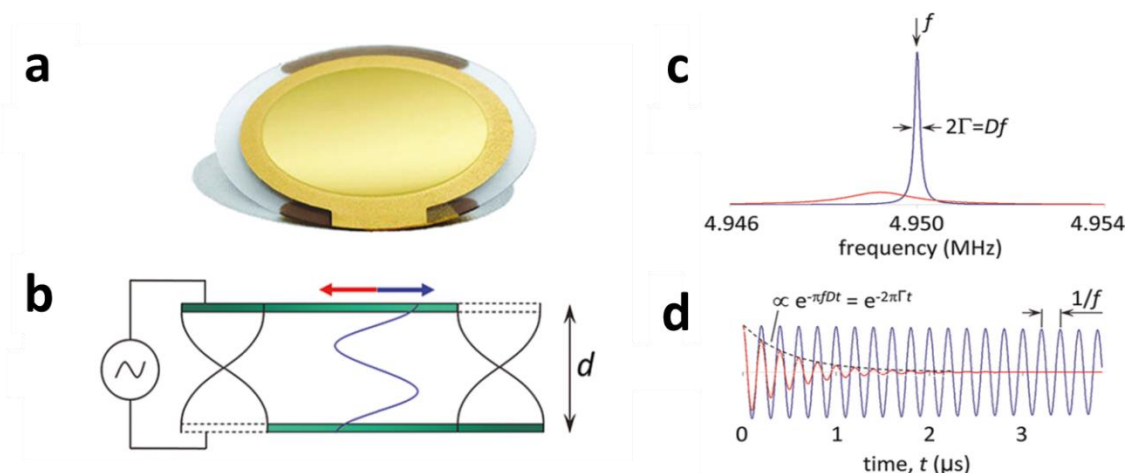


Figure 38. Schematics of QCM-D operation. (a) A photograph of a quartz crystal (b) Side view of the crystal. Application of oscillatory voltage results in a cyclical deformation, where top and bottom surfaces move in an antiparallel fashion. (c) Resonances observed when a crystal is in air (blue) or in liquid (red). Two parameters are used to characterize the resonance: its frequency f and its bandwidth Γ (d) While the driving voltage is intermittently switched off, the time decay of the oscillation is monitored. From the decay curve, the resonance frequency f and the energy dissipation $D = 2\Gamma/f$ are extracted. The blue decay curve in this figure corresponds to a crystal oscillating in air. The two types of curves shown in parts c and d are related to each other by a Fourier transform. (Reviakine, et al. 2011)

The Sauerbrey model can be generally applied for cases where the dissipation factor is small (i.e. rigid film). For non-rigid films, the changes in frequency f and dissipation D can be described through a viscoelastic model (the Voigt-based representation of a viscoelastic solid). (Vandoolaeghe, et al. 2008, Voinova, et al. 1999)

QCM-D was used in this work to probe the formation of SLBs and to investigate the interaction between SLBs and CNCs and between CNCs and XG (Chapter 4).

2.5. Optical microscopy

Several optical microscopy techniques were used in this work: phase contrast, fluorescence, confocal and structured illumination (Apotome) microscopy (Chapter 5 and 6). In this sub chapter, the basic principles and operational mode of each technique will be described.

Phase contrast

When light passes through a transparent material, small phase shifts occur, which are invisible to the human eye. In a phase contrast microscope, these phase shifts, are converted into changes in brightness, which can be observed as differences in image contrast. In phase contrast microscope configuration, the condenser aperture diaphragm is replaced by a phase stop, that illuminates the specimen via the condenser as illustrated in figure 39.

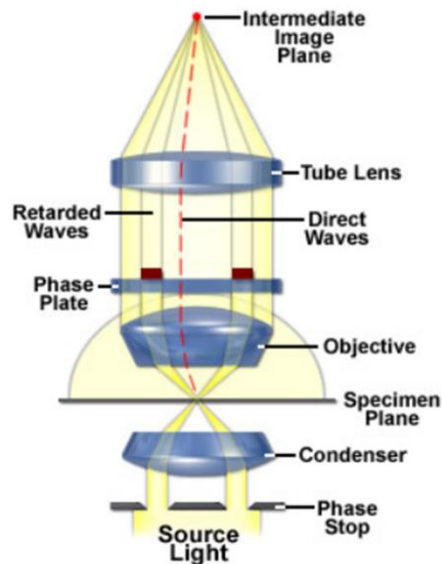


Figure 39: A general scheme of phase contrast microscope.

Light enters the objective and an image of the phase stop is formed in the rear focal plane. A phase ring is positioned within the objective rear focal plane adding a constant phase shift to this light. If the specimen contains sub-structures that have mixed refractive indices, these entities guide the light from the direct waves into new paths (red dotted line in figure 39). Light diffracted by the specimen, that contains structural information, will not pass through the phase ring in the objective, meaning that they will not be attenuated or retarded. All of the wave fronts are ultimately recombined to form the intermediate image by the tube lens.

Fluorescence microscopy

Fluorescence microscopy is based on a phenomenon termed photoluminescence, occurring through excitation of a fluorescent molecule by ultraviolet or visible light. Figure 40a shows a general scheme of a fluorescent microscope setup. This type of optical microscopy consists of irradiating the sample with a specific band of wavelengths corresponding to the excitation spectrum of the molecule, and detect light emitted by the fluorescent molecules at a wavelength corresponding to its emission spectrum (Figure 40b). The interest of this technique is to allow the observation of the spatial and temporal distribution of marked molecule in the sample.

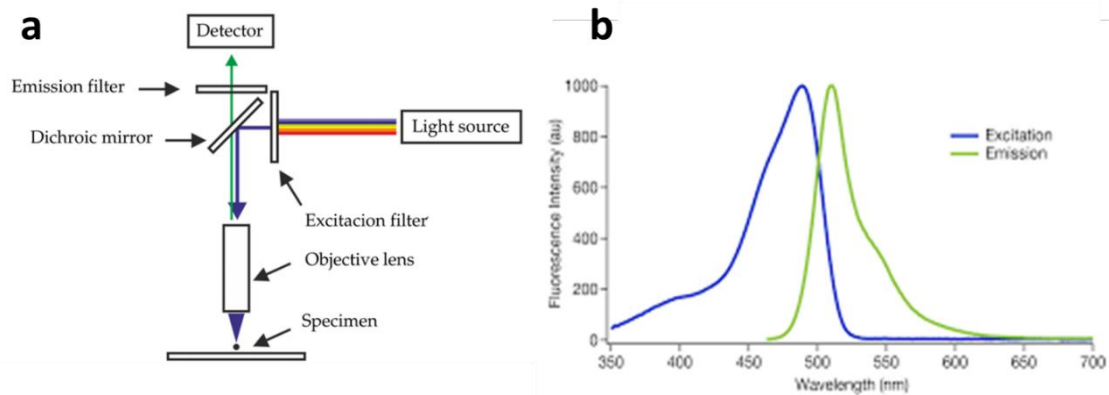


Figure 40: (a) A general scheme of fluorescence microscope (b) typical excitation/emission spectra of fluorescent molecules.

Total internal reflection fluorescence microscopy (TIRF or TIRFM)

Total internal reflection fluorescence microscopy (TIRF) is a technique a laser light is focused into the rim of back focal plane of the objective in a way that the laser light is totally reflected at the glass/ water interface (figure 41 green line). An evanescent wave is thus created whose intensity decays within a few hundred nanometers. Thereby, only a small sample thickness is illuminated within the solution. The advantage of TIRF is the possibility to excite only fluorophores close to the surface which makes it suitable for investigation of membrane adsorption processes.

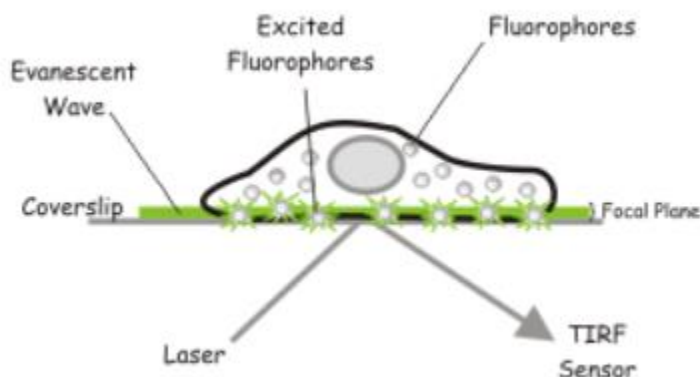


Figure 41. A scheme of total internal reflection fluorescence microscope (TIRF) configuration.

Due to these advantages, TIRF has become a preferred method for single molecule detection and tracking (Jaqaman, et al. 2008) as well as for the investigation of biological events involving adsorption of particles on lipid membranes. (Axelrod 2001) TIRF was also used to probe the formation of thin films (Blacklock, et al. 2010) and is a useful tool to probe their homogeneity at a microscopic length scale.

TIRF was used in this work to probe the formation of SLB-CNC constructs in the micrometer scale.

Structured illumination microscopy (SIM)

In thick specimens, the fluorescence signal from the focal plane is compromised by the out of focus light coming from planes above and below this plane. The result is a blurred, low contrast image. Some techniques were developed to remove the out of focus light, either optically (Confocal) or mathematically (ApoTome). In the ApoTome, a grid is inserted in the illumination pathway of a conventional fluorescence microscope. A plane-parallel glass plate is placed in front of the grid and it tilts back and forth projecting the grid in the image in 3 different positions. For each depth, 3 raw images with the projected grid superimposed in 3 different positions are taken (figure 42). The software uses the projected images of the grid to calculate and remove the out of focus light. The principle is based on the fact that if the grid is visible, the information is in focus. If not, that signal corresponds to out of focus light and it is removed from the final image. The software combines the 3 images into 1 for each stack.

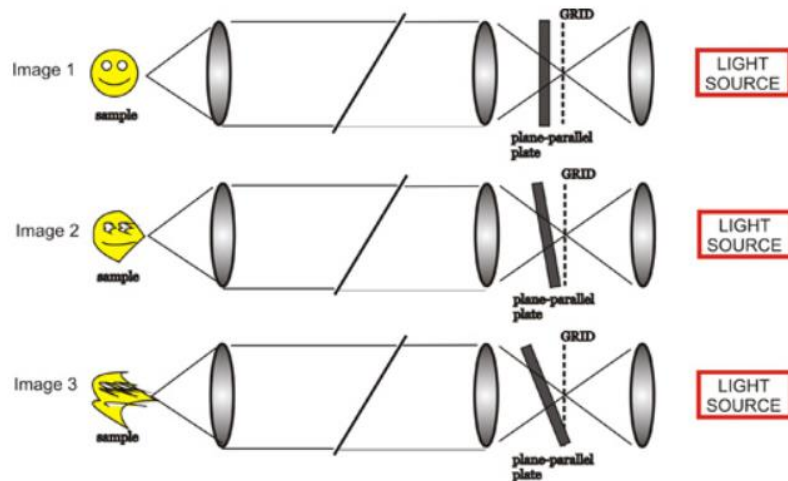


Figure 42. A schematic representation of SIM. The difference between the three situations is the grid position.

Transmission electron microscopy (TEM)

Transmission electron microscopy (TEM) is a microscopy technique in which a beam of electrons is transmitted through a thin specimen, interacting with the material as it passes through it. An image is formed from the interaction of the electrons transmitted through the specimen; the image is magnified and focused onto an imaging device, such as a fluorescent screen, on a layer of photographic film, or to be detected by a sensor such as a charge-coupled device. TEMs are capable of imaging at a significantly higher resolution than light microscopes, thanks to the small wavelength of electrons. (Egerton 2005, Fultz and Howe 2012)

In cryo-TEM, the sample is spread on a grid and subjected to rapid freezing, typically in liquid ethane. The advantage of this technique is that it enables the observation of specimens that have not been stained or fixed in any way, showing them in environment that is close to native. (Al-Amoudi, et al. 2004, Danino, et al. 2001, Kuntsche, et al. 2011) One disadvantage of this technique emerges from the fact that the samples are observed in a vitreous ice layer of 100-200 nm, therefore only objects

that are smaller than these dimensions can be observed without effecting their original shape.

In this work TEM and cryo-TEM were used to visualize the CNCs and liposomes as well as CNC-liposomes and CNC-XG complexes (chapters 3 and 4).

2.6. Atomic-force microscopy (AFM)

Atomic-force microscopy (AFM) or scanning-force microscopy (SFM) is a type of scanning probe microscopy (SPM), which demonstrates spatial vertical resolution on the order of fractions of a nanometer and can measure forces as small as several piconewtons. A scheme of the AFM configuration is shown in figure 43. The information is obtained from the interaction of the surface with a mechanical probe, namely a cantilever mounted on a special chip (Figure 43 a). Its principle of operation is based on the interaction between a small probe, the cantilever tip (Figure 43b), and the surface atoms of the sample to be analyzed, where the force (F) is linearly related to the cantilever deflection (s) and its spring constant (k). (Figure 43c)

The spring constant can be calculated from either (i) the material properties and dimensions of the cantilever (ii) by measuring the intensity of thermal noise (iii) by directly applying a known force to the end of the cantilever and measure the resulting deflection, as demonstrated in Figure 43c.

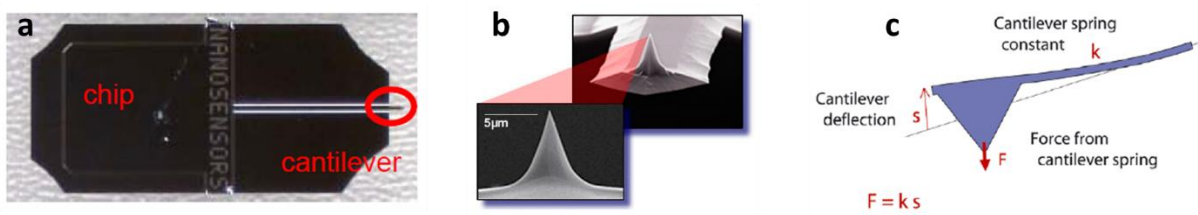


Figure 43. (a) A cantilever mounted on a chip (b) SEM image of an AFM tip (c) a schematic diagram of cantilever.(JPK instruments 2012)

The attractive or repulsive force between the tip and the sample causes a deflection of the cantilever, changing the angle of a reflecting laser beam and a change

of amplitude of tip oscillation. At each moment the spot falls on a different part of a quadrant photodetector and the signal from the four quadrants are compared in order to calculate the deflection signal. (figure 44a) The three-dimensional image of the surface that is generated, is thus reflecting the probe-surface interaction. A typical force-distance curve shows the different regimes of tip-sample interaction. (Figure 44b)

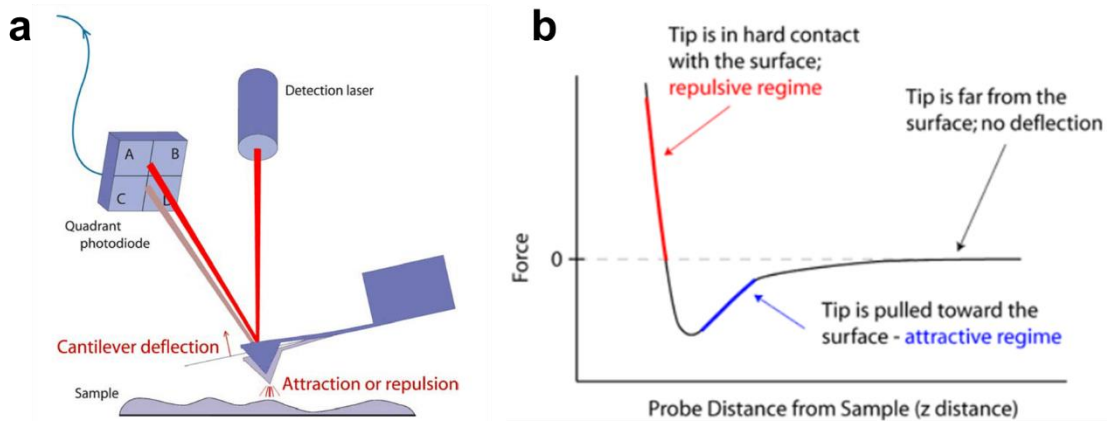


Figure 44. (a) photodiode (b) Typical approach retract curve.(JPK instruments 2012)

Piezoelectric tube scanner facilitating accurate movements, enables very precise scanning thus provide information about the topography of surfaces as well as mechanical properties of 2D and 3D structures.

AFM can operate in **contact mode** where there is direct contact between the tip and the sample, or in a **dynamic mode** where either intermittent contact or no contact exists between the tip and the sample.(Butt, et al. 2005, Chen 1993)

Since AFM can measure forces of the order of the tenths of piconewton, it can be used for characterization of the viscoelastic behavior of a surface and to extract the elastic modulus from force-strain measurement (force spectroscopy). **The peak force (PF) and the quantitative imaging (QI) modes** are types of force spectroscopy.

AFM was used in this work to evaluate the thickness and topography of the 2D constructs and to extract the elastic modulus of the biomimetic films.

Chapter 3

Preparation of building blocks

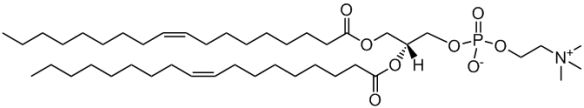
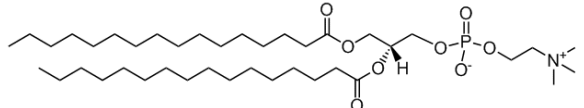
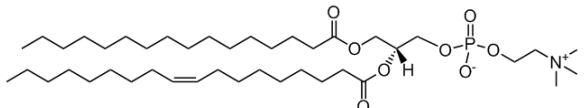
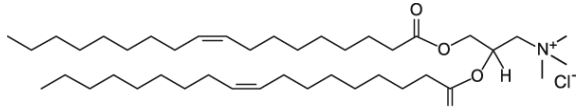
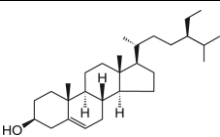
In this part, we will deal with the characterization of the building blocks chosen to represent the PCW architecture, namely, lipid membranes, CNCs, XG and pectin.

3.1. Building blocks characterization

3.1.1. Lipids and lipid vesicles

Lipids used

Table 6. Structure and physical properties of the Lipids used.

Lipid	Mw g/mol	Tm [°C]	Chemical structure
DOPC 1,2-dioleoyl-sn-glycero-3-phosphocholine	786.1	-18	
DPPC 1,2-dipalmitoyl-sn-glycero-3-phosphocholine	734.0	41	
POPC (1-palmitoyl-2-oleoyl-glycero-3-phosphocholine)	760.1	-2	
DOTAP 1,2-dioleoyl-3-trimethylammonium-propane (chloride salt)	698.5	~0	
SS B-Sitosterol 22,23-dihydrostigmasterol	414.7	136	

Phospholipids and sterols were purchased from Avanti Polar Lipids Inc. (Birmingham, U.S.A.) and dissolved without further purification in a chloroform/methanol mixture (9/1 %V/%V) to a total concentration of 10 mg mL⁻¹. The solutions were stored at -20 °C until used.

Liposomes

Lipid solutions in chloroform/methanol mixture were transferred into a round-bottom flask and the organic solvent was removed by evaporation under high vacuum pumping for 2-4 h, until complete evaporation of the solvent. The lipid film was then hydrated in an appropriate amount of buffer solution at room temperature above the melting point of the lipids. Multilamellar vesicles were then obtained by vortexing for 30 min. The resulting suspensions were then successively extruded 20 times through 200 and 100 nm polycarbonate membranes using a miniextruder (Avanti Polar Lipids). (Figure 45)

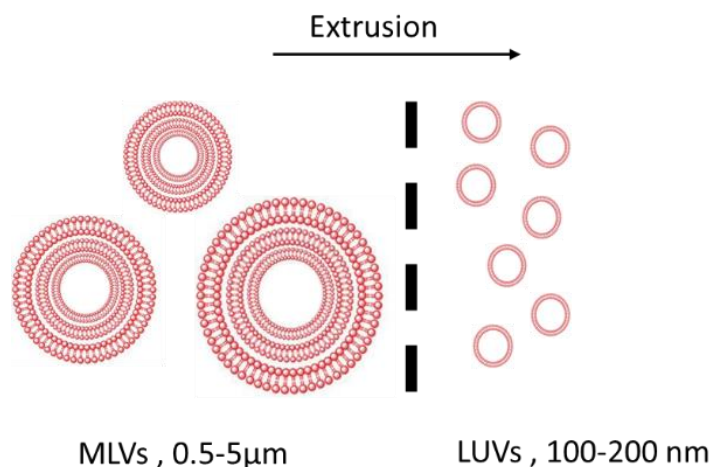


Figure 45. Liposome preparation with extrusion through polycarbonate membranes with defined sizes.

The liposomes were finally characterized by cryo-TEM, DLS and ζ -potential. Typical characterization of DOPC and DOPC/DOTAP liposomes is shown in figure 46.

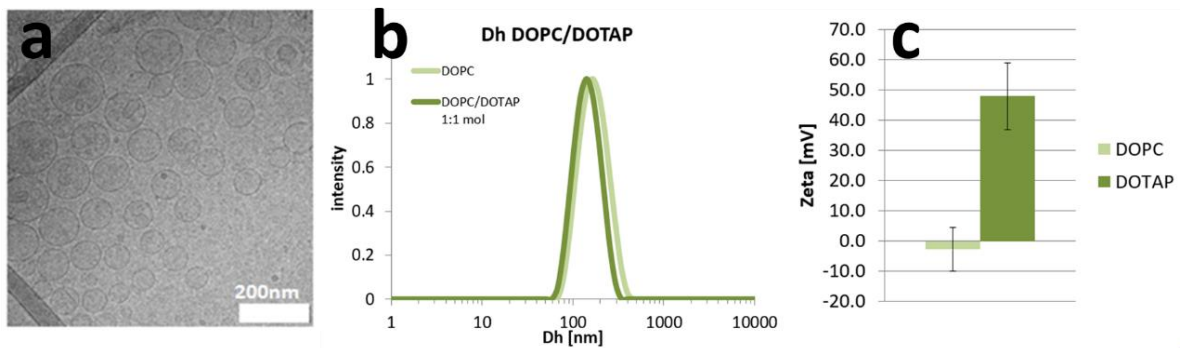


Figure 46. (a) cryo-TEM image of DOPC liposomes. (B) hydrodynamic diameter distribution of DOPC (light green curve) DOPC/DOTAP (dark green curve). (c) ζ -potential values obtained for the same liposomes. DOPC (light green column) DOPC/DOTAP (dark green column).

DOPC liposomes were mostly unilamellar with a narrow size distribution, corresponding to a monodispersed sample (PDI=0.11). The hydrodynamic diameter obtained for DOPC resemble the dimensions observed by cryo-TEM. Notably, although prepared using similar protocols, a slight variation in the size of the liposomes is observed with the composition. The hydrodynamic diameter was 151.5 ± 44.1 and 176.6 ± 51.2 for DOPC and DOPC/DOTAP respectively.

The ζ -potential values, measured here at neutral pH, were -2.8 ± 7.3 and 48.0 ± 11.0 mV for DOPC and DOPC/DOTAP respectively. DOPC is known to be zwitterionic, at a neutral pH it is slightly negatively charged. DOTAP however is a positively charged lipid, contributing to the change in charge sign as reflected by positive ζ -potential.

For bare vesicles, the DLVO theory discussed in chapter 4.1.2, allows a good approach of the stability of liposome suspensions by comparing the attractive VdW and the repulsive electrostatic interactions. In the case where electrostatic forces dominate, the objects stay isolated in solution, whereas if the VdW interactions govern the system, the particles aggregate. In this case, the non-zero value of the ζ -potential can explain the observed stability of the vesicles.

SLBs

Lipid mixtures (DOPC or DOPC/DOTAP 2:1 molar ratio) dissolved in chloroform were transferred to a round bottom flask and the chloroform was removed by evaporation under vacuum (100 mbar) for five hours. The lipid film was hydrated by vortexing in the appropriate buffer to obtain a lipid concentration of 1 g L^{-1} . Typically, 3 mL of vesicle suspension was obtained. The resulting multilamellar vesicles were sonicated with a tip sonicator (Branson 450, Emerson, USA) for 5 minutes in an ice bath until clarity, followed by centrifugation (10 minutes at 20100 RCF, ambient temperature) to remove the metallic particles detached from the sonicator tip. Before subsequent measurements, the resulting small unilamellar vesicles were diluted to 0.1 g L^{-1} into a solution of the appropriate buffer. Vesicles prepared in this way fuse onto hydrophilic surfaces to form SLBs either on QCM-D silica coated quartz crystal or on Piranha treated microscope cover slides for fluorescence microscopy applications.

3.1.2. CNCs

CNC suspensions were prepared by acid hydrolysis of cotton linters (Buckeye Cellulose Corporation) according to the method described by Dong and Revol (Dong, et al. 1998). Briefly, the almost pure cellulosic substrate was treated with 64% sulfuric acid during 30 min at $63 \text{ }^\circ\text{C}$. The suspensions were washed by repeated centrifugations, dialyzed against distilled water until constant conductivity of the dialysis bath was reached, and ultrasonicated for 4 min with a Branson Digital sonifier 450W equipped with a 13 mm titanium tip (Emerson, USA). Operating at 30% of maximum power, the total energy delivered to the sample was equal to 9 kJ g^{-1} . After these treatments, the suspension was filtered through $8 \text{ }\mu\text{m}$ then $1 \text{ }\mu\text{m}$ cellulose nitrate membranes (Sartorius). The resulting CNC suspension had a mass content of $2.0 \pm 0.1 \text{ wt } \%$. It was then mixed with 20 mM PBS (Sigma-Aldrich) up to the desired concentration of $1.0 \pm 0.1 \text{ wt.} \%$ at $\text{pH}=7.2$. In these conditions, cellulose is in its salt form. The suspension was lyophilized and redispersed in Mili-Q water prior to each experiment, followed by mild sonication (0.2 kJ g^{-1}) to eliminate the presence of large aggregates.

TEM DLS and ζ -potential

Figures 47a and 47b show a TEM image and hydrodynamic diameter distribution profile respectively, of CNCs prepared according to the described protocol.

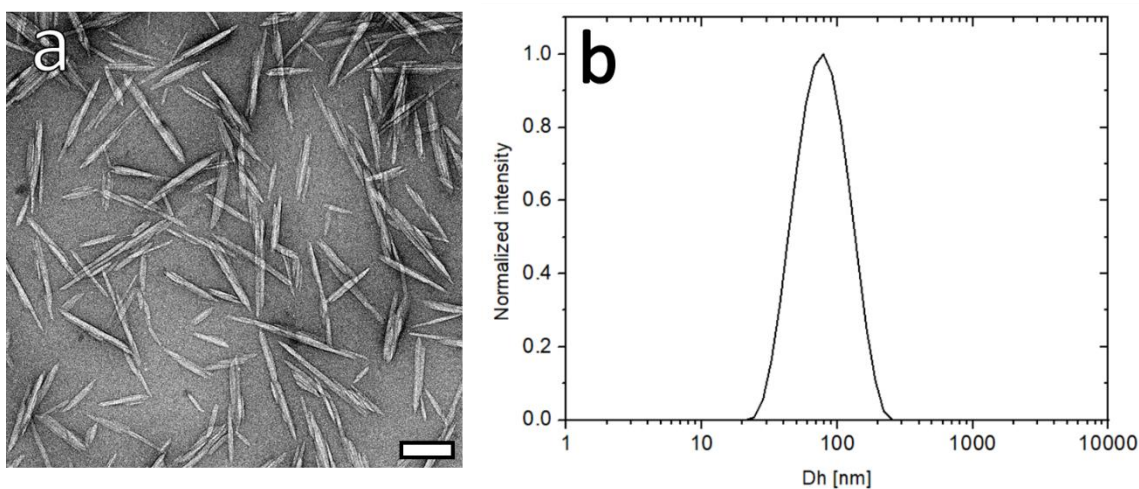


Figure 47. (a) TEM image of negatively stained CNCs prepared by cotton hydrolysis, scale bar: 100 nm (b) DLS profile showing the hydrodynamic diameter of CNCs. (TEM image taken by Jean-Luc Putaux, CERMAV)

The TEM images reveal needle-shaped particles which are, in fact, bundles of 3-5 individual crystallites, in agreement with previous studies on CNCs prepared with the same protocol.(Elazzouzi-Hafraoui, et al. 2007, Jean, et al. 2009) The corresponding DLS curve shows a hydrodynamic diameter of 90.2 and PDI of 0.17. Although the interpretation of DLS analysis using Stokes-Einstein relationship is limited to spherical objects, it gives a reasonable assessment for the overall size of the objects.(Foster, et al. 2018)

Conductometric titration

The surface charge density of CNCs can be determined using conductometric titration of the H_3O^+ ions, the counterions of the sulfate half-ester groups left after acid hydrolysis. By following the conductivity of CNC suspension during titration with a

strong base, NaOH in this case, we can determine the equivalent point from which the surface charge density can be determined.

The titration is done under stirring with a conductometer CDM 210 (Thermoscientific, USA) equipped with an electrode CDM 614T. Figure 48 shows the conductivity as a function of added NaOH volume.

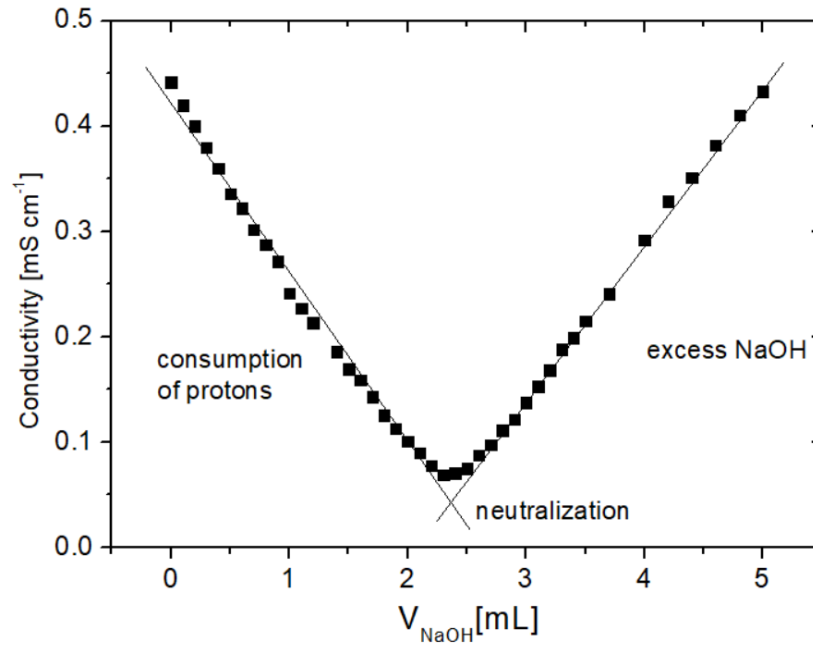


Figure 48. Conductometric titration: conductivity as a function of NaOH volume. The charge density can be determined from the equivalent point.

The equivalent point is determined from the inflection point and related to the amount of half sulfate ester groups by the following relationship (Dong, et al. 1998):

$$(Eq. 11) \quad C_{NaOH}V_{eq} = n_{so_3^-}$$

Where C_{NaOH} is the concentration of NaOH used for titration, $n_{so_3^-}$ is the number of moles of sulfate ester groups in the sample and V_{eq} is the volume at the equivalent point. The degree of substitution is defined as:

$$(Eq. 12) \quad d_s = \frac{n_{so_3^-}}{m_{cellulose}} \frac{mmol}{kg}$$

Where $m_{cellulose}$ is the mass of cellulose in the sample in kg. For the equivalent volume of 2.4 mL, d_s is 240 mmol kg^{-1} which falls within the range reported in the literature for surface charge densities: 80-350 mmol kg^{-1} .(Foster, et al. 2018)

Since the interaction with CNCs occurs on the surface, it is of interest to determine the surface charge expressed in electrons per unit of surface. By taking into consideration the CNC crystal dimension, the surface charge density can be derived. Here, CNCs from cotton are considered as parallelepipeds with length (l) width (w) and height (t) of 150 nm 21 nm and 7 nm respectively.(Elazzouzi-Hafraoui, et al. 2007)

Each SO_3^- group contributes one electron, thus the total number of electrons in the sample, defined as n_e , is equal to $6.022 \cdot 10^{23} \cdot n_{\text{SO}_3^-}$.

The total surface area in the sample, A_{tot} , is defined as:

$$(Eq. 13) \quad A_{tot} = N_{crys} \cdot 2(l \cdot w + l \cdot t + t \cdot w)$$

With $N_{crys} = m_{cellulose}/m_{crystal}$ is the number of crystals in the sample, calculated from the CNC density and the volume of one crystal with the given dimensions and density of cellulose 1.6 g cm^{-3} .

From these relations, the surface charge density is:

$$(Eq. 14) \quad \sigma_{CNC} \left[\frac{e^-}{\text{nm}^2} \right] = \frac{n_e}{A_{tot}}$$

We obtain $\sigma_{CNC} = 0.52 e^- \text{ nm}^{-2}$, in agreement with previously reported values using similar hydrolysis conditions.(Radavidson 2016)

3.1.3. Xyloglucan (XG)

Class 3A tamarind seed XG was purchased from Dainnipon (Osaka, Japan) and purified to remove protein traces bound to the polymer using the protocol described by Muller et al.(Muller, et al. 2011) The resulting white powder was dissolved at room temperature in water up to concentration of 1 wt.% and ultrasonicated using Branson digital sonifier 450W, equipped with a 13 mm titanium tip (Emerson Electric, USA)

operating at 30% of maximum power. Sonication was carried out on a 20 mL sample in a cylinder glass vial which was placed in an ice bath to avoid over heating of the sample. The sonication was performed in cycles of 1 min each with 4 min rest periods between cycles to allow the cooling of the solution, providing 405 kJ g^{-1} per cycle. A total of 10 cycles were performed, the total energy delivered to the sample was equal to $4 \cdot 10^3 \text{ kJ g}^{-1}$. The sonication was followed by centrifugation $13.4 \cdot 10^3 \text{ rpm}$ for 10 min (Eppendorf, Germany) to remove metal particles from the sonicator tip. The suspension was then ultrafiltrated using a 10 kDa membrane and then lyophilized and kept in a sealed glass vial. Samples were prepared by dissolving the lyophilized XG in the appropriate buffer up to the desired concentration. The samples were filtered prior to measurement with a $0.2 \mu\text{M}$ syringe filter to eliminate the presence of dust and aggregates. Figure 49 shows the number averaged (M_n) and weight averaged (M_w) molecular weights as a function of the energy provided to the sample from GPC measurements

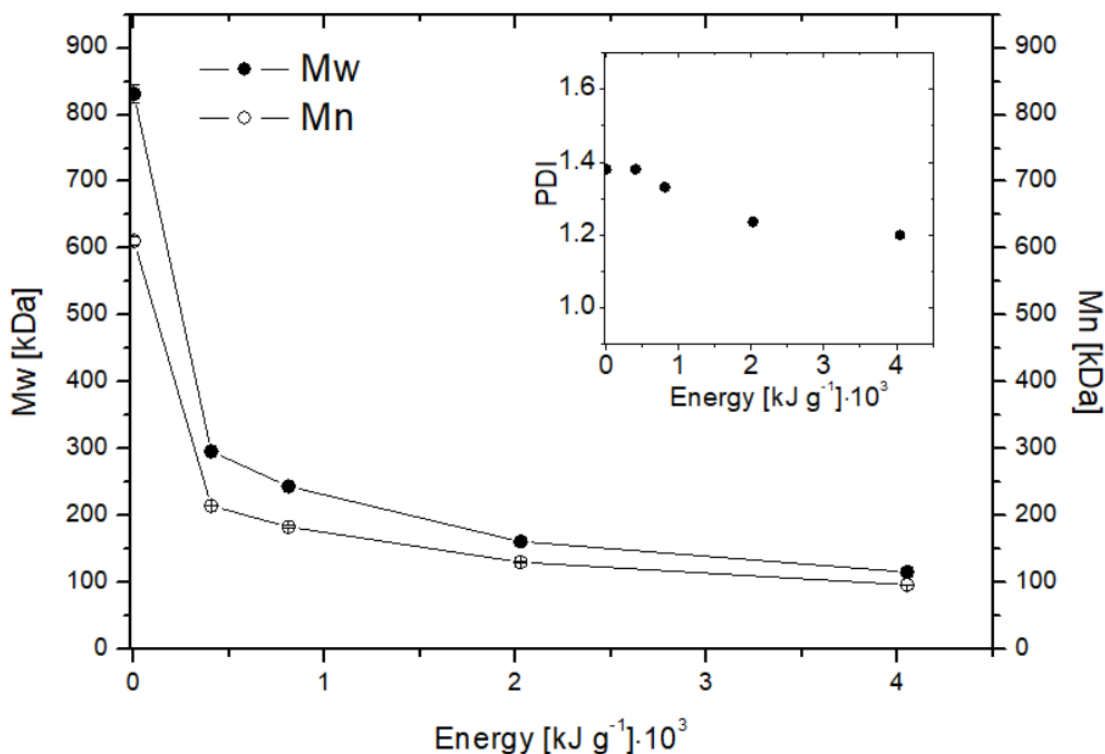


Figure 49. Molar mass of sonicated XG as a function of the energy provided to the sample. Inset: PDI as a function of the energy provided to the sample. The sonication of XG was carried out as detailed in the experimental section.

The PDI, defined as M_w/M_n , is shown in the inset. (note: Although both describe the degree of "non-uniformity" of the sample, PDI from GPC experiments should not be confused with PDI from DLS experiments the latter is defined from the analysis of the cumulants fit to an auto-correlation function).

XG in this work was used in the **sonicated form** ($M_w=100$ kDa).

3.1.4. Pectin

Pectin (98% homogalacturonan from citrus) was purchased from Cargil (Cargil, France). Two types of pectin with different degrees of methyl esterification were tested. P35 and P71 with manufacturer reported DE =35 and DE=71 respectively, where DE is the degree of methyl-esterification defined previously in chapter 1.2.3.

Pectin samples were dissolved in Mili-Q water containing 20 mM of EDTA at pH 8, to remove possible calcium contamination. The samples were then dialyzed for 10 days against water until the conductivity was stable and then passed through ultrafiltration membrane with a cutoff of 10 kDa to remove the low M_w oligomers. The samples were then centrifuged at 33000 RPM with ultracentrifugation (manufacturer) to remove possible aggregates, lyophilized and kept in glass vials in the absence of light and humidity until used. The degree of methyl esterification was determined using ^1H NMR using a method described by Grasdalen et al. (Grasdalen, et al. 1988) The average molecular weight distribution was determined with GPC for the two samples. Table 7 summarizes the results:

Table 7. M_w , M_n and R_g obtained from GPC for P35 and P71. ^adegree of methyl esterification determined by ^1H NMR.

Sample	DE [%] ^a	M_w [kDa]	M_n [kDa]	M_w/M_n	R_g [nm]
P35	29	123.9±0.1	59.0±0.5	2.10±0.02	27 ± 2
P71	60	150.7±4.5	68.0±2.1	2.22±0.01	33± 3

Taking the average molecular weight of galacturonic acid monomer and the methyl esterified monomer to be 194.1 and 253.1 g mol⁻¹ respectively, we can calculate the average theoretical molecular weight M_{av} :

$$(Eq. 15) \quad M_{av} = 194.1 \cdot (1 - DE) + (253.1 \cdot DE)$$

and obtain the degree of polymerization:

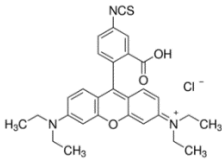
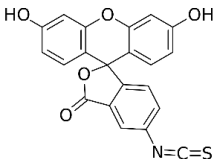
$$(Eq. 16) \quad DP = \frac{m_n}{m_{av}}$$

The calculated DP were 278 and 289 for P35 and P71 respectively.

3.1.5. Grafting of Fluorophores on CNC, XG and Pectin

CNCs, XG and pectin were fluorescently labeled in order to enable their visualization via fluorescence microscopy. The fluorophores used were Rhodamine-B Isothiocyanate (RBITC) for the CNCs and Fluorescein isothiocyanate (FITC) for the soluble polysaccharides- XG and Pectin (P35). Table 8 shows the chemical structure, molecular weight and the excitation/ emission wavelength of each fluorophore.

Table 8. Chemical structure, Mw and Excitation/Emission wavelengths of the fluorophores used for this study.

	Rhodamine B	FITC
Chemical structure		
Mw [g mol⁻¹]	536.1	389.4
Excitation/Emission	$\lambda_{ex}=540\text{nm}/\lambda_{em}=580\text{nm}$	$\lambda_{ex}=490\text{ nm}/\lambda_{em}=520\text{ nm}$

The following equations were used in order to calculate the required mass of fluorophore with respect to polysaccharide.(Dong and Roman 2007, Nielsen, et al. 2010)

$$(Eq. 17) \quad m_{RBITC} = 0.032 \cdot m_{cnc} \cdot m_{w,RBITC}$$

$$(Eq. 18) \quad m_{FITC} = 0.32 \cdot m_{XG \text{ or } Pectin} \cdot m_{w,FITC}$$

Where $m_{w,RBITC}$ and $m_{w,FITC}$ are the molar masses of Rhod-B and FITC respectively. In the case of CNCs, the mass was divided by 10 in order to avoid excess substitution which may alternate the interaction with the other polysaccharides.(Radavidson 2016)

CNC labeling

CNCs were labeled according to previously described protocols by Nielsen and Dong(Dong and Roman 2007, Nielsen, et al. 2010) with slight modifications. Cellulose nanocrystals (250 mg) were suspended in 25 mL of 0.1 M NaOH together with 7.5 mg of RBITC (Sigma-Aldrich) and stirred for 4.5 days in the dark at ambient temperature. The suspension was centrifuged for 20 min and 20000 g and the orange supernatant removed. The precipitate was redispersed in water and dialyzed using a 10 kDa membrane against deionized water for 10 days until the pH was stable, and then freeze dried. The obtained pink powder was stored in a sealed vile and kept in the dark. Prior to use, the powder was dissolved into to the desired buffer and sonicated using tip sonicator for 60 seconds to break any formed aggregates.

XG and pectin labeling

Polysaccharides (xyloglucan and pectin) were labeled using a similar protocol to the one used for CNC labeling. 25 mL of polymer solution (1% wt.) was mixed with NaOH 0.2M and 75 mg of FITC (Sigma-Aldrich). The mixture was stirred for 4 days in the dark at ambient temperature and the resulting solution was dialyzed against water until the pH was stable. The solution was then transferred to an ultrafiltration cell and passed through a cellulose nitrate membrane (Amicon) with a 10 kDa cutoff for 24

hours under constant water flow, to remove the excess of unbound fluorophores. The resulting solution was lyophilized and kept in sealed vials in the absence of light.

Calibration curves

In order to calculate the number of grafted groups, a calibration curve was generated for the two types of fluorophores using UV-vis spectrometer. RBITC and FITC solutions with known fluorophore concentrations were prepared, and the absorbance value was recorded with a specific excitation wavelength for each type of fluorophore, according to their characteristic excitation/emission spectrum (see table 8).

Figure 50 shows the calibration curves and the linear fits.

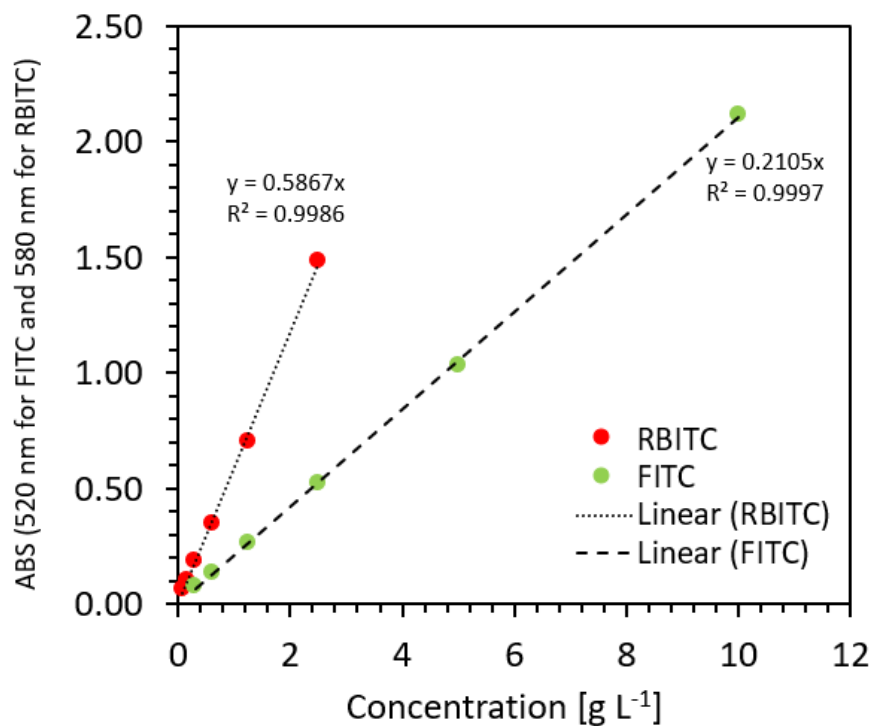


Figure 50. Calibration curves for RBITC (red circles) and FITC (green circles) with the linear fits (dashed lines)

Determination of the grafting density

In order to determine the grafting density, a 1%wt. CNC-RBITC suspension and 0.2% wt. XG-FITC or P35-FITC suspensions were used. The absorbance values obtained were 0.332, 0.154 and 0.228 for CNC-RBITC, XG-FITC and P35-FITC respectively. By using the linear fits from the calibration curves, a relationship between the absorbance at a specific wavelength and the fluorophore concentration can be derived:

$$(Eq. 19) \quad ABS_{580} = 0.5867 \cdot C_{RBITC}$$

$$(Eq. 20) \quad ABS_{520} = 0.2105 \cdot C_{FITC}$$

By using equations 19 and 20 we obtain 0.19 g L⁻¹ for RBITC, 0.03 g L⁻¹ for XG-FITC and 0.04 g L⁻¹ for P35-FITC respectively. Knowing the molar mass of the fluorescent moiety and the solution concentration, we can derive the amount of grafting expressed in units of mol fluorophore/mg CNCs.

The values obtained were 3.6 μmol g⁻¹ for CNC-RBITC, 41 μmol g⁻¹ for XG-FITC and 61 μmol g⁻¹ P35-FITC. These low grafting densities were chosen in order to minimize the effect of grafting in the physical properties of the materials.

3.2. Summary

In this chapter we have studied the preparation and characterization of the building blocks that will be used for interaction studies and biomimetic constructs.

Table 9 gives a recap of the main results.

Table 9. Summary of the main results from the building blocks characterization.

Component of PCW	Role in planta and % of total PCW mass	Representative building block in vitro	Size	Charge
Lipid	Plant plasma membrane- Scaffold	Supported lipid bilayers Lipid vesicles Liposomes GUVs	Flat, t= 4-5 nm Spherical, D= 50-500 nm Several μm	Zwitterionic, positive or negative
Cellulose	Crystalline fibers, main bear loading component, 25-30%	Cellulose nano crystals (CNCs) from cotton	Colloidal crystals with rectangular cross section, dimensions: w: 20-21 nm l:100-250 nm t: 5-8 nm	Negative $\sim 0.5 \text{ e nm}^{-2}$
Hemi-cellulose	Connects to cellulose to create bear loading network, 10-30%	Xyloglucan (XG)	800 kDa 100 kDa	Neutral
Pectin	Matrix polymer, present throughout the wall and in the middle lamella, 20-50%	Homogalacturonan Two degrees of ME: 29 and 60%	100 kDa (DE=29) 160 kDa (DE=60)	Negative

In the next chapter we will study the interaction between these building blocks in 2D and 3D configurations.

Chapter 4

Interaction studies

The interaction between PCW components plays an important role in cell biosynthesis and growth. Understanding these interactions is important for developing new strategies to design biomimetic constructs, which can serve as simplified PCW models (Cosgrove 1997, Ochoa-Villarreal, et al. 2012, Somerville, et al. 2004). Thus, identifying the factors governing the interaction between the building blocks is an essential strategic step towards the creation of biomimetic constructs.

In the previous chapters we have introduced the building blocks. In this section, following a short introduction on intermolecular forces, we will focus on the study of the interactions between pairs of building blocks, namely, CNC-Lipid, CNC-XG, and CNC-Pectin, in 2D and 3D systems.

In the 3D systems, the measurements are carried in the bulk solution, meaning that the individual components are mixed and the interactions between them are studied with various experimental techniques such as light scattering, ITC, NMR, and TEM. For the 2D systems, the interactions take place in the vicinity of a surface, thus, in this case we use surface sensitive techniques such as AFM, TIRF, NR, and QCM-D.

Note: chapter 4.2.1 and chapter 4.2.2 were published in peer reviewed journals, see annex I.

4.1. Theoretical background- intermolecular forces

4.1.1. Intermolecular forces

This sub-chapter will provide a short review of the intermolecular forces responsible for the micro- and macroscopic behavior of various natural systems.

Generally, four distinct forces exist in nature. Two of these forces, called strong and weak interactions, act between **elementary particles** (neutrons, protons, electrons) and have a very short range of action, less than 10^{-5} nm. The other two forces are the electromagnetic and gravitational forces that act between **atoms and molecules**. These forces are effective over a larger range of distances, from subatomic to practically infinite distances, and therefore govern the behavior of all common systems.

Table 10. Intermolecular forces and their characteristics.

Force/Bond	Strength	Distance	Origin
Covalent	10^2 - 10^3 kJ/mol	70-200 pm	Wave function overlap, valence shell electron pair repulsion
Ionic	10^2 kJ/mol	0.1-2 Å	Columbic force, maximum packing rules
Hydrogen	1-2 kJ/mol (weak) <160 kJ/mol (strong)	Short range	A strong type of directional dipole-dipole interaction
Electrostatic (coulomb)	Varies with the charge and size of the objects	Long range, nanometers	Columbic force
Van der Waals (VdW)	2-3 kJ/mol	Short range, few Å to few hundreds of Å	(i) dipole-dipole force (ii) dipole-induced dipole force (iii) dispersion forces (charge fluctuation)
Hydrophobic	strong	Long range	A combination of intermolecular forces arising from poor solvent affinity
Depletion	like VdW	Short range ~Rg	Entropic - excluded volume, surrounding macromolecules
Specific binding	Strong combination of multiple forces	Short range	'Lock and key' mechanism

Electromagnetic forces are considered to be the source of intermolecular interactions while gravitational forces account for many cosmological phenomena. Table 10 summarizes the main type of forces exists between atoms and molecules as characterized, when possible, by the strength, distance and origin of the interaction. When acting together, these forces determine a wide variety of phenomena. (Israelachvili 2015) In the following sections, we will see how the relationships between these forces can help us understand interaction mechanisms.

4.1.2. Derjaguin, Landau, Verwey, and Overbeek (DLVO) theory

The well-known DLVO theory was established by Derjaguin, Landau, Verwey, and Overbeek in the 1940s (Derjaguin and Landau 1941, Verwey and Overbeek 1948) and describes the case where Van der Waals (VdW) forces are present in combination with electrostatic forces. The theory is based on the assumption that the electrostatic double layer forces and the VdW attractive forces are independent and therefore can be superimposed, or added, at each interacting distance D . In the case of spherical particles of radius R with surface charge density σ_1 and σ_2 , the VdW attractive interaction energy equals: $W_A(D) = -\frac{AR}{6D}$

In cases that σ_1 and σ_2 have similar charge sign, the repulsive interaction free energy $W_R(D)$ can be approximated as:

$$(Eq. 21) \quad W_R(D) = \frac{2\sigma_1\sigma_2}{\epsilon\epsilon_0\kappa} e^{-\kappa D}$$

Where A is the Hamaker constant and $\kappa = 1/\lambda_D$ is the inverse Debye length. Combining the VdW attraction and the electrostatic double layer repulsion we obtain the DLVO energy between two charged objects:

$$(Eq. 22) \quad W_T(D) = W_R(D) + W_A(D)$$

Figure 51 shows schematic energy as a function of distance profiles of DLVO interaction.

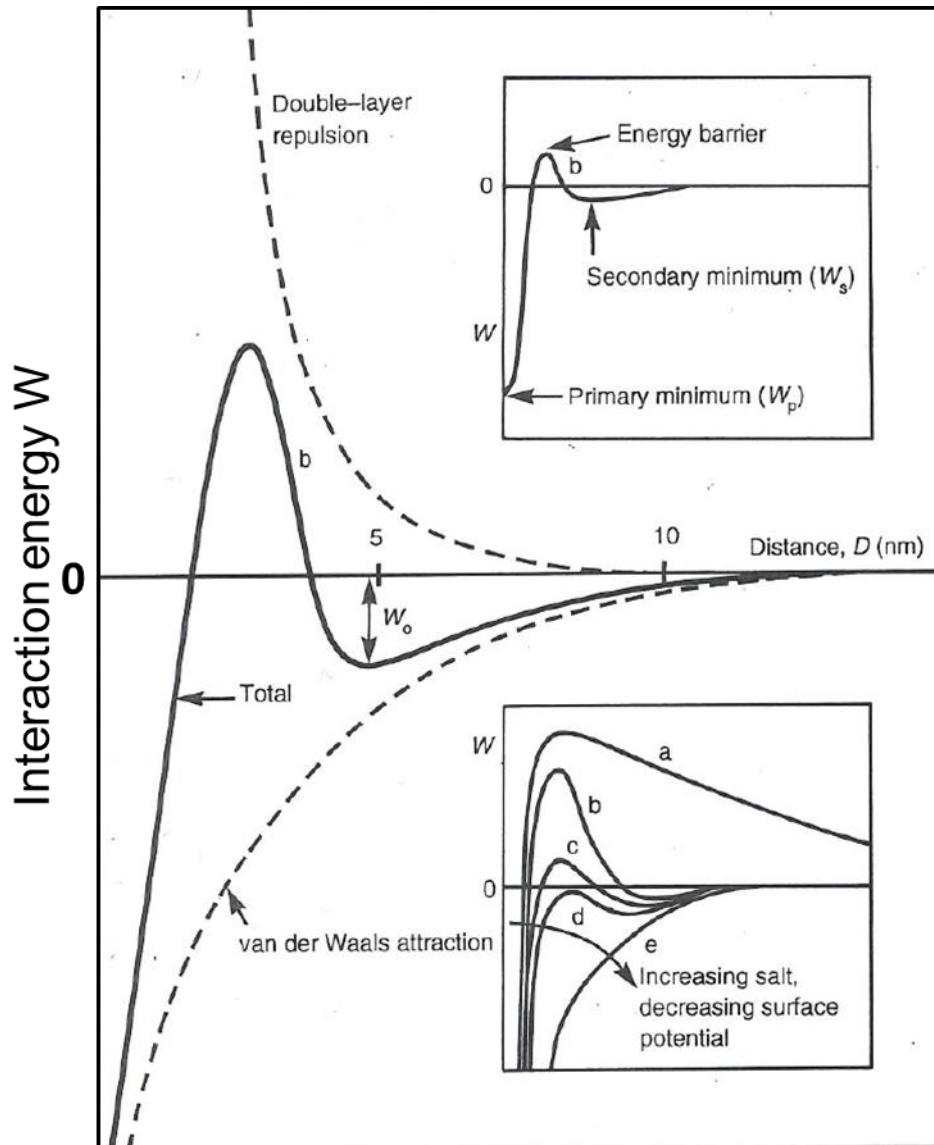


Figure 51. Schematic energy as a function of distance profiles of DLVO interaction. (a) surfaces repel strongly, small colloidal particles remain stable (b) surfaces come into stable equilibrium at a secondary minimum if it is deep enough (c) colloids coagulate slowly (d) the critical coagulation concentration, colloids coagulate rapidly (e) surfaces and colloids coalesce rapidly. (Israelachvili 2015)

From these analyses we see that in order to maintain the stability of the colloidal system, the repulsive forces must overcome the attractive ones. There are two fundamental mechanisms that affect dispersion stability: electrostatic and steric interactions (figure 52).

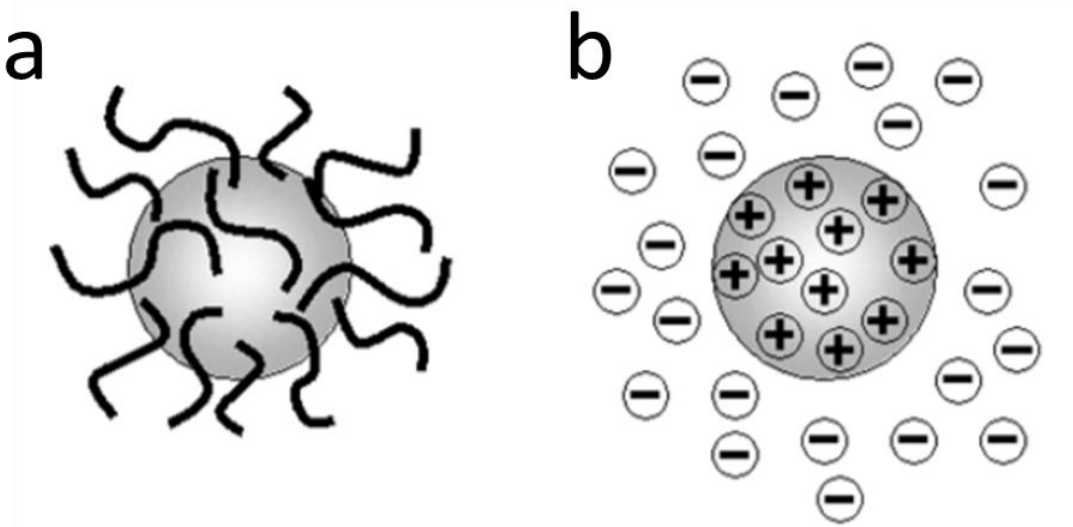


Figure 52. Steric (a) Vs electrostatic (b) colloidal stabilization mechanisms.

- (i) Steric repulsion - involves polymers added to the system adsorbing onto the particle surface and preventing the particle surfaces coming into close contact. If enough polymer adsorbs, the thickness of the coating will be sufficient to keep particles separated by steric repulsions (excluded volume) between the polymer layers, and at those separations the VdW forces are too weak to cause the particles to adhere.
- (ii) Electrostatic or charge stabilization - this is the effect on particle interaction due to the distribution of charged species in the system and greatly affected by the charge and size of the particle and the ionic strength of the medium.

DLVO theory gained appreciation in the scientific community thanks to its intuitive nature and the successful match to experimental results. However, it fails at high salt concentrations, and other forces beyond the DLVO construct (e.g., hydrogen bonding and the hydrophobic effect, hydration pressure, charge transfer, Lewis acid base interactions, and steric interactions) have been reported to also play a major role in determining colloid stability. (Hesselink, et al. 1971)

4.1.3. The electrical double layer (DL)

Charged polymers or particles in solution carry a net charge on their surface, the development of which results in an increased concentration of counter ions, ions of opposite charge to that of the particle, close to the surface. Thus, an electrical double layer exists round each particle (figure 53).

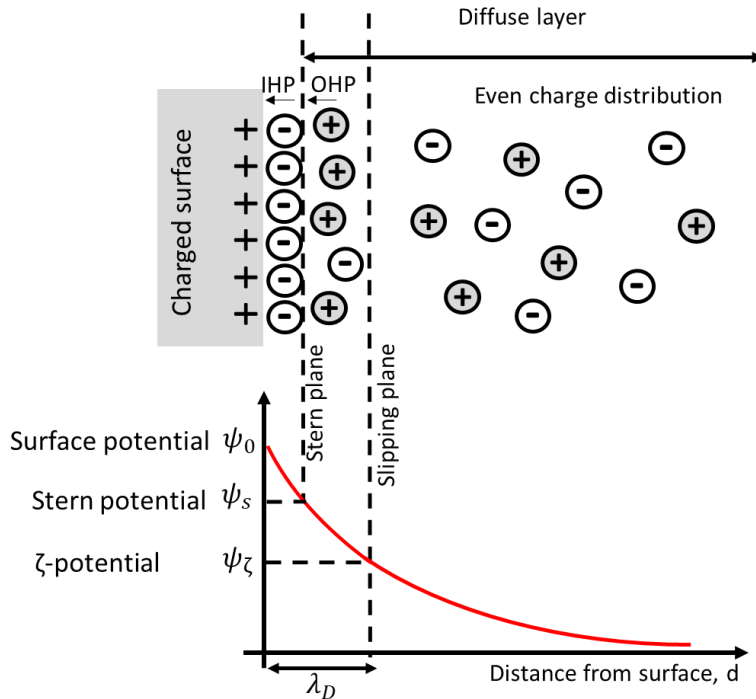


Figure 53. Schematic representation of the ion distribution near a charged surface. The stern layer composed of inner and outer Helmholtz planes (IHP and OHP respectively). The slipping plane corresponds to the layer in which counterions are attached to and move together with the charged particle/surface. λ_D is the Debye screening length. The potential decreases linearly with the distance from the charged surface, in the Stern layer, and exponentially towards zero, in the diffuse layer

The electrical double layer surrounding a charged object is composed of two distinct regions:

- (i) The stern layer - consists of chemically adsorbed ions onto the surface, this layer can be subdivided in two parts: the inner Helmholtz plane (IHP) composed of a monolayer of chemisorbed dehydrated co-ions (ions of the same sign as those of

the surface) and the outer Helmholtz plane (OHP) formed of hydrated counterions of opposite charge.

- (ii) The second layer is composed of ions attracted to the surface charge via Coulomb force, electrically screening the first layer. This second layer is loosely associated with the object. It is made of free ions that move in the fluid under the influence of electric attraction and thermal motion rather than being firmly anchored. It is thus called the "diffuse layer".

The electrical potential ψ decreases linearly until reaching the external boundary of the Stern layer (OHP). Beyond this point the potential obey the Poisson-Boltzmann equation and decrease exponentially.

The characteristic thickness of the DL can be calculated from Poisson-Boltzmann equation by assuming that ψ is small everywhere in the DL: $\psi \ll k_B T$ (Debye-Hückel approximation). (Hiemenz and Rajagopalan 2016, Hunter 2013) The obtained value for the electrical double layer using this approximation is called the Debye length, λ_D . It is reciprocally proportional to the square root of the ionic strength I , at a given temperature T :

$$(Eq. 23) \quad \lambda_D = \sqrt{\frac{e^2 I}{\epsilon \epsilon_0 k_B T}}$$

Where e is the elementary charge, ϵ and ϵ_0 are the dielectric constants of the medium and vacuum respectively, and k_B is the Boltzmann constant. I is the ionic strength of the electrolyte solution, $I = \frac{1}{2} \sum c_i z_i^2$, c_i and z_i are respectively the concentration and the valency of the species i .

At the Debye length, electrostatic interactions are screened in the presence of salt. In a monovalent solution like NaCl the Debye length can be approximated as $0.304/\sqrt{[NaCl]}$ [nm] and for 0.1 M NaCl it is ~ 0.96 nm.

When a particle moves due to thermal motion or gravity, ions within the slipping plane boundary move with it. Ions beyond this boundary stay with the bulk dispersant. The potential at this boundary (surface of hydrodynamic shear) is called the ζ -potential

and have practical significance in the field of particle stabilization. Measurement of ζ -potential is done by measuring the electrophoretic mobility and applying approximations for the size and double-layer thickness of the particle. This method was discussed in detail in chapter 2.2.

4.1.4. Adsorption of polymers on surfaces

Polymers can adsorb on surfaces in various conformations depending on their structural parameters, which alters their behavior compared to their state in solution. An important length scale is the root mean square radius of polymer in solution also called the radius of gyration (R_g). In real (non-ideal) solution the unperturbed radius can be larger or smaller than R_g and is sometimes referred to as Flory radius. (R_F) Adsorbed polymers can be present in the form of loop trains or tails. (Israelachvili 2015)

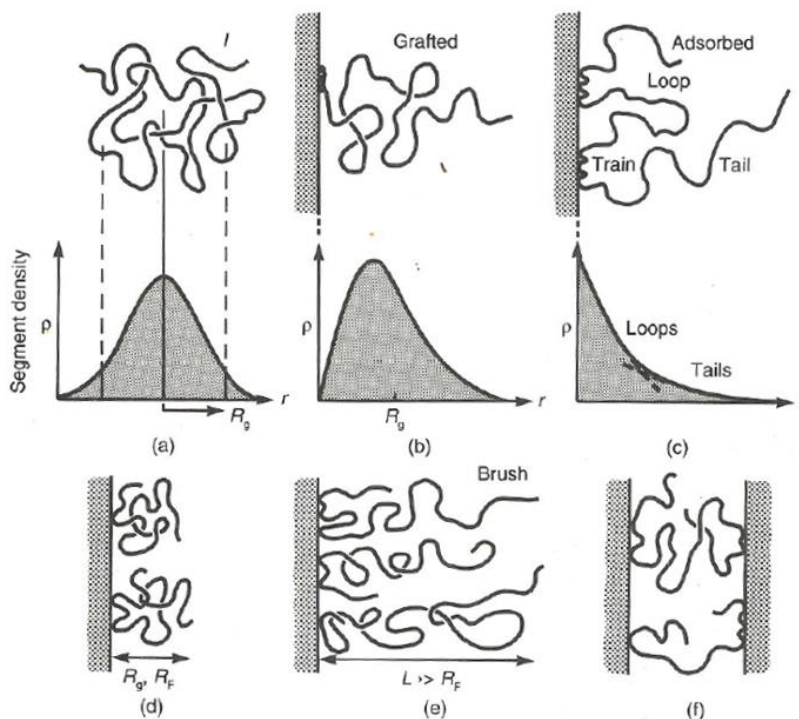


Figure 54. (a) Polymer in solution (b) chemisorbed (end-grafted) copolymer (c) physisorbed homopolymer (d) adsorption at low surface coverage with no nearest neighbor overlap (e) adsorption at high coverage (brush) (f) bridging. (Israelachvili 2015)

Figure 54 shows schematic representation of the behavior of polymers near surfaces. The segment density, ρ , as a function of the distance, r , from a surface is shown in figure 54 a b and c, for a free, grafted and adsorbed polymers respectively, the radius of gyration, R_g , is also indicated.

The conformation of the polymer, often depends on the concentration and solvent, can determine the nature of adsorption as well as the surface coverage. In addition, when additional surface is added, like in the case of layered structures, bridging forces come into play, presenting an additional mechanism of interaction. These features are characteristic for polyelectrolytes as well as for non-charged polymers and can determine the structural properties of biomimetic constructs.

After revising the importance of intermolecular forces in governing interaction phenomena, we will now present the main results from the interaction studies between the selected building blocks.

4.2. CNC-Lipids

4.2.1. Interaction of CNCs with lipid vesicles

In this study, we used CNCs and liposomes made from the zwitterionic lipid 1,2-dioleoyl-sn-glycero-3-phosphocholine (DOPC), from the phospholipid family, the main group of lipids in the plasma membrane (up to 60% of the lipids in plasma membrane are phospholipids (Furt, et al. 2011, Liu, et al. 2015)), with the purpose of studying the interaction between these two representative components of PCWs.

As shown in chapter 3.1.2, CNC are negatively charged, regardless of the pH due to sulfate half-ester groups on their surface. However, DOPC is zwitterionic, meaning that its charge is dependent on the pH of the solution in which it is dissolved. We

therefore combined several characterization techniques in order to test the effect of pH on the interaction between DOPC liposomes and cotton CNCs. Dynamic light scattering (DLS) and electrophoretic mobility measurements respectively provided the size and ζ -potential values for both CNCs and liposomes. ITC was used to obtain the thermodynamic parameters of the interaction, and cryo-transmission electron microscopy (cryo-TEM) was used to directly visualize the CNC/liposome complexes.

4.2.1.1. Materials and methods

Materials

Acetic acid, sodium hydroxide, sodium acetate, sodium chloride (99% pure or higher) were purchased from Sigma Aldrich (Germany). Phosphate buffered saline (PBS) tablets were purchased from Sigma Aldrich and dissolved in 200 mL of deionized water followed by dilution to the desired concentration and ionic strength. 1,2-dioleoyl-*sn*-glycero-3-phosphatidylcholine (DOPC) and 1,2-dioleoyl-3-trimethylammonium-propane (DOTAP) was purchased from Avanti Polar Lipids Inc. (Birmingham, USA) and dissolved without further purification in a chloroform/methanol mixture (9/1 v/v) to a total concentration of 10 mg mL⁻¹. The solutions were stored at -20 °C until use. All other reagents were of analytical grade. All solutions were prepared using deionized water from Milli-Q Millipore system with a resistivity of 18.2 Ω cm. Aqueous acetic acid/sodium acetate buffer was prepared at a total concentration of 100 mM to obtain a solution with pH 3. 120 mM PBS buffer adjusted with small amounts of 0.1 M HCl/NaOH was used to prepare a pH 7 buffer.

Preparation of LUVs

The lipid solution (DOPC or 70/30 mol % / mol % DOPC/DOTAP) in 9/1 v/v chloroform/methanol mixture was transferred into a round-bottom flask and the organic solvent was removed by evaporation under high vacuum pumping for 2 h, until complete evaporation of the solvent. The lipid film was then hydrated in an appropriate amount of buffer solution at room temperature well above the melting point of the lipids to yield suspensions with concentrations of 0.5 – 2.8 mM. Multilamellar vesicles

were then obtained by vortexing for 30 min. The resulting suspensions were then successively extruded 20 times through 200 and 100 nm polycarbonate membranes using a miniextruder (Avanti Polar Lipids). The vesicle size distribution was finally characterized by dynamic light scattering measurements.

Preparation of CNCs

According to the method described by Revol et al., (Revol, et al. 1992) CNC suspensions were prepared by acid hydrolysis of cotton linters (Buckeye Cellulose Corporation, USA). The almost pure cellulosic substrate was treated with 65 % sulfuric acid during 30 min at 63 °C. The suspensions were washed by repeated centrifugations, dialyzed against distilled water until constant conductivity of the dialysis bath and ultrasonicated for 4 min with a Branson Digital sonifier (Emerson, USA) After these treatments, the suspensions were filtered through 8 μm then 1 μm cellulose nitrate membranes (Sartorius). The resulting CNC suspensions had a dry mass content of 2.0 ± 0.1 wt. %. They were then mixed with the appropriate buffer solution to reach a total ionic strength of 100 mM and the pH (2, 3, 5 or 7) was adjusted using small amounts of 0.1 M HCl/NaOH. The final CNC concentration was 1.0 ± 0.1 wt. %.

Dynamic Light Scattering (DLS) and ζ -potential

DLS measurements were performed with a Malvern NanoZS instrument operating with a 2 mW HeNe laser at a wavelength of 632.8 nm and detection at an angle of 173°. All measurements were performed in a temperature-controlled chamber at 20 °C (± 0.05 °C). Three measurements of 15 runs each were usually averaged. The intensity size distribution was obtained from the analysis of the correlation function using the multiple narrow mode algorithm of the Malvern DTS software. The electrophoretic mobility of vesicles and CNCs was measured by using the same Malvern NanoZS apparatus performing at 17° from which the ζ -potential values are determined by applying the Henry equation. The ζ -potential values and the ζ -deviation were averaged over at least 3 measurements with at least 30 runs per measurement was expressed as mean \pm SD ($n \geq 3$).

Isothermal Titration Calorimetry (ITC)

ITC measurements were performed with a VP-ITC microcalorimeter from MicroCal Inc. (Northampton, MA). All samples were degassed using an apparatus provided by MicroCal for 10 min shortly before starting the measurements in order to avoid the presence of air bubbles. The working cell (1.447 mL in volume) was filled with the liposome suspension (0.5 – 2.8 mM initial concentrations) at a given pH. One aliquot of 5 μ L followed by 28 aliquots of 10 μ L of a 0.5 – 1 wt. % CNC suspension (at the same pH as the liposome suspension) were injected stepwise with 300 s intervals into the working cell filled with the vesicle suspension. During the measurement, the sample cell was constantly stirred at a rate of 307 rpm and the measurements were performed at 25 °C. The data analyses were carried out using the Origin software provided by MicroCal. (MicroCal 2004) The heat of dilution, ΔH_d , was determined in control experiments by injecting the CNC suspension into the corresponding buffer solution. The heats of dilution were subtracted from the heats determined in the corresponding CNC-lipid binding experiments noted as ΔH_i . The quantitative evaluation of ΔH from the experimental data was thus based on the relationship:

$$\text{(Eq. 24)} \quad \Delta H = \Delta H_i - \Delta H_d$$

Transmission Electron Microscopy (TEM)

Drops of ca. 0.001 wt.% CNC or CNC / liposomes suspensions were deposited onto carbon-coated TEM grids freshly glow-discharged in an easiGlow plasma cleaning system (Pelco). After 2 min, the liquid in excess was blotted away with filter paper and a drop of 2 wt.% uranyl acetate negative stain was deposited before complete drying. After 2 min, the stain in excess was blotted and the remaining thin liquid film was allowed to dry. Cryo-TEM specimens were prepared by quench-freezing thin films of ca. 0.1 wt. % CNC / liposome suspensions formed on NetMesh lacy carbon films (Pelco) into liquid ethane, using a Leica EM-GP fast-freezing workstation equipped with a temperature- and humidity-controlled chamber. The specimens were mounted in a

Gatan 626 specimen holder cooled with liquid nitrogen, transferred into the microscope and observed at low temperature (-176 °C) under low illumination. Both negatively stained and quench-frozen specimens were observed using a Philips (FEI) CM200 'Cryo' microscope operating at 200 kV. The images were recorded with a TVIPS F216 TemCam camera (2040 × 2040 pixels) and processed using the imageJ software.(Schneider, et al. 2012)

4.2.1.2. Size and Morphology of CNC-lipid Complexes

Characterization of the Individual Constituents

DLS (Figure 55a) and ζ -potential measurements (Figure 55b) were performed in order to characterize the individual constituents of the system at different pH values.

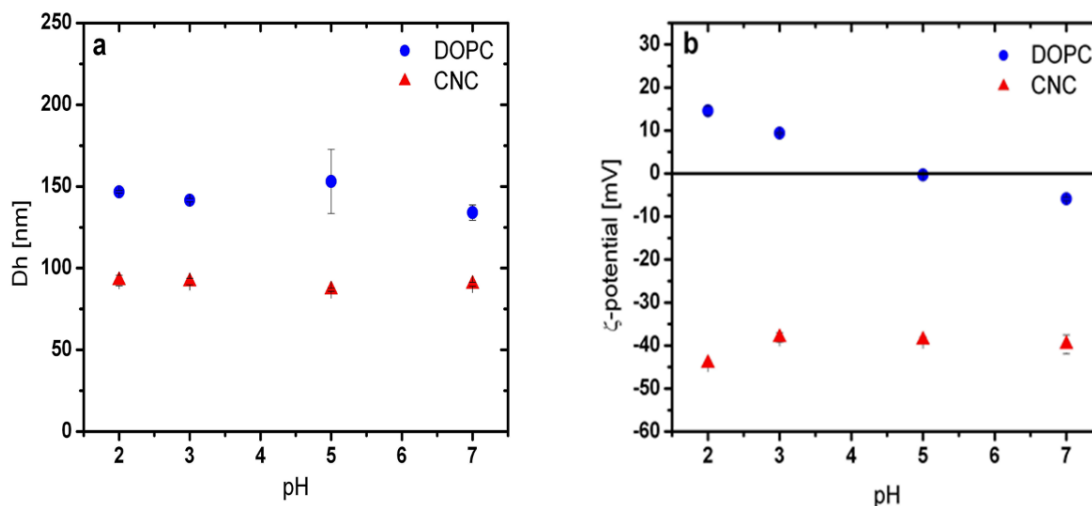


Figure 55. Hydrodynamic diameter (a) and ζ -potential (b) of 0.4 mM DOPC liposomes (blue disks) and 0.1 wt. % CNC (red triangles) suspensions at different pH values.

Table 11 shows the values obtained from light scattering for the individual objects. For the bare DOPC vesicles, the average hydrodynamic diameter was 130 – 160 nm over the considered pH range, indicating that pH had a minor effect on the vesicle size distribution. However, the charge sign of the vesicles varied with the pH. The ζ -

potential was positive at pH 2 and 3, close to neutral at pH 5 and negative at pH 7. These results correspond to what was previously observed for DOPC vesicles prepared in similar conditions.(Quemeneur, et al. 2008)

Table 11. Hydrodynamic diameter (Dh) and ζ -potential values of bare DOPC vesicles (0.5 mM) and CNCs (0.1 wt. %), from DLS data.

	pH	Dh [nm]	PDI	ζ -potential [mV]	ζ -deviation [mV]
DOPC	2	146.7 \pm 0.8	0.10 \pm 0.01	14.6 \pm 1.1	8.6 \pm 1.0
	3	141.6 \pm 1.1	0.08 \pm 0.01	9.4 \pm 0.2	4.9 \pm 0.5
	5	153.0 \pm 19.6	0.24 \pm 0.01	0.3 \pm 0.1	3.8 \pm 0.2
	7	134.0 \pm 4.7	0.06 \pm 0.01	-5.9 \pm 0.4	6.3 \pm 0.7
CNC	2	92.5 \pm 3.2	0.18 \pm 0.02	-44.1 \pm 0.6	12.2 \pm 0.8
	3	91.8 \pm 2.0	0.17 \pm 0.02	-38.1 \pm 1.1	14.3 \pm 2.9
	5	86.8 \pm 0.9	0.21 \pm 0.01	-38.7 \pm 0.7	17.6 \pm 2.4
	7	90.2 \pm 1.2	0.17 \pm 0.01	-39.7 \pm 2.2	13.6 \pm 0.4

DOPC is a zwitterionic lipid with a positively charged choline group and a negatively charged phosphate acid group, and its overall pKa is 0.8.(Moncelli, et al. 1994) Several hypotheses regarding the apparent charge of DOPC lipids exist in the literature. Makino et al. studied the charge of vesicles made of neutral lipids.(Makino, et al. 1991) They suggested that the orientation of the charged groups was responsible for the reverse in sign, the isoelectric point depending, in their case, on the type of lipid and ionic strength. Quemeneur et al. observed an isoelectric point at pH 4 for DOPC vesicles in 300 mM sucrose solution.(Quemeneur, et al. 2010) They suggested that the reverse in sign emerges from the presence of hydronium ions which represses the dissociation of the phosphate acid group at low pH. Then, the positive contribution of the amino group becomes dominant and the lipid becomes slightly positively charged.

We observed the isoelectric point at pH 5, the slight difference being perhaps due to the different ionic strength used in the different cases. It is expected that the charged vesicles exist as individual objects in a dilute medium. However, at pH 5, partial aggregation was observed, as indicated by the larger width of the size distribution. The instability of the vesicles close to the isoelectric point is not surprising since the nearly neutral charge causes a weaker electrostatic repulsion, thus promoting their spontaneous partial aggregation.

For the CNCs, the average hydrodynamic diameter was around 90 nm within the entire pH range. It is important to mention here that since light scattering measures the diffusion coefficient, which is then converted to a hydrodynamic diameter using the Stokes-Einstein relation, this value represents the diameter of a sphere with the same diffusion coefficient as the rod-like objects and not its actual dimensions. The size reported here is in agreement with previously reported values for cotton CNCs prepared using the same method. (Azzam, et al. 2010, Elazzouzi-Hafraoui, et al. 2007) The size and ζ -potential of the CNCs did not depend on pH, eliminating the possibility of aggregation of CNCs. The ζ -potential was around -38 mV for all pH conditions. CNCs are negatively charged, as expected due to the presence of ester sulfate groups on their surface after sulfuric acid hydrolysis, which also makes them stable over a wide pH range. (Dong, et al. 1998, Wang and Roman 2011)

These observations denote that concerning the individual objects, the sole parameter varying with the pH was the vesicle surface charge.

Addition of CNCs to DOPC vesicle suspensions

The addition of CNCs into lipid vesicle suspensions was investigated visually and by DLS under two different conditions: i) opposite charge sign (pH 3) and ii) similar charge sign of the components (pH 7). The samples were prepared by adding the CNC suspension in a stepwise manner to liposome suspensions prepared at pH 3 and 7. Fifteen aliquots of 10 μ L 1 wt. % CNC suspension were added to a vial containing 1.5

mL of 0.5 mM lipid vesicles. Mixtures of DOPC vesicles with 0.01, 0.05, and 0.1 wt. % CNCs were transferred to the NanoZS chamber for inspection.

Table 12 and figure 56 shows the variation of the average hydrodynamic diameter obtained by the titration of a vesicle suspension (0.5 mM DOPC) with different amounts of a 1 wt. % CNC suspension at two different pH values. At pH 3, with the addition of CNCs, the average size of the objects in the medium increases and the distribution becomes wider

Table 12. Hydrodynamic diameter (Dh) of DOPC+CNC complexes at pH 3 and 7.

pH	C _{CNC} [wt. %]	Dh [nm]	PDI
3	0.001	428.6 ± 33.1	0.25 ± 0.01
	0.01	1808.7 ± 161.1	0.27 ± 0.15
	0.1	2140.3 ± 351.7	0.29 ± 0.06
7	0.001	133.7 ± 5.6	0.09 ± 0.03
	0.01	131.3 ± 3.4	0.14 ± 0.01
	0.1	126.0 ± 4.2	0.16 ± 0.01

The results demonstrate the formation of large complexes at pH 3. At pH 7, no particles larger than the initial objects were detected upon addition of CNCs, implying that no aggregation occurred at this pH.

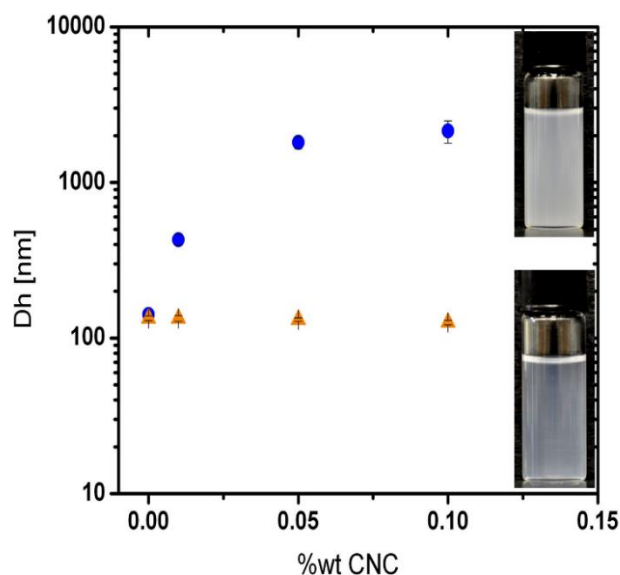


Figure 56. Hydrodynamic diameter variations upon addition of CNCs into a DOPC vesicle suspension (CDOPC = 0.5 mM) at pH 3 (blue disks) and pH 7 (orange triangles) at a constant ionic strength of 100 mM. Insets are photographs of the mixtures, taken 24 h after mixing, corresponding to the addition of 0.1 wt. % CNC at the two different pH values.

As shown in the insets of Figure 56, a clear difference between mixtures prepared at pH 3 and 7 was observed for the addition of CNCs into a suspension of lipid vesicles. At pH 3, aggregation, indicated by the immediate increase in turbidity, was detected with the addition of negatively charged CNCs to positively charged vesicles. However, at pH 7, no such aggregation was observed and the suspension was stable over a period of several weeks. It is suggested that the stability of the suspension at pH 7 arises from CNC-CNC, vesicle-vesicle and vesicle-CNC electrostatic repulsions due to the similar charge of the components.

Similar observations were made for the interaction of CNCs with cationic double tailed (Oikonomou, et al. 2017, Oikonomou, et al. 2018) and single tailed (Dhar, et al. 2012) surfactants, where addition of oppositely charged amphiphiles resulted in CNC aggregation.

Furthermore, this also demonstrates the efficiency of light scattering to probe, in more detail, the formation of complexes, as previously shown by Berret et al. for

electrostatic polymer-particle (Berret 2007) and lipid-nanoparticle (Mousseau and Berret 2018, Mousseau, et al. 2018) interactions.

In order to gain further information on the system, we investigated the interaction at different pH using TEM.

4.2.1.3. Electron microscopy observations of CNC-liposome complexes

The addition of CNCs into liposome suspensions was monitored by TEM. First, each component was imaged individually for reference. Figure 57a is a micrograph of CNCs dried from an aqueous suspension at pH 3. Negative staining was used to provide more contrast. The rod-like particles have a length of 50 - 200 nm and a width of 10 - 20 nm, which are typical dimensions for cotton CNCs. These CNCs are made of 3 - 5 elementary crystallites that were not separated during the acid hydrolysis and subsequent sonication treatment.(Elazzouzi-Hafraoui, et al. 2007) The particles are well dispersed due to the electrostatic repulsion from the charged sulfate groups on the particle surface, as previously explained.

Figures 57b and 57c show cryo-TEM micrographs of bare DOPC vesicles embedded in a film of vitreous ice at pH 3 and 7, respectively. At pH 3, the vesicles were mostly unilamellar and spherical with a diameter ranging from 100 to 200 nm, in fair agreement with the dimensions measured by DLS. A small number of multilamellar and elongated vesicles were also observed. At pH 7, the vesicles were mostly multilamellar with a diameter ranging from 100 to 200 nm. The vesicles were mostly spherical but several elongated objects were observed.

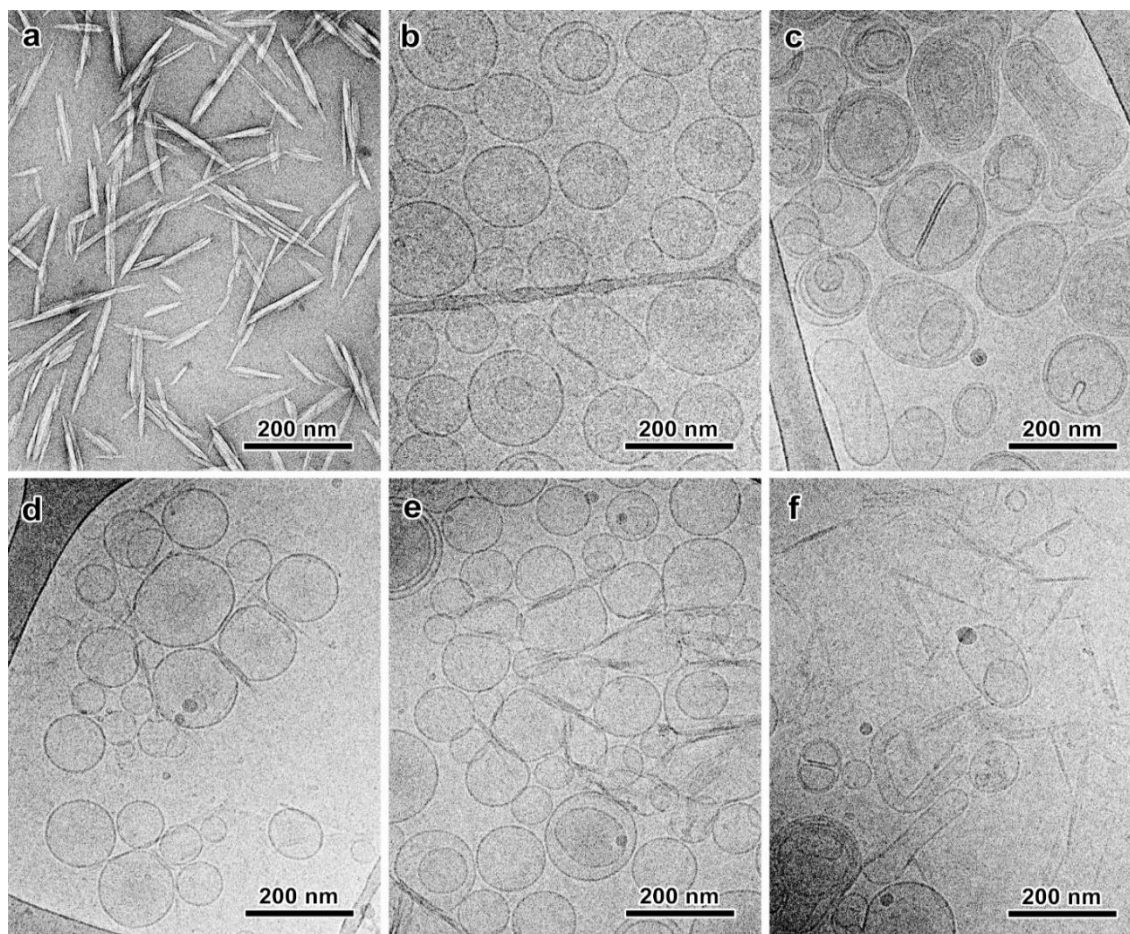


Figure 57. a) TEM images of negatively stained CNCs; b-f) cryo-TEM micrographs of DOPC vesicles at pH 3 (b) and pH 7 (c), and DOPC vesicle/CNC complexes at pH 3 (d,e) and pH 7 (f). All samples were prepared with a CNC/lipid mass ratio of 0.05. (cryo-TEM images taken by Jean-Luc Putaux)

Figures 57d and 57e are cryo-TEM micrographs of a mixture of DOPC vesicles and CNCs at pH 3, in a ratio corresponding to the first injection of an ITC experiment (*i.e.* 10 μ L of CNCs in 1.5 mL of vesicles, see ITC section for details). Several general features can be seen: i) all CNCs are in close proximity to the lipid vesicles, ii) no free CNCs were observed and iii) the adsorption of CNCs onto the surface of the lipid vesicle induced a deformation / flattening of the membrane. In addition, the shape and rigidity of the CNCs restrict the interaction with the entire surface area, mostly due the critical curvature radius beyond which the rigid rod-like CNCs lose contact with the flexible vesicles. Figure 57f shows a mixture of DOPC vesicles and CNCs at pH 7 in a ratio

corresponding to the first injection of the ITC experiment (*i.e.* 10 μ L of CNCs in 1.5 mL of vesicles). Well separated CNCs were observed, with no contact with the vesicles.

These TEM observations, together with the DLS experiments, therefore confirmed the pH-dependent formation of lipid-CNC complexes, which suggests that the charge of the constituents plays a major role in the interaction.

4.2.1.4. Thermodynamic characterization of CNC-liposome interaction

Heat flow measurements using ITC

ITC measurements were carried out in order to characterize and quantify the thermodynamic behavior and the stoichiometry of CNC adsorption onto the surface of DOPC vesicles. For consistency, all experiments were performed in similar conditions of pH and ionic strength as DLS and cryo-TEM analyses.

First, reference titrations were performed in order to determine the heat of dilution, *i.e.* titration of CNCs or vesicles suspension into buffer (Figure 58).

The titration of CNCs into the buffer solution resulted in small equal endothermic peaks resulting from the dilution of CNCs when transferred from concentrated to diluted medium. The measured enthalpy in this experiment is later subtracted from the enthalpy values obtained for the titration of DOPC with CNCs. The titration of bare vesicles into the buffer resulted in small equal exothermic peaks that were likely due to a rearrangement of lipid molecules when injected under stirring into the buffer solution.

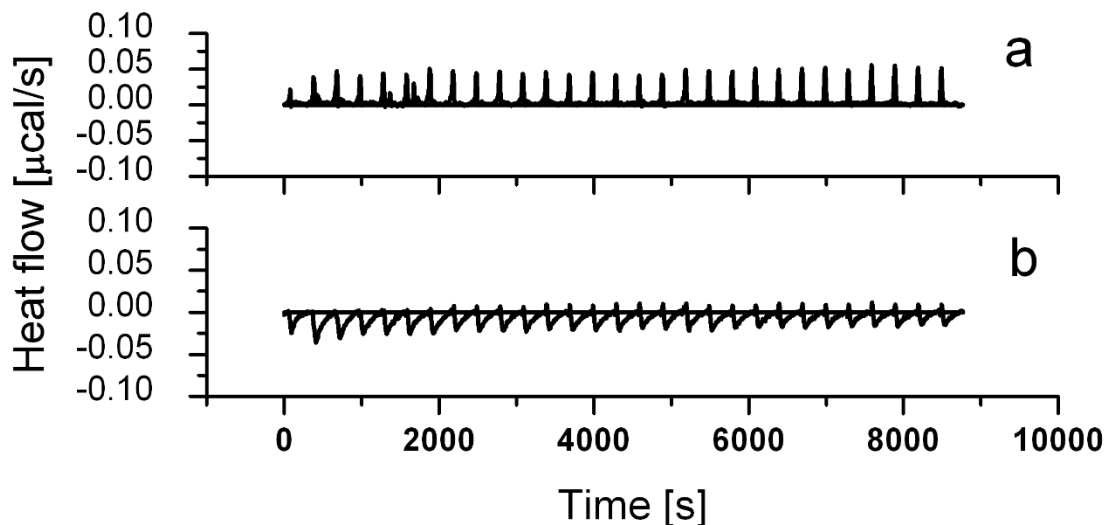


Figure 58. Titration of 1 wt. % CNCs (a) and DOPC vesicles (CDOPC = 2 mM) (b) into the buffer solution at pH = 3.0.

Following the determination of blank heats, we performed ITC titrations from the stepwise injection of a 1 wt. % CNC suspension into DOPC vesicle suspensions of various concentrations: 0.5, 1.0, 2.0 and 2.8 mM. Figure 59 shows the heat flow associated with stepwise addition of aliquots of a 1 wt. % CNC suspension into DOPC vesicle suspensions in buffer at pH 3. Each injection produced an endothermic peak and the heat flow profile exhibits a sigmoidal decrease with the increase in added mass of CNCs until the enthalpy decreases to values lower than $0.05 \mu\text{cal s}^{-1}$, which is the value obtained when CNCs are added into a DOPC free buffer solution.

The decrease in the heat flow magnitude is due to the fact that when CNCs bind to the membrane, they decrease the amount of lipid available for interaction in the bulk, until at the saturation point, defined as $\theta = 1$, where θ is the fraction of lipids in contact with CNCs, there are no more lipids available to interact with the CNCs and therefore no measurable heat of reaction.

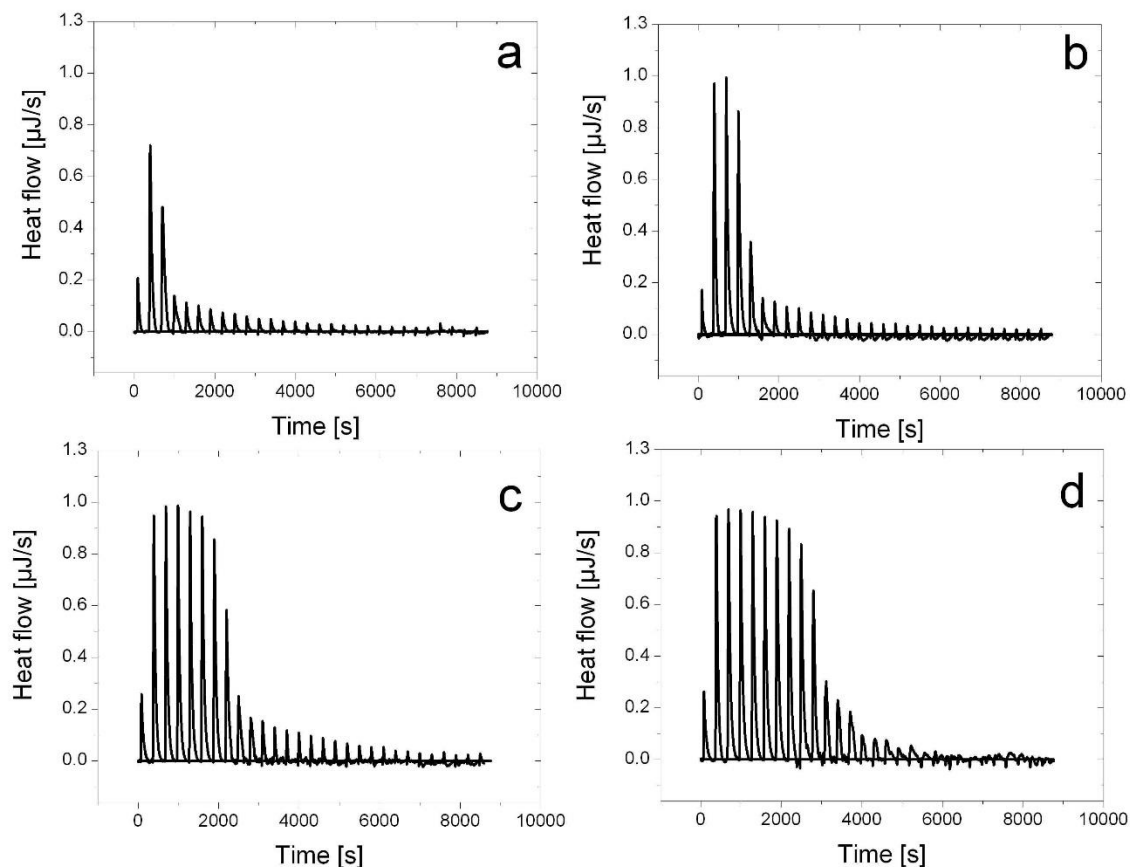


Figure 59. ITC titration curves obtained from the injection of aliquots of a 1 wt. % CNC suspension at pH = 3, I = 100 mM into DOPC liposomes suspensions at 0.5 mM (a), 1.0 mM (b) 2.0 mM (c), and 2.8 mM (d).

The capacity of the vesicles to adsorb CNCs on their surface increases with their concentration as demonstrated by the higher lipid/CNC ratio at which the signal decays. This result is highly important since it is the proof that the origin of the endothermic peak is the interaction between the components and not an artefact. Furthermore, the interaction was endothermic and the curves exhibit the same sigmoidal decrease for all DOPC concentrations examined, implying that at least in this experimental range, the concentration of lipids had no effect on the nature of the interaction.

Figure 60 quantitatively displays the dependency of the amount of added CNCs at $\theta = 1$ on the DOPC concentration present in the reaction vessel. The number of injections until saturation is the sum of all the injections that resulted in heat flow above the heat flow of the buffer, from which the mass of added CNCs is calculated (right axis

in figure 60). The linear relationship between the amount of DOPC and CNC at $\theta = 1$ suggests that n , the stoichiometric ratio of the components at saturation, was constant and, hence, was not affected by the concentration. This observation confirmed that the measured heat directly results from the interaction between the components and therefore allowed us to determine the most suitable range of concentration to be used for titrations at different pH conditions.

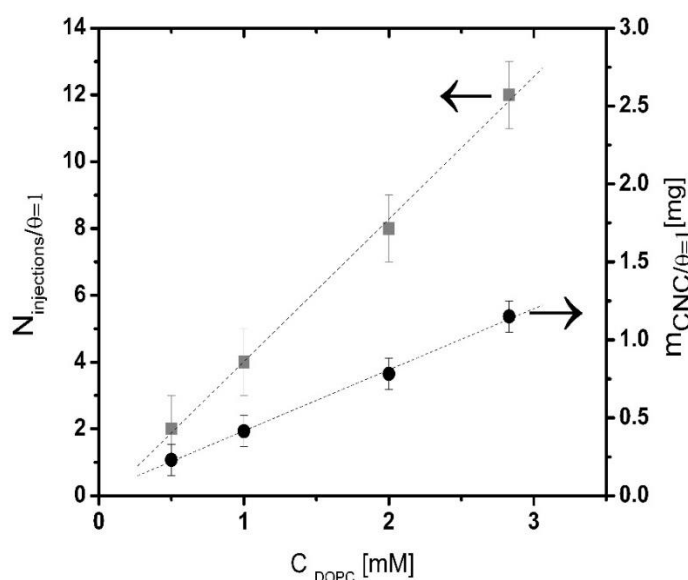


Figure 60. Number of injections (grey squares, left axis) and the corresponding mass of CNCs (black disks, right axis) at saturation as a function of DOPC concentration. The arrows refer to the axis that corresponds to each data set. The dashed lines are guides to the eye.

Interaction Modeling and Thermodynamic Parameters

The thermodynamic parameters of the CNC adsorption onto the external leaflet of DOPC liposomes were obtained from ITC experiments using a single set of identical sites model according to Langmuir adsorption isotherm included in the Microcal origin software in the ITC module. (MicroCal 2004) The analysis was performed using the least-squares fitting method. In this model, the binding constant, K , describes the

equilibrium between the concentration of the lipid-CNC complex and the concentrations of the free constituents can be expressed as:

$$(Eq. 25) \quad K = \frac{\theta}{(1-\theta)[X]}$$

where θ is the mass fraction of lipid occupied by CNC and $[X]$ is the concentration of free CNCs which can be expressed as:

$$(Eq. 26) \quad [X] = X_t - n\theta M_t$$

where X_t and M_t are the bulk concentrations of CNC and DOPC, respectively, and n represents the number of binding sites. In our case, since the concentration are expressed as mass ratios, n no longer represent the number of binding sites but the exact mass ratio as derived from the fitting procedure.

Substituting the expression for $[X]$ given in eq. 26 into eq. 25 yields a quadratic equation for the surface fraction θ . Solving this equation provides an expression for θ as a function of the lipid concentration. Then, the total heat content, Q , of the solution contained in the experimental volume V_o at a given θ is:

$$(Eq. 27) \quad Q = n\theta M_t \Delta H V_o$$

where ΔH is the enthalpy of CNC binding to a unit of mass on the membrane. Fitting the experimentally measured heat release for each step of injection with the expression in eq. 27 provides the fitting parameters n , K and ΔH .

Figure 61 shows ITC curves of titration of DOPC vesicles ($C_{DOPC} = 2$ mM) with ~ 1 wt. % CNC suspensions at pH 2, 3, 5, and 7.

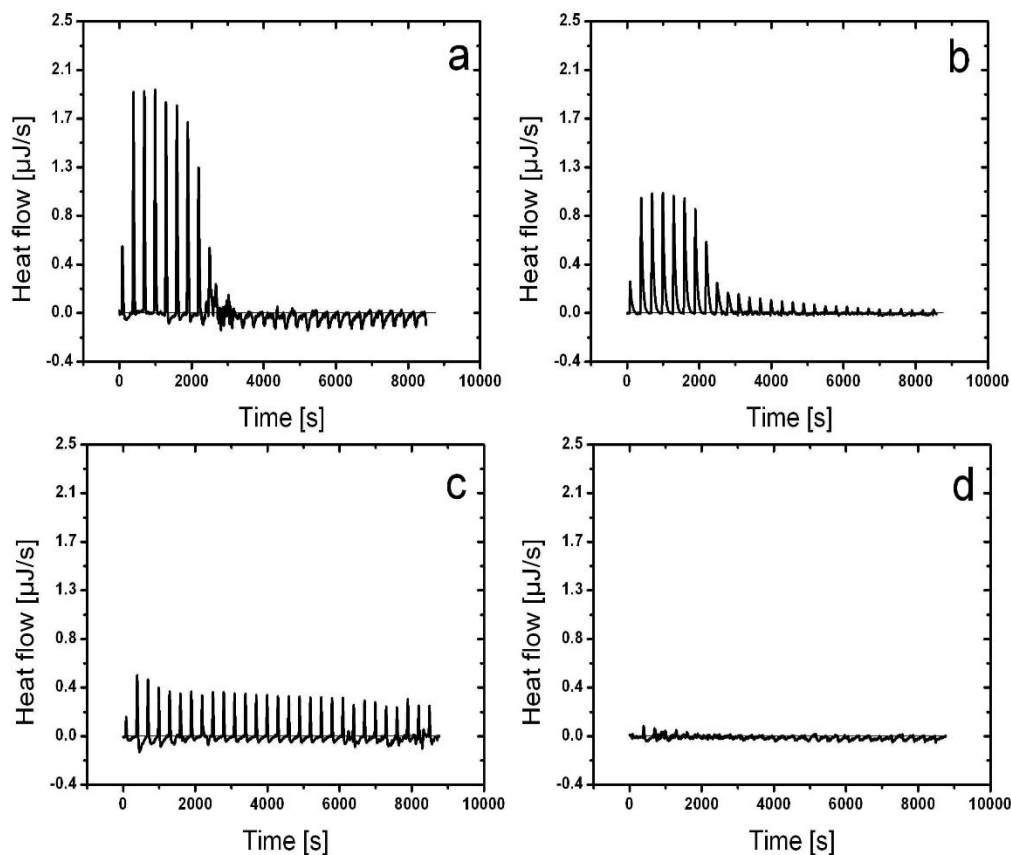


Figure 61. ITC titration curves obtained from the injection of aliquots of a 1 wt. % CNC suspension at pH = 3, I = 100 mM into DOPC liposomes suspensions at pH 2 (a), pH 3 (b) pH 5 (c), and pH 7 (d).

Figure 62 shows normalized heat values as obtained from ITC curves of titration of DOPC vesicles ($C_{\text{DOPC}} = 2 \text{ mM}$) with $\sim 1 \text{ wt. \%}$ CNC suspensions at pH 2, 3, 5, and 7. Each point represents the integration over time of the heat flow resulting from one injection of CNCs into the cell filled with DOPC vesicles. The solid lines represent the fitting to a single set of binding sites model. (Freyer and Lewis 2008) Endothermic peaks were observed for both pH 2 and 3, while very low heat flow was detected for pH 5 and 7 and therefore no thermodynamic parameters could be extracted for these systems.

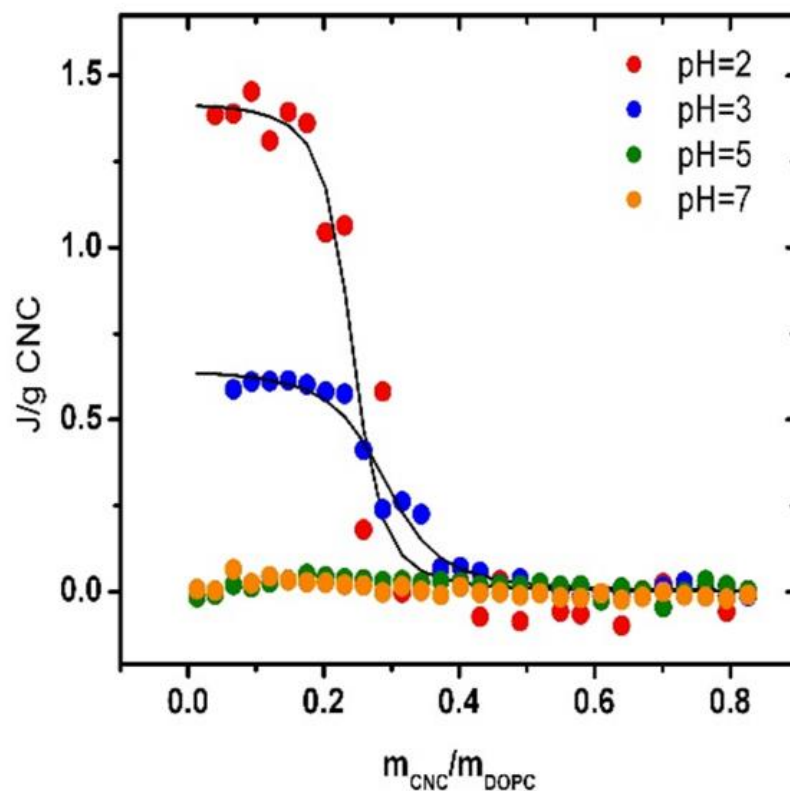


Figure 62. Total heat for the titration of DOPC liposomes (CDOPC = 2 mM) by CNCs (1 wt. %) extracted from the modeling of ITC data at pH 2 (red), 3 (blue), 5 (green) and 7 (orange).

The values of the thermodynamic parameters normalized to the mass of CNCs are presented in Table 13. Since the exact number of CNC particles is unknown, we could only obtain the stoichiometric ratio, n , the enthalpy of the process, ΔH and the binding constant, K_a . The amount of heat adsorbed per unit of mass of CNCs was larger at pH 2 than at pH 3 and no heat flow was detected as a result from titrations at pH 5 and 7 where the components possess a similar negative charge sign.

At pH 2 and 3, where the charge sign of the components is opposite, an endothermic interaction was detected with larger values of enthalpy and association constant at pH 2. The enthalpy values were 1.36 ± 0.08 and 0.70 ± 0.16 J g⁻¹ at pH 2 and 3, respectively. The association constant, K_a , is a measure of the affinity of the objects under inspection, the higher K_a , the stronger the association. K_a was 475 and 48 L g⁻¹ at

pH 2 and 3, respectively, indicating that the affinity between the CNCs and the liposomes is slightly stronger at low pH. n represents the stoichiometry of the components, *i.e.* their mass ratio at saturation. The values of n were 0.26 ± 0.06 and 0.34 ± 0.06 at pH 2 and 3 respectively. As this variation is not significant within the experimental error and sensitivity of the fitting procedure, it cannot be used to conclude on the effect of pH on the stoichiometry of the system.

Table 13. Thermodynamic parameters obtained for the titration of 2 mM DOPC vesicles with 1 wt. % CNC suspensions at pH 2 and 3.

pH	N	Ka [L g ⁻¹]	Kd [μg L ⁻¹]	ΔH [J g ⁻¹]
2	0.26 ± 0.06	475 ± 123	2213 ± 638	1.36 ± 0.08
3	0.34 ± 0.06	48 ± 11	21509 ± 5204	0.70 ± 0.16

Altogether, the thermodynamic parameters indicated that the CNC-liposome interaction only occurred when the charge sign of the components was opposite and was more pronounced at lower pH. The aggregation of liposomes mediated by particles with opposite charges was previously reported by Dimova et al. who showed that the addition of positively charged chitosan caused the aggregation of negatively charged liposomes. (Mertins and Dimova 2011) They proposed that the electrostatic attraction between oppositely charged particles was the origin of the measured heat. The lectin-mediated aggregation of lipid vesicles was also reported by Rando et al. (Slama and Rando 1980) However, in this case, hydrophobic interactions were suggested as the main mechanism for aggregation. Lombardo et al. (Lombardo, et al. 2017) studied the interaction between CNCs and bovine serum albumin (BSA) and showed that the adsorption of the protein depended on the charge displayed on the crystals. In all the above-mentioned works, the complexation process yielded positive enthalpy values and the process was assumed to be governed by the entropy gain associated with the release of water and counterions from the hydration shell of the particles.

Generally, the origin of the measured enthalpy in the ITC experiment is a sum of several contributions: 1) dilution of solvent/particles (that could be exothermic or

endothermic depending on the molecular interactions present in the system), 2) counterion release from the electrical double layer, typically endothermic and driven by entropy, and 3) electrostatic complexation.

Let us examine the different contributions with respect to our system. In our case, the heat resulting from the dilution of the particles into the buffer is subtracted from the total measured heat leaving a positive value of ΔH . Considering the fact that no heat was measured in the case of similar charges at pH 5 and 7, it is reasonable to assume that the charge of the particles plays a key role in the interaction and therefore the interaction is governed by electrostatics. However, the value of the measured enthalpy is positive. A possible explanation for this result could arise from the fact that the heat produced by the release of water molecules and counterions overcomes the heat produced due to electrostatic complexation and that coulombic interaction only weakly contributes to the measured heat flow. Since the Gibbs free energy must be negative for the complexation process, it implies that the value of $T\Delta S$ at both pH 2 and 3 is positive.

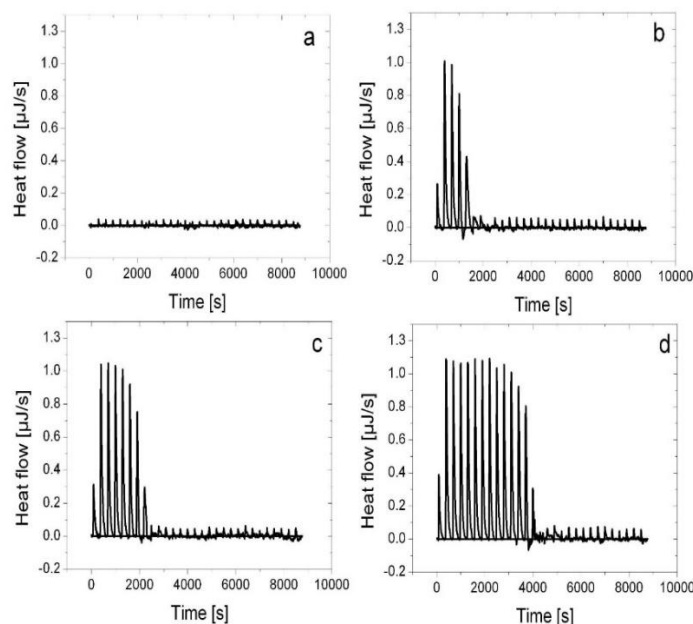


Figure 63. ITC curves of the titration of ~ 1 wt. % CNCs into DOPC/DOTAP vesicles (70/30 %/% mol at pH 7.2 in 120 mM PBS). Titration of CNCs into (a) buffer, and into vesicles at (b) 0.7 mM (c) 1.0 mM (d) 2.0 mM.

In addition, experiments were performed on DOPC/DOTAP formulations, where the charge sign of the vesicles was positive at pH 7. The interaction profile was similar to the one of DOPC at pH 3, yielding thermodynamic values in the same order of magnitude as the experiments performed on pure DOPC at pH 2 and 3, in agreement with the previous results, as shown in figure 63 and table 14.

Table 14: Hydrodynamic diameter (D_h) and ζ -potential values and thermodynamic parameters of DOPC/DOTAP vesicles as obtained from light scattering and ITC measurements respectively.

D_h [nm]	ζ -potential [mV]	n	K_a [$L g^{-1}$]	K_d [$\mu g L^{-1}$]	ΔH [$J g^{-1}$]
151.5 ± 1.7	$48.0 \pm 1.2a$	0.39 ± 0.01	401 ± 330	3676 ± 2238	0.99 ± 0.02

The effective positive charge on the surface of DOPC liposomes was slightly larger at pH 2 than at pH 3 as indicated by the ζ -potential measurements. Although the initial concentration of lipids in the cell is the same for pH 2 and 3, perhaps due to the presence of larger amount of multilamellar vesicles fewer lipids are available to interact, affecting the apparent CNC/Lipid ratio required to reach saturation. However, as previously discussed, it was not possible to obtain clear conclusion regarding the pH effect on the stoichiometry.

We have estimated the available surface for interaction of both DOPC vesicles and CNCs based on their average dimensions and their surface area. For 2 mM DOPC vesicles with a lipid head area of about 0.7 nm^2 , assuming an interaction on the external leaflet only, the available surface area per 1 mL is 0.42 m^2 . CNCs are rod like objects and their average dimensions are $150 \times 20 \times 7 \text{ nm}^3$ giving surface area of 8380 nm^2 . The approximate mass of one unit, with density of 1.6 g cm^{-3} is $3.36 \cdot 10^{-17} \text{ g}$. Thus, approximately 1.69 g is required to saturate the total available lipid surface, giving a ratio at saturation of 1.07. Considering the fact that the presence of multilamellar vesicles causes a significant reduction of the available surface area, this ratio is lower than what is observed from the ITC analysis. Since the association clearly takes place on the surface of the objects, the surface charge distribution is a key parameter.

As discussed before, CNCs are negatively charged due to sulfate ester groups on their surface, the amount of charges depending on the acidic treatment conditions and the cellulose source.(Dong, et al. 1998) However, since the charge densities may be too small to produce a detectable heat flow ($0.5 - 1 \text{ e nm}^{-2}$ for CNCs and 0.037 e nm^{-2} for lipids,(Chibowski and Szcześ 2016)) and they are partially screened by the presence of salt, the contribution to the heat flow in the system due to the release of counterions may be more significant than the contribution of electrostatic complexation. A possible scenario is that the electrostatic attraction acts on the system in a two-step process where the first step is bringing the particles to a critical distance on the edge of the electrical double layer (a process with no detectible heat) followed by second step which is the release of counterions (a process with measurable heat) which is more significant at lower pH.

A reminiscent two-step process was previously described for the complexation of oppositely charged polyelectrolytes. The complex formation was endothermic and an additional underlying coacervation process was found to be exothermic. An improved model was developed and used to describe the different contributions, based on the total heat response from the ITC experiment. (de Macedo, et al. 2020, Vitorazi, et al. 2014)

In the previously discussed review, Lombardo et al. (Lombardo and Thielemans 2018) have analyzed numerous published studies dealing with the adsorption of various compounds such as proteins, polymers, ions and small molecules onto cellulose surfaces. Their meta-analysis revealed that interactions of cellulose with charged molecules were mostly endothermic and purely entropy-driven. This implies that the adsorption onto nanocellulose surfaces may be described as an interaction between opposite charges, where the entropy increase that arises from the release of surface-structured water molecules and counterions from the electronic double layer, supplies the major contribution to the free energy of adsorption.

4.2.1.5. Summary- CNC-liposome interaction.

In this part, we used DLS, cryo-TEM and ITC to investigate the interaction between DOPC vesicles and CNCs. All techniques consistently revealed the formation of pH-dependent CNC-liposome complexes. The complexes were formed only when the charge sign of the particles was opposite and the complexation was more pronounced at lower pH where the charge of the vesicles was higher. The stoichiometry, enthalpy, and binding constant of the interaction were obtained using ITC. The results led to the conclusion that the charge of the vesicles plays a major role in the interaction and determines whether the complexation will take place or not. For oppositely charged components, the more positive the charge of the vesicles, the more pronounced the association with the CNCs, as demonstrated by a higher Ka value at pH 2. The origin of the measured heat in this case was attributed to the release of counterions from the hydration shell of the particles as the interaction takes place. For similarly charged components, the interaction was not favorable as indicated by the absence of measured heat. This combination of techniques, used previously to study the formation of electrostatic complexes (Courtois and Berret 2010, de Macedo, et al. 2020, Vitorazi, et al. 2014), was found to be a useful approach to investigate the interaction between CNCs and lipid vesicles, and may be applied to other types of complexes made from lipids and CNCs that present different characteristics in terms of charge and size.

In the next part we will use flat supported lipid bilayers in order to investigate the CNC-lipid interaction in a curvature-independent scenario.

4.2.2. Interaction of CNCs with supported lipid membranes- 2D

In the previous chapter we have shown, using light scattering, TEM and isothermal titration calorimetry (ITC), that the interaction between CNCs and lipid vesicles was strongly dependent on the charge of the lipid membrane, which could be controlled either by changing the membrane lipid composition or, in the case of zwitterionic lipids, by varying the pH of the suspension. In this work, we combine QCM-D, AFM and TIRFM data to follow the deposition of CNCs on top of lipid membranes with

the aim of identifying key parameters governing the formation of the constructs. We varied the SLBs lipid composition and buffer pH in order to test the effect of these parameters on the adsorption of CNCs on the SLBs. Finally, SFM and TIRFM were used to explore at different length scales the homogeneity of the films and to determine the effect of CNCs concentration in the solution on membrane surface coverage.

4.2.2.1. Materials and Methods

Materials

1,2-Dioleoyl-sn-glycero-3-phosphatidylcholine (DOPC) and 1,2-dioleoyl-3-trimethylammonium-propane (DOTAP) and 1-palmitoyl-2-(6-[(7-nitro-2-1,3-benzoxadiazol-4-yl)amino] hexanoyl)-sn-glycero-3-phosphocholine (NBD-PC) (powder, >99% purity) were purchased from Avanti Polar Lipids Inc. (Albaster, AL) and dissolved without further purification in a chloroform/methanol mixture (9/1 v/v) to a total concentration of 10 mg mL⁻¹. The solutions were stored at -20 °C until use. Deionized water from Milli-Q Millipore system with a resistivity of 18.2 Ω cm was used for all experiments. Sucrose, H₂SO₄ and H₂O₂ were purchased from Merck (Merck, France) and used without further purification. Rhodamine B isothiocyanate (RhodB), NaCl, D₂O, and Sodium acetate salt (Na⁺CH₃COO⁻, 99% pure) were purchased from Sigma Aldrich (France). All chemicals were of analytical grade.

Vesicle preparation

Lipid mixtures (DOPC or DOPC/DOTAP 2:1 molar ratio) dissolved in chloroform were transferred to a round bottom flask and the chloroform was removed by evaporation under vacuum (100 mbar) for five hours. The lipid film was hydrated by vortexing in the appropriate buffer to obtain a lipid concentration of 1 g L⁻¹. Typically, 3 mL of vesicle suspension was obtained. The resulting multilamellar vesicles were sonicated with a tip sonicator (Branson 450, Emerson, USA) for 5 minutes in an ice bath until clarity, followed by centrifugation (10 minutes at 20100 RCF, ambient

temperature) to remove the metallic particles detached from the sonicator tip. Before subsequent measurements, the resulting small unilamellar vesicles were diluted to 0.1 g L⁻¹ into a solution, which consisted of 200 mM sucrose/10 mM NaCl for pH 6 and 10 mM acetic acid/sodium acetate buffer for pH 3.

CNCs preparation

CNCs suspensions were prepared by acid hydrolysis of cotton linters (Buckeye Cellulose Corporation) according to the method described by Revol et al. (Dong, et al. 1998). The almost pure cellulosic substrate was treated with 65% sulfuric acid for 30 min at 63 °C. The suspensions were washed by repeated centrifugations, dialyzed against distilled water until constant conductivity of the dialysis bath and ultrasonicated for 4 min with a Branson Digital sonifier. After these treatments, the suspensions were filtered through 8 µm followed by 1 µm cellulose nitrate membranes (Sartorius). The resulting aqueous CNCs suspensions had a mass content of 2.0 ± 0.1 wt%. They were then diluted with appropriate amount of buffer to the desired concentration of 1·10⁻⁵-1 wt%).

In order to enable their visualization by fluorescence microscopy, the CNCs were labeled with a Rhodamine-B fluorophore as described by Nielsen et al. (Nielsen, et al. 2010). Briefly, following the grafting reaction, the CNCs were centrifuged at 11200 RPM for 30 minutes; the supernatant was then removed and the pellet re-dispersed into a solution of 0.1 M NaOH. This step was repeated twice and followed by dialysis against pure water until neutrality. The purification step was terminated with a rinsing step in an ultrafiltration chamber through a cellulose membrane of 10 kDa. The final product contained 2 wt%. CNCs and stored at 4 °C until use.

Dynamic Light Scattering (DLS) and ζ-Potential

DLS and ζ-Potential measurements were applied in order to verify the size and charge of the vesicles prior to the SLBs deposition. DLS measurements were performed with a Malvern NanoZS instrument operating with a 2 mW HeNe laser at a wavelength of 632.8 nm and a detection angle of 173°. All measurements were done within a temperature-controlled chamber at 20 °C (±0.05 °C). Three measurements of 15 runs

each were usually averaged. The intensity size distribution was obtained from the analysis of the correlation function using the multiple narrow mode algorithm of the Malvern DTS software. The electrophoretic mobility of vesicles and CNCs was measured by using the same Malvern NanoZS apparatus performing at 17° from which the ζ -potential values are determined by applying the Henry equation. The ζ -potential values and the ζ -deviation were averaged over at least three measurements with at least 30 runs per measurement. They were expressed as mean \pm SD ($n \geq 3$).

Quartz crystal microbalance with dissipation monitoring (QCM-D)

QCM-D experiments were performed using a Q-Sense E4 instrument (Q-sense, Gothenburg, Sweden) equipped with one to four flow modules. Experiments were conducted under continuous liquid flow of liquid with a rate of 50 μ L/min, using a multichannel peristaltic pump (ISM 935C Ismatec, Switzerland). The temperature of the solutions was stabilized using a temperature control chamber (Eppendorf, Germany) operated at 24 °C. A clean quartz crystal sensor was placed in the measurement chamber of the flow module; the resonance frequency and the dissipation factor were monitored in air and then in liquid for the fundamental 4.95 MHz as well as for the six odd overtones ($n=3-13$). Suspensions of small unilamellar vesicles (SUVs) or CNCs were injected into the measurement chamber until a stable baseline was reached ($\Delta F < 1$ Hz over 10 min and $\Delta D < 0.1 \cdot 10^{-6}$ over 10 min). The changes in dissipation and frequency presented here were normalized by the overtone number and reported only for the 7th overtone.

Substrate preparation

Silicon coated AT-cut quartz crystals (QSX 303) were purchased from Biolin Scientific (Stockholm, Sweden). The silicon coated disk shaped had a diameter of 14 mm, a surface roughness < 1 nm with a fundamental frequency of 4.95 MHz \pm 50 kHz. The sensors were rinsed with a 2 wt% SDS aqueous solution followed by abundant water rinsing and dried under a nitrogen stream. The sensors were then exposed to a UV/ozone lamp for 10 minutes prior to the measurements.

QCM-D data analysis

In the case of homogeneous, quasi-rigid films (for which $\Delta D / -\Delta f \ll 4 \cdot 10^{-7} \text{ Hz}^{-1}$), the frequency shifts are proportional to the mass uptake per unit area (m_{QCM}), which can be deduced from the Sauerbrey relationship: (Johannsmann 1999, Reviakine, et al. 2011)

$$(Eq. 28) \quad m_{QCM} = -C \Delta f$$

where C is the mass sensitivity of the crystal (17.7 ng cm⁻² Hz⁻¹ at $f_1 = 4.95 \text{ MHz}$). In the case of soft films, the adsorbed film was modeled as a homogeneous viscoelastic layer of acoustic thickness d_{QCM} , density ρ , and a complex shear modulus $G(f)$ with a storage modulus $G'(f)$ and loss modulus $G''(f)$. The frequency dependence of the viscoelastic properties was approximated by power laws with exponents α' and α'' :

$$(Eq. 29) \quad G'(f) = G_0' \left(\frac{f}{f_0} \right)^{\alpha'}$$

$$(Eq. 30) \quad G''(f) = G_0'' \left(\frac{f}{f_0} \right)^{\alpha''}$$

Where G_0' and G_0'' are the shear storage and loss moduli at a reference frequency, $f_0 = 35 \text{ MHz}$, d_{QCM} is the film thickness with a density of ρ . ρd_{QCM} , $\rho G_0'$, $\rho G_0''$, α' , and α'' were adjustable fitting parameters. The semi-infinite bulk solution was taken as water and was assumed to be Newtonian with a viscosity $\eta_1 = 0.89 \text{ mPa}\cdot\text{s}$ at $T = 25^\circ\text{C}$ and a density of $\rho_1 = 1.0 \text{ g cm}^{-3}$. Initially the CNCs film density ρ was fixed to 1.0 g cm^{-3} . Details of the fitting procedure have been described previously (Eisele, et al. 2012) and the specified errors represent a confidence level of one standard deviation (68%). The viscoelastic model contains exclusively the product terms $m_{QCM} = \rho d_{QCM}$, $\rho G_0'$, and $\rho G_0''$, and the fitting will therefore provide correct results for these product terms irrespective of the exact choice of ρ . The 5th, 7th, 9th, 11th and 13th overtones were used for the calculation.

Determination of coupled water with D₂O/H₂O solvent exchange

The water content of the film was determined by using a procedure described by Craig et al and by Kittle et al. (Craig and Plunkett 2003, Kittle, et al. 2011) by changing the water to deuterium oxide and comparing the scaled QCM-D frequency shifts. Water

was introduced to the flow cell at a flow rate of 0.1 mL min^{-1} on a bare crystal and on a lipid/CNC film. After reaching a stable base line, D_2O was introduced to the cell for few minutes until a stable baseline was obtained, and the frequency changes was recorded for the bare crystal (Δf_{bare}) and the lipid-CNC film ($\Delta f_{\text{n, film}}$). The cells were then rinsed with water until the frequency reached back to the initial value. The reported value is the areal mass of water in ng cm^{-2} .

Scanning Force Microscopy (SFM)

The SFM measurements were performed with a Dimension ICON instrument from Bruker Company. The surface topography was investigated via a pulsed force (PeakForce) mode, whereas the nano-shaving process was done under contact mode. Both modes were applied in situ in liquid medium to avoid the drying of the SLB layer, which could lead to the CNCs layer disassembly. Imaging was performed with an open liquid-cell and a ScanAsyst liquid cantilever-tip having a radius of around 20-30 nm and a spring constant of 0.7 N/m. (manufactory data).

In order to control all probing parameters and better adjust the tip to sample interaction, the SFM data was acquired without ScanAsyst technique. A 50 nm Peakforce amplitude was selected due to the actual low adhesion level and in order to minimize the hydrodynamic forces, which can hinder the measurements. For the same reason, a 1 kHz z-modulation was selected. The PeakForce set-point was kept below the SLB breaking force (i.e. 1 nN for the tip used here). Depending on the density of the CNCs in the film, this setpoint force was adjusted to limit the deformation of the fluid-like SLB below. A force of less than 150 pN was used in the case of a dispersed CNCs layer since the tip pressure is transferred to the SLB via a single cellulose nanocrystal thereby promoting the SLB deformation and in rare cases its disruption. On a contrary, in the case of a dense CNCs layer, a sharp image could be obtained by applying a force of 750 pN. This large force distributes over many CNCs within the layer, thereby promoting less deformation of the fluid-like SLB.

SFM images plotting and their data analysis were achieved with the Gwyddion free software.(Nečas and Klapetek 2012) To extract the thickness of the CNCs layer

after nanoshaving, a careful method needed to be followed since the sample surface was rough. A data leveling was first achieved in the well bottom, i.e. the flattest area, by fitting a plane through three points. After plane removing, different line profiles were plotted to control the plane subtraction. Finally, the step height was determined via averaging a maximum of scan lines passing through the well.

Total Internal Reflection Fluorescence microscopy (TIRF)

Total internal reflection fluorescence microscopy (TIRFM) experiments were carried out with a Leica DMI6000 B microscope. Samples were excited by total internal reflection illumination at 488 and 568 nm and images were captured with an Andor back-illuminated DU-897 EMCCD camera (512X512 pixels) controlled by Leica software (LAS-AF-6000, Leica Microsystems CMS GmbH, Germany). The fluorescence intensity values were evaluated by the Leica LASX software. A region of 50X50 μm^2 (220X220 pixels) was selected and the values were obtained for at least 10 different regions. Error bars indicate the standard deviations for the experimental values ($n \geq 10$).

TIRF observation flow cell preparation

The CNCs/SLBs constructs were generated in an observation cell consisting of a microscope glass slide 2X5 cm with parafilm spacers and sealed with a cover slip, creating observation channels with volume of 50 μL and surface of about 1 cm^2 (see figure 64a). The slides and cover slips were cleaned with piranha solution ($\text{H}_2\text{SO}_4/\text{H}_2\text{O}_2$ 70/30 V%), rinsed with ethanol and stored in milli-Q water until used. Prior to the deposition of the layers, the slides were dried under a nitrogen gas flow. The preparation protocol of sample for observation was the following: on a clean cell, a drop of the suspension was deposited on one side of the channel and pulled in due to capillary forces to the other side of the channel. Excess liquid was wicked off using a filter paper placed on the other side of the channel. The flow in the channel was laminar

so that exchange of material could be easily performed. During the filling process, care was taken to avoid the formation of bubbles during the flowing.

4.2.2.2. Formation of the CNCs/SLBs construct

The deposition of the vesicles was achieved in the following way: first, the channel was rinsed four times with a buffer composed of 200 mM Sucrose and 10 mM NaCl (pH~6). Then a vesicle suspension (DOPC/DOTAP 70/30 %/% mol., 1 gr L⁻¹) was deposited in the cell and incubated for 15 minutes at room temperature. The cell was then rinsed again with 4 volumes of suspension buffer. The SLBs was excited at 488 nm, close to the excitation spectrum maxima of the DOPC-NBD (461 nm). In the second step, a drop of 50 μ L of CNCs at the desired concentration (0-1·10⁻¹ wt%) was loaded into the flow cell and incubated for 15 minutes at room temperature and rinsed with four volumes of a 200 mM sucrose solution. We have chosen not to measure higher concentration of CNCs in order to ensure that the system is in the semi-dilute regime and to avoid influence of particle-particle interaction or a change in rheological properties, on the deposition process.

The deposition of the CNCs on top of the lipid bilayer was visualized by fluorescence, at an excitation wavelength of 561 nm, which is close to maximum in the excitation spectrum of Rhod-B (556 nm). Figure 64 shows the measurement configuration in TIRF and QCM-D modules.

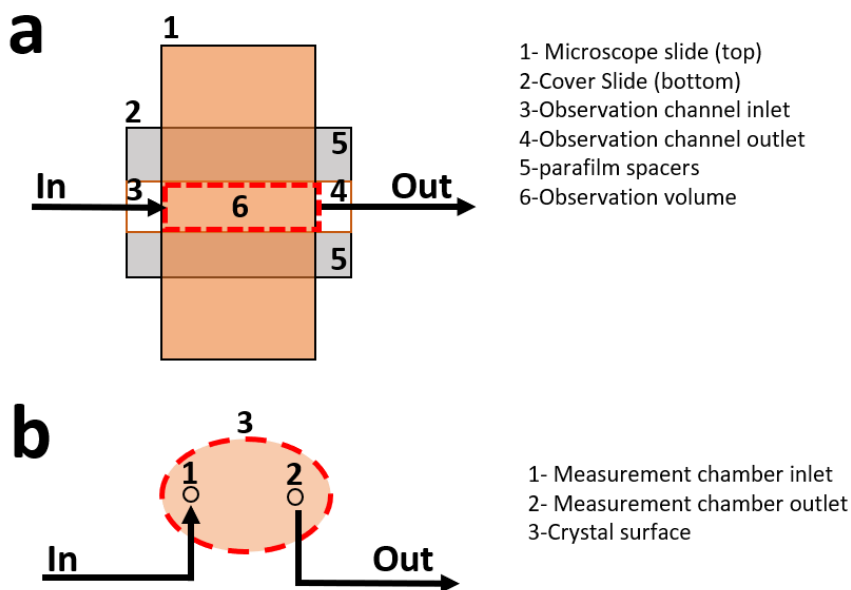


Figure 64. The measurement configuration in (a) the TIRF observation cell and (b) the QCM-D module. Arrows indicate the direction of flow of the solutions the probed area, which was 1 cm^2 with total volume of about $50 \mu\text{L}$ in both cases. Note that while in QCM-D the flow through is continuous, in the TIRF cell a user defined amount of material is flown the channel in each step with a settling time of several minutes between the various steps.

4.2.2.3. QCM-D monitoring of film deposition

QCM-D measurements were used to monitor the formation of the SLBs on the surface of a silica coated quartz crystal and the subsequent adsorption of CNCs onto the lipidic membrane. SLBs were prepared by fusion onto the quartz crystal of small unilamellar vesicles (SUVs) prepared from three different lipid compositions, the chemical structure of the lipids is shown in chapter 3.1.1. The vesicles were characterized for their size and charge using DLS and ζ -potential measurements. The vesicles charge varied according to the pH of the medium and the lipid composition used. DOTAP containing vesicles, showed ζ -potential value of $+47.3 \text{ mV}$ as expected from the positively charged lipid. For DOPC vesicles, The ζ -potential values at pH 6 and 3 were -2.1 and $+9.5$ respectively, the tunable charge of DOPC with pH being associated with its zwitterionic nature. (Makino, et al. 1991) DLS measurements were performed to estimate the average hydrodynamic diameter of the vesicles used to create the SLBs.

The z-averaged hydrodynamic diameters extracted from the cummulants fit to the auto-correlation function varied between 60-110 nm for all lipid compositions used with a PDI of 0.20-0.25.

Figure 65 depicts the QCM-D signals resulting from the mass accumulation on the quartz crystal sensor following the deposition process. After reaching a stable baseline, a suspension of SUVs was injected into the measurement chamber (arrow 1), which was followed by a rinsing step with pure water to ensure complete SLBs formation while removing lipids in excess (arrow 2). The water was replaced by the appropriate buffer, either at pH 3 or 6. (arrow 3). When a constant value of frequency and dissipation was achieved, 0.1 wt% CNCs suspension was injected into the measurement chamber (arrow 4) followed by rinsing step in order to eliminate the excess of non-adsorbed CNCs (arrow 5).

After SUV injection, a decrease in resonance frequency and a small change in dissipation were observed for all the SUV compositions or pH probed. Frequency changes of -24.7, -25.1 and -23.9 Hz were observed for DOPC at pH 3, DOPC at pH 6 and DOPC/DOTAP at pH 6 respectively. These values are in a good agreement with what was expected for the formation of a homogeneous bilayer on top of the quartz crystal sensor. (Richter, et al. 2003, Richter and Brisson 2005) The values of dissipation change were 0.8, 0.3, and $0.1 \cdot 10^{-6}$ for DOPC at pH 6, DOPC/DOTAP at pH 6, and DOPC at pH 3, respectively. These low dissipation values indicate the formation of a compact dense layer at the surface of the crystal, which allowed us to extract the areal mass density from the frequency shifts using the Sauerbrey relationship (eq. 28). Values in the range 420-450 ng/cm² were calculated for the three SLB layers investigated. Assuming a highly hydrated film with a density of close to that of water (1 g/cm³), the derived thickness was thus 4.2-4.5 nm, which matches what is expected for a pure phospholipid bilayer. Note that the frequency and dissipation were not dramatically influenced by the lipid composition or the pH conditions, in fair agreement with previous observations from DOPC and DOPC/DOTAP membranes.(Richter, et al. 2003) These results show the effective deposition of homogeneous SLBs and indicate that changing the membrane composition or the pH had little or no influence on the SLB formation.

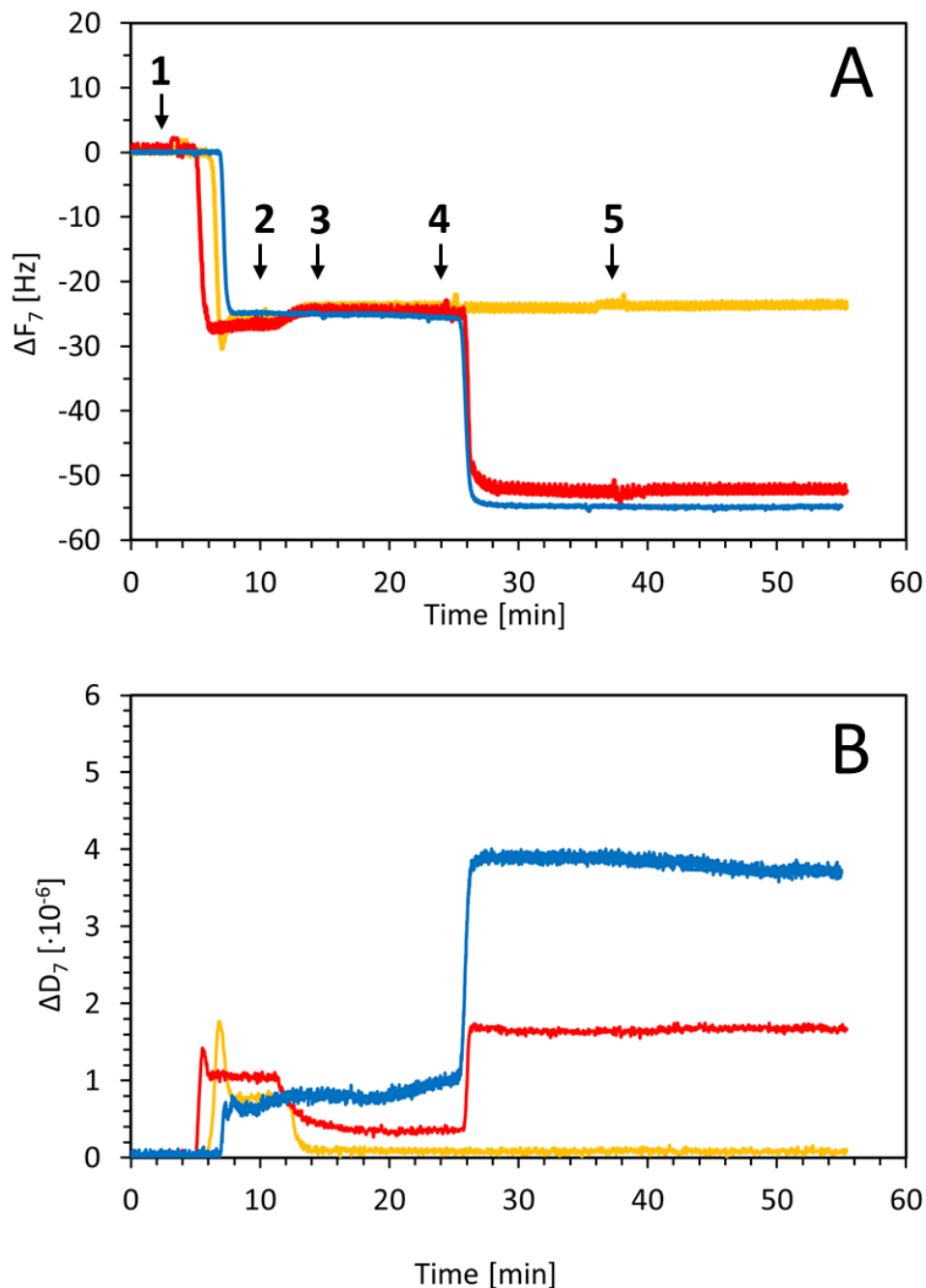


Figure 65. (A) QCM-D profiles showing the changes in frequency for the 7th overtone as a function of time, ΔF_7 , (A) and the corresponding dissipation values for the 7th overtone, ΔD_7 (B) following the injection of lipids and CNCs (0.1 wt%) into the measurement chamber for different lipid compositions and pH: DOPC at pH=6 (yellow), DOPC/DOTAP at pH 6 (red) DOPC at pH 3 (Blue). The arrows correspond to the injections of the following solutions: 1-vesicles, 2-water, 3-buffer, 4-CNCs and 5- water.

In the subsequent step, the adsorption of CNCs onto the SLBs of various compositions and surface charges was evaluated by QCM-D, following the injection of

0.1 wt% CNC suspensions. A notable decrease in frequency of -27.6 and -29.8 Hz was measured for DOPC/DOTAP at pH 6 and DOPC at pH 3 respectively (red and blue curves in figure 65), showing the successful deposition of the nanoparticles on top of the SLBs in these systems. Oppositely, no detectable change in frequency could be observed when the SLB was composed of DOPC at pH 6, reflecting that no CNCs adsorption took place in this case. These data qualitatively show that positively charged SLBs are required to make the adsorption of negatively charged CNCs possible. This result is in agreement with our previous observations of a 3D aqueous systems comprising liposomes and CNCs where the charge of the lipid membrane played the main role in the interaction with nanocrystals.(Navon, et al. 2017)

The ΔD values measured as result of CNCs film deposition were $1.4 \cdot 10^{-6}$ and $2.9 \cdot 10^{-6}$ for the DOPC/DOTAP and DOPC membranes respectively. The lower dissipation value in the DOPC/DOTAP case may be related to the surface charge of the membrane. The electrostatic attraction in the case of higher lipid charge led to a more rigid layer while for DOPC at pH 3 - which leads to a zwitterionic membrane- the effect of the surface charge was decreasing rapidly with the distance from the polar head, resulting in weaker attractive forces between the membrane and the CNCs and a more loosely bound layer indicated by the higher dissipation. Nonetheless, both films showed relatively low dissipation values, implying that in both cases the CNCs layer was indeed coupled to the SLB surface. The presence of an adsorbed CNC layer is further evidenced by the fact that the frequency and dissipation curves remained stable following the subsequent rinsing step.

Given the low dissipation values, the SLB layer thickness may be estimated directly from Sauerbrey relationship (eq. 28), however, in order to estimate the CNC layer thickness, a viscoelastic model should be applied. Table 15 provides a summary of the results obtained from the QCM-D experiments. The values shown in the table are derived from average value frequency and dissipation changes for the 7th overtone, ΔF_7 and ΔD_7 , measured over a stable region (minutes 17-22 for SLB and 44-52 for CNCs) and considering initial value of zero for both frequency and dissipation.

Table 15. Quantitative analysis of the QCM-D curves for SLBs and CNCs deposited on SLBs films. ^aEstimation based on the ζ potential values of the SUVs from which the bilayer was formed. ^bValues obtained using Sauerbrey relationship (see materials and methods). ^cValues extracted from viscoelastic modeling using the QTM software (see text for details).

DOPC/DOTAP Molar ratio	pH	ζ -potential [mV] ^a	Δf_{SLB} [Hz]	ΔD_{SLB} [$\cdot 10^{-6}$]	Δm_{SLB}^b [ng cm ⁻²]	Δf_{CNCs} [Hz]	ΔD_{CNC} [$\cdot 10^{-6}$]	Δm_{CNCs}^c [ng cm ⁻²]	d_{CNCs}^c [nm]
2:1	6	+47.3	-24.7	0.3	445.0	-27.6	1.4	565	5.7 (-0.3/+9.7)
1:0	6	-2.1	-25.1	0.8	436.6	+0.2	0.1	N/A	N/A
1:0	3	+9.5	-23.9	0.1	423.1	-29.8	2.9	668	6.7 (-0.2/+1.1)

The values obtained for the CNCs layer thickness were calculated by using the QTM software considering the CNC layer as homogeneous viscoelastic layer. The model takes as an input the frequency and dissipation changes measured for each overtone and extract the thickness for a given density with respect to a reference state, usually taken as pure water (which is justified by the very hydrated state of the layer). A quantitative analysis based on this model yielded adsorbed amounts of 565 and 668 ng for the DOPC/DOTAP SLB at pH 6 and the DOPC SLB at pH 3, respectively.

In the following experiments we focused on adsorption of CNCs on the DOPC/DOTAP membrane since it was found to be more robust and enabled working at nearly neutral pH while avoiding possible contributions from the addition of different salts usually needed for buffer solutions. Since the film is hydrated, its acoustic areal mass density (hydrated mass) will thus be composed of the areal mass densities of the CNCs and the hydrodynamically coupled water molecules and counterions. In order to estimate the amount of bound water, we have performed a solvent exchange experiment.

4.2.2.4. Estimation of CNCs water content using D₂O/H₂O solvent exchange

In order to better estimate the water content of the CNC film adsorbed on the SLB, we used a D₂O/H₂O solvent exchange procedure. (Craig and Plunkett 2003, Kittle, et al. 2011). In this method, the difference in the normalized frequency between the bare

crystal and the film, following the exchange of water with D₂O, is used for the calculation of coupled water according to eq. 31 and eq. 32, as follows:

$$(Eq. 31) \quad (\Delta f_n)_{water} = \frac{(\Delta f_n)_{film} - (\Delta f_n)_{bare}}{\left(\frac{\rho_{D_2O}}{\rho_{H_2O}}\right)^{-1}}$$

Where ρ_{D_2O} and ρ_{H_2O} are the densities of D₂O and H₂O respectively, (1.106 and 0.998 g cm⁻³ at 25°C), $\Delta f_{n,bare}$ and $\Delta f_{n,film}$ are the recorded frequency changes due to the exchange of D₂O with water for the bare crystal and the film respectively. For the case where the layer is comprised form the film and exchangeable water, then $\Delta f_{n,film}$ will contain the contribution from the crystal and the film plus exchangeable water. $\Delta f_{n,water}$ can then be calculated from the difference between $\Delta f_{n,bare}$ and $\Delta f_{n,film}$ according to equation 31 and the surface concentration, Γ_{water} , is calculated from equation 32:

$$(Eq. 32) \quad \Gamma_{water} = -C \cdot (\Delta f_n)_{water}$$

Where C is a constant, 17.7 ng cm⁻² Hz⁻¹.

Figure 66 shows the normalized frequency for the 7th overtone, obtained from the exchange of D₂O and water for the bare crystal (dashed black line) and the film (solid red line).

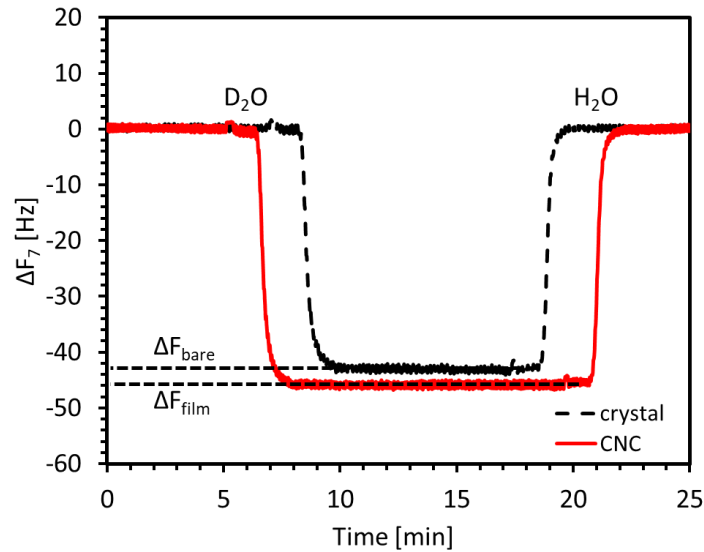


Figure 66. Normalized frequencies (n=7) following D₂O/H₂O exchange procedure for the bare crystal (dashed black line), and for the film (solid red line).

The experiment was done for DOPC/DOTAP SLB composition, where CNC adsorption is possible in pure water. The normalized frequencies at the 7th overtone were recorded and found to be -45.6 ± 1.1 Hz and -43.3 ± 0.6 Hz (mean \pm SD, $n \geq 3$) for the film and the bare crystal respectively. Γ_{water} was then calculated for the film according to equations 31 and 32 and was found to be 380 ± 90 ng cm⁻². The hydrated mass obtained for the same type of film was 565 ng cm⁻², resulting in dry mass of 185 ng cm⁻². The amount of water in the film may be directly derived from the hydrated and water masses, and it was found to be $67 \pm 15\%$.

4.2.2.5. Microscopic visualization of the constructs using TIRF

In order to investigate the structural properties of the CNCs/SLB constructs at tens of micrometers length scale, TIRF microscopy was used to directly image the formation of the lipid bilayer and the deposition of the CNCs on top of it. Especially, the effect of CNCs concentration on the formation and homogeneity of CNCs/SLBs films was investigated. CNCs samples were prepared from dilution of a 1% CNCs aqueous suspension at pH 6 and the resulting sample concentration varied from 0 to 0.1 wt%. We did not use 1 wt% sample in order to avoid viscosity variation which can influence the flow in the cell.

The experiments were performed in a flow chamber described in the experimental section, which is commonly used for biophysical studies (Gilboa, et al. 2009). In order to visualize the SLBs and CNCs simultaneously, two fluorescent probes were used: lipidic membranes were labeled using NBD-PC and CNCs using Rhodamine B (see experimental section for details). Figure 67 depicts the impact of CNCs concentration using 45×45 μm^2 top view images of the films in the case of SLB-only visualization (top row), CNCs-only visualization (middle row) and co-visualization (bottom row).

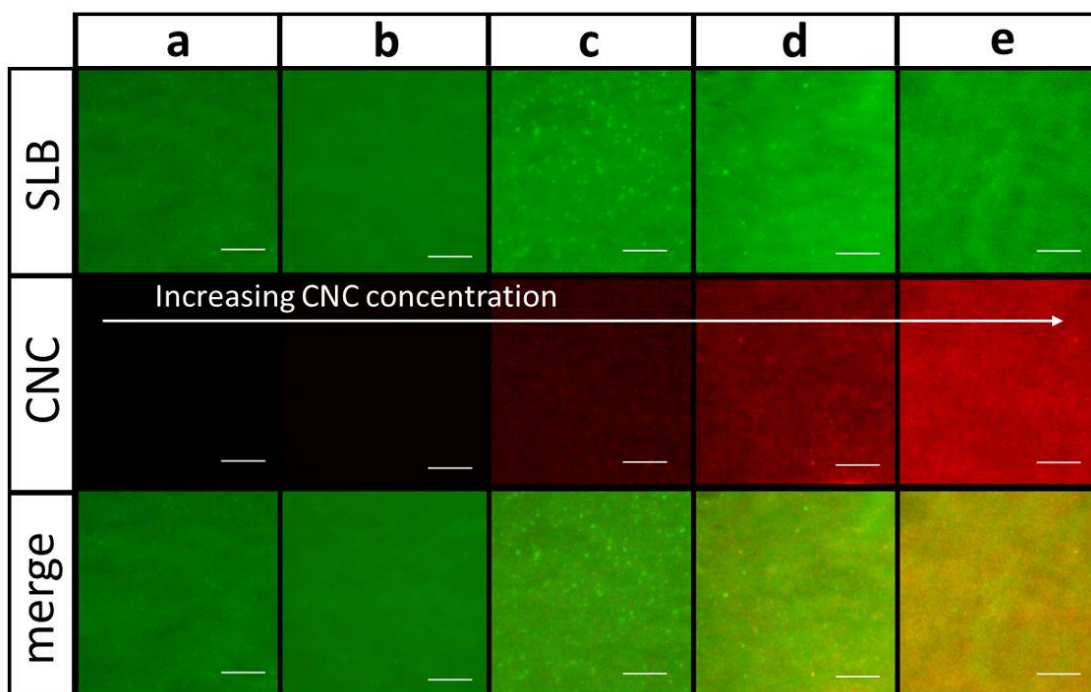


Figure 67. TIRF images of SLBs-CNCs thin films recorded with two excitation modes simultaneously at the same region of interest with increasing CNCs concentrations: 0 (a), $1 \cdot 10^{-4}$ (b), $1 \cdot 10^{-3}$ (c), 0.01 (d) and 0.1 wt% CNCs (e). Top: DOPC-NBD SLB signal (excitation at 568 nm) bottom: overlay of the two channels. The images were recorded under the same acquisition conditions for all samples (see methods). The scale bar is 10 μm .

As shown in the top row in figure 67, the images confirm the presence of a homogeneous, defect-free SLBs at the micrometer length scale in the observation cell whatever the CNCs concentration is. In Figure 67c and 67d, bright spots, most likely resulting from clusterization of NBD-PC fluorophores can be observed. However, it appears that the clusters had no apparent influence on the bilayer homogeneity nor on the fluorescence signal, as will be shown below. Since the same SLB deposition protocol and membrane composition were used for all samples, the fact that the fluorescence intensity remained roughly constant, using the same acquisition parameters, merely demonstrates the reproducibility of the SLBs deposition protocol, enabling to examine directly the effect of CNCs concentration on its deposition. In addition, the deposition of CNCs did not cause SLB removal or disruption as demonstrated by the fluorescence homogeneity on the merged image (bottom row in Figure 67).

In order to quantify the variation in fluorescence intensity and the homogeneity of the lipid bilayer we have performed a statistical analysis of fluorescence intensity on a series of TIRF images. It is important to mention here, that quantification of fluorescence signal should be carried out and interpreted carefully due to number and experimental sensitivity of the parameters that can influence the signal. To ensure the proportionality of the measured signal to the amount of fluorophore in the sample, we have kept the acquisition parameters (i.e. laser intensity, exposure time and camera gain) constant while varying only the CNCs concentration. Figure 68 shows the average fluorescence values obtained from statistical analysis of the images using the green (SLBs visualization) and red (CNCs visualization) channels for each CNCs concentration for a given region of interest. Typically, 10 regions were averaged and the errors were expressed as the standard deviation from this population ($n \pm SD$).

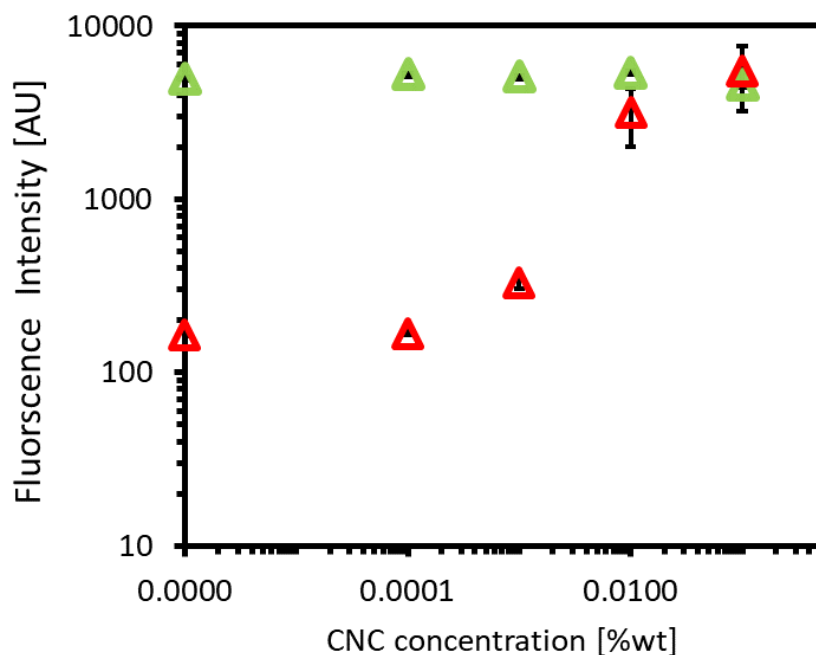


Figure 68. Average fluorescence intensity as a function of CNCs weight percent for the SLBs (green triangles) and CNCs layer (red triangles). Values correspond to mean \pm SD ($n=10$).

While the average fluorescence intensity of the SLBs remained roughly constant within measurement error 5070 ± 320 AU, the fluorescence intensity of the CNCs layer increased with the increase in CNCs concentration tending to a plateau around 0.01

wt%. CNCs. For CNCs concentrations of 0 and $1 \cdot 10^{-4}$ wt%, no fluorescence was observed above the noise level of 164 ± 2 AU, determined from the intensity value at zero CNCs concentration. An intermediate value of 327 ± 24 AU was observed at $1 \cdot 10^{-3}$ wt%, and at 0.01 and 0.1 wt%. the fluorescence intensity reached values of 3000 ± 1180 and 5290 ± 2250 AU respectively. The data shown in figures 67 and 68 confirm the deposition of a complete SLBs followed by adsorption of CNCs. The homogeneity of the independent layers and the resulting film in the micron scale was independent of CNCs concentration.

In order to locally probe the CNCs layer formation at the nanometric scale, we have performed SFM measurements under in hydrated condition as will be shown in the following section.

4.2.2.6. Constructs probed at the nanoscale by Scanning Force Microscopy (SFM)

Samples for SFM were prepared under the same conditions as for a typical QCM-D experiment. A lipid bilayer was deposited on a quartz crystal in an open module which enables the removal of the crystal from the QCM platform and directly transferring it to the SFM instrument while avoiding the drying of the sample. The samples were then characterized by SFM in liquid medium in order to investigate at the nanoscale the coverage, density and structure of the CNCs layer deposited on the SLBs in its non-dried state. A typical image of the surface topography is shown in figure 69A. It needs to be noted that an image of very good quality, comparable to what is usually reported for dried films, could be obtained. It reveals that the surface is almost fully covered by CNCs. Identical dense CNCs layers were observed when probing different areas of one sample or by investigating different samples, which confirms the homogeneity and robustness of SLBs formation and CNCs adsorption. A few nanocrystals still remained on the top of the dense layer even if several rinsing steps right after the deposition were applied. Being further away from the SLB surface such that the electrostatic interactions are lower, these CNCs are not strongly bounded causing some image blurring. A z-averaged profile of 128 scan lines taken around the white line in figure 69A is presented in figure 69B. The roughness of the continuous film at nanoscale level can easily be seen. In addition, isolated CNCs of 8 nm characteristic

height can be detected. Data therefore show that the adsorption of CNCs onto the SLBs occurred as a dense monolayer on top of which scarcely distributed CNCs were detected. This result is in full agreement with QCM-D data showing that the thickness of the adsorbed CNCs layer is intermediate between a monolayer and a double layer.

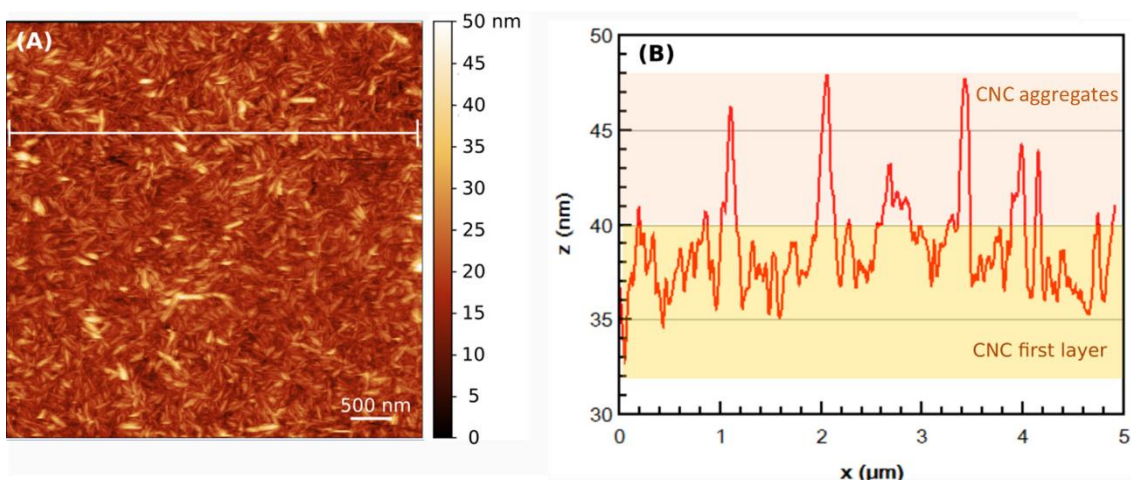


Figure 69. (A) Topography of SLBs/CNCs layer made from DOPC/DOTAP 70/30 %mol. at pH 6, on quartz substrate obtained by SFM in Peakforce mode in Milli-Q water. The PeakForce setpoint was 100 pN. Image is plotted after removing polynomial background, aligning rows and correcting horizontal scars. (B) Z-profile averaged over the 128 lines marked by the white line and its borders in figure 69A. Colored rectangles with 8 nm in height were added as an indication for the CNCs height. Few isolated CNCs lying on top of the construct are also clearly visible.

A nanoshaving of SLBs/CNCs film was applied in order to precisely determine the construct thickness. This procedure was performed in contact mode. In order to determine the working conditions, different tip loadings, *i.e.* friction forces, were first tested.

Figure 70A and B shows SFM image in contact mode made of 256 scanning lines and by changing every 25 lines the force load, expressed as cantilever-tip deflection in Volt. The change in z is due to the modification of the piezo tube position to obtain the required cantilever deflection. Three zones are distinguished. Between 0 and 0.3V, the construct is just slightly deformed. Starting around 0.3V, few CNCs were removed and above 0.7V deflection the whole film was peeled off. The granular surface of the

substrate is visible even at the lowest deflection and the lateral size of the grains increases with the load due to the deterioration of the tip radius.

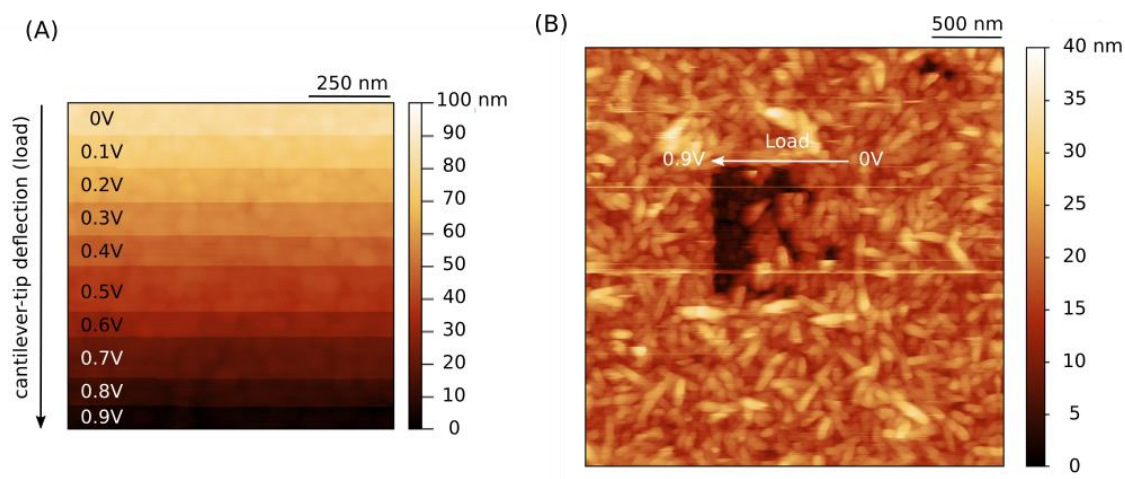


Figure 70. (A) SFM image in contact mode of variation of the scratching force load expressed as cantilever-tip deflection in Volt. The scan direction was selected to be at 90 degrees from the main cantilever axis in order to record a proper lateral signal. This one changes with a few hundreds of milliV. (B) $3 \times 3 \mu\text{m}^2$ topography image done at the zero angle with a PeakForce setpoint of 600 pN.

As an optimum parameter, the lowest force of 0.5 V cantilever-tip deflection was chosen to remove the layer without needing to use of a very blunt tip. A $1 \times 1 \mu\text{m}^2$ surface area was thus scanned in both directions (0 and 90 degrees) with a large number of lines (i.e. 1024), guarantying the shaving quality. The result of this process is presented in figure 71. This $3 \times 3 \mu\text{m}^2$ topography image was recorded using the non-invasive Peakforce mode and in the same liquid medium. Note that the surface that was not subjected to nanoshaving remained intact. However, the use of a blunt tip resulted in a doubling of the lateral size of the CNCs (from 20 to 40 nm). It can clearly be seen that the nanoshaving process resulted in the formation of a squarish well in the area where the hard contact mode was applied. As expected, the roughness inside the well (dark area in figure 71) has the same value as that of the quartz substrate, proving that both the CNCs layer and the SLBs have been removed. A z-averaged profile over 64 scanning lines taken along the white line in figure 71A is presented in figure 71B. This plot shows the roughness of the continuous film and the presence on top of it of some isolated particles in the range of 8 nm, comparable to the height of one CNCs. The SLBs/CNCs

construct thickness appears to be $13 \text{ nm} \pm 3 \text{ nm}$. These data are consistent with the deposited film being composed of a 4-5 nm thick SLBs covered by a dense monolayer of CNCs, with some isolated crystals on top. These values are in good agreement with the values obtained from QCM-D data when taking the total resonance frequency shift (i.e SLB + CNCs layers). Similar nanoshaving measurements were performed using a much higher 5V cantilever-tip deflection and the same step height was obtained, confirming the validity of the results.

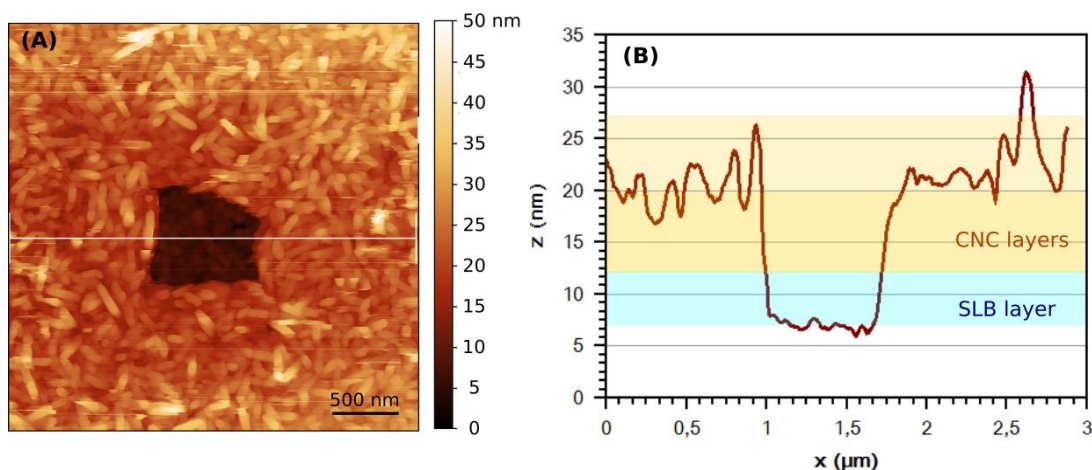


Figure 71. (A) Topography image of a SLBs/CNCs layer made from DOPC/DOTAP 70/30 mol.% at pH 6, obtained by SPM in Peakforce mode in Milli-Q after nanoshaving (see text). The PeakForce setpoint was 750 pN. The detail of the data treatment can be found in the supporting information. (B) Averaged step height showing the thickness of the whole construct. Color shade (5nm thickness for SLBs and 8nm for CNCs) were added as a visual guide. A typical roughness of the quartz substrate is found in the well, whereas a larger roughness on the surface corresponds to the CNCs layers organization.

The results obtained from the SFM experiments were compared to the QCM-D observations and the derived layer thickness calculation thereafter. Several aspects emerge from this comparison. The estimation of layer thickness, water content and homogeneity will be discussed in the following section.

4.2.2.7. Discussion

Several studies have shown that cellulose based films are swollen in aqueous medium, with the amount of water being dependent on the nature of the cellulose (native, regenerated, etc.) and mode of deposition (spin coating, dipping, etc.). In an

early study, Aulin et al. estimated the water content of cellulose films prepared in different conditions and measured 26% for spin coated CNC films by evaluating a normalized adsorbed mass measured by QCM-D and thicknesses by ellipsometry after exposure to a buffer solution.(Aulin, et al. 2009) Later on, Niinivara et al. found values of water by mass ranging from 28% for the thicker films to 79% for the thinner ones from QCM-D and ellipsometry experiments on CNC films obtained by spin coating and exposed to a relative humidity of 97%.(Niinivaara, et al. 2015) It is worth mentioning that since the case of relative humidity is different from the case of swelling in liquid water, different behavior is expected. Reid et al. found that swollen CNC films, also prepared by spin coating, contained 35% wt water.(Reid, et al. 2016) It has to be noted that all these results are obtained on films that have been prepared by spin coating followed by a drying step that enhances the cohesion of the CNCs in the film, ensuring its integrity.

Values of 74% wt water by mass have been measured by Kittle et al. for nanocrystalline cellulose films with various thicknesses as measured by ellipsometry, deposited by electrospinning at different concentration, dried, and then rehydrated.(Kittle, et al. 2011) They have estimated the water content using H₂O/D₂O solvent replacement on the CNC films deposited on a QCM-D crystal. These results are significantly different from the one evaluated from combined QCM-D and ellipsometry measurements, that evaluate lower amounts of water.

It has to be noticed that, in addition, neutron reflectometry measurements on phospholipid bilayers revealed a bound water layer between the substrate and the hydrophilic head: up to 7% of water by volume in the hydrophobic tails region and up to 35% in the headgroup region.(Montis, et al. 2016, Wacklin 2010) This should account for additional adsorbed water molecules, which can also contribute to the total mass fraction of water in our film, but to a limited extent.

In our case, by knowing these masses we may calculate a corrected film density by using equation 33:

$$(Eq. 33) \quad \rho_{film} = \frac{m_{QCMD}}{\frac{m_{dry}}{\rho_{CNC}} + \frac{m_{water}}{\rho_{water}}}$$

Where ρ_{film} is the film density, m_{QCMD} is the hydrated mass, m_{dry} and m_{water} are the dry and water mass respectively and ρ_{CNC} and ρ_{water} are the densities of cellulose and water respectively. The film density obtained from this calculation was 1.14 g cm^{-3} .

By using the calculated density value as the input value in the viscoelastic model, assuming the same water uptake for both films, we obtain thicknesses of 5.7 and 6.7 nm for the DOPC/DOTAP and DOPC films, respectively. The best fit of QTM modeling of QCM-D data for the CNC layer thickness from the model in the case of DOPC/DOTAP system (5.7 nm) is slightly lower compared to the known dimensions of CNCs from cotton prepared under the same conditions ($7.5 \pm 1 \text{ nm}$) and compared to the thickness measured by us using SFM ($8.0 \pm 2 \text{ nm}$). Indeed, the value given for the thickness represents the minimum solution, yet thickness with 1 standard deviation (0.683) is in the range of 5.4–14.2 and 6.5–7.5 nm for the DOPC/DOTAP and DOPC system, respectively.

The χ^2 landscape, representing the difference between the theoretically predicted and the experimental values, is calculated for both systems as shown in figure 72:

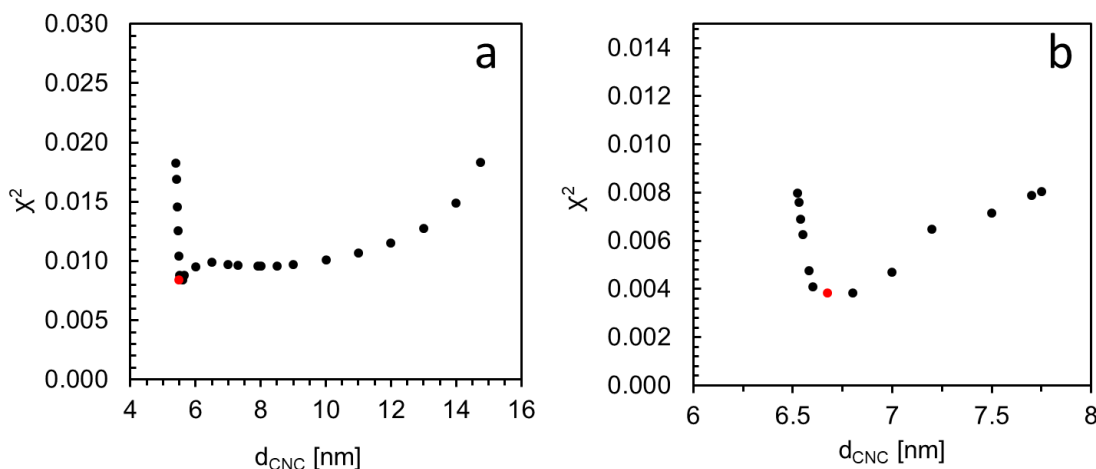


Figure 72. χ^2 landscape for the CNCs layer deposited on DOPC/DOTAP (a) and DOPC (b) systems. The red point indicates the minimal solution and the extreme points represents the solution boundaries for confidence interval of 0.683 or one standard deviation.

For the DOPC case the χ^2 landscape comprises a skewed bell shape distribution, where for the DOPC/DOTAP system, a single sharp minimum appears around $d=5.6$ nm followed by a secondary smeared minimum around $d=8$ nm. The values of thicknesses fall in the range of the estimated layer thickness from SFM, 13 ± 3 for the total film thickness SLB+CNC.

It can therefore be estimated that the positively charged SLB surfaces were covered by a monolayer of CNCs, on average, with some loosely bound isolated crystals on top of it. This situation is reminiscent of the case of the adsorption of double layers of CNCs onto positively charged poly(allylamine hydrochloride) (PAH) polymer layers, which was ascribed to charge complexation and counterions release effects. (Jean, et al. 2008) In the case of CNCs adsorbed onto PAH, it was further shown that the second layer was twice less dense than the first one.

Theoretically, if all the surface is covered with one layer of cellulosic material, the areal mass is equal to the mass of a cylinder with thickness of 7 nm multiplied by the cellulose density, 1.6 g cm^{-3} . This calculation gives 1050 ng cm^{-2} , representing the maximum dry mass in case of perfect packing. The adsorbed dry mass in our case was 185 ng cm^{-2} for the DOPC/DOTAP, which infers a lower surface coverage compared to the ideal case. The SFM images support this observation, showing that the CNCs are randomly distributed, leading to a porous network of entangled rods. Taking the average film thickness from SFM measurements, the water content from $\text{D}_2\text{O}/\text{H}_2\text{O}$ exchange experiment and the maximum estimation from QTM model for DOPC/DOTAP system, we converge to a CNC hydrated layer composed of 70–80% wt water with a total thickness of 6–8 nm.

In summary, our results showed that the water content of our deposited layers account for more than 2/3 of the total mass, in agreement with the results of Kittle et al. (Kittle, et al. 2011) but in fair contrast with other estimation from combined ellipsometric and QCM-D measurements, which lead to values closer to 1/4 water content. However, evaluation of random packing of rods in the case of sedimentation of colloids or compaction of anisotropic powders leads to volume fraction at maximum

compaction that strongly decreases with increasing aspect ratio, especially for the longer ones.(Philipse 1996)

If compacity around 0.6 can be expected in the case of sphere, the maximum volume fraction for anisotropic particles is 0.3 for an aspect ratio of around 10, 0.2 for 40, and 0.1 for 80. Even if an average aspect ratio of CNCs is rather difficult to precisely evaluate, as they are constituted of polydisperse particles with dimension around $7 \times 21 \times 150 \text{ nm}^3$, (Elazzouzi-Hafraoui, et al. 2007) a rough estimation based on a circumscribed cylinder gives an aspect ratio around 10, leading to an expected compacity of 0.3 that is 70% water, in fair agreement with our results. Consequent variations around the estimated aspect ratio of 10 will not change that much the maximum compacity. Whether compacity values as high as 0.75 (around 25% of water), obtained for different CNC systems as previously mentioned, are due to preparation (especially compaction upon drying) and/or substrate differences or systematic methodological deviation, may be further investigated in the future.

4.2.2.8. Summary

In this part, we have demonstrated the formation of multilayer thin film made by adsorption of CNCs on top of a lipid bilayer. The adsorption of the CNCs particles and the layer viscoelastic properties were found to be dependent on the charge of the lipid membrane. A positive charge of the membrane (DOPC/DOTAP at pH = 6 and DOPC at pH = 3) resulted in a quantitative deposition of a CNC layer, while for the negative charged membrane (DOPC at pH = 6) CNC adsorption was not observed as evidenced by QCM-D experiments.

Considering the low dissipation values obtained by QCM-D, the reproducibility and the crystal dimensions, it is likely that the cellulose adsorbs as a cohesive but loose monolayer on top of the SLBs in the case of positively charged supported membranes as described tentatively in figure 73.



Figure 73. A schematic description of CNC deposited on a supported lipid bilayer.

SFM and TIRF images confirmed the formation of SLBs and of homogenous CNCs coverage at the micrometer scale, while QCM-D measurements were used to extract the value of the adsorbed CNCs mass at saturation of about 600 ± 70 ng and an approximated height of 6-8 nm. This height was confirmed via SFM nanoshaving. QCM-D experiments using solvent exchange with D_2O demonstrate the formation of a continuous monolayer of CNCs on top a lipid membrane with a compacity around 0.3. Altogether, the results demonstrate a formation of a continuous monolayer of CNCs on top a lipid membrane and shed light on the key factors governing the interactions of these two bio-based building blocks.

Notably, QCM-D, SFM, and TIRF proved to be a useful combination of methods to probe the formation of multilayer 2D constructs from the nanometric to the micrometric length scale. This information will serve us in the following parts for the construction of biomimetic capsules in chapter 5.

4.3. CNC-XG study

Xyloglucans (XG) interact with cellulose microfibrils via hydrogen bonds, VdW interactions, and polar interactions. (Hayashi and Maclachlan 1984, Lopez, et al. 2010, Mazeau and Charlier 2012) These interactions lead to the formation of a flexible network, which is a key factor in maintaining cell wall integrity. In this part, we were interested in studying and optimizing the interaction between CNC and XG building blocks, with the aim to utilize these elements for the construction of synthetic PCW.

4.3.1. CNC-XG interaction in (3D)

CNCs were used in this case as a model of the naturally-occurring cellulose nanofibrils, but with improved colloidal stability thanks to charged sulfate ester groups which are grafted on their surface as previously discussed. Since XG is a neutral polysaccharide, we expect the electrostatic interaction between the CNCs and XG to be negligible compared to the other intermolecular forces present in this system. In the following sections, we will describe our observations on CNCs and sonicated XG system using complementary data from dynamic light scattering (DLS), nuclear magnetic resonance (NMR) spectroscopy, isothermal titration calorimetry (ITC) and transmission electron microscopy (TEM).

4.3.1.1. Materials and methods

Nuclear magnetic resonance (NMR). Proton NMR spectra were recorded with a Bruker Avance 400 spectrometer (Bruker, Germany) operating at a frequency of 400.13 MHz for 1 h. Samples were solubilized in D₂O at a temperature of 25 °C. Residual signal of the solvent was used as the internal standard at 4.80 ppm at 25 °C. Proton spectra were recorded using 90° pulses with a 4006 Hz spectral width, 32768 data points, 4.089 s acquisition times, 10 s relaxation delays, and 32 scans.

The samples were prepared in the same way as for the DLS and ITC, i.e. stepwise addition of 10 µL aliquots 1 wt % XG₁₀₀ into a vessel containing 1 mL of 1 wt % CNCs where both XG and CNCs in D₂O. $1.1 \cdot 10^{-4}$ wt % dimethyl sulfoxide (DMSO) was added to each sample for integral normalization.

Transmission electron microscopy (TEM). Droplet of ca. 0.001 wt.% CNC or XG-CNC complex suspension were deposited onto freshly glow-discharged carbon-coated copper grids and negatively stained with 2 wt % uranyl acetate. The specimens were observed with a Philips (FEI) CM200 microscope operating at 200 kV and equipped with a TVIPS TemCam F216 digital camera.

Atomistic modeling. We have considered a molecular model of the (100) surface of cellulose I β (Mazeau 2011). Periodic boundary conditions were applied in order to generate an infinite surface. We have also considered a typical repeat unit of tamarind XG, XXLG, whose initial coordinates were extracted from a previous study (Hanus and Mazeau 2006). Modeling strategy and simulation conditions are fully described elsewhere (Mazeau and Charlier 2012). Briefly, the XG molecule was placed above the cellulose surface and molecular dynamics (5 ns at constant number of particles, volume and temperature) was used to search for the most stable organization of the complex. At the end of the molecular dynamics trajectory, the total energy of the system was constant and the XG was stabilized on the surface as its location and orientation with respect to the cellulose surface remained stable. Several snapshots taken at the equilibrium stage were extracted from the trajectory to estimate the area of the cellulose surface covered by the XG fragment.

4.3.1.2. Heat response from the addition of XG into a CNC suspension by ITC

ITC was used to evaluate the thermodynamic parameters of the interaction between CNCs and XG with high and low M_w . The experimental setup is described in the method section. Briefly, aliquots of 1 wt.% XG solution were added dropwise to a 1 wt.% CNC suspension and the heat response was measured. For both XG₈₀₀ and XG₁₀₀, a pronounced heat flow was observed, with an overall exothermic behavior. The addition of non-sonicated XG into a CNC suspension resulted in broad peaks of increasing magnitude. In a typical ITC experiment, the heat values resulting from the integration of the heat flow over time are decreasing in magnitude with the addition of titrant. In the case of XG₈₀₀ (high M_w), the peaks continuously increased during the experiment. No return to the baseline was observed and thus a clear ITC profile could not be obtained and no valuable data could be extracted. This observation may imply that the timescale of interaction, and therefore heat flow, is longer than the timescale of an ITC experiment.

A possible explanation for this phenomenon may emerge from the rearrangement of XG chains, a process that influence the heat flow and has characteristic time of up to several hours in the case of high- M_w XG (Villares, et al. 2015). We have tried to enable a clear return of the heat signal to the baseline after each injection by increasing the time between injections up to 3000 s, 10 times higher than the interval used a typical ITC experiment. However, in the timescale of the experiment, we did not achieve robust response and reproducibility and, therefore, no conclusive data could be obtained for the stoichiometry and thermodynamic parameters of XG₈₀₀, apart from the exothermic nature of the interaction.

In the case of XG₁₀₀, the peaks could be distinguished. The kinetics was faster enabling the return to the baseline and identification of the stoichiometric point where no additional heat flow was observed above the baseline. Figure 74 shows the variation of the normalized heat value as a function of the mass ratio of XG to CNC which will be noted R, from the titration of a 1 wt % CNC suspension with 1 wt % XG₁₀₀. Each injection resulted in an exothermic peak and the integration of the peak over time yielded the heat release during a single injection.

The heat flow due to the injection increased until reaching a maximum point at the fifth injection corresponding to a mass ratio $R = 0.03$ and heat value of $-2.2 \text{ kcal mol}^{-1}$ XG. After reaching this value, further addition of XG resulted in a decrease in the heat value until after 8 injections, corresponding to a mass ratio of $R = 0.05$, no heat flow was observed with further addition of XG. Similar results were obtained for lower initial XG concentrations, as well as for larger time intervals between injections. Since ITC provides the overall heat release due to the interaction, it is rather difficult to unambiguously determine which type of interaction dominates the complexation process. The heat response is in fact a sum of the enthalpy changes due to several origins among them the dilution of the polymer, formation of hydrogen bonds, release of water molecules and counterions from both polymer and crystal surfaces and finally, rearrangement of XG on the surface of cellulose.

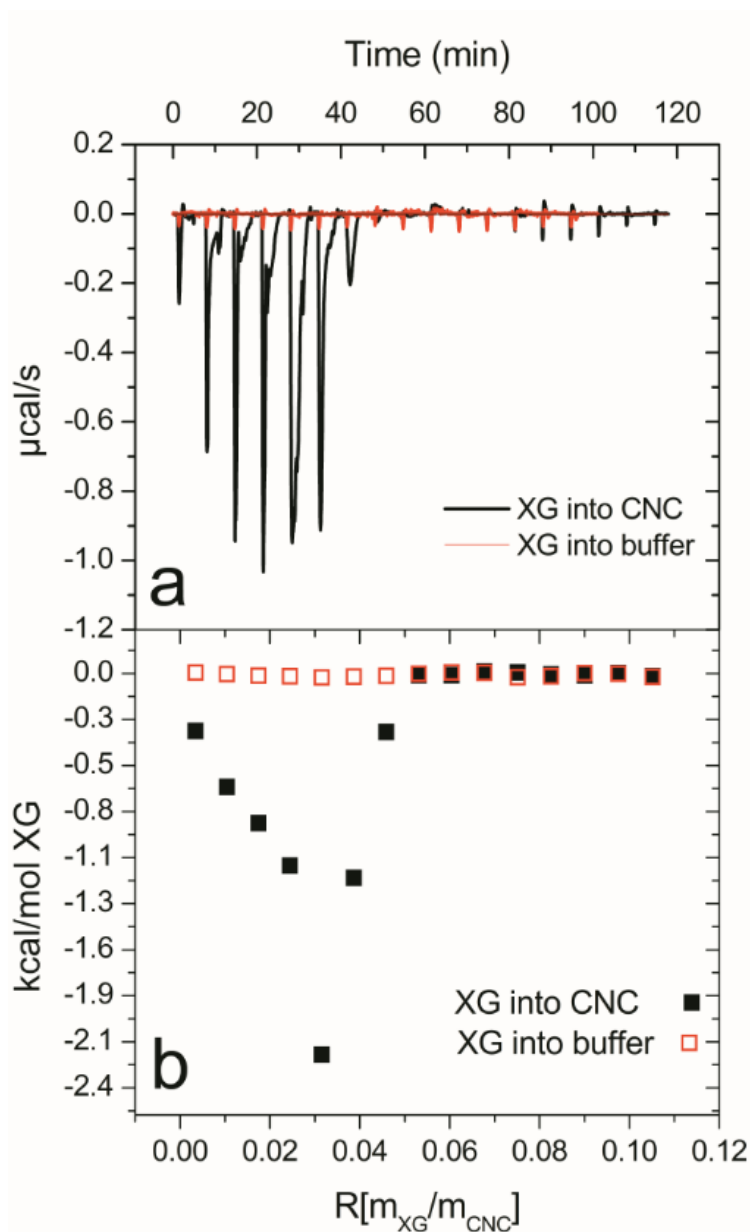


Figure 74. ITC data obtained from the titration of 1 wt.% CNC suspension with 1 wt.% XG. (a) Raw heat flow from the injection of XG into buffer (red curve) and into CNC suspension (black curve). (b) Normalized heat values for the titration of XG into buffer (open red squares) and into CNC suspension (closed black squares). All the experiments were carried out at ambient temperature and in 20 mM PBS, pH 7.2.

We suggest two possible explanations for this profile. The first is cooperative binding. The initial binding of XG onto the crystal surface promoted further interaction with the CNCs. In the first injection, XG binds to the CNC surface as indicated by the heat response of the system. Once bound, XG acts as a mediator facilitating further binding

via specific interactions with the additional XG chains, thus releasing larger amounts of heat in the following injections. The process reaches a maximum when there are no more free "binding sites" on the total crystal surface.

The second explanation is the coexistence of two underlying processes occurring simultaneously or consecutively. One process is endothermic, with positive entropy related to the release of water molecules and counterions from the particle hydration shell. A second process is exothermic and is related to the formation of hydrogen bonds between the hydroxyl group of the glucose unit in XG and the parallel unit in cellulose. Superimposing the ITC profiles of these two processes yields a curve with similar characteristics.

Due to the complexity of the heat release profile, ITC did not help distinguish between the different hypotheses and thus no conclusive results could be obtained for the association constant or the enthalpy attributed to each process. Nonetheless, the stoichiometric ratio of XG-CNC was determined from the point where no more heat release is observed above a certain threshold which is determined by a control experiment of XG into CNC free buffer. The stoichiometric ratio was found to be 0.05 for the case of XG₁₀₀ for the XG concentration range examined, implying that there is a finite number of binding sites available for XG to interact.

Lopez et al. (Lopez, et al. 2010) found two underlying processes for the adsorption of XG oligomers on bacterial and cotton cellulose substrates. The authors applied a Scatchard model which revealed a cooperative mechanism where the initial binding of XG molecules acts as an anchor which facilitate further adsorption on the crystal until the saturation of the surface. Their analysis is in line with the results obtained here, and may explain the gradual increase in heat release observed for the beginning of the titration, from $-0.33 \text{ kcal mol}^{-1}$ XG on the first injection to a maximum of $-2.1 \text{ kcal mol}^{-1}$ XG on the fifth injection. Notably, the XG-CNC system does not fit to the definition of a single set of identical binding sites with no interacting species, where the heat response decreases in its absolute value with addition of titrant.

Overall, ITC indicated the global exothermic nature of the interaction and the stoichiometric saturation point at which no additional heat response is observed above the baseline. In order to verify this result, an adsorption isotherm was determined using NMR.

4.3.1.3. Adsorption isotherm studied by liquid state NMR

NMR was used to gain further knowledge on adsorption behavior of XG on CNCs. The advantage of NMR is that in contrast to batch experiments, where high-*g* centrifugation cycles are used for complex sedimentation, here there is no need to precipitate the objects, a process which causes dragging phenomena which may lead to errors in the determination of the stoichiometric ratio at saturation.

The analysis is based on the fact that in a typical NMR experiment, only the mobile phase (i.e. unbound XG chains) can have a relaxation mode and the XG that is bound to cellulose is therefore no longer detectable and thus provides information on the stoichiometry, by comparing CNC and CNC-free samples with the same XG content. The ratio of XG to CNC was varied between 0 and 0.5 and two series of experiments were performed with and without cellulose, the later denoted as blank.

Figure 75a (red curves) and 75b (blue curves) shows the variation of the ^1H NMR spectra of XG and XG+CNC, respectively, as a function of the concentrations of XG, from 0 to 5 mg mL⁻¹. For convenience, we use the notation $R = m_{\text{XG}}/m_{\text{CNC}}$ for both XG and XG+CNC series in order to compare similar amounts of XG with and without CNCs. The NMR spectrum was characteristic of XG, with a broad series of peaks between 2.6 and 3.7 ppm. The relative amount of free XG in each sample was determined by integrating the broad peak series related to XG (2.6-3.7 ppm) with respect to the DMSO standard.

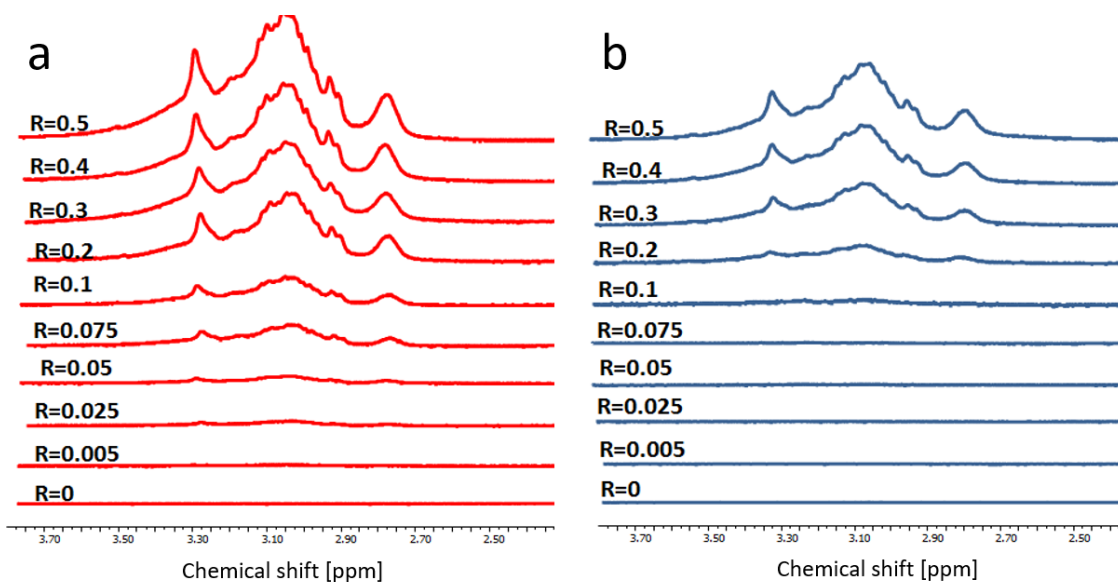


Figure 75. ^1H NMR spectra of (a) XG ($\text{CXG} = 0\text{-}5 \text{ mg mL}^{-1}$ or $R = 0\text{-}0.5$) and (b) CNC-XG complexes with corresponding XG concentrations. For convenience, $R = m\text{XG}/m\text{CNC}$ was used to compare similar amounts of XG, with and without CNCs.

Figure 76a shows the normalized integral values attained for the blank series containing XG only (red circles) and XG+CNC (black squares). For the blank series (figure 76a, red circles), the value of the integral increased linearly with increasing amounts of XG, the fitted a linear curve yielding $R^2 = 0.9993$. The high R^2 value implies that the sensitivity of NMR for the detection of mass in the range of concentration examined is sufficient.

For the CNC-XG series, (figure 76a, black squares), the sample containing only cellulose (i.e. $R = 0$) did not yield any signal as expected due to the immobilized cellulose units. The normalized integral values obtained up to the ratio of 0.05 yielded a value of zero, implying that below this ratio, all the XG was bound to CNCs and therefore no free XG were detected.

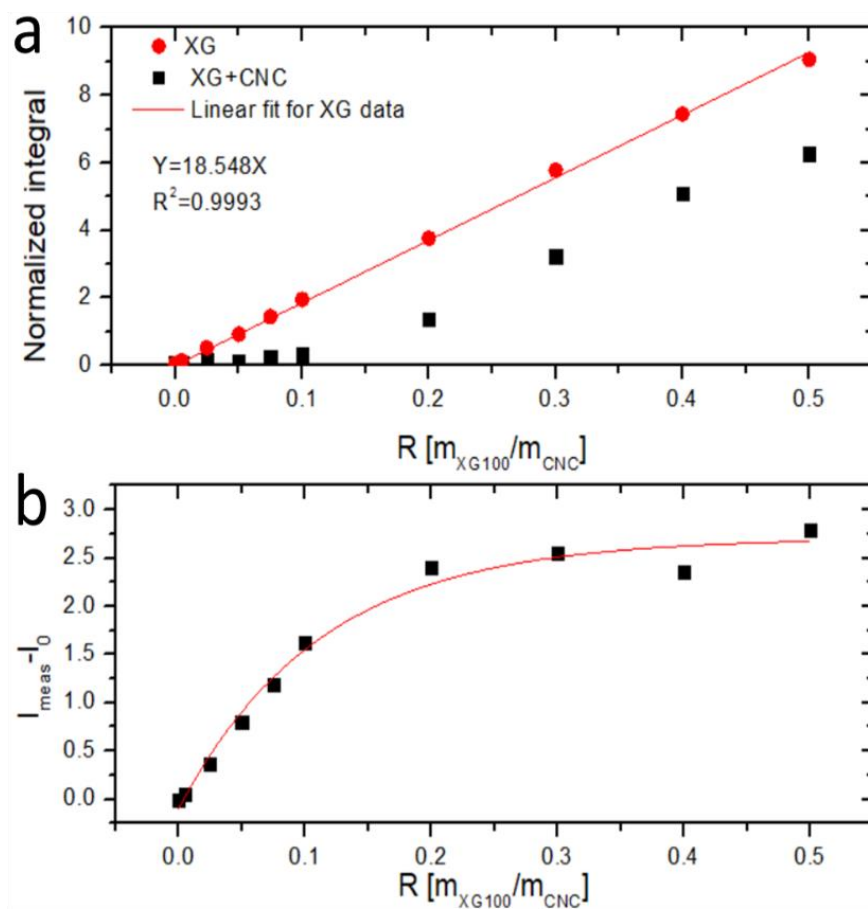


Figure 76. (a) Normalized integral values obtained from integration of the XG peak between 3.7 and 2.6 ppm as a function of XG-CNC ratio for XG (red circles) and XG+CNC (black squares). The red line represents a linear fit to the data. (b) Subtracted integral as a function of XG-CNC ratio. The red line is a guide to the eye.

Above $R = 0.05$, a signal was detected, and from a value of about $R = 0.1$, a linear increase in the integral values was observed with the increase in XG/CNC mass ratio for the series containing cellulose, and the slope in that case was similar to the slope of the blank series, indicating the accumulation of non-adsorbed XG in the bulk.

Figure 76b shows the difference between the integral values for the XG and the XG-CNC series as a function of R . This difference reached a nearly constant value, implying a saturation of the available binding sites and thus no further adsorption was observed. However, it should be mentioned that the value at which the system reaches saturation cannot be estimated from the plateau of this curve. We did not attempt to fit the result to the classical Langmuir model since the assumptions used in this model (i.e.

monolayer adsorption, reversibility, identical binding sites, and no adsorbate-adsorbate interaction), do not apply to the CNC-XG system. (Lombardo and Thielemans 2018)

In order to gain insight on the complexation process at the mesoscale, and to inspect the adsorption phenomena in a high XG-CNC ratio, we performed DLS experiments as will be discussed in the following section.

4.3.1.4. Light scattering experiments reveal the formation of CNC-XG complexes

We have examined the addition of XG₁₀₀ into CNCs in suspension using light scattering. Each sample contained a suspension of 1 wt % CNCs to which a 1 wt % XG solution was added up to the desired XG/CNC ratio, in aliquots of 10 μ L under constant stirring at ambient temperature. This procedure is similar to the one performed during an ITC experiment, but instead of measuring the heat response due to addition of XG into CNC, we measure the intensity of the scattered light from the resulting mixture and estimate the size of the objects from their diffusion coefficients.

Figure 77a plots D/D_0 as a function of R , where D and D_0 are the hydrodynamic diameter of the complex and bare CNCs respectively and R is the mass ratio of XG to CNC. For $R = 0$ (i.e. no XG), a single peak was observed, corresponding to a hydrodynamic diameter of about 80 nm, which was taken as the size of bare CNCs and noted here as D_0 (Figure 77b, blue curve). It is important to mention that the Stokes-Einstein relationship enables to extract hydrodynamic diameter from a diffusion coefficient in the case of a **spherical object**. In the case of **rod-shaped particles**, we assume the same diffusion coefficient as a sphere with the reported size, which fits well with the dimensions of cotton CNC measured by TEM. (Elazzouzi-Hafraoui, et al. 2007)

With the addition of XG₁₀₀ into CNC, the diameter of the objects increased, until a maximum value for D/D_0 of about 300 at a mass ratio corresponding to 0.05. With further addition of XG, the size of the complexes decreased until, at a ratio of 1, a single

peak was observed, corresponding to a diameter of about 140 nm or D/D_0 of 1.7, (Figure 77b, red curve).

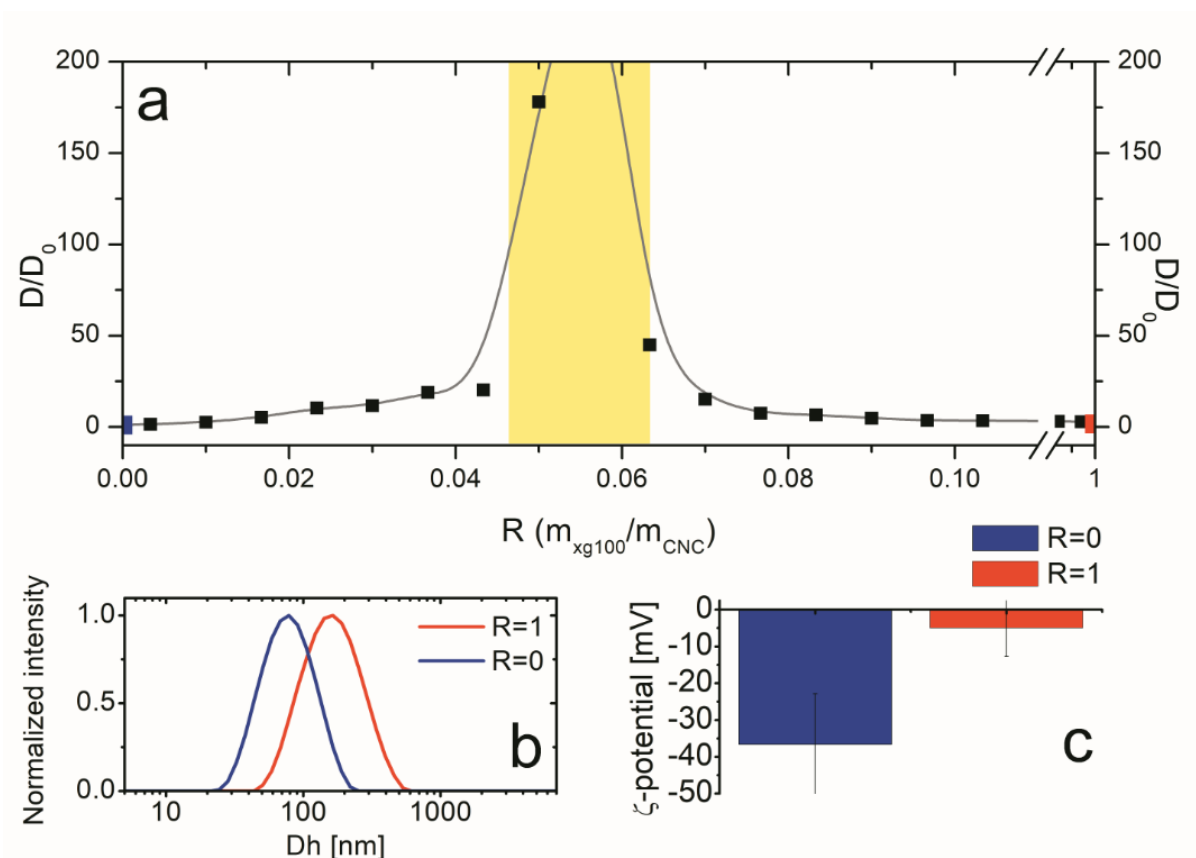


Figure 77: (a) Z-average hydrodynamic diameter as a function of XG/CNC mass ratio as obtained from DLS following the sequential addition of 1 wt % XG into 1 wt % CNC suspension. The grey line is a guide to the eye and has no physical meaning. The yellow shading represents the aggregation zone (see text for details) (b) normalized intensity and (c) ζ -potential values for bare CNCs (blue curve and column) and decorated CNCs (red curve and column). The corresponding points in graph (a) are labeled in blue ($R=0$) and red ($R=1$).

The maximum diameter observed by light scattering was 300 times the initial diameter at a mass ratio of 0.05, a size which is **beyond the detection limit** of the apparatus used ($\sim 4\text{-}5\ \mu\text{m}$). In fact, all values obtained for $0.045 > R > 0.065$ (yellow shading in figure 77a) were beyond the detection limit of the apparatus in the actual working conditions, and consequently have **no real physical meaning**. Therefore, we do not conclude for a definite size in this region but **merely note the trend observed**, and define the stoichiometric point as the middle point in this region.

Since the scattering from XG alone, at this concentration range, has little to no effect on the overall scattering intensity and it is negligible compared to the scattering from the CNCs, we can assimilate the increase in hydrodynamic diameter of the objects to the adsorbed polymer on the crystal surface which slows down the movement of the objects causing the decrease in measured diffusion coefficient.

Figure 77c shows ζ -potential values of bare CNC ($R = 0$) and XG decorated CNCs ($R = 1$). The ζ -potential value for $R=0$ and $R=1$ were -36.6 and -5.0 mV respectively. Being negatively charged colloids, CNCs carry an electrical double layer containing ions and water molecules which are present close to the crystal surface and moves in similar speed. Any adsorption of another object, whether it is a surfactant or a polymer, will enforce a rearrangement of the double layer and will change the electrical properties of the surface. Since electrophoretic mobility is closely related to surface charge, and is relatively easy to measure, it may be used as a method to confirm adsorption of polymers and other molecules onto cellulose. (Oikonomou, et al. 2017, Stana, et al. 1995)

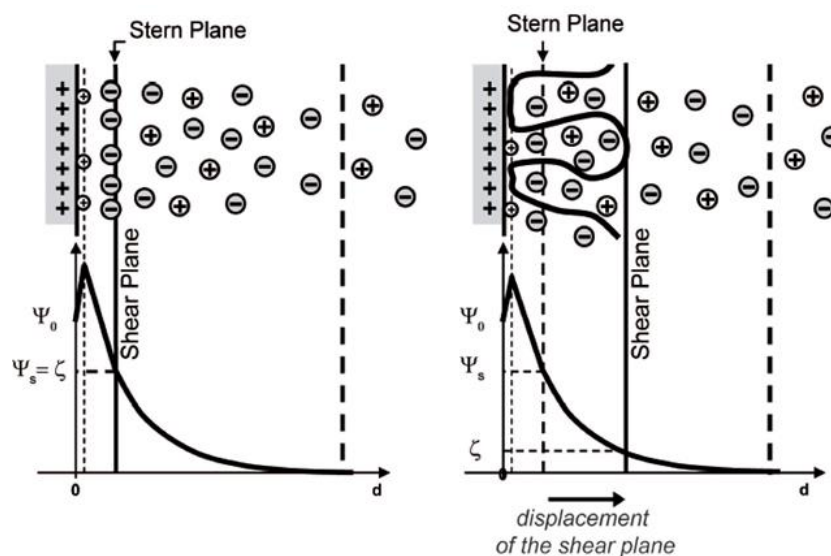


Figure 78. The reduction of measured ζ -Potential is attributed to the displacement of the shear plane upon adsorption of polymer on a surface.(Quemeneur 2010)

Taken together with the value of hydrodynamic diameter of the complexes at $R = 1$, we attribute the change in electrophoretic mobility to the presence of the adsorbed polymer on the surface of the CNCs. In fact, the ζ -potential is the potential at the shear plane, which is displaced due to adsorption of a polymer on a surface (figure 78), in our case XG on the CNCs.

Unlike salt mediated aggregation, where the aggregates continue to grow with addition of salt, in the case of XG-CNC complexes, beyond a critical ratio, the aggregates separate, leading to a decrease in apparent diameter.

From the ITC, NMR and light scattering experiments, several characteristic adsorption regimes can be identified, defined by the XG/CNC mass ratio R . At $R = 0$ (no XG), CNCs are colloidally stable due to electrostatic repulsion. At $0 > R > 0.05$, an adsorption of XG leads to the formation of CNC-XG complexes by bridging of adjacent crystals, causing a gradual increase in aggregate size. At $0.05 < R < 1$ a gradual decrease in aggregate size and separation of large bundles is observed. At this regime, the CNCs are covered by a polymer layer, as indicated by the DLS and ζ -potential values at $R = 1$.

In order to gain further information regarding the organization of the CNC-XG complexes in the nanoscale, we observed the samples by TEM in these representative adsorption regimes, as will be discussed in the following section.

4.3.1.5. TEM enables the visualization of the formed complexes

We used TEM to observe the nanostructure of the CNC-XG complexes. Figure 79 shows TEM images of negatively stained mixtures of CNC and XG in mass ratios corresponding to $R = 0, 0.05$ and 1 .

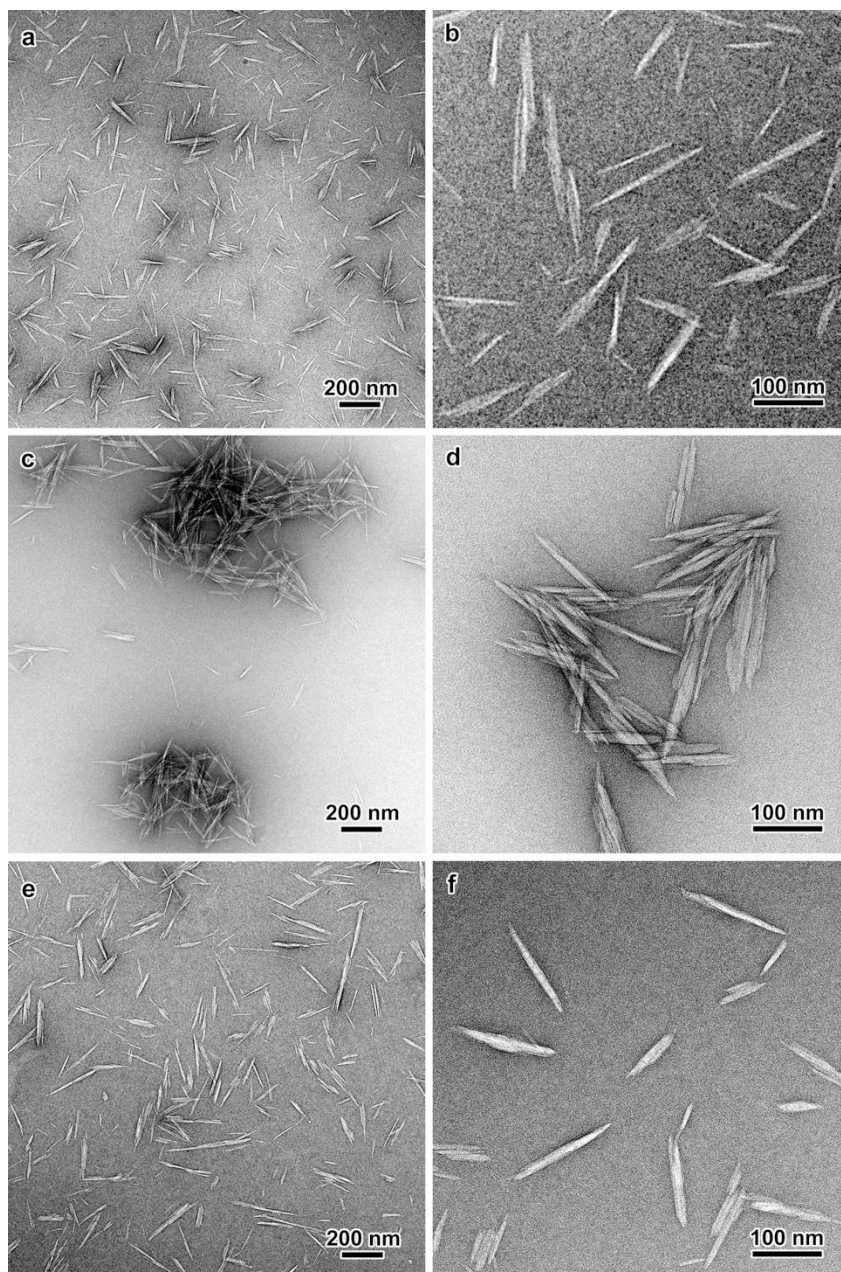


Figure 79. TEM micrographs of negatively stained bare CNCs (a,b) and CNC-XG complexes at $R = 0.05$ (c,d) and at $R = 1$ (e,f). $R = mXG/mCNC$. (TEM image by Jean-Luc Putaux, CERMAV)

Figure 79a and b corresponds to the bare CNCs ($R=0$). CNCs appear as bundles of 3-5 elementary crystallites, with average length of 150 nm, width of 20 nm and height of 7 nm, in agreement with previous observations (Elazzouzi-Hafraoui, 2007). The objects are separated due to electrostatic repulsion, as previously discussed.

At a ratio of 0.05, (Figure 79c and d) the distance between the crystals dramatically decreased and the CNCs appeared to be aggregated. It is reasonable to assume that the aggregates observed in the case of $R = 0.05$ are, in fact, fragments of the large aggregates detected by light scattering, as shown in the previous section, having an approximate diameter from few hundred nanometers up to several microns. At $R = 1$ (figure 79 e and f), the separation between crystals increased compared to $R = 0.05$ and resembles the separation between crystal bundles in the case of bare CNCs.

There was no direct evidence of the presence of XG in the TEM images. XG is non-crystalline and in a non-aggregated molecular state, it is likely that negative staining is not sufficient to reveal the polysaccharide. Therefore, it is not possible to conclude, at this resolution, on the spatial distribution of XG.

These results are in agreement with the ones obtained by Dammak et al. (Dammak, et al. 2015) who studied the adsorption of XG onto cellulose in different adsorption regimes by enzymatic degradation. The authors have identified two main adsorption regimes in which, at low XG/CNC ratio, XG tightly adsorbed on cellulose, inducing aggregation of CNCs, and at high XG/CNC ratio, the crystals were separated.

4.3.1.6. Surface covered by XG at $R = 0.05$ from atomistic modeling

We have complemented the experimental results by atomistic simulations in order to estimate the cellulose surface covered by XG at $R = 0.05$. 1 g of cellulose contains $3 \cdot 10^{16}$ nanocrystals. Each nanocrystal exhibits a usable area for XG adsorption of 6000 nm^2 estimated from its measured dimensions: $150 \times 20 \times 7 \text{ nm}^3$ (Elazzouzi-Hafraoui, et al. 2007) so the total surface area of 1 g of cellulose is $1.8 \cdot 10^{20} \text{ nm}^2$.

For the polymer adsorption, 0.05 g of XG contains $2.2 \cdot 10^{19}$ repeat units, considering that the molar mass of one unit of XG (4 glucose units, 3 xylose, and 1 galactose) is 1350 g mol^{-1} . The projected dimensions of the XG repeat unit in the molecular model at equilibrium are 2.1 and 2.2 nm (Figure 80). XG repeat thus covers a surface of 4.6 nm^2 . Assuming the ideal flat conformation with maximal coverage identical to that observed in the simulation, 0.05 g of XG would theoretically covers a total surface area of $1.0 \cdot 10^{20} \text{ nm}^2$.

Comparing the two values, the cellulose area of $1.8 \cdot 10^{20} \text{ nm}^2$ estimated from experimentally measured dimensions versus the theoretical area that XG can covers from modeling of $1.0 \cdot 10^{20} \text{ nm}^2$, suggests that $R = 0.05$ is slightly below the monolayer regime.

However, for the calculation of the theoretical crystal surface, we have used a single value for the length which was 150 nm. Bearing in mind the shape polydispersity of the 50-250-nm-long CNCs, as also evident from the TEM images, the values obtained from theoretical calculation suggest that sonicated XG adsorbed in a flat conformation referred to as "trains" on the surface. These results support those of Villares et al. who found that **sonicated XG** (low Mw) tended to adsorb in a flat conformation on the surface of CNCs while **non-sonicated XG** (high Mw) tended to form "loops" and "tails".(Villares, et al. 2015, Villares, et al. 2017)

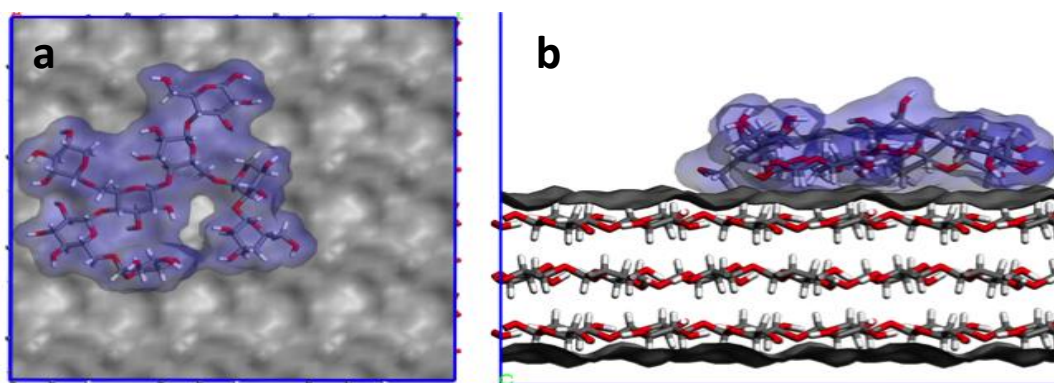


Figure 80. Simulated XG repeat unit adsorbed on the (100) cellulose crystal surface. (a) top view, (b) side view. (By Karim Mazeau, CERMAV)

4.3.1.7. The addition of salt to CNC-XG complexes confirms steric stabilization

In order to verify the presence of a XG layer which presents a steric barrier between the CNCs, salt was added to the CNC-XG complex at $R = 1$. In order to eliminate the effect of unbound polymer molecules, the excess XG was removed by centrifugation of the complex and redispersion in aqueous medium. For comparison, salt was added to bare CNC and XG-decorated CNCs. Figures 81a and 80b shows images of bare and decorated CNCs respectively, with addition of NaCl. At NaCl concentrations of 0.1, 0.5 and 1.0 M, the bare CNC suspensions became turbid and the turbidity slightly increased with increasing salt concentration. We attribute this apparent turbidity to the formation of large aggregates, indicating the screening of electrostatic repulsion between the CNCs.

In contrast, addition of salt to decorated CNCs did not result in the increase of apparent turbidity, for the NaCl concentration range examined. In order to get a clearer view of the objects size with the addition of salt, we have estimated the mean hydrodynamic diameter of the objects as a function of NaCl concentration for bare and decorated CNCs using DLS (Figure 81c).

The mean hydrodynamic diameter obtained for the bare CNCs dramatically increased from about 80 nm with no salt to few hundred nanometers for 0.1, 0.5 and 1.0 M NaCl. It must be mentioned that the addition of salt in the case of bare CNCs resulted in a multimodal distribution. Thus, the calculated average size obtained by the fit to the correlation function merely emphasizes the increase in aggregate size rather than providing an accurate measure for the hydrodynamic diameter of the objects.

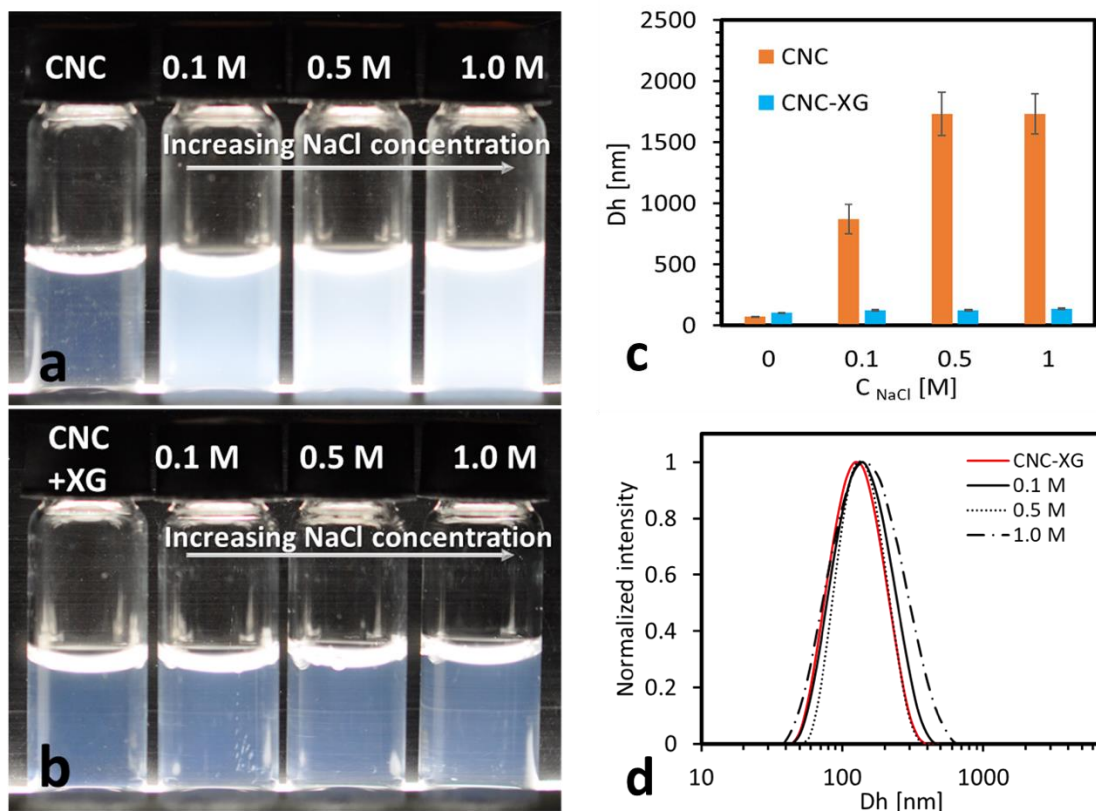


Figure 81. (a) Bare CNCs (0.1 wt.%) with increasing salt concentration. (b) CNC-XG complex (0.1 wt.%) with increasing salt concentration. (c) Hydrodynamic diameter as a function of added NaCl concentration, obtained from DLS measurement for bare (orange columns) and decorated CNCs (blue columns). (d) Normalized intensity as a function of hydrodynamic diameter for XG-CNC complex with no added NaCl (red curve) and with added NaCl at 0.1 M (continuous black curve), 0.5 M (dotted black curve) and 1.0 M (dashed black curve).

In the case of the decorated CNCs, the distribution was monomodal for all NaCl concentrations examined. As previously seen, for the CNC-XG complex, the hydrodynamic diameter was about 140 nm. With addition of salt the hydrodynamic diameters increased to 157, 150 and 272 nm for 0.1, 0.5 and 1.0 M NaCl, respectively. Figure 81d shows the size distribution as extracted from DLS measurement of the CNC-XG complexes. Indeed, with the addition of NaCl the polydispersity index slightly increased from 0.22, in the case of no salt, to 0.25 for 1 M (Table 16). Overall, the response to addition of salt was significantly more pronounced for the case of CNCs than for the bare CNC-XG complexes.

Table 16: Hydrodynamic diameter and PDI values obtained from CONTIN (CON) and cumulants (CUM) analyses of the autocorrelation function measured by DLS for bare and decorated CNCs with the addition of salt (expressed in M). PDI is the polydispersity index.

Sample	D_h [nm, CUM]	PDI	D_h [nm, CON]
CNC	74 ± 1	0.18 ± 0.02	91 ± 3
CNC+ (0.1 M)	874 ± 120	1.00	1428 ± 351
CNC+ (0.5 M)	1732 ± 179	1.00	383 ± 66
CNC+ (1.0 M)	1731 ± 166	1.00	400 ± 72
CNC-XG	107 ± 1	0.22 ± 0.01	137 ± 1
CNC-XG+ (0.1 M)	124 ± 4	0.21 ± 0.01	157 ± 4
CNC-XG+ (0.5 M)	124 ± 4	0.18 ± 0.02	150 ± 4
CNC-XG+ (1.0 M)	134 ± 6	0.25 ± 0.03	272 ± 104

Taken together with the ζ -potential measurements, these results suggest that the electrostatic stabilization in the case of bare CNCs, was replaced by a steric stabilization in the case of CNC-XG complexes. Moreover, the removal of unbound XG from the system did not alter the decorated crystal shape, leading us to the conclusion that at high XG/CNC ratio, a CNC-XG core-shell particle was formed, stabilized by steric repulsion in place of the original electrostatic repulsion of the bare CNCs.

4.3.1.8. Summary and conclusions

In this part we have followed the formation of CNC-XG complexes using multiple techniques. The data confirms the presence of a complex adsorption process with a specific stoichiometry. The adsorption process seems to include two main steps: (i) The rapid adsorption of XG onto the CNC surface, a physical process which leads to the occupation of most binding sites and creates a diffusion barrier for the next XG molecules, while bridging two or more adjacent crystal bundles to form large aggregates. (ii) Slower adsorption, rearrangement and entanglements with other XG molecules, and finally separation of the formed CNC-XG aggregates.

The results also suggest that the aggregation and formation of bundles may be reversed with further addition of XG molecules. Possibly, the addition of XG molecules changes the solution properties in a way that favors the dissolution of the loosely bound XG layer back to the solution, reducing the diameter of the observed complexes until, at a XG/CNC mass ratio of 1, only the irreversible tightly bound first layer of XG is remained.

From this study, we conclude that the following points:

- XG will be used in its sonicated form in order to promote tighter and faster adsorption.
- The ratio between the mass of CNC and the mass of XG in the biomimetic constructs will be tuned to be 0.1, slightly above the saturation ratio to ensure complete adsorption and optimal surface coverage.
- Addition of salt can promote the adsorption, therefore 1-10 mM of NaCl will be added in the biomimetic constructs.

To gain further information, in the following chapter we will examine the interaction between CNC and XG using a 2D configuration.

4.3.2. CNC-XG interaction in 2D

The interaction of CNC with XG was examined in 2D with QCM-D. The limitations of this method regarding this system are (1) long rearrangement times of XG chains on the CNC surface (already shown in the 3D experiments) (2) loss of signal after the 2nd layer of CNC due to high dissipation leading to low accuracy. We therefore focus on the first CNC-XG layer, deposited in this case on SLB from DOPC/DOTAP 70/30 % mol./%mol. in 0.2M sucrose at pH 6. We used 0.1 %wt. CNCs and 0.01 %wt. XG suspensions dissolved in 0.2 M glucose solutions, to mimic as close as possible the conditions in which the biomimetic constructs will be prepared. Figure 82 shows QCM-D profile from the deposition of SLB, CNC and XG layers.

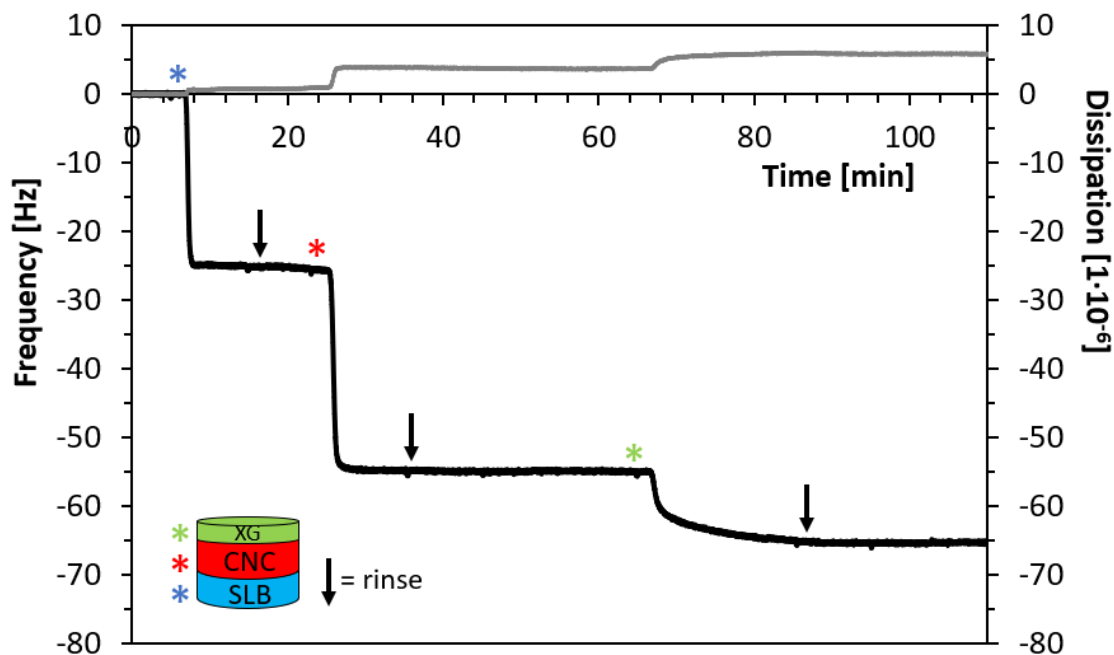


Figure 82. QCM-D profile showing the deposition of SLB, CNC and XG. The frequency (black line) and the dissipation (grey line) for the 7th overtone, are plotted on the left and right axes respectively. The different steps are labeled with a colored star (blue=SLB, red=CNC, green=XG) and arrows (rinsing steps).

The adsorption profile shows fast, almost immediate adsorption of SLB on the quartz crystal followed by fast adsorption of CNCs. The adsorption of XG was slower (~20 min), yet resulted in a final stable baseline, implying that the adsorption process was completed within the time scale of the measurement. In addition, the rinsing steps (black arrows) did not result in removal of mass as indicated by the stable frequency value for all deposition steps.

Given the low dissipation values, Sauerbrey relationship was used for the calculation of adsorbed mass, taking the film density as the one of water. Table 17 shows the values obtained for the frequency, dissipation, mass and calculated thickness of the SLB CNC and XG layers composing the film.

The values of frequency and dissipation for the SLB were -25.2 Hz and $0.8 \cdot 10^{-6}$ respectively, resulting in SLB thickness of 4.5 nm. values of frequency and dissipation for the CNC layer were -29.7 Hz and $2.9 \cdot 10^{-6}$ respectively, resulting in CNC thickness of 5.3 nm, in agreement with the previous results obtained for SLB-CNC system (chapter

4.2.2). The values of frequency and dissipation for the XG layer were -10.3 Hz and $2.2 \cdot 10^{-6}$ respectively, resulting in XG layer thickness of 1.9 nm. Similar results were obtained for XG on top of CNC layer. (Bensselfelt, et al. 2016) in that case the thickness of the XG layer was 1.4 nm deposited on spin-coated CNC layer.

Table 17. Data obtained from QCM-D for the deposition of SLB, CNC and XG layers. ^aadsorbed mass from Sauerbrey relationship. ^bthickness was calculated assuming a density of water.

	ΔF [Hz]	ΔD [$\cdot 10^{-6}$]	^a Δm [ng cm ⁻²]	^b Δh [nm]
SLB	-25.2	0.8	453.5	4.5
CNC	-29.7	2.9	534.4	5.3
XG	-10.3	2.2	185.7	1.9

Villares et al. (Villares, et al. 2015) studied the kinetics of adsorption of XG on spin coated CNC layers. In their work the XG concentrations were lower (0.01 - $20 \mu\text{g mL}^{-1}$), and the XG molar mass was higher, resulting in slower adsorption of ~ 1 hr. However, the frequency changes and adsorbed masses were in agreement with our findings.

Comparing to the 3D case, the polymer/particle mass ratio calculated from the adsorbed mass in the QCM experiment was 0.35. this number is higher than 0.05 found in the bulk experiments. A possible explanation is that, unlike the bulk (3D) configuration, in a QCM-D experiment (2D), the CNC layer is stagnant and the XG solution is constantly flowing enabling reorganization and higher surface coverage. Furthermore, while in the 3D experiment- theoretically all the surface is able to interact, in QCM (2D) the surface exposed to the external solution represents less than half of the actual mass of CNC adsorbed, since only the upper face of the CNCs is free to interact (the bottom and the sides are blocked by the SLB and the neighboring CNCs in the layer). A precise calculation is rather difficult since the anisotropic CNCs are laid on top of each other in a disorganized way. However, a rough estimation, that only a third of the adsorbed mass is available for the XG, yields a polymer/particle mass ratio of 0.1 at saturation, a result which is not far from the one obtained for the 3D experiment ($R=0.05$).

To conclude on the findings from this experiment:

- XG adsorbed on CNC, while the latter is deposited on SLB layer.
- The change in buffer to glucose/sucrose system did not significantly change the nature of the interaction.
- The time scale of XG adsorption on CNC was found to be 20-30 minutes.

These findings together with the 3D experiments provide the optimization of building blocks and the basic conditions for the construction of micron scale biomimetic capsules/ multilayers. In the following chapter we will introduce an additional building block, pectin, and study its interaction with CNCs.

4.4. Pectin-CNC interaction

As discussed in the introduction, whether or not cellulose interacts directly with pectin side chains or back bone *in vivo* is not yet well understood, mostly due to the complex nature of the cell wall polymers. Several studies showed evidence of pectin-cellulose close contacts *in vitro* models using binding assays (Gu and Catchmark 2013, Zykwinska, et al. 2008, Zykwinska, et al. 2005) or enzymatic degradation (Zykwinska, et al. 2007). Solid state NMR studies showed direct cellulose–pectin spatial contacts exist in the *Arabidopsis* primary cell wall, where up to 50% of the cellulose chains exhibit close contact with pectins. (Dick-Pérez, et al. 2011, Wang, et al. 2012, Wang, et al. 2015) These studies pointed out that pectin-cellulose contacts exist, but they are weaker than the xyloglucan-cellulose interaction and rely on the neutral side chains of pectin such as RGI and RGII, and to less extent on the HG backbone. However, the nature of this intermolecular interaction is not completely understood.

It should be mentioned that while *in vitro* binding experiments consists of dilute solutions of polymers allowed to adsorb to cellulose surfaces, the PCW environment is assembled in a confined space where crowding, entanglements, competing interactions, and enzymatic modifications may greatly influence the interactions among wall components.(Cosgrove 2014)

Regardless if cellulose-pectin links exist *in vivo*, understanding of its interaction with the other components of the system is essential for their incorporation in our biomimetic constructs. Since XG and pectin are not believed to be interacting directly *in vivo*, we rely on possible interaction between CNCs and pectin. Both CNC and pectin being negatively charged, one as a colloid and the other as a polyelectrolyte, electrostatic repulsion has to be overcome in order to promote the adsorption of pectin on the crystal surface. Three possible mechanisms may be taken into account:

1. Screening the electrostatic repulsion using monovalent electrolyte.
2. Creating coordinative binding through calcium mediated interaction.
3. Gelation of the pectic chain via egg-box type or entanglement mechanism followed by entrapment of cellulose aggregates in the network.

In order to address these points, a series of experiments was performed. First, CNCs were simply mixed with pectin at constant CNC concentration and increasing pectin concentration for two types of pectin: P35 and P71, and 3 types of medium: water, NaCl 10 mM and CaCl₂ 3.3 mM representing similar ionic strength of 10 mM. The mixtures were left under stirring overnight for equilibrium, then observed or measured with DLS.

4.4.1. Screening experiments

Figure 83 shows mixtures of CNC (1 %wt.) and pectins (1% wt., P35 and P71) at increasing polymer/particle ratio. The first point, at R=0 corresponds to pure CNCs. The mixing was performed dropwise under stirring and the order of addition was CNC, pectin and electrolyte solutions consecutively with 10 minutes delay between pectin and electrolyte solution, to ensure proper mixing of the two first components.

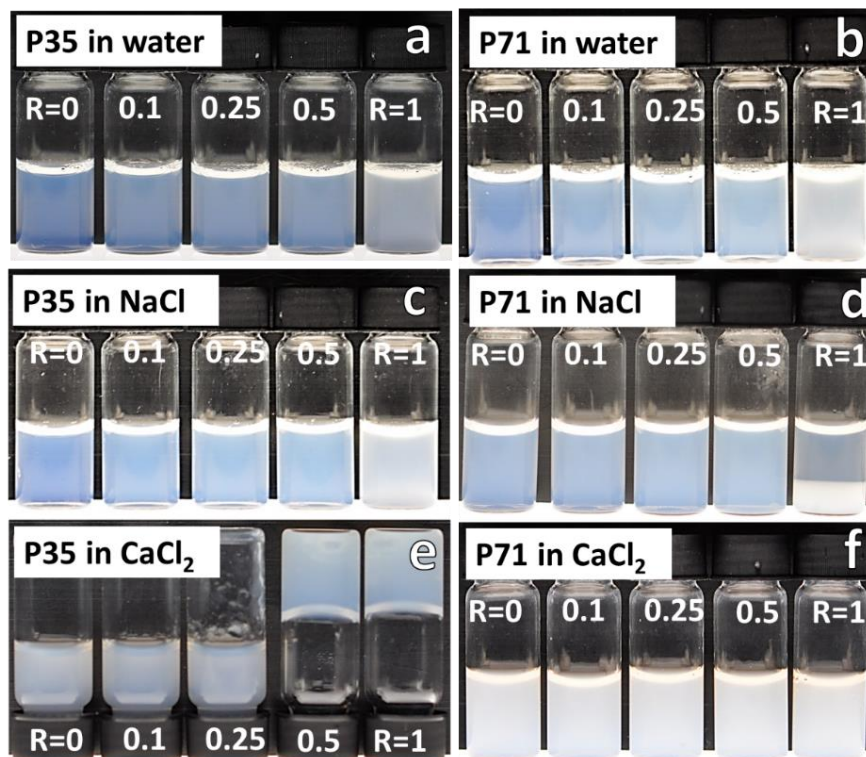


Figure 83: Mixtures of CNC-pectin in water (a,b) NaCl 10mM (c,d) and CaCl₂ 3.3 mM. for low degrees of methyl esterification: P35 DE=0.35 (a,c,e) and P71 DE=70 (b,d,f)

The first evident observation is that with the increase in polymer/particle ratio, a minor increase in the turbidity of the mixtures is observed, with a sharp increase in turbidity for R=1. This phenomenon is observed for both P35 and P71 even without the presence of salt, suggesting that depletion forces exist at high ratio due to the presence of high amount of polymer and reduction of the available free volume. Such phenomena was observed for other particle/polymer systems carrying similar charge sign. (Toyotama, et al. 2016) Noticeably, the sum of electrostatic, depletion and VdW forces needs to be taken into account. At high polyelectrolyte concentration, the contribution of depletion to the total sum of forces reduces the separation distance between two components enabling contact and eventual aggregation.

Effect of solvent and pectin type

The effect of ionic strength and valency of ionic species can be addressed by comparing the behavior of a given type of pectin in water and in salt. For P35 the difference in turbidity between water and NaCl is not significant for the same R. At high polymer/particle ratios, the mixture gels in the presence of calcium. In fact, P35 alone also gels upon addition of calcium but the calcium concentration threshold for gelation is higher (10 mM for 0.5% wt. Pectin), emphasizing the contribution of the CNC particles the gelling behavior.

In the case of P71, the difference in turbidity between mixtures in water and NaCl is notable, and at high polymer/particle ratio, large pectin-CNC clusters eventually sediment. This can be explained by the fact that since P71 is less charged than P35 (see ζ -potential values, figure 84b), the screening with NaCl is more efficient. From the same reason, P71 does not gel in the presence of similar amount of CaCl_2 even for the high ratios.

4.4.2. DLS and ζ -potential measurements

The observations from screening experiments were further confirmed with DLS measurements performed on the same mixtures shown in Figure 83a, b, c and d. The measurement on the CNC-pectin mixtures in CaCl_2 were excluded, since the solutions were too viscous and thus particles and complexes cease to follow classical Brownian motion. In addition, extra care has to be taken in the analysis, as both pectin and CNCs are at the limit of overlap concentration which can potentially lead to multiple scattering effects. Taking advantage of the low scattering from pectin alone (attenuator values are 10-11 and 6-7 for pectin and CNC respectively), it can be assumed that the signal obtained during the measurement is due to the scattering from CNC aggregates alone. Therefore, increase in objects diameter is interpreted as an increase in CNC aggregation number caused either by particle aggregation or polymer particle bridging.

Figure 84a shows the intensity size distribution as obtained using the CONTIN algorithm on the auto correlation function for the P71-CNC system in NaCl. CONTIN was

chosen over cumulants in this case, since the PDI of the mixtures was between 0.15-0.4, i.e. polydisperse sample.

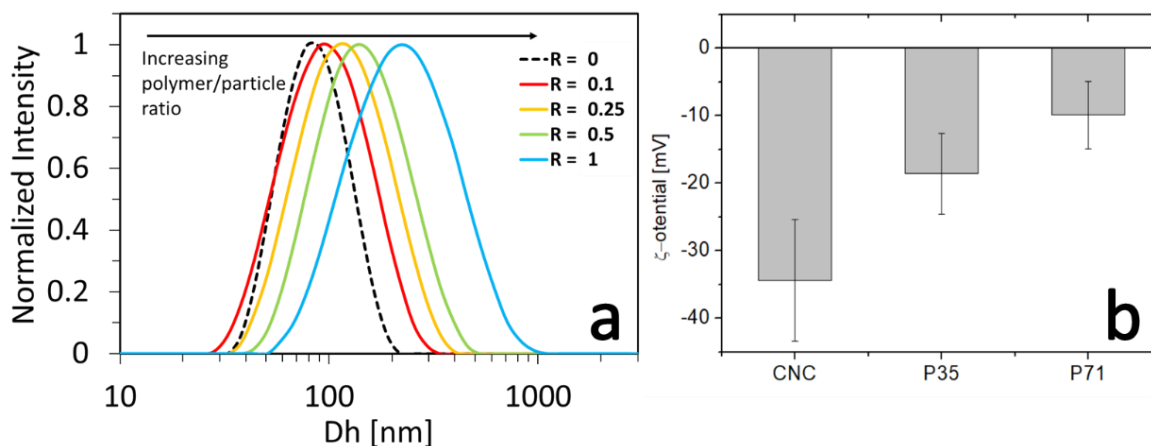


Figure 84. (a) Hydrodynamic diameter of CNC-P71 complexes with increasing polymer/particle ratio. R=0 (bare CNCs) dashed black curve, R=0.1 (red), R=0.25 (yellow), R=0.5 (green), R=1 (blue). (b) ζ -Potential values of CNC, P35 and P71 in 10 mM NaCl.

Both complex size and width of distribution increase with increasing polymer/particle ratio. Figure 85 shows a summary of hydrodynamic diameter values for mixtures of CNC-P35 (a) and CNC-P71 (b) in water (white column) and 10 mM NaCl (black column).

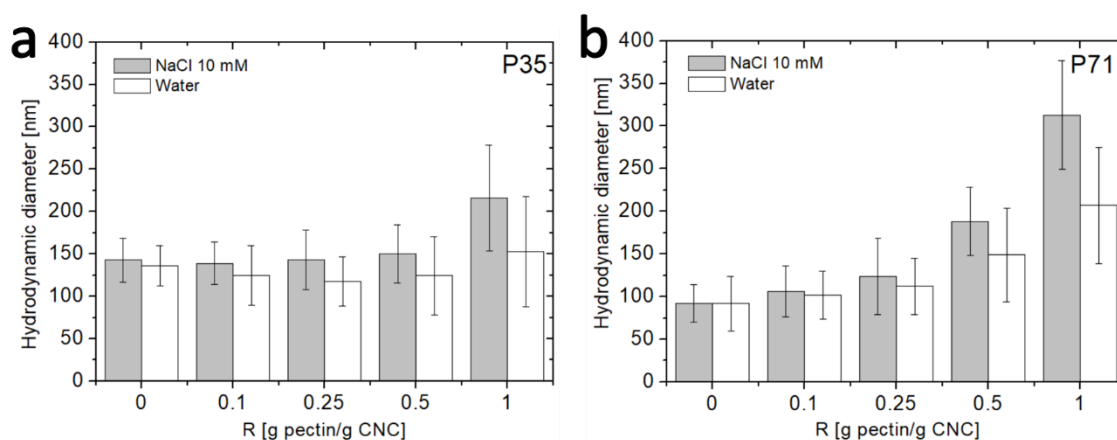


Figure 85. Hydrodynamic diameter of pectin-CNC complexes as a function of polymer/particle ratio R. in water (white columns) and 10 mM NaCl (gray columns) for P35 (a) and P71 (b).

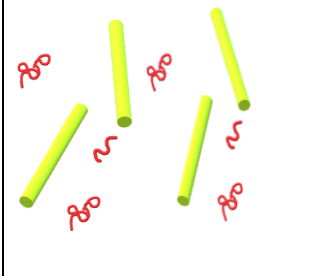
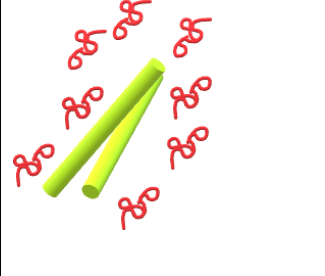
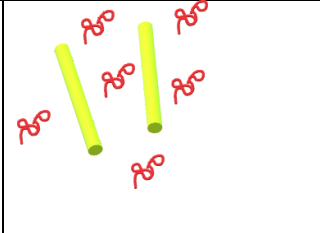
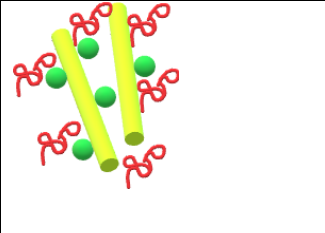
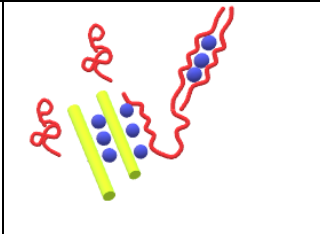
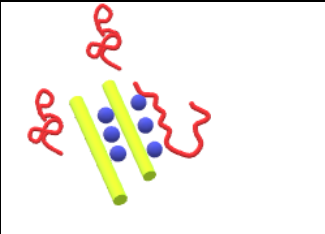
A notable increase in hydrodynamic diameter is observed for the highest polymer/particle ratios in all conditions. The difference in D_h between water and NaCl for the same ratios was higher for P71 than for P35. This is backed up by the observation of the complexes in naked eye (Figure 83).

4.4.3. Summary

- The interaction between CNCs and pectin depended on polymer/particle ratio, pectin charge, the ionic strength of the medium and the valency of the electrolyte solution.
- At high polymer/particle ratios, depletion forces could be overcome the electrostatic repulsion, causing CNC aggregation.
- In the presence of monovalent salt, screening effect takes place at higher ratios, effect that is more pronounced in the case of P71 due to the lower DE and thus lower negative charge.
- In the presence of divalent salt, P35 gels at high polymer/particle ratios.

These conclusions are summarized in table 18.

Table 18, An illustrated summary of the proposed mechanisms for CNC-Pectin interaction. CNCs are denoted as yellow rods, XG as red lines, Na^+ and Ca^{2+} ions are represented by green and blue spheres, respectively.

		Low R	High R
Effect of polymer/particle ratio	Depletion		
		Low Ionic strength	High Ionic strength
Effect of ionic strength	Screening+depletion		
		Low DE	High DE
Effect of DE in the presence of calcium	Calcium bridges+screening+depletion		

Since the CaCl_2 had proven to be efficient in bridging the interaction between CNC and pectin, it was chosen to work with P35 which has the most tendency to form such links.

4.5. Summary of the interaction studies

Table 19 summarizes the main conclusions from the interaction studies shown in this chapter. For the CNC-Lipid system, both 3D and 2D studies support electrostatically driven interaction. For the CNC-XG system, specific adsorption of XG on CNCs was confirmed and it was found that low Mw, XG adsorbs faster and tighter on cellulose. For the pectin-CNC system, electrostatic repulsion can be compensated either by high pectin concentration (depletion) or by calcium mediated interaction (bridging).

Table 19. A summary of the conclusions for the interaction studies

System	Type of interaction	Resulting information
CNC-Lipid	Electrostatic interaction	Work at low pH where the charge sign is opposite, or use positively charged lipid
CNC-XG	Hydrophobic, VdW, H-bond	Work at low polymer/particle mass ratio. Short (sonicated) XG chain promotes tight adsorption
CNC-Pectin	Depletion, calcium induced aggregation	Work with low degree of methyl esterification and use CaCl ₂

In the previous chapters we have prepared and characterized the building blocks and defined the parameters governing the interaction between them. In the following chapter we will use these design principles in order to prepare biomimetic constructs in 2D and 3D.

Chapter 5

Biomimetic constructs: assembly and characterization

The preceding parts dealt with the characterization of the building blocks chosen to represent the PCW elementary bricks (chapter 3), and the interactions between them (chapter 4). This part deals with the realization of the biomimetic constructs in 2D and 3D. The LbL technique mentioned in the introduction was used to create multilayered films (2D) and decorated lipid vesicles (3D) with alternating layers of CNC, XG and pectin. Figure 86 shows the experimental setup chosen for the 2D and 3D systems.

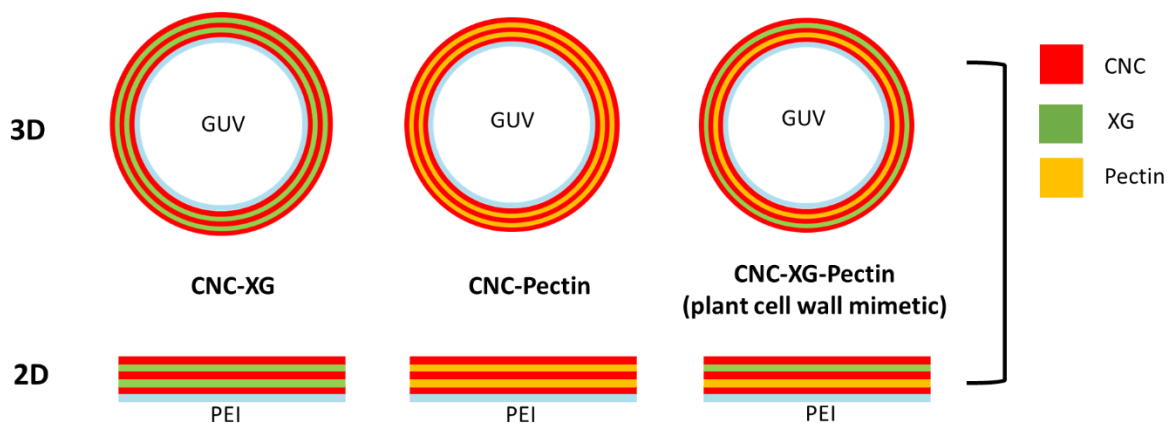


Figure 86. Experimental setup in 2D and 3D.

A similar composition was chosen for the 2D and 3D constructs in order to facilitate the comparison and to examine possible effect of curvature on the adsorption. In the case of the 2D system, the lipid bilayer was replaced with polyethyleneimine (PEI) since the 2D systems are prepared with intermediate drying which might cause the complete disruption of a lipid bilayer and the adsorbed material.

5.1. 2D configuration

5.1.1.2D assemblies: multilayered films

The deposition of CNCs, sonicated XG ($M_w=100$ kDa) and pectin (P35) was performed using the LbL method in dip coating procedure, according to the scheme shown in figure 87. First, a layer of PEI was deposited on a microscope slide, previously cleaned with ethanol followed by plasma treatment. PEI is used here since it is a positively charged polyelectrolyte which is known promote the adsorption of the first CNC layer. (Jean, et al. 2008, Jean, et al. 2009) Then, the LbL protocol was applied to grow thin multilayer film. While CNC and XG readily interact, CNC and pectin are both negatively charged and therefore calcium ($I=10$ mM) was used during the rinsing step. The following scheme shows the different steps in multilayer preparation, in the case of CNC/XG and CNC/pectin films.

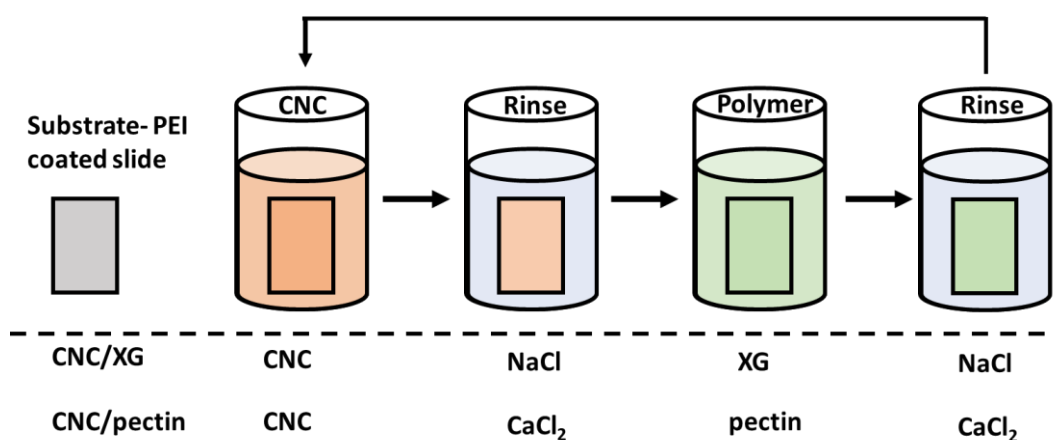


Figure 87. LbL protocol for the multilayered films. NaCl and CaCl₂ ($I=10$ mM) were used for CNC/XG and CNC/Pectin respectively.

The surface coverage of the slides was probed with fluorescence microscopy by labeling the uppermost layer of the film with fluorescent CNCs. The coverage was found to be homogeneous over the slide area. The growth and mechanical properties of the films were probed using AFM and will be further discussed in the following chapters.

5.1.2. Characterization of layer thickness using AFM

Prior to obtaining force curves, it is highly important to have *a priori* knowledge on the film thickness and topography. In order to obtain this information, an AFM tip (RTESPA-300, Bruker, USA) mounted on a cantilever ($k=40$ N/m, Bruker, USA) was used in two modes: **QI mode** was used for imaging, while **contact mode** was used to generate a square shaped well, also referred to as 'groove', in the film by scratching the surface, in order to measure its thickness. This process, previously termed "nano-shaving" was similar to the one used in chapter 4.2.

First, a $10 \times 10 \mu\text{m}^2$ (150×150 pixel) scan was performed in QI mode. A set point of 0.1 V and z-length of 500 nm were typically used. After obtaining the image, a smaller area of $3 \times 3 \mu\text{m}^2$ was chosen in the center of the previous scan, where the material was removed. To this purpose, AFM was operated in contact mode setting a large set point (8V) and virtually switching off the feedback loop (by using typically P gain = 0.0001 and I gain = 0.1). The scan was repeated 3 times and then a new topographic map, acquired on the original $10 \times 10 \mu\text{m}^2$ area, was used for the thickness analysis. Typically, 1-3 scratches were performed for each sample.

As can be seen in figure 88, a square shaped groove was obtained following the scratching process, indicating efficient removal of material. The material removed from the film accumulated on the edges of the square and in several cases some of the material fell back to the bottom of the formed well. Figure 88a shows a 3D image of the scanned area after scratching.

In order to obtain thickness values, Gwyddion (V 2.54) software was used. First, a mask was applied on the scratched area in order to exclude it and plane leveling procedure was performed in order to remove offset and tilt from height values and set the mean height to zero. Then, a new mask was applied, this time on the scratch edges in order to exclude them from the analysis. A histogram of the height was calculated using the 1D statistical function toolbox, yielding two peaks corresponding to the top of the layer and the exposed substrate (the microscope slide). Each peak may be fitted with a Gaussian function (Figure 88b). The Gaussian peak represents the mean height

for the bottom and the top planes of the image, the distance between the peaks is the average height.

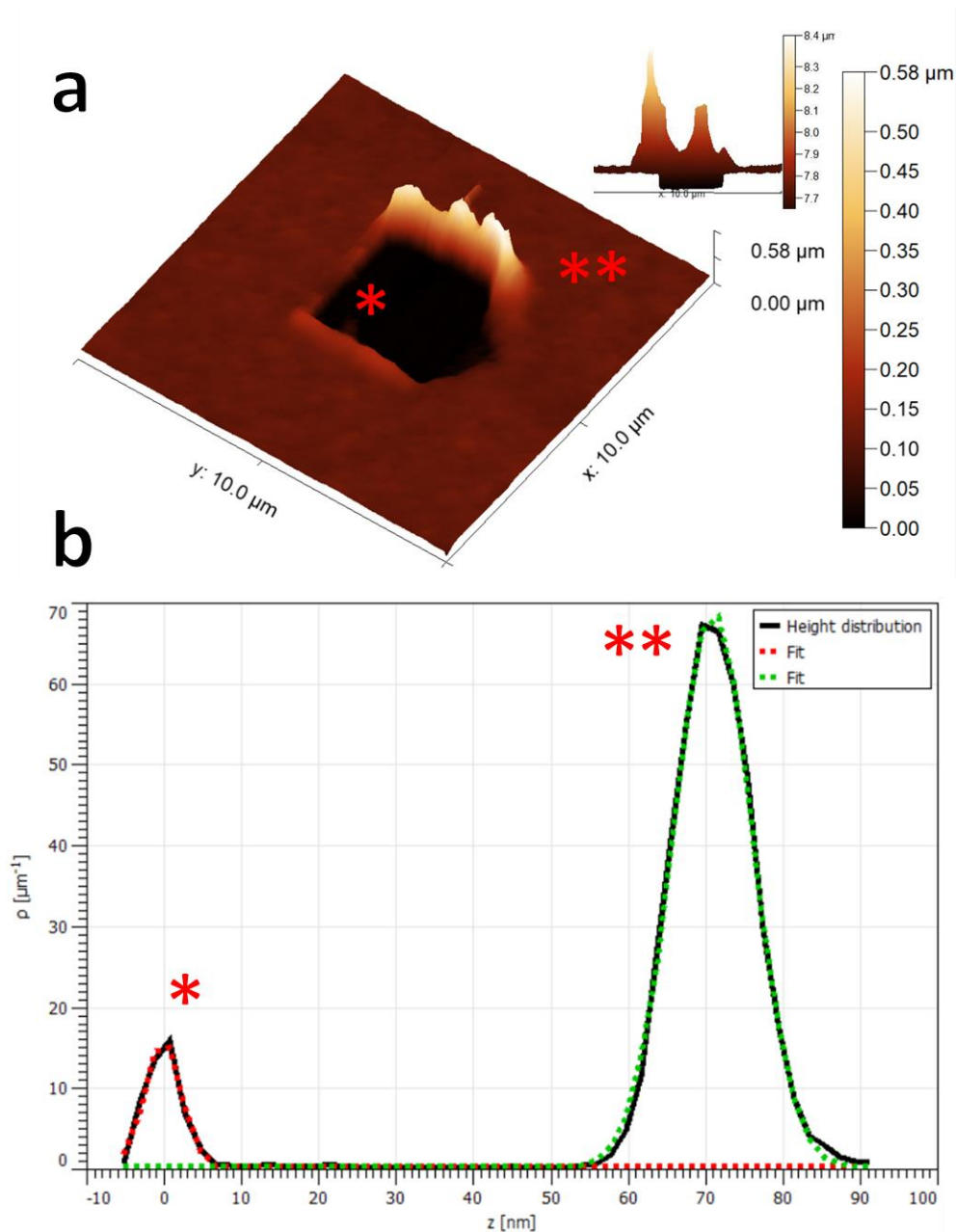


Figure 88.(a) A typical height profile obtained following the scratching process, the inset shows a side profile of the same image (b) A gauss fit to the two main peaks found using image analysis. Height distribution (black line), a fit to the bottom plane- groove (red dashed line) and a fit to the upper plane sample surface (green dashed line) the z distance between the two peaks is the calculated sample thickness.

The error is represented as the RMS roughness (Sq) of the film and calculated with Gwiddon software the following formula:

$$(Eq. 34) \quad RMS \text{ roughness } (Sq) = \sqrt{\frac{1}{l} \int_0^l z^2(x) dx}$$

Figure 89 shows a typical height profile of a CNC surface:

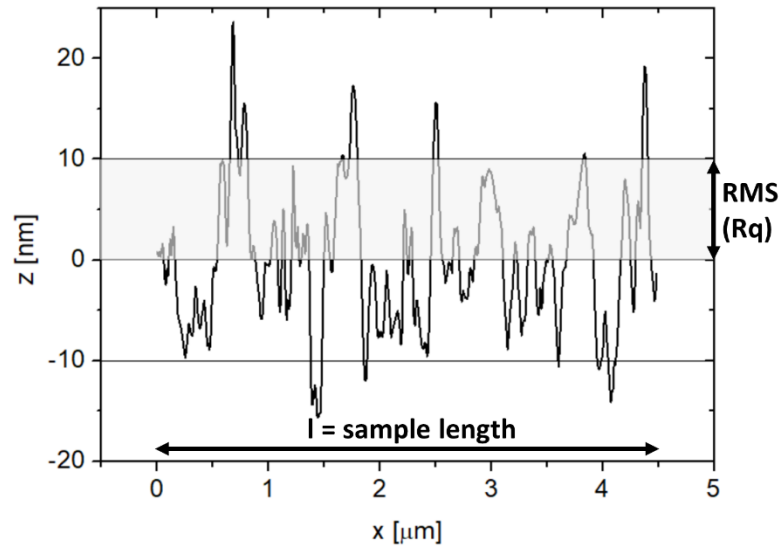


Figure 89. A typical line profile of CNC surface. the RMS roughness is calculated over the entire image (excluding the groove) using equation 34.

Notably, due to the scratching process, the quality of the tip may have been degraded during the measurement reducing the spatial resolution. This could lead to an underestimation of the surface roughness resulting in lower roughness than the real roughness of the CNC surface.

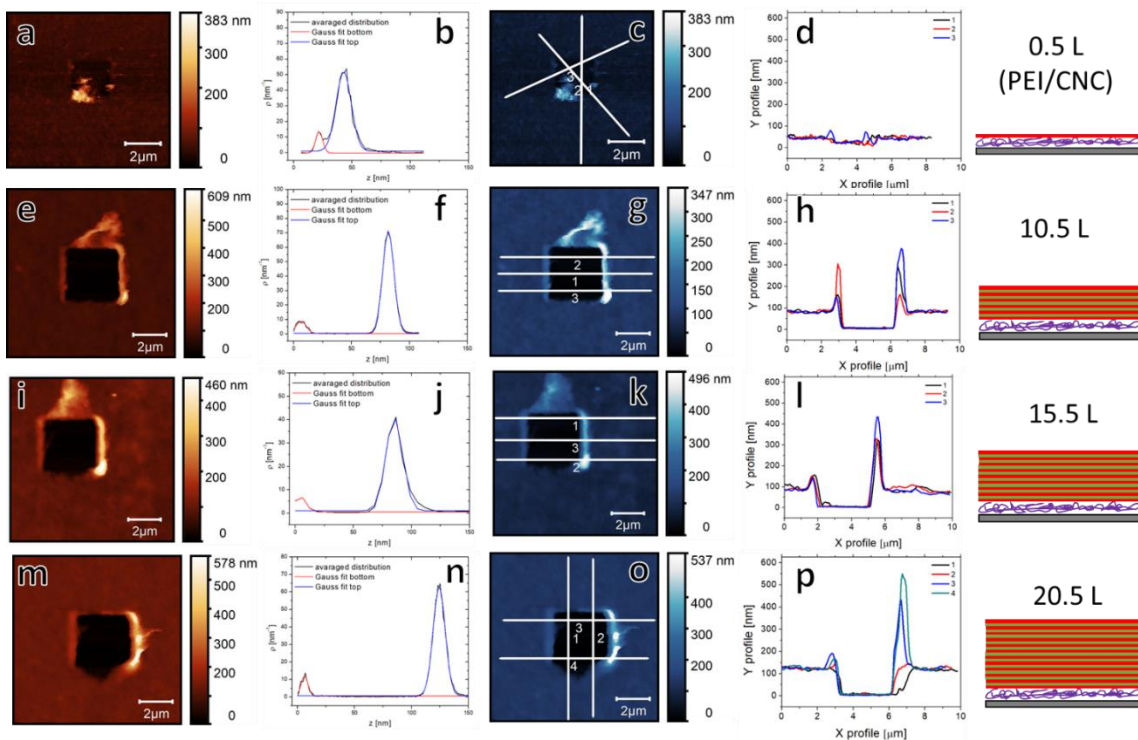


Figure 90: From the left in columns: AFM topography image of CNC/XG film after scratch, (a,e,i,m) Gaussian fit to the height distribution (b,f,j,n), line profiles used to calculate the film thickness (c,g,k,o), height profiles obtained from the lines (d,h,l,p) and an illustration of the multilayered films. Results are shown for varying number of layers: PEI/CNC (a-d), 10.5 Layers (e-h), 15.5 Layers (i-j), 20.5 Layers (m-p). One layer corresponds to a CNC/XG section.

This technique was used in order to probe 3 types of systems: (i) CNC/XG, (ii) CNC/pectin and (iii) CNC/XG/pectin. For the XG system, a simple LbL process was performed with NaCl rinse ($I=10$ mM) between each deposition step. When pectin was present (systems ii and iii) the sample was rinsed with CaCl_2 ($I=10$ mM) between CNC and pectin layers. The deposition was done with and without intermediate drying. A summary of the calculated heights for the different systems is shown in table 20:

Table 20. Calculated thickness of the multilayered films from AFM experiments.

System	Number of layers	Thickness [nm]	
		Intermediate drying	No intermediate drying
PEI/CNC	0.5	13.6±4.4	24.1±10.4
CNC/XG	5.5	-	124.1±21.0
	10.5	75.3±11.2	200.0±27.5
	15.5	97.2±12.0	-
	20.5	119.8±11.6	325.1±24.2
CNC/Pectin	5.5	-	48.0±13.2
	10.5	24.4±11.1	82.3±15.2
	15.5	31.6±11.5	-
	20.5	25±11.4	105.6±20.0
CNC/XG/Pectin	5.5	-	75.7±18.3
	10.5	17.4±12.2	124.1±32.3
	15.5	69.6±13.2	-
	20.5	81.6±12.3	181.9±43.2

Figure 91a and 91b show the calculated thickness of the multilayered film prepared without and with intermediate drying steps respectively.

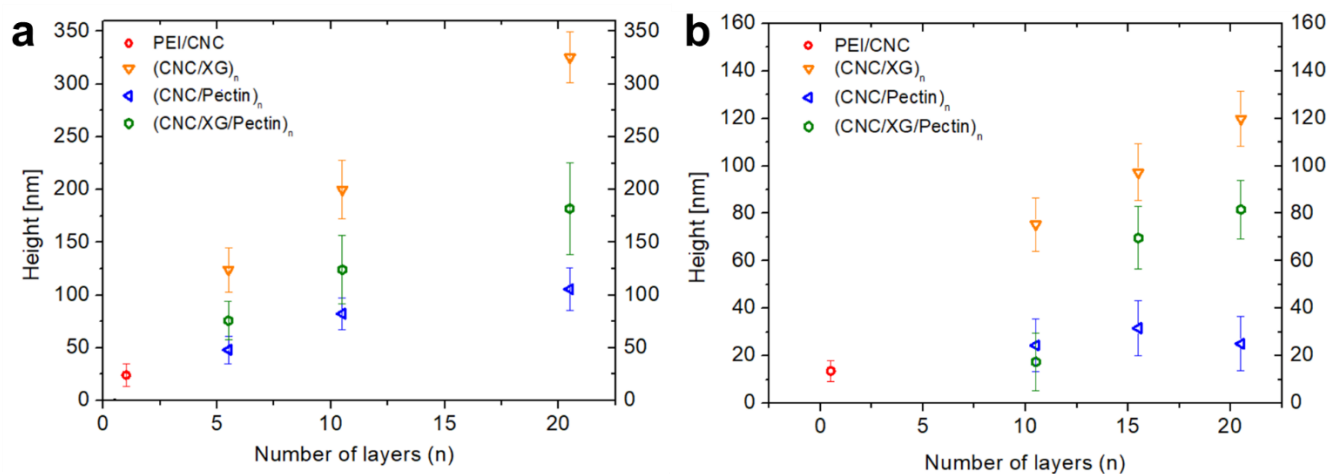


Figure 91. Calculated height for the CNC/biopolymer systems without (a) and with (b) intermediate drying steps. PEI/CNC (red circles), (CNC/XG)_n (orange triangles), (CNC/Pectin)_n (blue triangles) and (CNC/XG/Pectin)_n (green circles).

Let us discuss the result with respect to the different parameters.

Effect of intermediate drying

Comparing figures, 91a and b for systems with similar composition, notably, including intermediate drying steps resulted in thinner films. This applies for all the systems investigated, regardless of composition. This effect may be further visualized when comparing a system with similar composition, in this case CNC/XG system, with and without intermediate drying steps (figure 92).

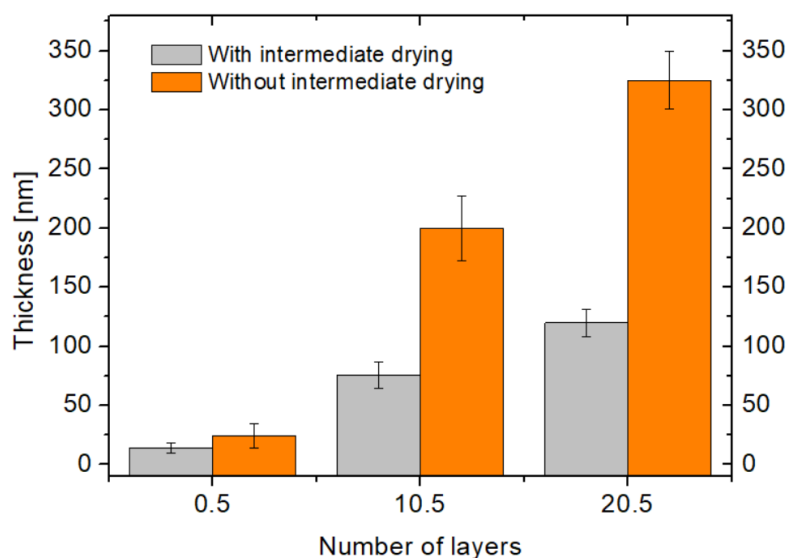


Figure 92. Multilayer thickness for CNC/XG system as a function of number of layers. With (grey columns) and without (orange columns) intermediate drying steps.

This observation could be attributed to the collapse of the polymer and the particles upon drying. When water is removed from the layer, individual CNCs approach closer towards the short range VdW attraction regime, resulting in tighter arrangement and reduction of the thickness.

Figure 93 shows the proposed structure based on the thickness of the film prepared with and without intermediate drying steps.

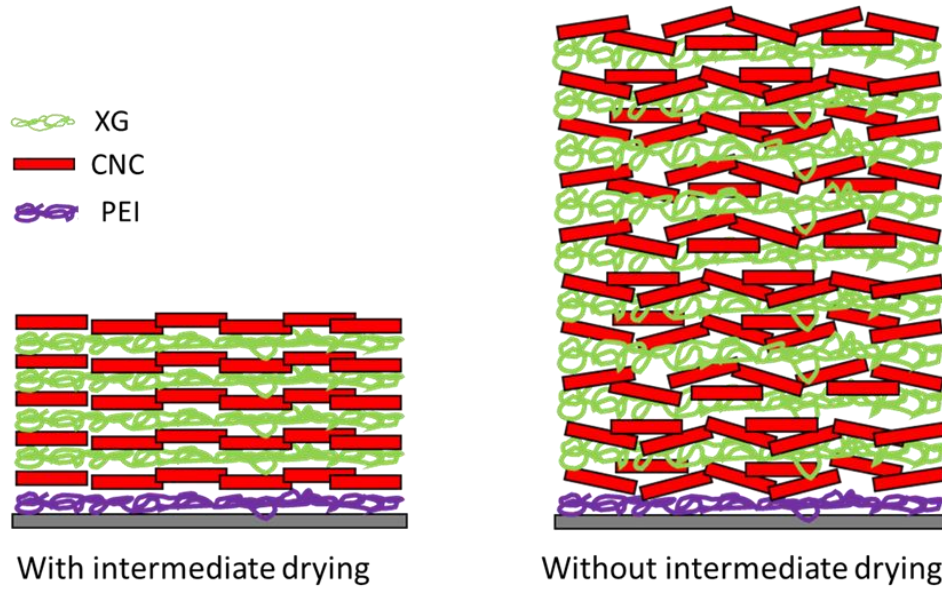


Figure 93. A scheme showing the proposed film structure prepared with and without intermediate drying steps. PEI (purple line), CNCs (red rectangles) and XG (green lines) are deposited in alternative manner on a flat substrate (grey rectangle). The image is not to scale.

In order to estimate the volume fraction of water in the films, an AFM nanoshaving experiment was done on the same multilayered sample, in air. An estimation of the difference in the volume fraction of water ϕ_v can be obtained, considering similar surface area, by subtracting the thickness of the system prepared without intermediate drying measured under **liquid** (t_h) and in **air** (t_d) according to the following equation:

$$(Eq. 35) \quad \phi_v = \frac{\Delta v_i}{v_{tot}} = \frac{\Delta t_i}{t_{tot}} = \frac{t_h - t_d}{t_h}$$

This results in the volume fraction of water in the film due to hydration. ϕ_v was 0.67, measured on the same sample (XG/CNC)_{5.5}. This result, showing high water content in the film, is in fair agreement with the results obtained in chapter 4.2, where water content of up to 70% was found in the CNC layer adsorbed on SLBs.

Effect of film composition

The largest growth per bilayer was observed for the CNC/XG system. The calculated increase in thickness was 16.4 and 5.7 nm per bilayer for with and without intermediate drying steps respectively. The growth was close to linear considering the high R^2 value from the linear fit (see table 21). The CNC/pectin and CNC/XG/pectin systems could not be described by linear growth model. It seems that whenever pectin was included in the film, the growth of the film was perturbed, which can imply that the electrostatic repulsion between pectin and CNCs in these conditions could not be overcome by simply adding Ca^{2+} ions between deposition steps. The minor growth of the film especially in the never dried protocol could be attributed to additional CNC layers. In the case of mixed CNC/XG/pectin, the growth was closer to the one of CNC/XG system, however it is possible that only the XG layers contributed to the total thickness.

Effect of drying and rehydration

In order to test the effect of drying and rehydration, the never dried CNC/XG system was subjected to drying at room temperature and then rehydrated. The height profile was obtained for the same sample before and after drying and rehydration (Figure 94). No significant difference in thickness was observed.

The conclusion that can be drawn from this experiment is that the preparation protocol plays the main role in the determination of the final thickness of the layer. Once the layers have been formed, the drying and rehydration have a minor effect on the final structure and resulted thickness of the layer.

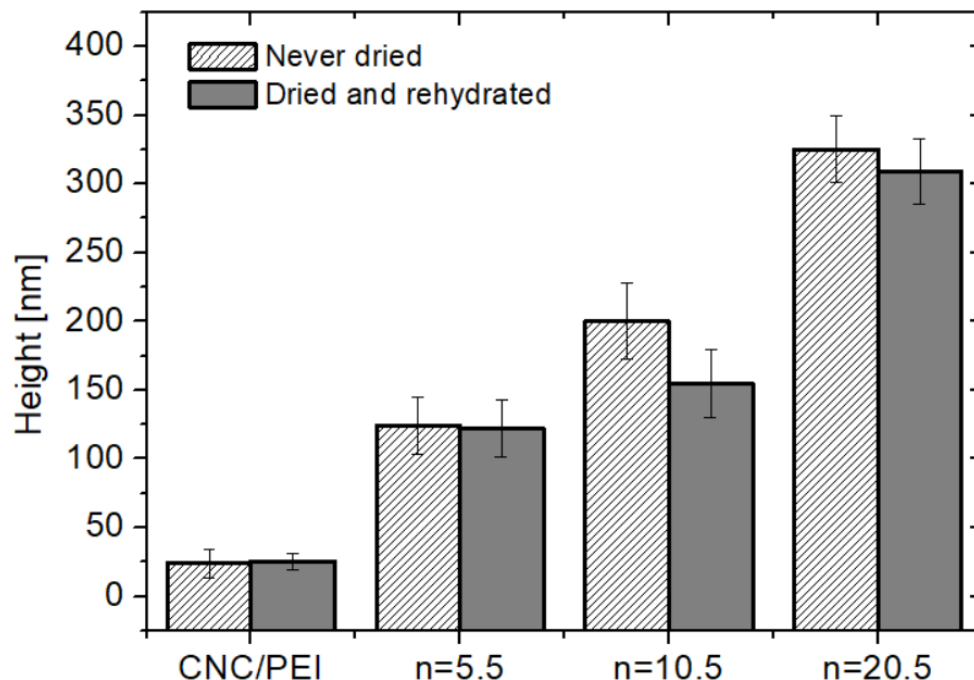


Figure 94. Thickness of CNC/XG films measured by AFM before drying (white columns) and after drying and rehydration (grey columns).

This situation is reminiscent of the one found for CNC/Gibbsite nanoplatelets multilayered films prepared by LbL. (Martin, et al. 2017) In their work Martin et al. showed using AFM and neutron reflectometry, that and the drying protocol (with drying or without drying after the deposition of each new layer) had a major influence on the structural parameters of the resulting films. Films prepared with intermediate drying were thinner than the ones prepared with intermediate drying and had stratified final architecture. They attributed the difference to a combination of electrostatic interaction forces and particle-particle hydrogen-bonding when water is removed.

A similar result was obtained by Cerclier et al. for spin coated CNC/XG system upon drying and rehydration, the difference in thickness was 1 nm for $n=5$. (Cerclier, et al. 2010)

The increment in thickness per bilayer was calculated and compared to the works of Jean and Cerclier and shown in table 21:

Table 21. Increase in thickness per bilayer for CNC/XG systems prepared with LbL technique.

System	Increment [nm per bilayer]	Ref.
Never dried	16.4	-
Measured in liquid	(R ² =0.969)	
Intermediate drying	5.7	-
Measured in liquid	(R ² =0.986)	
Never dried measured in air	6.8	-
Intermediate drying (measured in air)	9	(Jean, et al. 2009)
Spin coating (measured in liquid)	10.2	(Cerclier, et al. 2010)

CNCs from cotton are about 8 nm in height, about 21 nm wide and 100-200 nm in length (see chapter 3.1.2). Since the packing of the needle like crystal bundles is not perfect and they are randomly oriented, the expected thickness is one of 1-2 layers which is 8-16 nm.(Jean, et al. 2008) Adding to this the polymer layer (1.5-2 nm) the thickness of PEI/CNC layer is expected to be within the range of 10-18 nm. The value obtained for the PEI/CNC layer was 13.6 ± 4.4 and 24.1 ± 10.4 with and without intermediate drying respectively, in fair agreement with these studies.

The PEI layer in those cases was examined separately and found to have average value of 7 nm with aggregates of about 15 nm covering the entire surface. Since the radius of gyration of branched PEI is 16-43 nm for similar molecular weights,(Park and

Choi 1996) these aggregates could be considered as PEI coils, adding an additional thickness to the layer.

Conclusions:

- Films prepared without intermediate drying result in thicker multilayered constructs than systems prepared with intermediate drying.
- The thickness is slightly reduced upon drying and rehydration of the sample.
- CNC/XG systems are the closest to linear growth and are the most robust.
- Systems which include pectin did not show linear growth in thickness, implying that the electrostatic repulsion between CNC and pectin cannot be overcome by simply adding calcium ions.

The results obtained in this part are significant for the characterization of the 2D systems, since the thickness of the layer is an important factor to be considered when probing the mechanical properties using nano indentation, as will be shown in the following chapters.

5.2. 3D assemblies: bare and decorated vesicles

5.2.1. GUV preparation

GUVs were prepared using electroformation technique. This method was chosen since it produces almost entirely unilamellar micron sized vesicles. (Fenz and Sengupta 2012, Walde, et al. 2010) Figure 95 shows a scheme of GUV preparation by electroformation.

The apparatus used for the electroformation was provided by Thomas Podgorsky (LiPhy, Grenoble). It was made from two indium-tin oxide (ITO) slides with a spacer, connectors and a low frequency generator. 50 μL of a lipid mixture (1 g L^{-1}) in

chloroform/methanol 9/1 V/V, were deposited on each titanium slide and the organic solvent was evaporated at ambient temperature. The cell was then filled buffer and a voltage of 0.4 volt was applied with sinusoidal current with amplitude of 10 Hz. Typically, after several hours the vesicles were collected to a glass vile and kept at 4°C until used. Vesicles prepared in this way were stable over a period of several months.

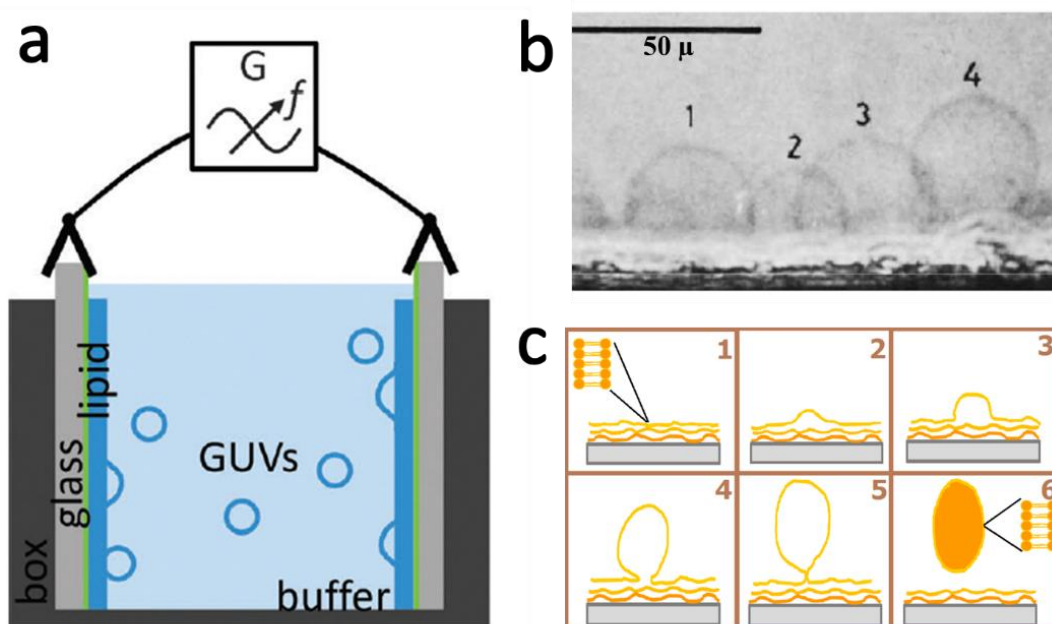


Figure 95. A scheme of GUV formation via electroformation (a) Systems components (b) micrograph of the formed vesicles (c) the stages of vesicle formation by rehydration and swelling of a dry lipid film in a aqueous buffer solution. (Angelova and Dimitrov 1986, Fenz and Sengupta 2012)

5.2.2. Observation of GUVs in optical microscopy

In order to observe the GUVs under optical microscopy, a round shaped silicone spacer with a diameter of 2 cm and thickness of 5 mm was placed on top of a clean microscope slide. The cylinder-shaped compartment with a total volume of about 500 μL (Figure 96), enabled the visualization in phase contrast and fluorescence modes.

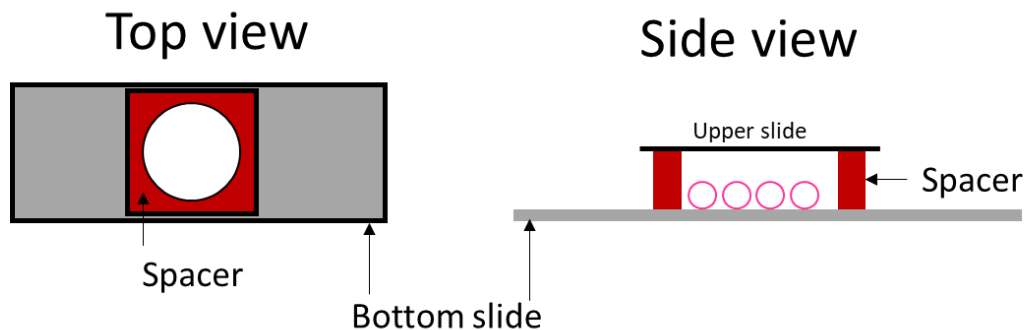


Figure 96. A drawing of the experimental compartment used for GUV observation.

Typically, about 480 μL of solvent was introduced to the well, followed by 20 μL of vesicle suspension. The vesicles were left to sediment for about 10 minutes before observation. Vesicles were observed using a Zeiss Axio observer microscope (Carl Zeiss, Germany) in X20 and X40 objectives, operating in phase contrast, fluorescence and Apotome modes. The microscope is equipped with a digital camera (Hamamatsu ORCA flash 4.0 LT, model C1440). A Colibri 7 multiple led illumination source and white light LED illumination source (microLED) were used for fluorescence and phase contrast modes respectively. The images were post treated using ZEN 2.3 pro software. Figure 97 shows optical microscope images of vesicles observed in phase contrast (a) fluorescence (b) and Apotome (c) modes.

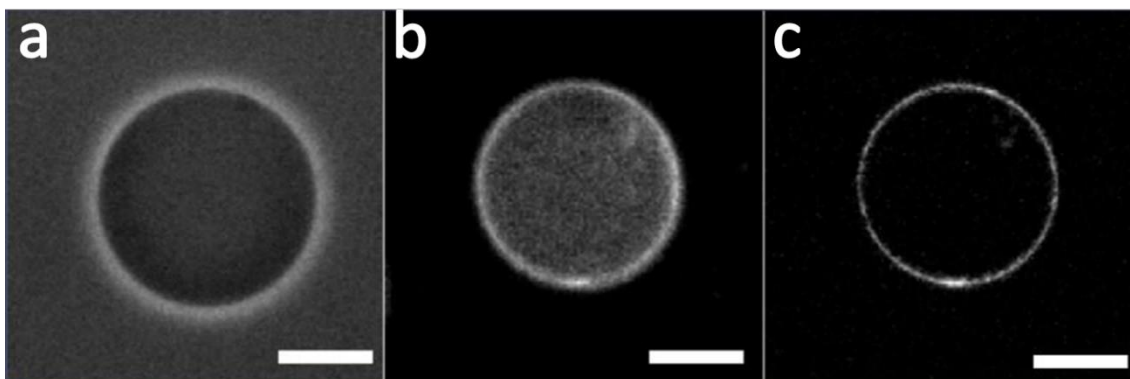


Figure 97. Observation of GUVs in optical microscopy. (a) phase contrast (b) fluorescence (c) SIM (Apotome). Scale bar: 10 μm .

These operational modes will be used in the following sections to characterize bare and decorated vesicles and explore their behavior under external stresses.

5.2.3. Decoration protocol

Inspired by the LbL technique, GUVs were decorated with alternating layers of CNC/polymer by incubating a suspension of GUVs with the desired component. Figure 98 shows a scheme demonstrating the decoration and rinsing process.

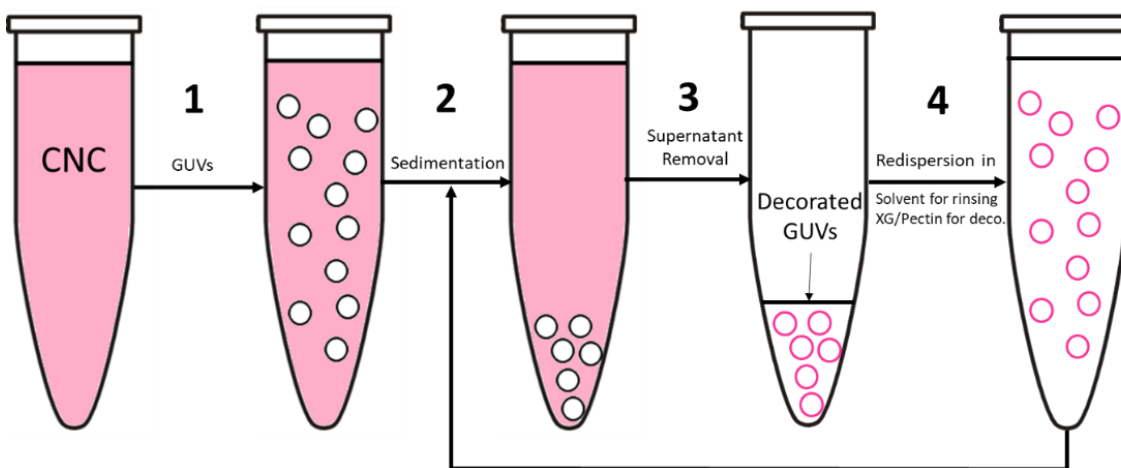


Figure 98. A scheme of the decoration procedure. In step 1- bare GUVs are mixed with CNC suspension. Step 2- Sedimentation. Step 3- Supernatant removal. step 4- redispersion in either solvent for rinsing (200 mM Glucose, 1 mM NaCl) or in a polymer solution for decoration.

CNCs, XG and pectin in powder form were dissolved in 0.2 M glucose solution and 1mM NaCl, a solute concentration similar to the one of sucrose present in the GUVs, in order to avoid an osmotic pressure difference that will lead to a mechanical stress on the vesicle. The pH was adjusted to 3 to give a slightly positively charged GUVs which promote the adsorption of CNCs, according to the results obtained in chapter 4.2.

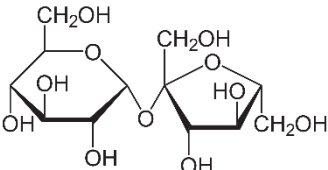
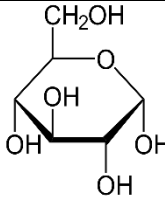
100 μ L of GUV suspension were mixed with 300 μ L 0.1% wt CNC suspension (**step 1**) A stirring wheel operating at 10 RPM for 60 seconds was used to ensure proper mixing. The Eppendorf was then removed from the stirring wheel and the vesicles were left to sediment. Due to the difference in density, the GUVs tend to sediment to the bottom phase after 20-30 minutes. (**step 2**) An additional centrifugation step was

typically used in order to speed the process and increase the number of objects in the bottom phase. The supernatant (300 μL) was then removed (**Step 3**) and the decorated GUVs were then rinsed with 300 μL of Glucose solution. (**Step 4**) The rinsing step is important in order to reduce the excess CNC or polymer in the bulk and to remove any unbound material. Following the rinsing step, a decoration step was performed, this time by the XG or Pectin.

5.2.4. Bare vesicles

Giant Unilamellar vesicles (GUVs) were chosen as the starting element, a scaffold on top of which the CNC, XG and pectins will be deposited. GUVs were produced via electroformation and then decorated with alternating layers of CNC and XG or Pectin. Table 22 shows the structure, Mw and refractive index of sucrose and glucose:

Table 22. Structure and physical properties of sucrose and glucose.

	Sucrose	Glucose
Chemical formula	$\text{C}_{12}\text{H}_{22}\text{O}_{11}$	$\text{C}_6\text{H}_{12}\text{O}_6$
Chemical structure		
Mw, g mol⁻¹	342.30	180.16
Density, g cm⁻³	1.59	1.54
Refractive index	1.3428	1.3360

The use of sucrose and glucose in the interior and exterior of the vesicles respectively, serves two main purposes: (i) due to the difference in density between the interior and exterior, vesicles that are filled with sucrose will sediment in a glucose solution, which facilitate the process of separation, rinsing, and successive decorations. (ii) the difference in refractive index enables the visualization of the objects using

optical microscopy (phase contrast or DIC). Figure 99 shows a phase contrast image of DOPC vesicles filled with 0.2 M sucrose right after deposition into 0.2 M glucose solution (a) and 10 minutes after sedimentation on the microscope slide (b).

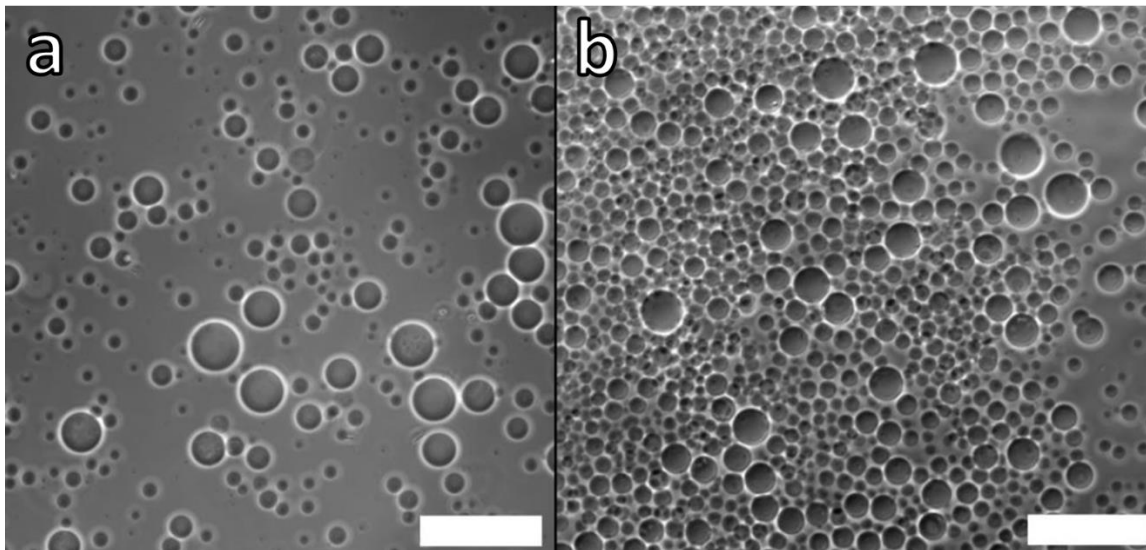


Figure 99. Phase contrast image of DOPC vesicles right after deposition (a) and after sedimentation of 30 minutes (b). Scale bar- 100 μm .

The sedimentation time could be further reduced by mild centrifugation. (2 minutes at 5000 RPM). This procedure results in the presence of 95% of the vesicle population in the bottom part of the eppendorf, which prevents loss of objects during the removal of the supernatant throughout the rinsing steps.

5.2.5. Decorated vesicles

In order to create a multilayered shell, the LbL protocol described previously was used. Alternating layers of CNC and polymer were deposited and the resulting capsules were observed optical microscopy. Figure 100 shows an image of decorated GUV-(CNC/XG) n with $n=1$ (a) $n=5.5$ (b) and $n=10.5$ (c). The fluorescence intensity profiles are shown for each case. No significant difference was observed for the intensity values, which is expected since only the last layer contains fluorescently labeled building blocks.

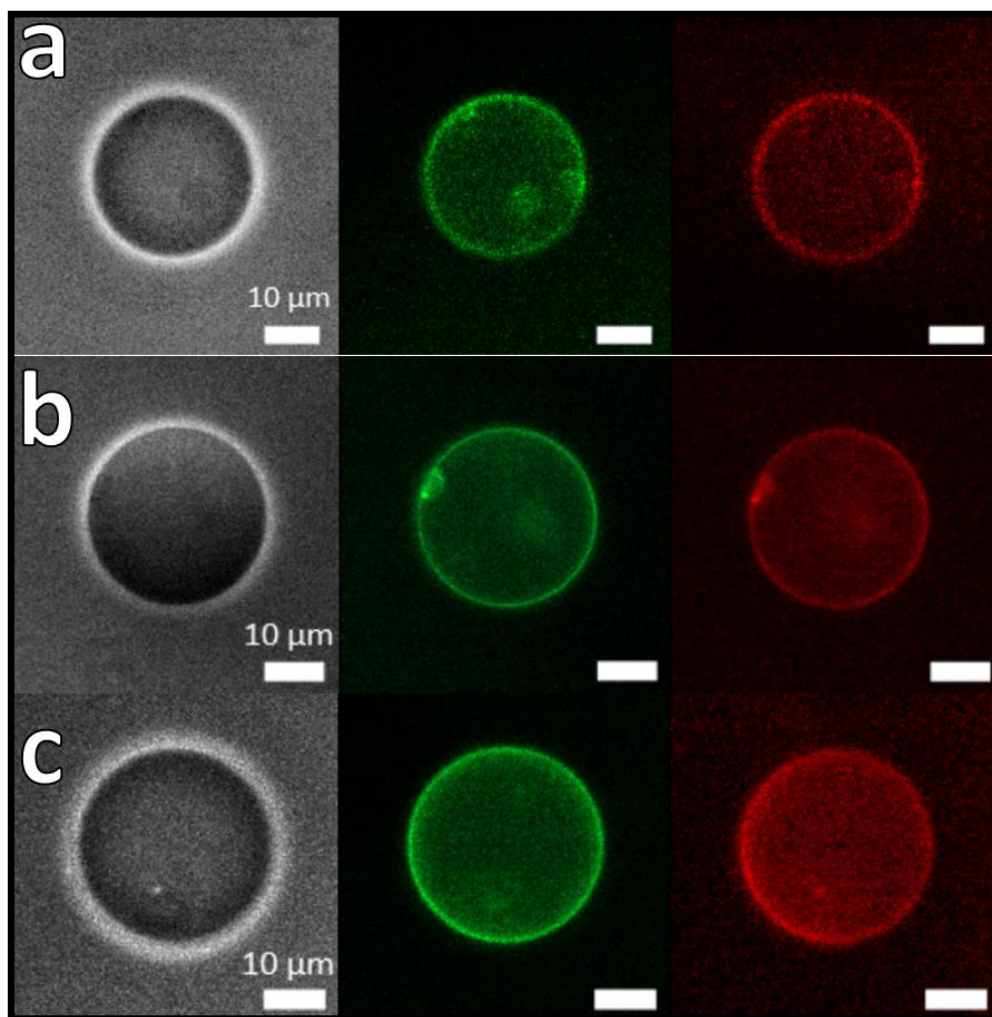


Figure 100. Optical microscopy images of GUV(CNC/XG) $_n$, for $n=1.5$ (a) $n=5.5$ (b) and $n=10.5$ (c).

Figure 101 shows the size distribution of bare and decorated capsules. The determination of vesicle size distribution was performed manually since the size depends on the position of each vesicle with respect to the microscope focal plane. Phase contrast mode was used for the determination of vesicle diameter using the tools provided by the Zen software.

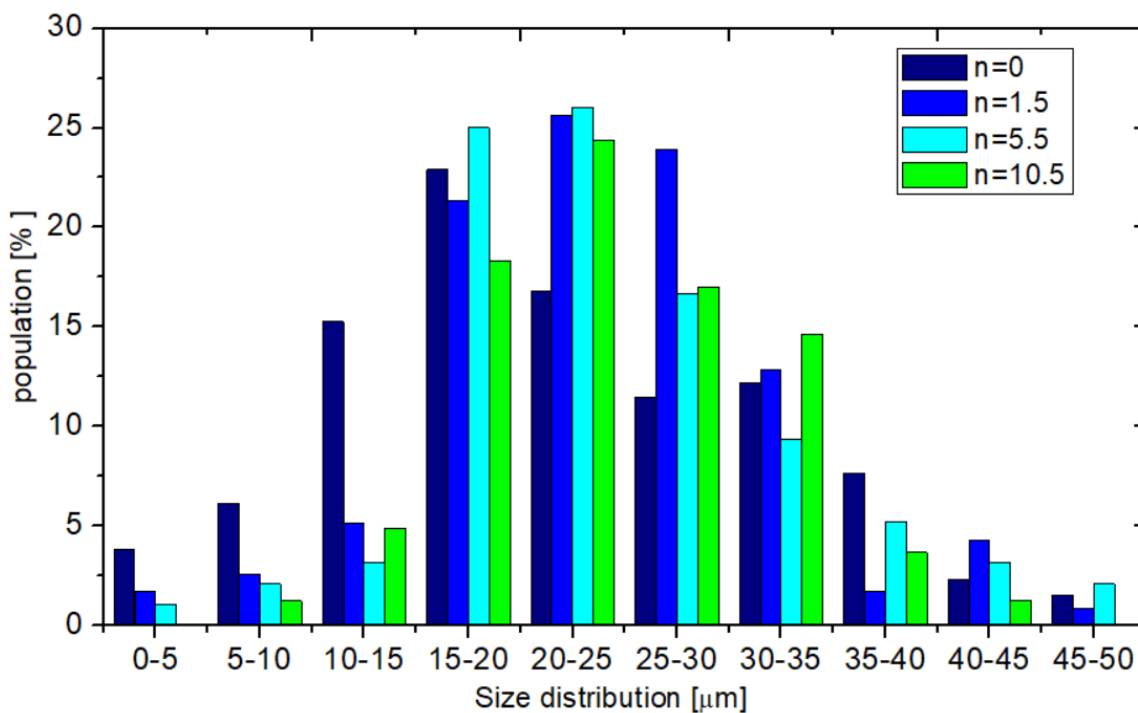


Figure 101. Size distribution (diameter) of bare and decorated GUVs.

Table 23 shows the average diameters of the vesicles obtained for bare and decorated vesicles with 1.5, 5.5 and 10.5 layers.

Table 23. Average diameter of bare and decorated vesicles.

Sample	Number of layers	Average diameter [μm]
GUV	0	22.3±12.2
GUV (CNC/XG) _{1.5}	1.5	25.3±9.5
GUV (CNC/XG) _{5.5}	5.5	24.6±10.6
GUV (CNC/XG) _{10.5}	10.5	25.2±10.2

The size distribution of the vesicles is in agreement with previous work on CNC/XG decorated vesicles. (Radavidson 2016)

As can be seen from the histogram, no significant effect of the number of layers was found on the size distribution of the vesicles. However, the total amount of the vesicles decreased with increasing number of layers, due to loss of objects during decoration cycles. In the following chapter we will examine the response of these objects to osmotic shocks.

5.3. Vesicles under osmotic Shocks

5.3.1. Observation of GUVs for osmotic shocks

Figure 102 shows the setup used for the osmotic shock experiments. A silicon spacer was placed on a clean microscope slide, creating an open chamber with a volume of $500 \pm 5 \mu\text{L}$. The chamber was filled with GUV suspension and the volume was completed to $500 \mu\text{L}$ with 0.2 M glucose solution. A porous aluminum oxide membrane with diameter of 25 mm and pores of 200 nm (Whatman, Anodisc 25 mm , Germany) was placed on top of the liquid, and an additional spacer was placed on top of the membrane to create a second upper chamber.

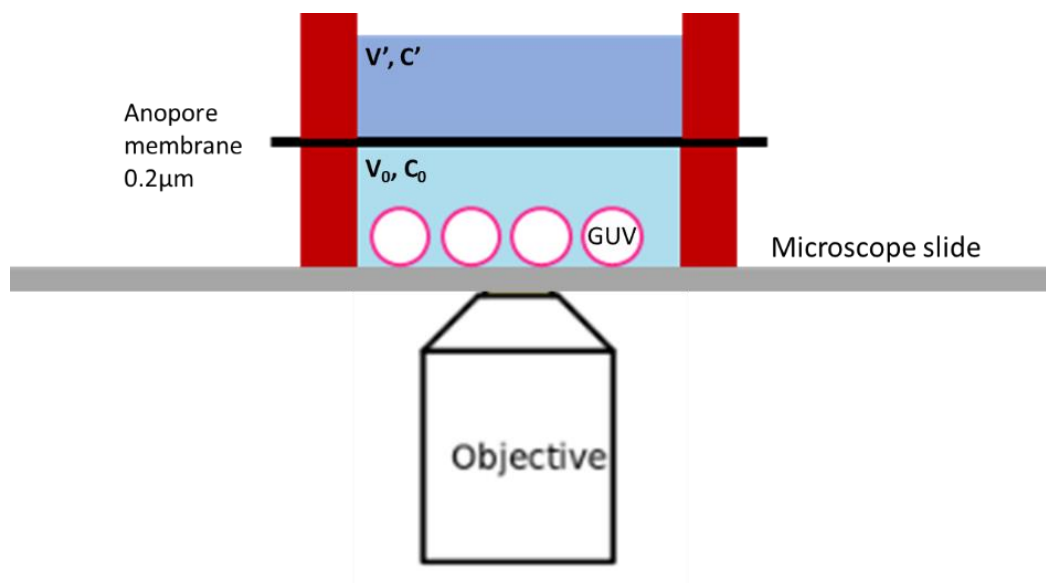


Figure 102. A scheme of the observation chamber for the osmotic shock experiments.

The presence of the porous membrane between the lower and upper compartment prevents the movement of the liquid of the liquid in the lower compartments upon addition of liquid, thus facilitating the observation of a single vesicle upon osmotic shock.

The upper chamber was then filled with desired solution by addition of concentrated glucose solution or electrolyte (hypertonic) or water (hypotonic). The difference in concentration due to the addition ΔC is then:

$$(Eq. 36) \quad \Delta C = C_0 - C_f = C_0 - \left(\frac{C_0 V_0 + C' V'}{V_0 + V'} \right)$$

For hypertonic solution $\Delta C > 0$ and for hypotonic solution $\Delta C < 0$.

5.3.2. Bare vesicles

As shown in chapter 1.2.4, lipid vesicles deform when subjected to osmotic shock, due to transport of water molecules in or out of the membrane. This can be visualized in optical microscopy by imposing a difference in osmolarity between the interior and the exterior of the vesicles and measuring the variation in diameter with time. The tools provided with the ZEN software (Zen Blue, V. 2012, Carl Zeiss) enables determination of the vesicle's diameter, assuming a circular geometry.

5.3.2.1. Glucose shocks

Figure 103 shows a series of images of bare DOPC GUVs taken at different times, following the addition of a concentrated glucose solution to the upper compartment of the observation cell.

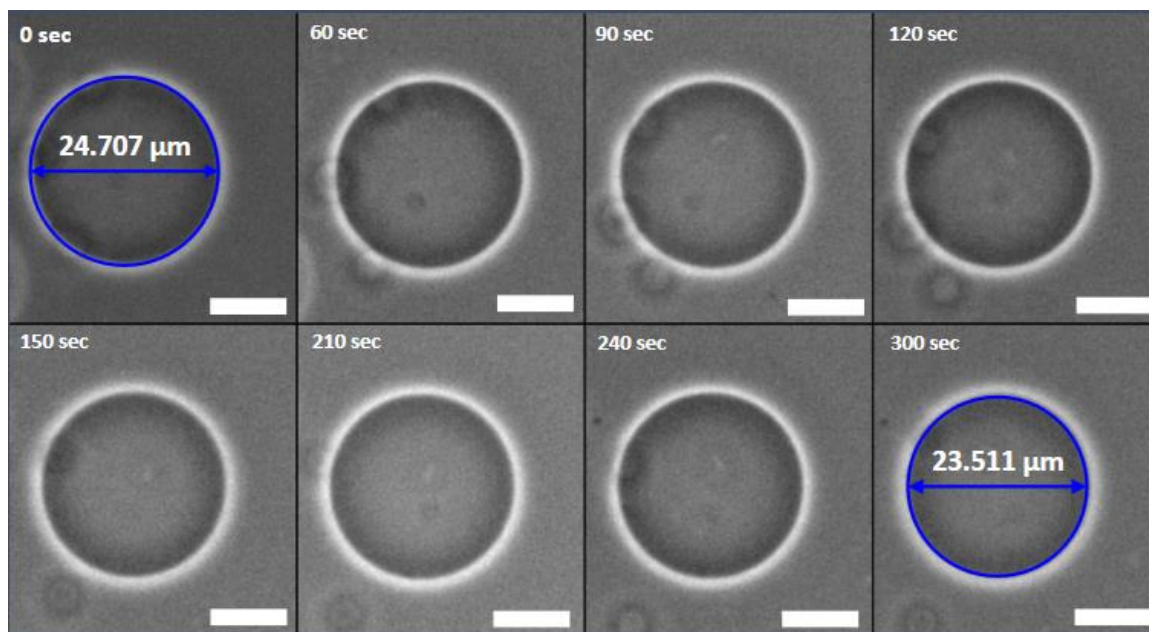


Figure 103. Variation of DOPC vesicles diameter with time upon osmotic shock (glucose, $\Delta C=100\text{mM}$). Scale bar= $10\ \mu\text{m}$.

The vesicle deflated equally in all directions (isotropic deflation) upon addition of glucose with $\Delta C=100\ \text{mM}$. The decrease in diameter while maintaining a spherical shape is possible thanks to the fluid nature of the DOPC membrane which is in the liquid disordered phase at room temperature. Additionally, due to the elastic nature of the membrane, the deformation is reversible. In order to verify the reversibility, a consecutive deflation/inflation experiment was performed. After the addition of glucose and reaching state of equilibrium, the upper compartment was emptied and filled with water instead of glucose. This caused a decrease in the total glucose concentration, and thus osmotic shock of $\Delta C=C_f-C_0=-100\ \text{mM}$ where C_0 is the glucose concentration before the shocks and C_f is the final glucose concentration (figure 104).

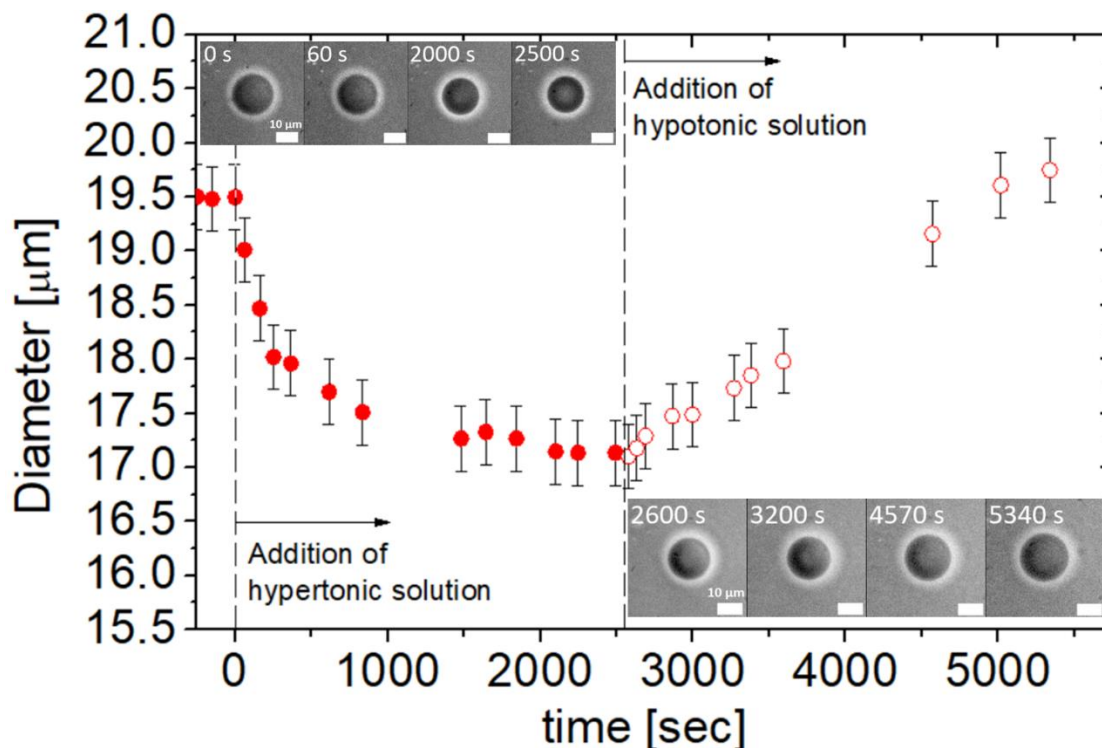


Figure 104. Vesicle diameter as a function of time, due to the addition of hypertonic solution (filled circles, 0-2500 sec) followed by addition of hypotonic solution (hollow circles, 2500-5500 sec). A reversible and isotropic (in plane) deformation is observed while maintaining membrane integrity (corresponding insets).

In fact, this type of deformation implies a reduction of the vesicle surface area, $\Delta S = 4\pi(r_1^2 - r_2^2)$ where r_1 and r_2 are the radii before and after the osmotic shock. This change in surface can be compensated either by a more compact packing of the lipids in the membrane (Kummrow and Helfrich 1996) or by the formation of tubes (Quemeneur 2010) or daughter vesicles connected to the original vesicle. (Bernard, et al. 2002, Boroske, et al. 1981)

In our case, no visible tubes or daughter vesicles were found upon glucose shocks of bare vesicles. While possibly existing, these type of membrane deformations are below the resolution of the microscope in this setup. Whatever the mechanism of size reduction, the deformation was isotropic, which enabled the determination of permeability values as will be shown in chapter 5.4.

6.3.2.2. NaCl and CaCl₂ shocks

Mono and divalent ions such as sodium and calcium are important ionic species that play a key role in many internal and external cellular processes such as energy and charge transfer, osmotic pressure regulation and modulation the mechanical properties of the cell wall.(Hepler and Winship 2010) Since the lipid membrane has very poor permeability to these ions, as discussed in chapter 1.2.4, they are transported in vivo across the plasma membrane via trans membranal proteins that facilitate their passage. In our system, ions are typically used to promote adsorption of components by screening of electrostatic interactions and bridging, according to the theoretical considerations discussed in chapter 4.1. It is therefore important to evaluate the response of our biomimetic capsules to addition of these types of salts.

Hence, we will explore the behavior of bare and decorated vesicles in response to salt shocks, beginning with the bare vesicles, as a reference. Upon addition of NaCl, vesicles exhibit osmotic shock, where the concentration difference is two times the electrolyte concentration in the case of NaCl, since both Na⁺ and Cl⁻ ionic species contribute to the osmotic pressure. An isotropic deflation was observed, similarly to the case of glucose shock, and permeability values calculated show a slight increase in membrane permeability. This is not surprising, since charged ions are known to interact readily with the lipid polar head and enhance membrane tension as well as membrane porosity, promoting the transport of water through the membrane or even invagination.(Contini, et al. 2018, Montis, et al. 2014, Wang, et al. 2008)

Upon calcium shock, ($\Delta C=5$ mM) bare vesicles exhibit a dramatic change in their size and morphology. Figure 105 shows time evolution of bare DOPC vesicles upon exposure to CaCl₂ shock.

Approximately one minute after addition of CaCl₂ solution in the upper compartment of the cell, an apparent decrease in diameter was observed and small micron size vesicles started to appear in the interior of the GUVs (Figure 105a and b).

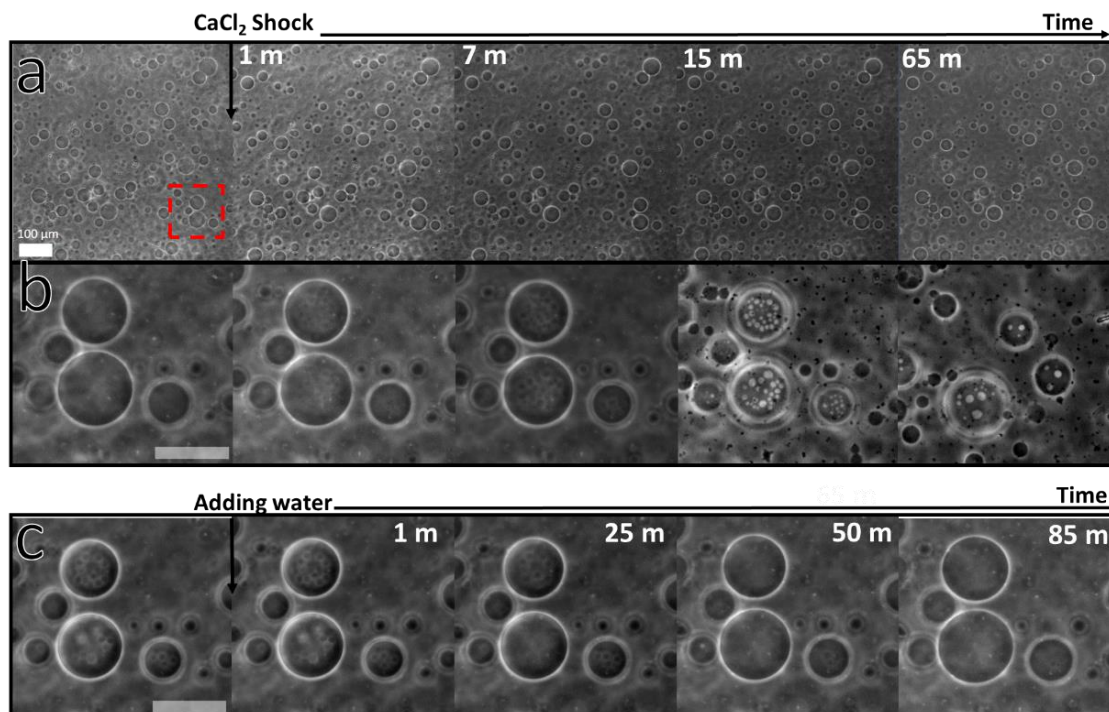


Figure 105. DOPC GUVs upon calcium shock. $\Delta C=5$ mM. (a) time evolution following the addition of CaCl_2 , scale bar= $100\ \mu\text{m}$. (B) a closeup on the square area framed in red dashed line (c) reverse shock by addition of water $\Delta C=-100$ mM. The scale bar for (b) and (c) is $20\ \mu\text{m}$.

The appearance of daughter vesicles was visualized using under focus conditions, because the focal plane of the daughter vesicles is not similar to the focal plane of the mother GUV. Formation of daughter vesicles was previously observed for egg-PC vesicles upon osmotic shock of NaCl (Boroske, et al. 1981) as well as glucose (Bernard, et al. 2002) Since the cohesion energy of lipid molecules is lower than the bending energy, the lipid membrane is able to detach a daughter vesicle while maintaining the favorable spherical shape. In order to examine the reversibility of the daughter vesicle formation, hypotonic solution was consecutively added to the upper compartment, similarly to the procedure described earlier for the glucose shocks.

Figure 105c shows a series of images taken after addition of water into the upper compartment of the cell (hypotonic solution). Two phenomena were observed: (i) the daughter vesicles disappeared and (ii) the mother vesicle diameter increased. This shows that upon exposure to hypotonic solution, daughter vesicles can fuse back into the GUV membrane in order to compensate the new imposed difference in chemical potential, or in other words, the process is reversible. It also implies that the material

conserved within the mother vesicle volume, is available to be secreted back to the outer membrane by fusion, similarly to the first steps of exocytosis in living organisms.

The response of bare GUVs to osmotic shocks is interesting from the fundamental point of view and serve as a point of reference for the examination of decorated vesicles, which will be discussed in the following section.

5.3.3. GUV-(CNC)

Following the decoration process, the capsules were subjected to similar osmotic shocks as the bare GUVs. Upon addition of high glucose concentration in the upper compartment of the observation cell, a shape transformation from a convex spherical shape to concave complex shape takes place. Anisotropic (out of plane) deflation of the vesicles was observed within several minutes (Figure 106a).

The images were taken simultaneously in phase contrast and fluorescent mode in order to observe the morphology of the CNC layer. Several deformation points were observed, with number of depressions between 2 and 8.

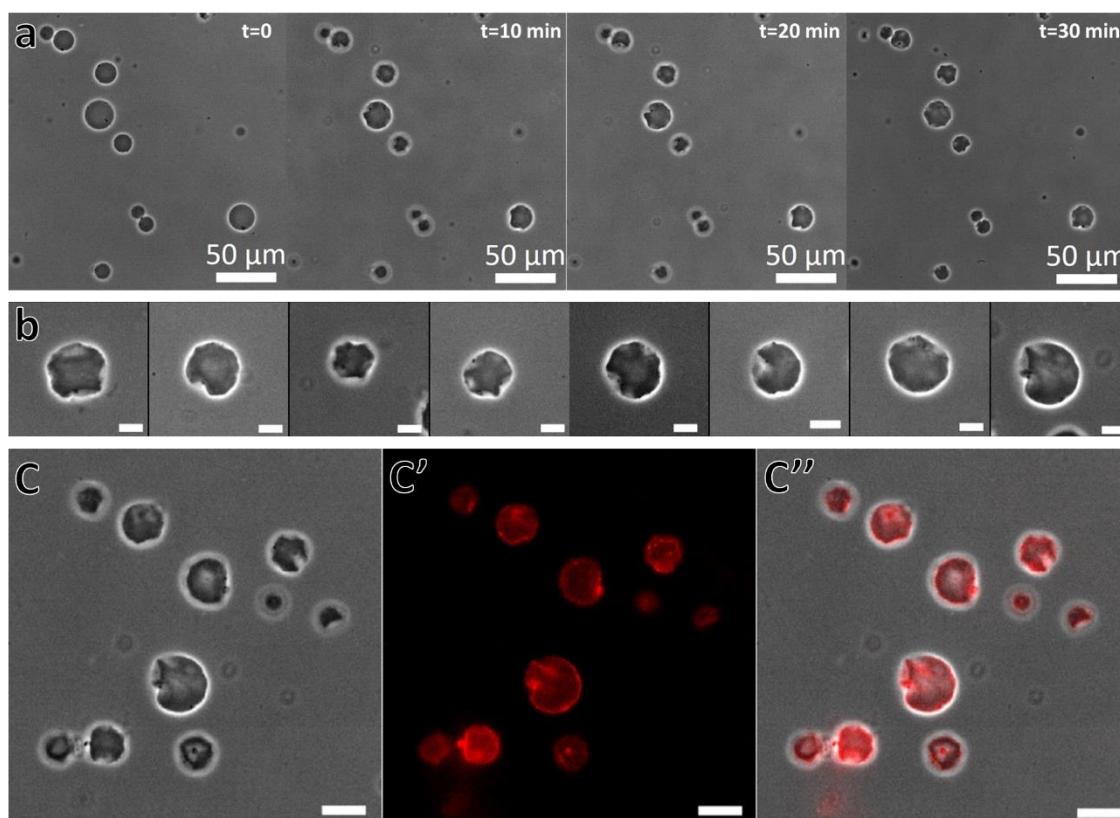


Figure 106. GUV-CNC under osmotic shock glucose $\Delta C = -200$ mM: (a) time evolution during the first 30 minutes following the osmotic shock (b) various deformed shapes obtained during the osmotic shock (c,c',c'') the final state of the vesicles (phase contrast c, fluorescence c', and overlay c''). The scale bars are 50, 10 and 20 μm for a, b and c respectively.

Following the addition of glucose, the capsules reached a stable state where no further deformation was observed. Figure 106b shows several individual deflated vesicles after reaching equilibrium and figure 106c' and 106c'' shows a larger view of the sample taken in phase contrast and fluorescent modes respectively. Figure 106c'' shows an overlay of the phase contrast and fluorescent channels. In the majority of the cases, the integrity of the lipid membrane was maintained, as evident from the contrast difference between the interior and exterior of the vesicles.

This behavior differs from the one of bare vesicles in the liquid disordered phase and reminiscent of the behavior of gel phase vesicles made from 1,2-ditetradecanoyl-*sn*-glycero-3-phosphocholine (DMPC) vesicles under osmotic shocks. Figure 107 shows a time sequence of DMPC GUV in the gel phase under osmotic shock. (Quemeneur 2010, Quemeneur, et al. 2012)

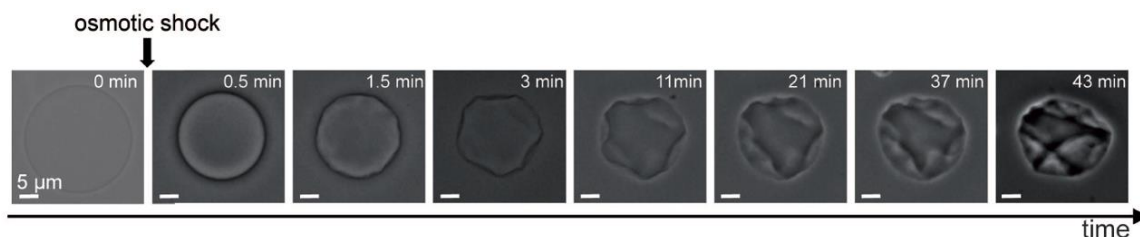


Figure 107. Time sequence of a DMPC GUV at 15°C under osmotic shock, $C = \Delta 200$ mM (Quemeneur 2010)

In the same work, Quemeneur et al. generated numerical surface simulations and were able to predict most of the equilibrium shapes of the gel phase vesicles by minimizing the elastic energy of the surface upon the reduction in surface area. (Quemeneur, et al. 2012)

In our case, introducing an additional rigid layer of anisotropic particles such as CNCs on the lipid membrane, may cause rigidification of lipid membrane similar to the case of gel phase lipids. This could explain the reduced visible membrane fluctuations, and 'out of plane' deformation.

In order to investigate the reversibility of the deformation, the same sample was subjected to an additional osmotic shock, this time by addition of water (hypotonic solution). Figure 108 shows a series of images taken following the addition of water ($\Delta C = +100$ mM).

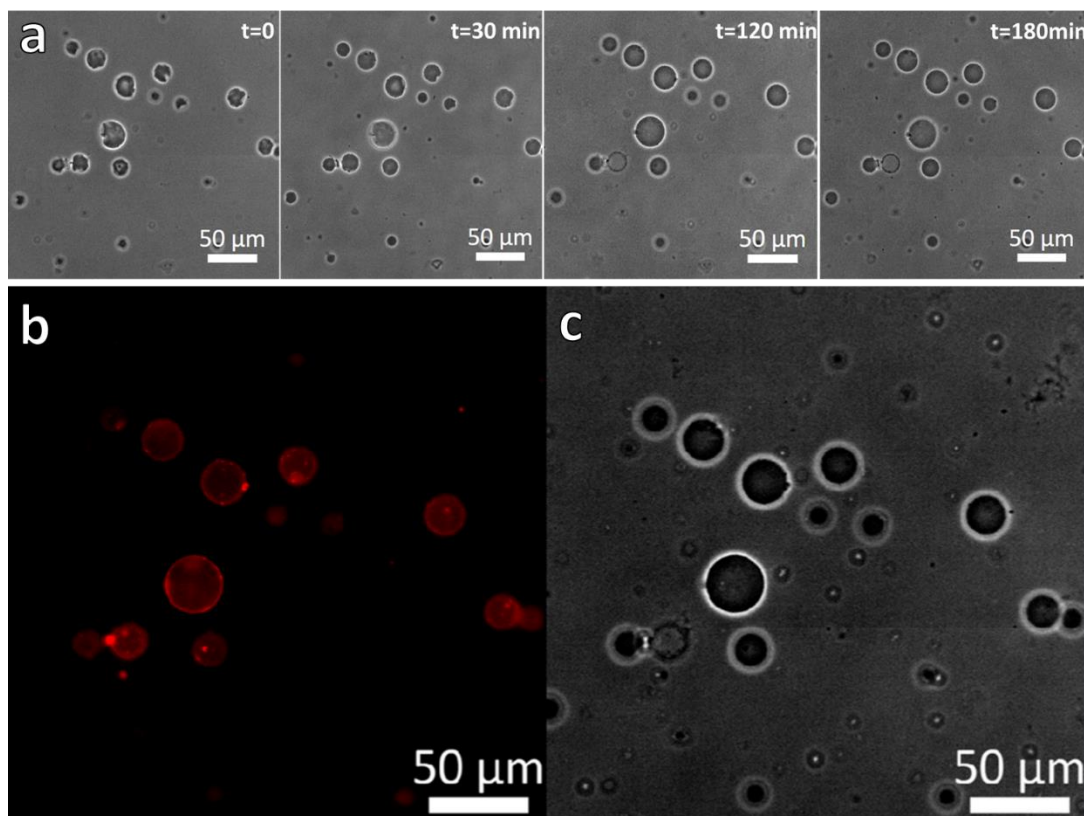


Figure 108. (a) GUV-CNC subjected to a glucose osmotic shock ($\Delta C = 100$ mM). (b) and (c) shows the final state, 180 minutes after shock, for the red channel and phase contrast respectively.

Upon addition of water, the deformed vesicles inflated back until retrieving the original spherical shape within 180 minutes. The inflation process was slower than the deflation, perhaps due to a more compact organization of the nano particles on the shell and reduced water permeability.

The observed deformation of GUV-CNC under osmotic shock resembled the one of bare vesicles in the gel phase as demonstrated in figure 107. Indeed, the adsorption of nanoparticles on the lipid membrane reduces the mobility of lipids that are attached to the adsorbed particles, in addition to the formation a rigid shell, resulting in the decrease of membrane fluidity.

As long as membrane integrity is maintained, the sucrose solution is entrapped within the vesicle and contributes to the contrast difference resulting in a darker interior. However, when the membrane tension exceeds a critical value, the lipid membrane ruptures, releasing the sucrose and resulting in hollow shell as shown by the similar color inside and outside of the capsule. In the case of decorated vesicles, the shell was thick enough to be clearly observed in optical microscopy, while bare vesicles were invisible following rupture, since the lipid membrane is only 4-5 nm thick. We now move forward to investigate the addition of the second building block, XG, as an additional layer.

5.3.4. GUV-(CNC/XG)_{1.5}

In the previous part we have explored the behavior, under osmotic shock, of bare vesicles and vesicles with a single CNC layer. We shall now explore the behavior of multilayer films composed of CNCs and XG when subjected to similar shocks. Figure 109 shows osmotic shock experiments performed on GUVs decorated with a CNC-XG-CNC shell ($n=1.5$). Upon osmotic shock $\Delta C=200$ mM, the vesicles deflate unisotropically with several depressions similar to what was observed for the GUV-CNC case. Most of the vesicles preserved the membrane integrity as shown by the contrast difference between the interior and the exterior of the vesicle.

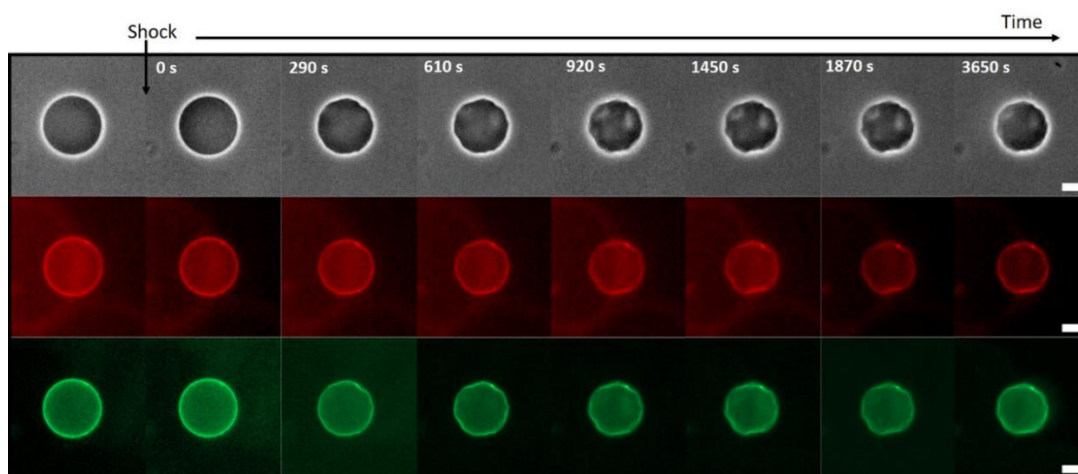


Figure 109. Osmotic shock ($\Delta C=200$ mM) of GUV decorated with a CNC-XG CNC layer ($n=1.5$). scale bar= $10 \mu\text{m}$. Upper, middle and bottom rows correspond to phase contrast, red and green channels respectively.

The onset of visible deformation occurs after several minutes, a bit longer than for the bare vesicles and similar to the vesicle-CNC system.

The reversibility of the process was investigated by adding hypotonic solution. Figure 110 shows a decorated vesicle after deflation, upon addition of water into the upper compartment of the cell.

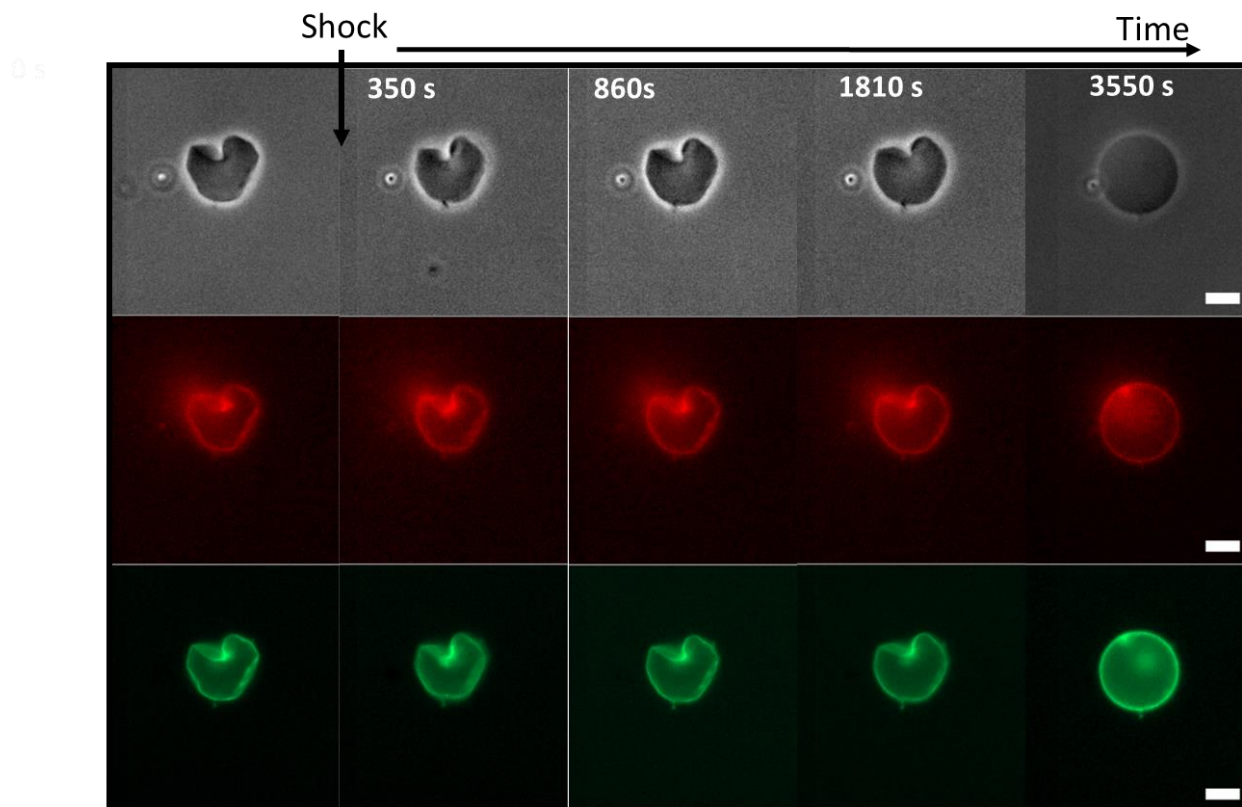


Figure 110. Reversible deformation of GUV-CNC-XG-CNC ($n=1.5$) upon osmotic shock in water. $\Delta C=200$ mM, scale bar= $5 \mu\text{m}$. Upper, middle and bottom rows correspond to phase contrast, red and green channels respectively.

As can be seen from figure 110, the deformation is reversible. However larger number of vesicles explode during the deflation/inflation cycles, leaving only the hollow shell. As shown in the previous sections, the interaction between the CNCs and XG promote the formation of crosslinks between CNC layers, making the shell more resistant to shock, similarly to what is observed for electrostatically driven multilayers.(Quemeneur 2010)

5.3.5. GUV-(CNC/)_{5.5} and GUV (CNC/XG)_{10.5}

Figure 111 shows a time series following osmotic shock performed on GUVs decorated with 5.5 layers. Typically, fewer depressions are observed for this type of systems, in agreement with the fact that the shell is thicker and thus more resistant to similar osmotic pressure difference.

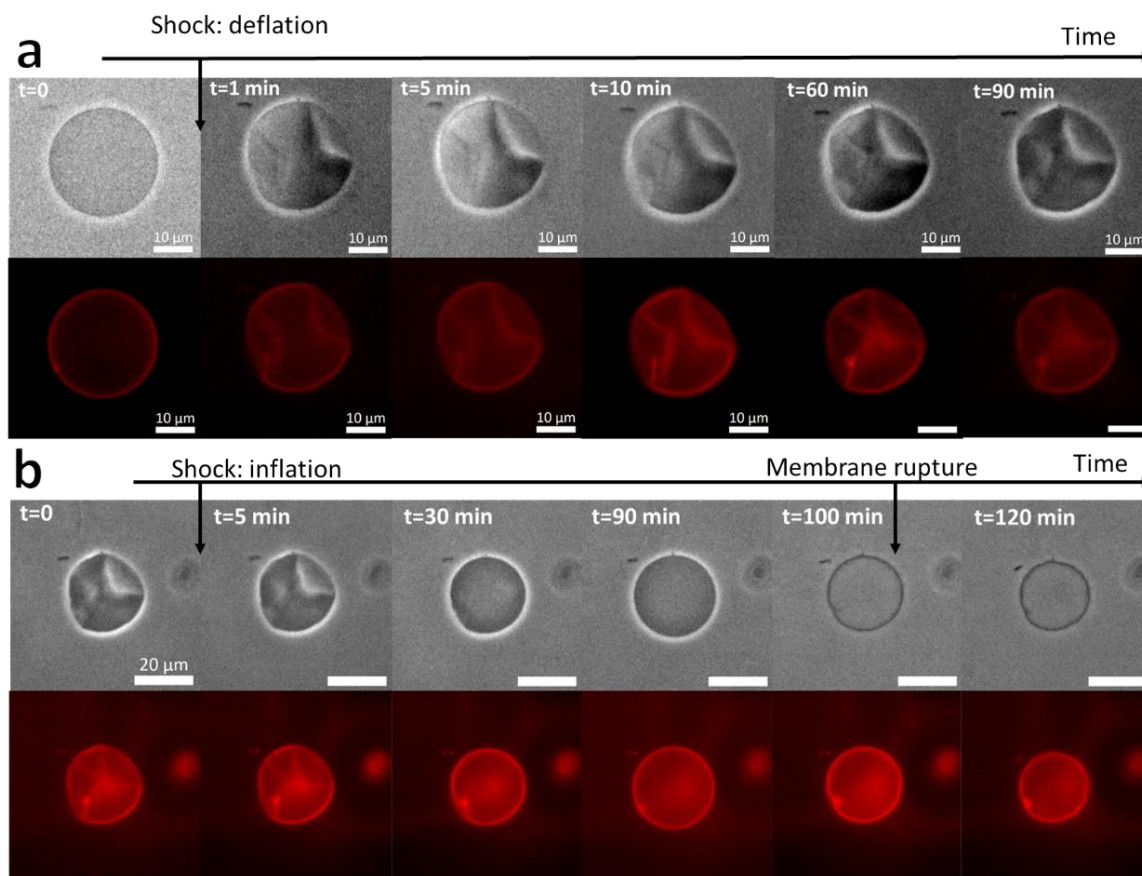


Figure 111. GUV (CNC/XG)_{5.5} under osmotic shock ($\Delta C = 200$ mM) (a) deflation, scale bar $10 \mu\text{m}$ (b) inflation, scale bar $20 \mu\text{m}$.

The behavior was also reversible, (figure 111b) and in some cases the lipid membrane collapse, leaving a hollow shell (figure 111b, after 100 min). However, due to resolution limitations, it was not possible to determine whether the lipid membrane stays attached to the shell or completely collapse.

In the case of 10.5 bilayers, anisotropic deformation was not observed upon glucose osmotic shock up to $\Delta C = 500$ mM. The vesicles deflate slightly and resist buckling in contrast to the vesicles with small number of layers.

5.3.6. 3D reconstructions of decorated vesicles

The apotome (SIM) mode enables a 3D reconstruction by scanning the sample in the z direction, perpendicular to the focal plane. Reminiscent of confocal microscopy, the advantage of this technique over conventional fluorescence is that it facilitates the examination of shells shapes by avoiding the excess fluorescence from the whole sample. Figure 112 a shows an apotome image of several vesicles in the x-y plane, while figure 110 b, c, and d show an example of a z-scan performed on a single vesicle. The colors in b, c and d correspond to the different planes.

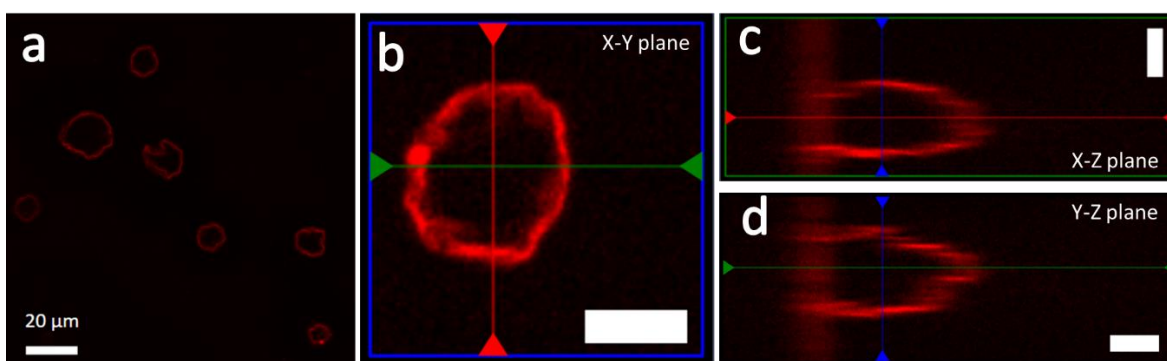


Figure 112. Apotome images of decorated vesicles (CNC/XG $n=5.5$). (a) a cross section of few vesicles after deflation upon osmotic shocks. Z-scan of a single vesicle: (b) x-y plane (c) x-z plane and (d) y-z plane. Scale bar is 20 μm .

Figure 113 shows the three planes of observation following 3D reconstruction. The plane colors correspond to the ones in figure 112 (i.e. blue, red and green for the XY, YZ and XZ planes respectively).

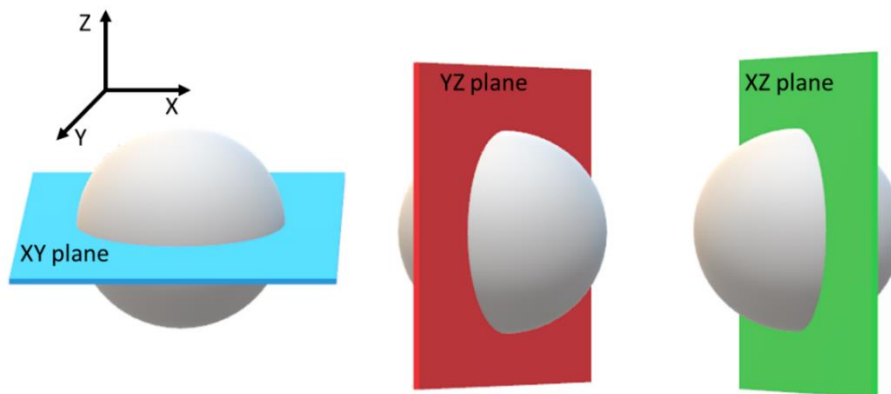


Figure 113. The three planes of observation following 3D reconstruction.

The 3D reconstruction revealed that the shells were indeed self-supported 3D objects. Furthermore, a complete 3D projection was performed on a single deflated vesicle after an osmotic shock (Figure 114).

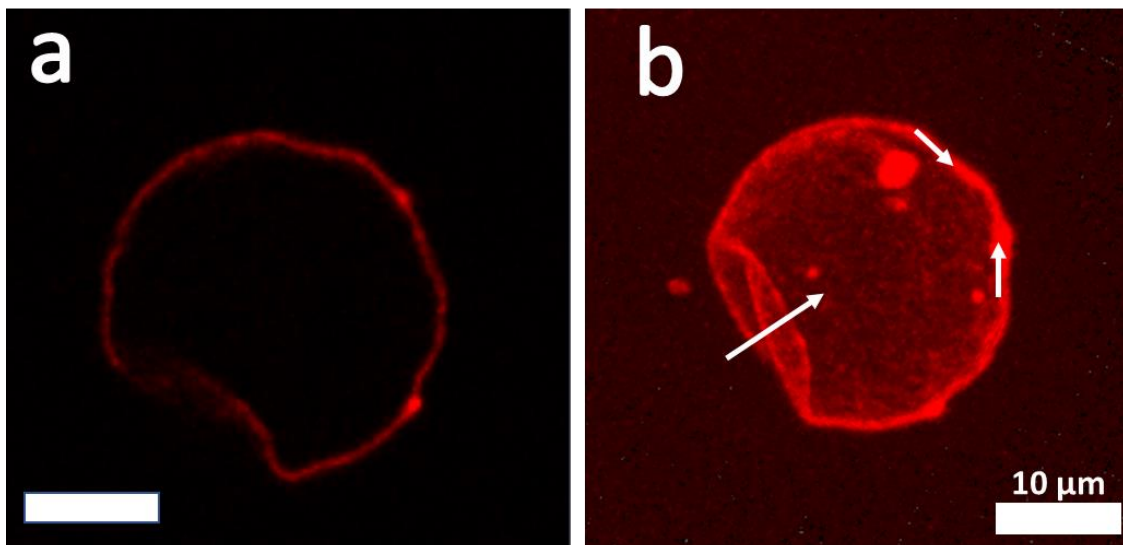


Figure 114. Apotome images of a single vesicle after osmotic shock (CNC/XG $n=5.5$). (a) x-y plane (b) full 3D reconstruction. The white arrows show the direction of main deformation of the initially spherical vesicle. Scale bar is 10 μm .

The 3D reconstruction further emphasize that the decorated vesicles behaves as elastic shells which deforms above a critical osmotic pressure difference. It is also evident from the images that the deformation is not restricted to a single point (white arrows). A schematic showing the transition from in-plane to out-of-plane deformation is shown in figure 115.

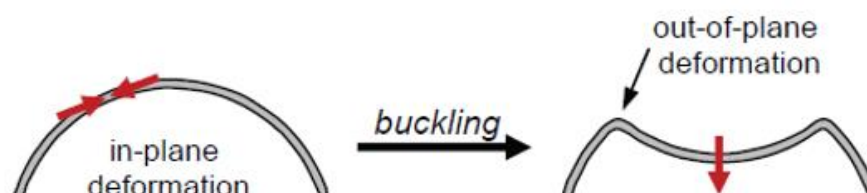


Figure 115. A scheme showing the deformation of thin elastic shells upon osmotic shock.

The critical pressure for buckling transition (P_c) can be calculated from the minimal glucose concentration required to induce such buckling, through eq. 1. The critical pressure for buckling transition increased with the number of layers. The onset for buckling was observed at concentrations of 100, 175 and 200 mM for $n=0.5, 1.5$ and 5.5 respectively. Table 24 summarizes the results obtained from this experiment.

Table 24. Critical buckling pressure (P_c) values of decorated capsules from the osmotic pressure experiments. ^a estimated from AFM experiments (chapter 5.1.2).

Number of layers	Thickness δ , [nm] ^a	P_c [kPa]
0.5	20	247.7
1.5	40	432.6
5.5	120	495.5
10.5	340	>2500

We made an attempt to extract the elastic modulus of the capsules from the critical buckling pressure, according to Gao et al. (Gao, et al. 2001) In their model, the Young's modulus of a hollow capsule can be derived from the critical concentration for buckling transition from convex (spherical) to concave (deformed) shape. When such transition happens, the work performed by the external pressure is equal to the elastic energy of the shell, with a given thickness, δ and radius R .

$$(Eq. 37) \quad P_c = \frac{2E}{\sqrt{3(1-\sigma^2)}} \left(\frac{\delta}{R}\right)^2$$

Where P_c is the critical buckling pressure, E is the Young's modulus and σ is the Poisson's ratio, assumed as $\sigma=0.5$. This equation holds under the following conditions: (i) the capsules deform without stretching (ii) the material is homogeneous and isotropic. Practically, since the modulus scales with the square of the vesicle's radius, this analysis is highly dependent on the size of the objects, and differences of up to order of magnitude were observed within the same experiment. In addition, the conditions under which the equations hold were not completely fulfilled in our case since the material is not homogeneous nor isotropic and did not reach equilibrium within the

time scale of the experiment. We therefore could not conclude on the elastic modulus of the vesicles using this analysis, reflecting the need of a more direct measurement in order to access the mechanical properties of the objects.

5.3.7. Decorated vesicles under CaCl_2 shocks

Unlike bare vesicles, exposure of decorated vesicles to mild calcium shocks does not result in the formation of visible daughter vesicles, but to aggregation of the objects. The aggregation was found to be related to the surface coverage of vesicles on the microscope slide. In the case of high initial surface coverage (Figure 116a) vesicles can coalesce to a tissue like structure. Figure 116 shows the formation of tissue like structure upon calcium shock $\Delta C=5$ mM for high (a,b) and low (c) initial surface coverage.

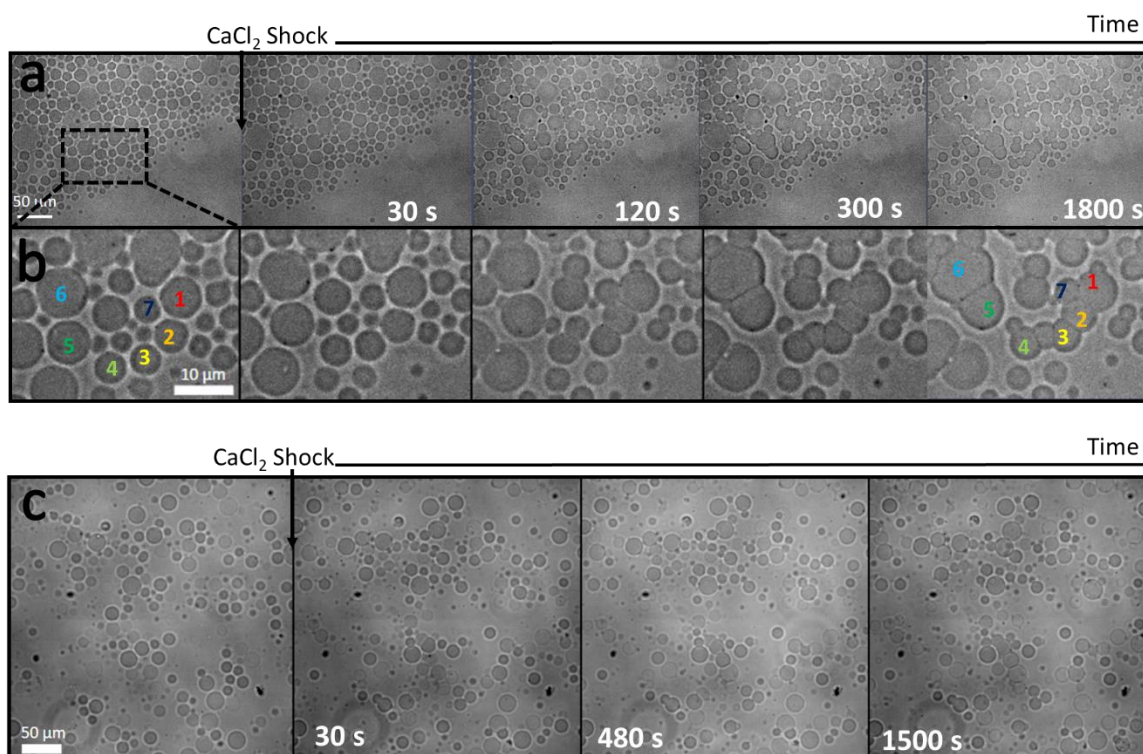


Figure 116. A phase contrast images showing the evolution of GUV(CNC/Pectin)_{5.5} during calcium osmotic shock. In high initial coverage (a and b) and low initial coverage (c). the numbers in (b) demonstrate the cluster formation by following individual vesicles.

Interestingly, although subjected to relatively high CaCl_2 concentration, which potentially increase dramatically the permeability, the aggregated vesicles can contain the encapsulated liquid up to several hours pointing out the integrity of the lipid membrane. Eventually, when water finally leaks out, the shells maintain the tissue like morphology. Figure 117 shows the morphology of aggregated vesicles, right after formation (a,b) and after 24 hours (c,d).

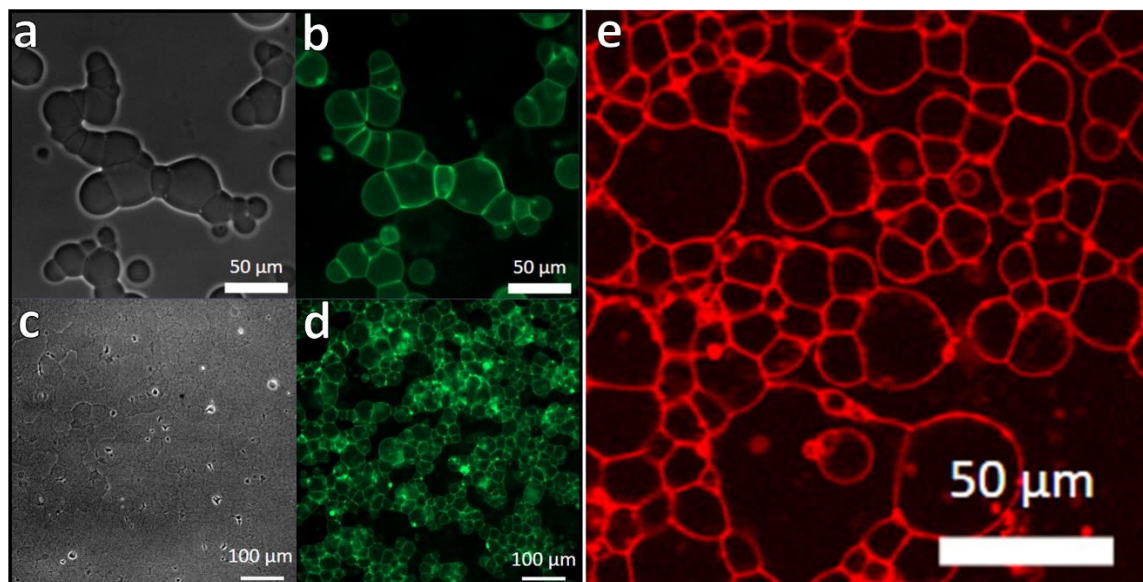


Figure 117. Optical fluorescence microscopy image of aggregated decorated vesicles right after aggregation (a and b) and (c,d) after 24 hours. Membrane rupture results in the loss of water leaving hollow shells. Green fluorescent labeling is from XG-FITC (e) Apotome image of aggregated vesicles after 24 hours. Red fluorescent labeling is from CNC-RhodB.

The aggregated vesicles created a tissue like structure after several hours. This structure could emerge from crosslinking of the shell of two or more vesicles in proximity. Considering outer layer of CNCs, the presence of oppositely charged divalent ions could result in bridging of adjacent shells.

5.4. Permeability analysis

As shown in the introduction chapter 1.2.4, lipid membranes are semipermeable. This property may be used in order to probe the influence of various parameters on the behavior of the vesicles. In the case of isotropic deformation, as shown earlier for bare

vesicles, the permeability P can be calculated from osmotic shock experiments (Boroske, et al. 1981)

$$(Eq. 38) \quad J = -P \Delta c$$

Where J is the molar flux and Δc is the difference of molar concentration between the interior and the exterior of the vesicle. For a spherical vesicle with radius R we can write:

$$(Eq. 39) \quad \frac{dR}{dt} = -\alpha P \Delta c$$

α being the molar volume of water ($18 \cdot 10^{-6} \text{ m}^3 \text{ mol}^{-1}$). Equation 39 describes a linear decrease of R with time. The radius of the vesicle can be determined with phase contrast microscopy following the addition of a solution with higher or lower osmolarity. The permeability can be calculated from the following relationship:

$$(Eq. 40) \quad \frac{R}{R_0} = 1 - \frac{\alpha P \Delta c}{R_0} t$$

Figure 118 shows a plot of R/R_0 as a function of the t/R_0 for several vesicles with different initial diameters, upon glucose osmotic shock ($\Delta C=100 \text{ mM}$).

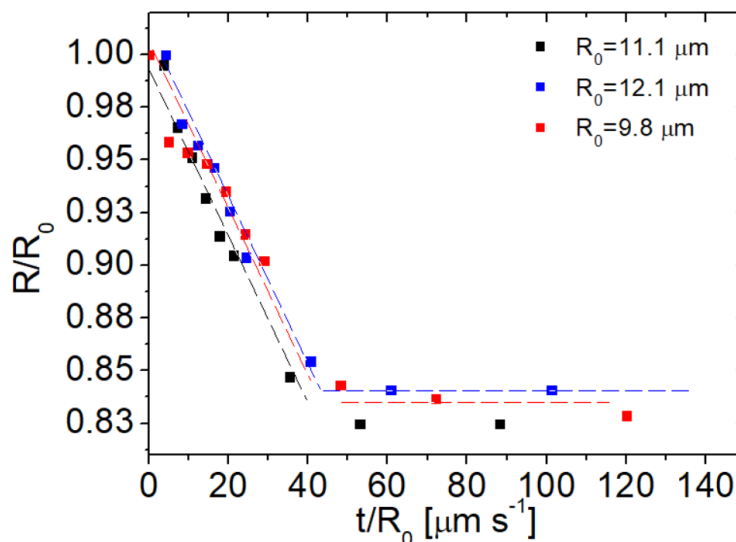


Figure 118. Shrinkage of bare GUVs with different initial radii, $R_0 = 11.1 \mu\text{m}$, black squares; $R_0 = 12.1 \mu\text{m}$, blue squares; $R_0 = 9.8 \mu\text{m}$. The vesicles were submitted to glucose osmotic shock ($\Delta C=100 \text{ mM}$).

The average permeability was $2.26 \pm 0.39 \mu\text{m s}^{-1}$ for pure DOPC vesicles. This value is lower than the value found by Boroske ($17\text{-}47 \mu\text{m s}^{-1}$) and resembles the values found by Quemeneur and Radavidson, ($\sim 1 \mu\text{m s}^{-1}$).

Effect of sterols

The presence of sterols in the lipid membrane makes it more rigid and less permeable. (Bittman and Blau 1972, Mathai, et al. 2008) This effect was investigated by subjecting vesicles with varying amounts of sitosterol to similar osmotic shocks. The results are shown in figure 119.

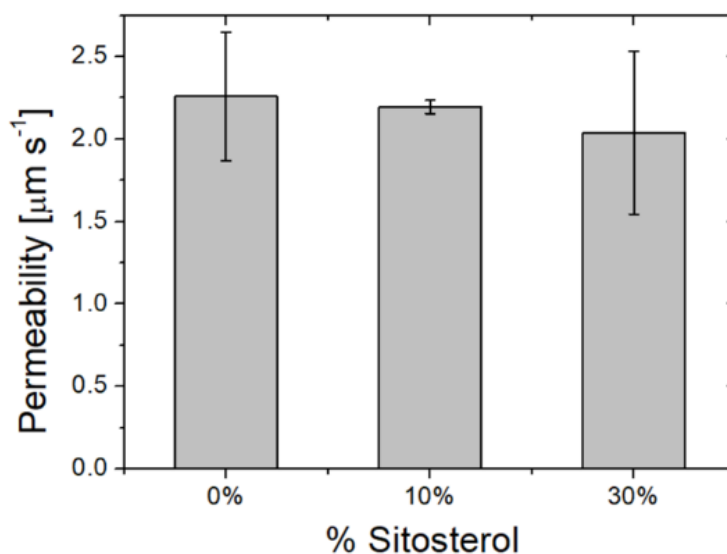


Figure 119. Permeability as a function of Sitosterol content.

Indeed, the measured permeability decreased from 2.26 to $2.09 \mu\text{m s}^{-1}$, however the values vary significantly from one vesicle to the other which make it difficult to conclude on the role of sterol in membrane permeability using this method.

Nonetheless, the amount of sterol did not seem to play a significant role, at least in short time scales, on the adsorption of the first CNC layer nor on the integrity and stability of the bare vesicles. We typically used 30% sitosterol in the membrane, since the presence of sterols reduce membrane fluctuations and may reduce CNC desorption. In addition, plant membranes contain up to 50% sterols, making it an essential component of biomimetic membranes.

5.5. Conclusions

In this part we have investigated the response of decorated vesicles to osmotic shocks. Clear differences in the morphology of the objects upon shock were observed between bare and decorated vesicles and between different types of shocks. Figure 120 summarizes the main observations from this part:

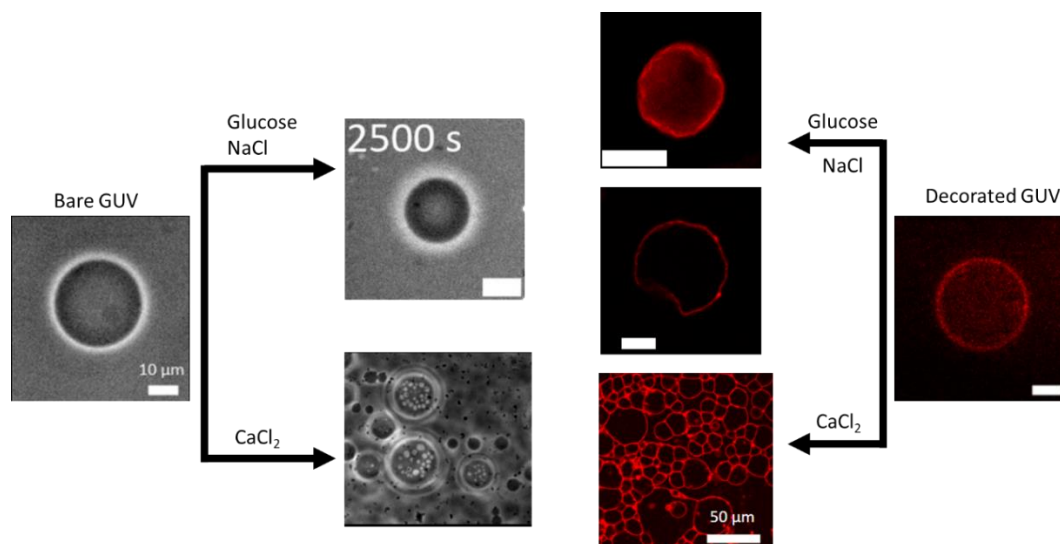


Figure 120- A summary of vesicles response to osmotic shocks

- The deformation of bare lipid vesicles was isotropic with permeability values of about $2.3 \mu\text{m}/\text{sec}$.
- The addition of sitosterol into the membrane effected slightly the permeability values, the deformation was isotropic and reversible.
- Vesicles decorated with up to 5.5 layers deformed anisotropically with several depressions (buckling) and the deformation was reversible.
- The critical pressure for buckling increased with the number of layers, while vesicles with 10.5 layers resisted to glucose shock.
- Upon exposure to CaCl_2 or NaCl shocks, bare vesicles formed daughter vesicles, while decorated vesicles aggregated and form a tissue like structures.
- Based on inflation/deflation experiments, it was found out the shells retain their original form, suggesting elastic deformation.

In the following part we will examine the mechanical properties of our biomimetic constructs using AFM indentation experiments.

Chapter 6

Mechanical properties of biomimetic constructs

AFM was used to determine quantitatively the Young's (indentation) modulus, of the 2D and 3D biomimetic constructs. The experiments were carried out by Dr. Simone Bovio at the RDP lab at ENS Lyon (directed by Prof. Arezky Boudaoud), and by Dr. Franck Dahlem from SPG team in CERMAV, UGA. The measurements were performed in two operational modes: (i) indentation with a colloidal probe and (ii) peak force mode. Figure 121a shows the cantilever used for the indentation measurements with a borosilicate bead ($R=2.5\ \mu\text{m}$) attached at its edge.

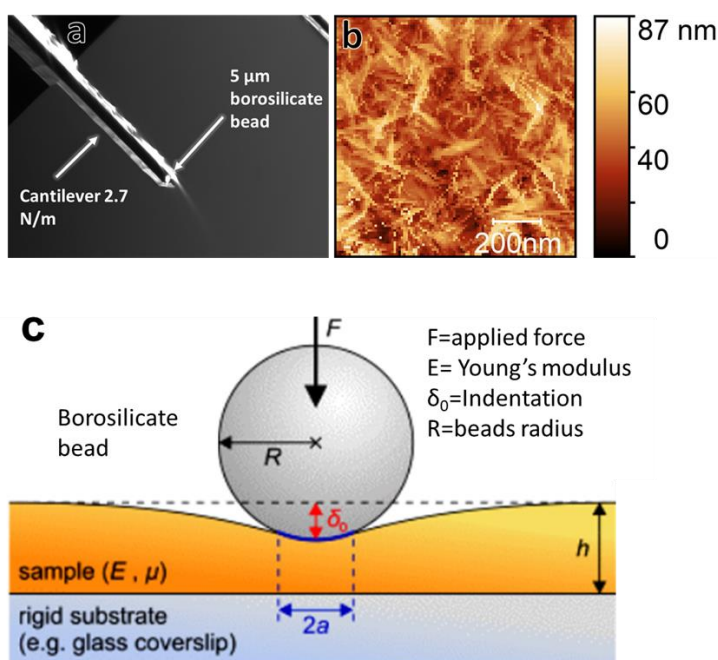


Figure 121. AFM experimental setup: (a) Cantilever with a colloidal probe used for indentation experiments, (b) topography image of the probed surface (CNC/XG, 15.5 layers), (c) a scheme of the probe and substrate in an indentation experiment (not to scale).

Figure 121b shows a typical topography image of the probed surface (CNC/XG, 15.5 layers), taken with MLCT tip in contact mode. The CNC layer deposited on the polymers (either PEI or XG) showing isotopically scattered CNC particles, with some larger aggregates. Figure 121c shows a scheme of the indentation experiment with a spherical probe. Let us discuss some important aspects of the AFM indentation method.

General considerations

- A good sample adhesion is required in order to extract reliable data.
- The sample should be thick enough to avoid contributions from the substrate to the overall measured properties.
- The material under study is considered homogeneous and isotropic.

Given that these conditions are fulfilled, a model (Hertz or Sneddon for sphere or cone shape tip, respectively) may be fitted to the approach retract curves obtained from tip sample interaction.

Influence of the medium on tip sample interaction

In order to evaluate the mechanical properties of the sample, the contribution of the electrostatic interaction to the force curve needs to be reduced to the minimum. This can be done by changing the ionic strength of the medium.

In the case of ionic solution, the presence of salt can partially eliminate the positive shift in vertical deflection and thus affects the calculation of the contact point. Since the Hertz model was fitted only to the initial part of the curve, such shift in vertical deflection in the case of high ionic strength leads to an increase in the initial slope, resulting in higher Young's modulus.

This effect have been demonstrated by Cranston et al. who have shown the dependence of adhesion on the ionic strength in PEI/CNC nanocomposite films.(Cranston, et al. 2010) In their case the forces were attractive, therefore, with the decrease in ionic strength, these interactions become more pronounced. For the repulsive force in approach, it was shown that upon changing the charge of both tip and

surface, the shape of the force curve changed and a higher slope was observed with decrease in ionic strength.

Having discussing the experimental considerations and limitations, we shall now focus on the AFM experiments on the 3D and 2D systems.

6.1. Mechanical properties of 3D constructs

We tried to estimate the Young's modulus of the elastic shell covering the capsules by approaching with the AFM tip to the top of a single decorated vesicle. **We focused here only on the CNC/XG system** and the samples were prepared as described in section 5.2.1. Figure 122 shows the cantilever on top of a vesicle and a simulated force map from the scanning of the vesicles surface.

The vesicle was probed with MLCT C tip with a cantilever spring constant of 0.006 N/m and conical tip shape with a nominal diameter of 20 nm.

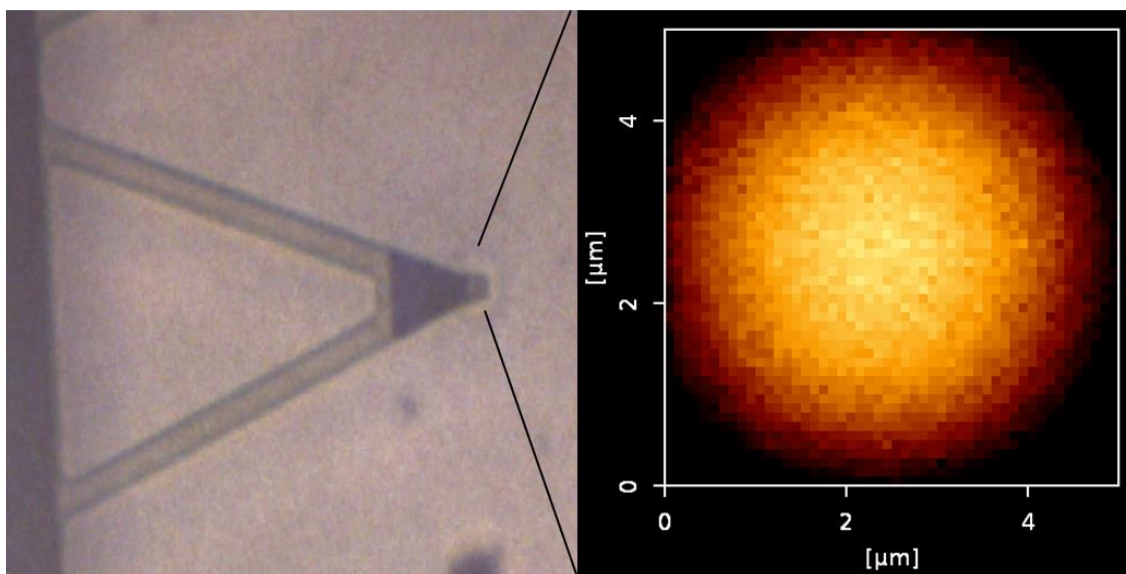


Figure 122. A microscope image of a cantilever on top of a vesicle and the resulting image obtained for a decorated vesicle using QI mode, with a spring constant of 0.006 N/m (calibrated) and MLCT tip.

Due to weak adhesion to the substrate, the majority of the vesicles displaced upon tip approach thus, it was not possible to engage on the vesicles surface. The movement

of the vesicles during the approach of the tip could originate from two main factors: (i) drag force of liquid surrounding the vesicle during tip approach and (ii) electrostatic repulsion between tip and sample, both cause a displacement of the vesicle upon contact.

We tried to address those points by enhancing the adhesion of the CNC covered capsules, first by placing them on surfaces covered with positively charged electrolyte (PEI) and then by using XG as a surface mediating layer. However, the vesicles were still not stable enough to enable reproducible measurements of Yong's modulus. We also tried to eliminate electrostatic repulsion by using high ionic strength solution, but this did not reduce the movement of the vesicles upon approach and in addition caused large number of vesicles to explode due to osmotic shock, making them invisible to the optical system.

We have tried to extract force curves from few vesicles however, the behavior was significantly different from vesicle to vesicle, the curve general shape was different each time and thus, not reproducible.

To conclude on the experiments on decorated vesicles, the mechanical properties of the 3D constructs could not be evaluated from AFM experiments due to lack of sample-surface adhesion. Nonetheless, this technique rests interesting given that the adhesion issue is addressed. Several additional topics should be mentioned:

- The shell thickness can be estimated from nano shaving of corresponding 2D samples, assuming similar film structure.
- Contributions from turgor pressure may be neglected given very small indentations, up to 10% of the total film thickness.
- As the tip could deform both the shell and the entire vesicle, both local and global deformation modes should be taken into account when interpreting the data.
- The curvature of the vesicles should be also taken into account. Measuring only on the very top of the surface where the tip is perpendicular to the surface, can decrease error in the value of mechanical properties.

In the following section we will focus on evaluating the mechanical properties of the 2D constructs- the multilayer films.

6.2. Mechanical properties of 2D constructs

The samples were prepared as described in chapter 5.1. The force curves were obtained using 2 methods:

- (i) Indentation with spherical borosilicate ball with radius of 2.5 μm (figure 121a) and an analysis of the approach retract curves using Hertz model (Eq. 2, Ch.1.5).
- (ii) Using a conical tip with radius of 20 nm in peak-force mode to produce approach retract curves fitted with Sneddon model (Eq. 3, Ch. 1.5).

The advantage of the 2D system (multilayered films) over the 3D system (decorated GUVs) is the inherent adhesion to the substrate and the absence of curvature which could possibly affect the results.

Indentation experiment

Indentation experiments were typically done with spherical probe mounted on a cantilever. An analysis process was then systematically launched on each curve of a force map, yielding average values from about 20-50 measurements. Typically, three force maps were performed and analyzed for each sample.

The analysis included several steps: tip calibration, baseline subtraction, contact point determination and calculation of the vertical tip position axis (calculated as piezo displacement – cantilever deflection). The Hertz model was fitted to 2-50% of the curve and the indentation at 0.1 of the force (i.e. ~ 10 nN) was calculated. Since it was seen that only the thickest films are thick enough to be measured, we focused the analysis on the samples with 20.5 and 15.5.

Peak force mode

Elastic modulus values were calculated from the Sneddon model fit to the peak force curves at each point in the sample. A mechanical properties map is then generated over the whole sample area and a statistical averaging is performed using the Gwyddion software to yield average value of Young's modulus (see annex II for details).

Treatment of force curves

First, the cantilever spring constant was calibrated using a sapphire reference curve. This curve was used to measure the deflection sensitivity and also to verify the tip condition from time to time during the experiment. A thermal tune was then used to measure the cantilever spring constant. Figure 123a shows typical force curve of a CNC/XG sample with 20.5 layers in PBS at a set point of 100 nN. Figure 123b shows overlay of the force curves on sapphire (blue curve) and on the film (black curve).

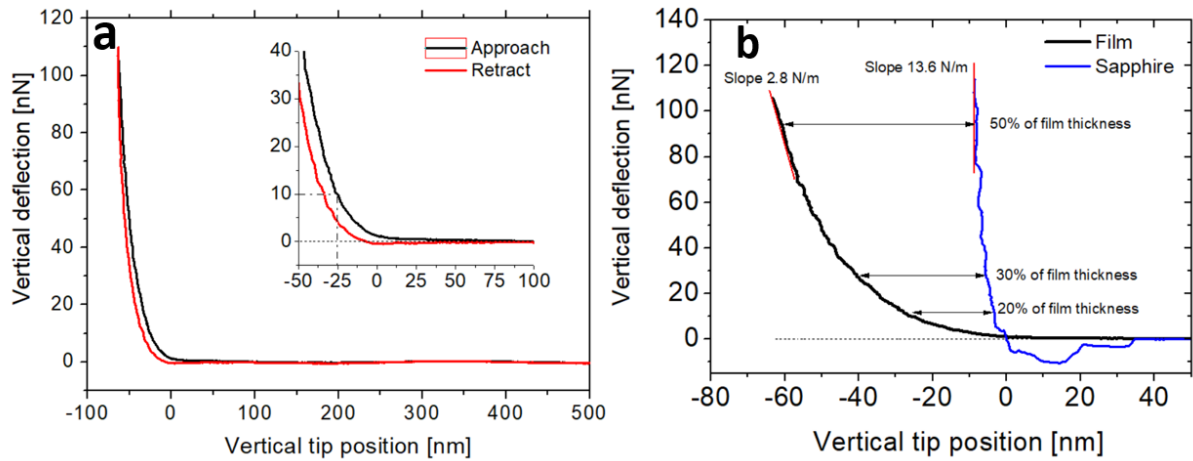


Figure 123: (a) Approach (black line) and retract (red line) force curves done on CNC/XG film with 20.5 layers in PBS and set point of 100 nN. the inset shows a magnification of the original plot in the range close to zero and the dashed line shows the indentation at 0.1 of the maximal force (i.e. 10 nN) (b) force curve of film (a) and the sapphire (blue) in the range close to the contact point. The slopes at 2% from the maximal force and the indentations corresponding to 50, 30 and 20% of the total film thickness (~ 120 nm in the case of CNC/XG with 20.5 layers).

In the case of the sapphire, during the approach, an attractive short-range attraction appears followed by a sharp increase in the deflection signal. The calculated slope in the final part of the curve (2% from the maximal deflection) is 13.3 N m^{-1} . The indentation at 0.1 of the force (about 10 nN) is 1-2 nm. The retract curve is characterized by a strong adhesion signal, characteristic of attractive VdW forces between the tip and the surface. In the case of the film, the deflection signal increased with tip approach, until reaching a maximal slope of 2.8 N m^{-1} . The indentation at 0.1 of the force is about 25 nm. The difference in the appearance of the force curve between

the sample and the sapphire reference can thus be attributed to the presence of the thin film and reflects tip-sample interaction.

Having verified the presence of thin film with different mechanical properties than bare substrate, and having established the tip calibration, we move to examine the influence of different parameters on the force curves and the obtained modulus of the films.

Effect of ionic strength and drying

In order to test the effect of ionic strength on the mechanical properties, the same sample was probed in different ionic environments namely: H₂O, 0.1 M NaCl and PBS (X1) with ionic strength of 0, 0.1 M and 0.176 M respectively (figure 124).

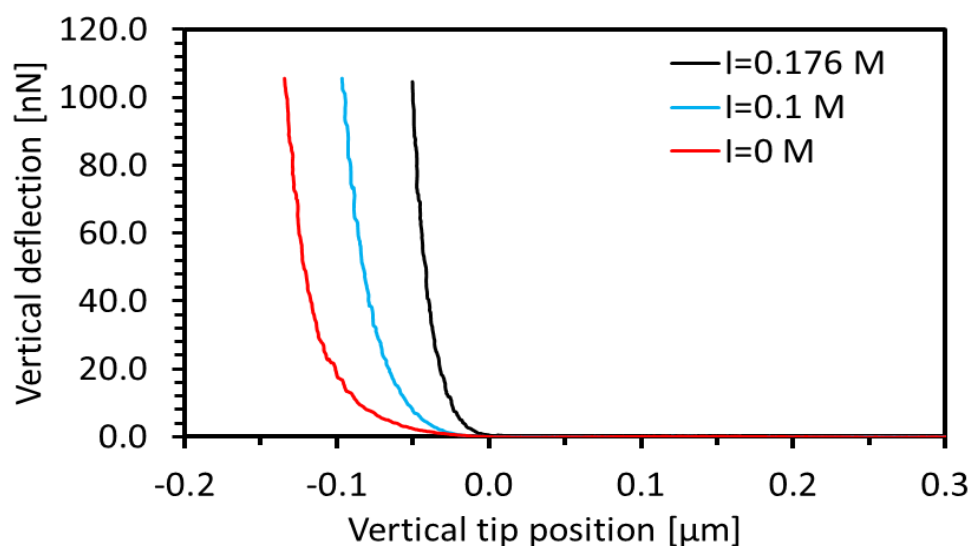


Figure 124. Effect of ionic strength on the shape of the force curves. $I=0.176$ M, PBS (black line), $I=0.1$ M, NaCl (blue line), $I=0$ M, water (red line).

The evaluated moduli were 470, 728 and 873 kPa for water, NaCl and PBS respectively, reflecting the influence of ionic strength on the tip sample interaction (Figure 125a). As explained earlier, the increase of modulus with the increase in ionic strength is attributed to the elimination of electrostatic repulsive forces between the tip and the surface causing a positive shift in vertical deflection and a higher modulus.

These results stand in agreement with our experiment, putting in evidence that the measurement in PBS environment could possibly eliminate the contribution of the electrostatic repulsion between the tip and the sample. The measurements were thus typically done in PBS to screen possible electrostatic interactions between the tip and the surface.

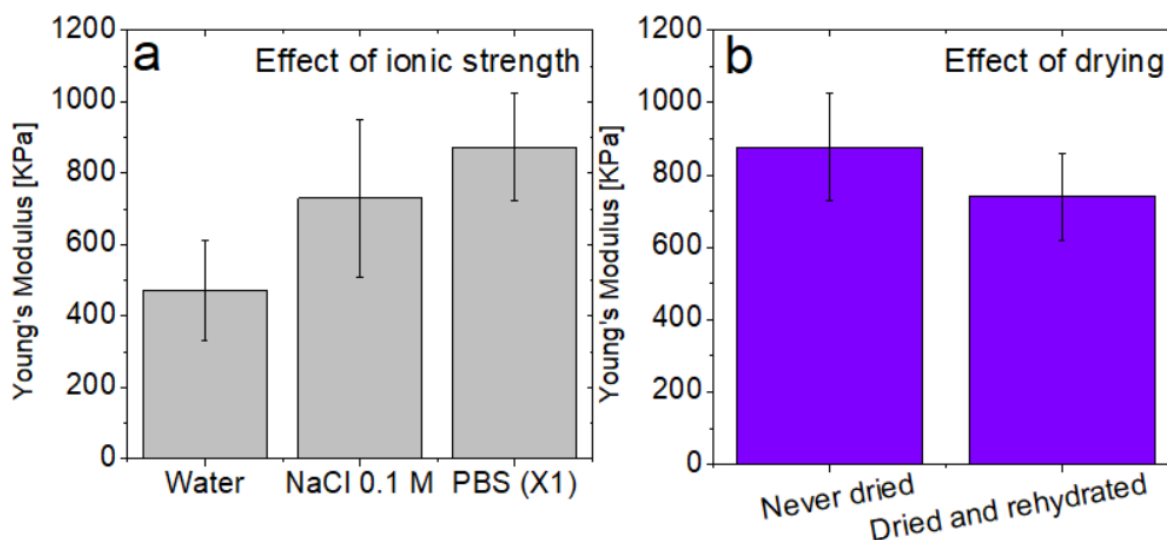


Figure 125. Elastic modulus obtained from Hertz fit to the approach retract curves of CNC/XG films with thickness of ~ 120 nm. (a) effect of ionic strength (b) effect of drying.

It is important to mention that the presence of high ionic strength solution such as PBS may also affect the measured mechanical properties. With the increase in ionic strength the distance between particles may be reduced, creating a denser network and enhancing the mechanical properties of the film.

Furthermore, we have investigated the effect of drying on the mechanical properties of the sample. (Figure 125b) The same sample was measured once without drying (never dried) and once after drying and rehydration, in PBS. The Young's modulus of the never dried sample was slightly higher than the rehydrated sample (876 compared to 740 kPa). It was shown in chapter 5.1.2, that drying and rehydration caused a slight reduction of sample thickness, which could be the reason for the lower modulus values in the case of rehydrated sample.

Nonetheless, given the measurement error, both never dried and rehydrated samples stayed within the same range of Young's modulus values, implying that drying and rehydration does not dramatically affect the mechanical properties of the sample.

Effect of film composition

In order to mimic as close as possible the natural environment, never dried samples with the largest number of layers were used for the evaluation of the mechanical properties of films with varying compositions.

Measurements were performed in PBS and samples with $n=20.5$ for three different systems: (i) CNC/XG (ii) CNC/pectin (iii) CNC/XG/Pectin

Figure 126 shows Young's modulus values obtained with indentation experiment using a colloidal probe (a) and with peak force experiment using conical shaped probe (b). (for original force curves refer to the annex)

For both methods, the Young's modulus was in the range of 300-900 kPa, the CNC/XG system showing the highest Young's modulus.

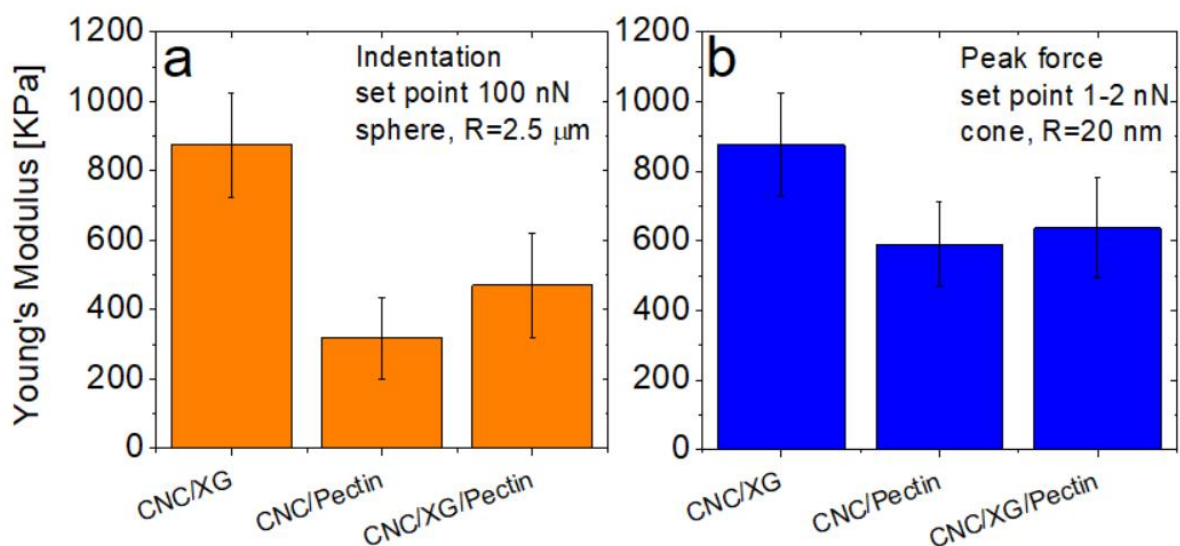


Figure 126. Elastic modulus obtained from AFM experiments on multilayer films ($n=20.5$) of different compositions (a) analysis of the force curve from indentation with spherical tip using Hertz model (b) analysis of force curves from peak-force mode using Sneddon model.

For the CNC/pectin sample, the modulus was lower than for the CNC/XG sample in both indentation and peak force experiments. This could be the result of a weak contact between CNC and pectin resulting in softer films. It should be pointed out that the growth of CNC/pectin film was not linear and resulted in thinner and less homogeneous films, possibly affecting the mechanical properties.

The obtained values, in the range of several hundred kPa, correspond to what was obtained with AFM indentation, with colloidal probe and small cantilever spring constants up to 2.7 N/m, for plant cell walls of *Arabidopsis thaliana* shoot apical meristem (Peaucelle, 2011, Braybrook and Peucelle, 2013) and epidermal cells/dark grown hypocotyl (Peaucelle, 2015). These values are lower than the ones found for onion epidermis (Beauzamy 2015) or for pollen tubes (Burri, 2019), however the other studies used stiffer cantilevers of 42 and 72 N/m (see table 4).

It is important to mention the fact that our in vitro system contains the basic elements however, it cannot represent their diversity in terms of architecture (colloidal cellulose nano-crystals in vitro versus micron sized fibers in planta), composition (only one type of polysaccharide from each representative group) and absence of specific interactions related to structural proteins.

Nonetheless, the results obtained on our simplified model system are in fair agreement with the results obtained for various types of cell walls measured in planta, using similar probing techniques, emphasizing the importance of those key components in constructing plant cell wall mimetic models.

Summary

- Measurement on 2D constructs were achieved using AFM indentation and peak force modes.
- The measurement conditions were optimized: thick layers $n > 15.5$ or $h > 120$ nm and measurement in PBS to minimize tip-sample interaction.
- The indentation (Young's) modulus was in the range of 300-900 kPa.
- The effect of film composition was investigated and it was found that CNC/XG films had higher Young's modulus than the films that included pectin, perhaps due to weak CNC-pectin interaction.

Outlook

- The adhesion of GUVs to the substrate should be further addressed.
- Investigate more deeply the effect of composition on the mechanical properties after tuning CNC-pectin interaction.
- Measurement of free-standing films prepared by casting and comparison with LbL films. This comparison could resolve the question of film thickness dependence of the mechanical properties, since free standing films are prepared with casting and generally have thickness of few hundred microns.

Chapter 7

Summary and outlook

This work was aimed to present a bottom up approach for the rational design of biomimetic constructs inspired from the PCW. To do this it was divided to three main parts: **(i)** building block characterization **(ii)** interaction studies **(iii)** realization and characterization of 2D and 3D plant cell wall mimetic constructs. In this overview we will describe the main findings from each part and propose some future outlook.

Initially, the building blocks of the system were identified and chosen to represent the naturally occurring components of the PCW. The lipid membrane served as a scaffold for LbL assembly while cellulose nano crystals were used to mimic the naturally occurring cellulose fibers. Xyloglucan and homogalacturonan represented the hemicellulose and pectin families respectively.

In the first part of the work we have characterized the structural parameters and physical properties of the individual building blocks. Interaction studies were carried out in the second part (ii), in order to optimize the conditions for assembly of biomimetic constructs. Characterization of the constructs using optical microscopy and AFM was finally established in the third part (iii).

Lipid-CNC interaction was probed in 2D (thin films) and 3D (bulk) experiments. In both configurations, it was found that the main factor governing the interaction was **electrostatic attraction** between positively charged membrane and negatively charged CNCs. (Navon, et al. 2017) 2D experiments revealed that CNCs adsorb on flat supported bilayers as highly hydrated film comprised of 1-2 layers of particles, with an average thickness of 6-8 nm.(Navon, et al. 2020) It should be mentioned that adsorption of CNC could be visualized by optical microscopy also for pH 5.5, however the highest adsorption was indeed observed for pH<4. Hence, further experiments should include a more quantitative study, by for example gradually changing the charge of CNCs and

measuring the interaction stoichiometry and thermodynamic parameters. In addition, molecular dynamic simulations could be used to predict the contribution of other intermolecular forces like VdW and hydrogen bonding, on the interaction of lipids and CNCs.

We then proceed for the study of CNC-XG interaction. The molar mass of XG was reduced by sonication, and it was shown using TEM, ITC, DLS and NMR that the stoichiometric mass ratio of XG/CNC at saturation was 0.05 mg XG to 1 mg CNC. ITC experiments suggest that the interaction of the XG chains with the CNC surface is of exothermic nature and consists of slow rearrangement of chains on the surface. With further addition of XG, at high XG/CNC ratio, the CNC-XG aggregates separate, resulting in CNC particles covered by XG, the particles were stabilized by steric repulsion.

2D experiments on lipid-CNC-XG system with QCM-D, revealed that the XG layer covering the CNCs is about 2 nm thick and composed from highly swollen XG chains. Important factors, that could be further investigated quantitatively, are the effect of size and solubility of XG on the adsorption on CNC surfaces.

The interaction between CNCs and homogalacturonan representing the pectin family, was investigated in the presence of monovalent and divalent ions. It was found that electrostatic repulsion between the two negatively charged species prevented the interaction of pectin with CNCs. However, this repulsion could be compensated with attractive depletion forces at high polymer concentration and high polymer/CNC ratio. In addition, it was found that divalent ions promoted the formation of a gel at high polymer/particle ratios and low degree of methyl esterification. A more comprehensive study on pectin CNC interaction may include adsorption of pectins on model CNC surfaces of different charges, and characterization of the interaction, as well as the structural parameters of the resulting films with surface sensitive techniques such as QCM-D or AFM. In addition, a physical characterization of pectin, is required to better understand the effect of structural parameters such degree of ME, degree of blockiness and solubility on the adsorption onto cellulose surfaces.

After studying the factors governing the interaction between the PCW building blocks, we used the optimized parameters to build 2D and 3D constructs using LbL deposition on spherical (GUVs) and flat (multilayered films) surfaces.

For the 3D constructs, we examined the effect of layer thickness and composition on the response to osmotic shocks of decorated vesicles and evaluated permeability values for bare vesicles.

A clear difference in the response to osmotic shocks was observed between bare and decorated vesicles. While bare vesicles deflated **spherically** upon osmotic shock, decorated vesicles tended to **buckle** into deformed shapes, similarly to what is observed for polyelectrolyte decorated capsules and gel phase vesicles. (Gao, et al. 2001, Quemeneur, et al. 2012)

At high number of layers ($n > 10.5$), decorated vesicles resisted osmotic shock and ceased to deform. The critical glucose concentration required to induce buckling increased with the increasing number of layers, confirming the increase in layer thickness due to successive deposition cycles.

The theoretical relations and the derived equations should be refined using theoretical simulations that will take into account the anisotropy of the material and the contribution from both z (bending) and x - y (stretching) moduli. In addition, the osmotic pressure can be generated using uncharged polymers such as polyethylene glycol (PEG) instead of glucose. By doing so, a larger osmotic pressure difference could be generated, possibly deflating the shells with large number of layers, helping to better understand the effect of shell thickness and composition on the mechanical properties. Additional experiments should be performed on larger number of objects to ensure statistical reproducibility.

Upon addition of divalent ions, decorated vesicles aggregated to form tissue like structures. The resulting structures resemble the composition and morphology of real plant tissue thus, could be useful to investigate biological phenomena such as enzyme activity or modulation of the mechanical properties, similarly to what was done with natural plant tissues. (Beauzamy, et al. 2015, Bidhendi and Geitmann 2019, Milani, et al. 2011)

Due to weak adhesion between the vesicle and the substrate, the mechanical properties of 3D vesicles could not be extracted. Future experiments should therefore focus on developing the experimental conditions required for sufficient adhesion of the vesicles to the substrate.

The structural features and mechanical properties of the 2D structures could be evaluated using AFM experiments on flat multilayered films prepared via LbL method. Films were prepared from CNC/XG, CNC/pectin and a mixed system of CNC/XG/pectin, with different number of layers ($n=5.5, 10.5, 15.5$ and 20.5). It was found that the preparation protocol had a striking influence on the resulting film thickness. Film prepared with intermediate drying were thinner than the ones prepared without intermediate drying, for the same number of layers and composition. This suggests that the intermediate drying enables the closer contacts between CNCs and themselves and between CNC and polymer, creating an irreversible shrinkage of the CNC-polymer matrix. Upon rehydration, the sample slightly decreased in thickness, which could result from closer packing of the CNCs and the polysaccharides upon drying.

The mechanical properties of the multilayered films were probed using both peak-force and indentation experiments. It was found that the Young's modulus of the films was 200-900 kPa, lower for what was found for CNC/XG decorated vesicles (Radavidson 2016) and resembles the one found for *Arabidopsis thaliana* cell walls. (Peaucelle, et al. 2011, Radotić, et al. 2012) The methodology could be further developed, following tuning the interaction between CNC and pectin, to include measurements on films with different composition.

The work presented here provides a platform for the rational design of PCW mimetic materials. This type of biomimetic structures, designed as multilayered films or decorated lipid vesicles, could serve for drug delivery, biodegradable coatings, food packaging as well as serving as a simplified model of the primary wall for the study of biological phenomena, such as transport of molecules or regulation of mechanical properties by enzymes.

References

- Al-Amoudi, A.; Norlen, L. P.; Dubochet, J., Cryo-electron microscopy of vitreous sections of native biological cells and tissues. *Journal of structural biology* **2004**, *148* (1), 131-135.
- Albersheim, P.; Darvill, A.; Roberts, K.; Sederoff, R.; Staehelin, A., *Plant Cell Walls*. Garland Science, Taylor and Francis Group: New York, 2011.
- Alem, H.; Blondeau, F.; Glinel, K.; Demoustier-Champagne, S.; Jonas, A. M., Layer-by-layer assembly of polyelectrolytes in nanopores. *Macromolecules* **2007**, *40* (9), 3366-3372.
- Angelova, M. I.; Dimitrov, D. S., Liposome electroformation. *Faraday discussions of the Chemical Society* **1986**, *81*, 303-311.
- Aulin, C.; Ahola, S.; Josefsson, P.; Nishino, T.; Hirose, Y.; Österberg, M.; Wågberg, L., Nanoscale Cellulose Films with Different Crystallinities and Mesostuctures-Their Surface Properties and Interaction with Water. *Langmuir* **2009**, *25* (13), 7675-7685.
- Axelrod, D., Total internal reflection fluorescence microscopy in cell biology. *Traffic* **2001**, *2* (11), 764-774.
- Azzam, F.; Heux, L.; Putaux, J.-L.; Jean, B., Preparation by grafting onto, characterization, and properties of thermally responsive polymer-decorated cellulose nanocrystals. *Biomacromolecules* **2010**, *11* (12), 3652-3659.
- Bailly, A. Elaboration and deformability of biomimetic systems. Université Grenoble Alpes, 2012.
- Battista, O.; Coppick, S.; Howsmon, J.; Morehead, F.; Sisson, W. A., Level-off degree of polymerization. *Industrial & Engineering Chemistry* **1956**, *48* (2), 333-335.
- Beauzamy, L.; Derr, J.; Boudaoud, A., Quantifying hydrostatic pressure in plant cells by using indentation with an atomic force microscope. *Biophysical Journal* **2015**, *108* (10), 2448-2456.
- Benselfelt, T.; Cranston, E. D.; Ondaral, S.; Johansson, E.; Brumer, H.; Rutland, M. W.; Wågberg, L., Adsorption of xyloglucan onto cellulose surfaces of different morphologies: an entropy-driven process. *Biomacromolecules* **2016**, *17* (9), 2801-2811.
- Bernard, A.-L.; Guedeau-Boudeville, M.-A.; Jullien, L.; di Meglio, J.-M., Raspberry vesicles. *Biochimica et Biophysica Acta (BBA)-Biomembranes* **2002**, *1567*, 1-5.
- Berret, J.-F., Stoichiometry of electrostatic complexes determined by light scattering. *Macromolecules* **2007**, *40* (12), 4260-4266.
- Bidhendi, A. J.; Geitmann, A., Relating the mechanics of the primary plant cell wall to morphogenesis. *Journal of Experimental Botany* **2015**, *67* (2), 449-461.
- Bidhendi, A. J.; Geitmann, A., Methods to quantify primary plant cell wall mechanics. *Journal of Experimental Botany* **2019**, *70* (14), 3615-3648.
- Bittman, R.; Blau, L., Phospholipid-cholesterol interaction. Kinetics of water permeability in liposomes. *Biochemistry* **1972**, *11* (25), 4831-4839.
- Blacklock, J.; Vetter, A.; Lanckenau, A.; Oupický, D.; Möhwald, H., Tuning the mechanical properties of bioreducible multilayer films for improved cell adhesion and transfection activity. *Biomaterials* **2010**, *31* (27), 7167-7174.

- Bledzki, A.; Gassan, J., Composites reinforced with cellulose based fibres. *Progress in Polymer Science* **1999**, *24* (2), 221-274.
- Boroske, E.; Elwenspoek, M.; Helfrich, W., Osmotic shrinkage of giant egg-lecithin vesicles. *Biophysical journal* **1981**, *34* (1), 95-109.
- Braccini, I.; Pérez, S., Molecular basis of Ca²⁺-induced gelation in alginates and pectins: the egg-box model revisited. *Biomacromolecules* **2001**, *2* (4), 1089-1096.
- Braybrook, S. A.; Peaucelle, A., Mechano-chemical aspects of organ formation in *Arabidopsis thaliana*: the relationship between auxin and pectin. *PloS one* **2013**, *8* (3), e57813.
- Burri, J. T.; Vogler, H.; Munglani, G.; Läubli, N. F.; Grossniklaus, U.; Nelson, B. J., A Microrobotic System for Simultaneous Measurement of Turgor Pressure and Cell-Wall Elasticity of Individual Growing Plant Cells. *IEEE Robotics and Automation Letters* **2019**, *4* (2), 641-646.
- Burton, R. A.; Gidley, M. J.; Fincher, G. B., Heterogeneity in the chemistry, structure and function of plant cell walls. *Nature chemical biology* **2010**, *6* (10), 724-732.
- Butt, H.-J.; Cappella, B.; Kappl, M., Force measurements with the atomic force microscope: Technique, interpretation and applications. *Surface Science Reports* **2005**, *59* (1-6), 1-152.
- Cacas, J.-L.; Buré, C.; Grosjean, K.; Gerbeau-Pissot, P.; Lherminier, J.; Rombouts, Y.; Maes, E.; Bossard, C.; Gronnier, J.; Furt, F., Revisiting plant plasma membrane lipids in tobacco: a focus on sphingolipids. *Plant Physiology* **2016**, *170* (1), 367-384.
- Caffall, K. H.; Mohnen, D., The structure, function, and biosynthesis of plant cell wall pectic polysaccharides. *Carbohydrate research* **2009**, *344* (14), 1879-1900.
- Carpita, N. C.; Gibeaut, D. M., Structural models of primary cell walls in flowering plants: consistency of molecular structure with the physical properties of the walls during growth. *The Plant Journal* **1993**, *3* (1), 1-30.
- Castellana, E. T.; Cremer, P. S., Solid supported lipid bilayers: From biophysical studies to sensor design. *Surface Science Reports* **2006**, *61* (10), 429-444.
- Cerclier, C.; Cousin, F.; Bizot, H.; Moreau, C. I.; Cathala, B., Elaboration of spin-coated cellulose-xyloglucan multilayered thin films. *Langmuir* **2010**, *26* (22), 17248-17255.
- Chambat, G.; Karmous, M.; Costes, M.; Picard, M.; Joseleau, J.-P., Variation of xyloglucan substitution pattern affects the sorption on celluloses with different degrees of crystallinity. *Cellulose* **2005**, *12* (2), 117-125.
- Chanzy, H., Aspect of cellulose structure. In *Cellulose Sources and Exploitation. Industrial Utilization, Biotechnology and Physico-Chemical Properties.*, Kennedy, J. F.; Phillips, G. O.; Williams, P. A., Eds. Ellis Horwood Ltd. : Chichester, 1990; pp 3-12.
- Chen, C. J., *Introduction to scanning tunneling microscopy*. Oxford University Press: 1993; Vol. 4.
- Chibowski, E.; Szczeń, A., Zeta potential and surface charge of DPPC and DOPC liposomes in the presence of PLC enzyme. *Adsorption* **2016**, *22* (4-6), 755-765.
- Contini, C.; Schneemilch, M.; Gaisford, S.; Quirke, N., Nanoparticle-membrane interactions. *Journal of Experimental Nanoscience* **2018**, *13* (1), 62-81.

Cosgrove, D. C., Comparative structure and biomechanics of plant primary and secondary cell walls. *Frontiers in plant science* **2012**, *3*, 204.

Cosgrove, D. J., Assembly and enlargement of the primary cell wall in plants. *Annual review of cell and developmental biology* **1997**, *13* (1), 171-201.

Cosgrove, D. J., Growth of the plant cell wall. *Nature reviews molecular cell biology* **2005**, *6* (11), 850-861.

Cosgrove, D. J., Re-constructing our models of cellulose and primary cell wall assembly. *Current opinion in plant biology* **2014**, *22*, 122-131.

Courtois, J.; Berret, J.-F., Probing oppositely charged surfactant and copolymer interactions by isothermal titration microcalorimetry. *Langmuir* **2010**, *26* (14), 11750-11758.

Craig, V. S.; Plunkett, M., Determination of coupled solvent mass in quartz crystal microbalance measurements using deuterated solvents. *Journal of colloid and interface science* **2003**, *262* (1), 126-129.

Cranston, E. D.; Gray, D. G.; Rutland, M. W., Direct surface force measurements of polyelectrolyte multilayer films containing nanocrystalline cellulose. *Langmuir* **2010**, *26* (22), 17190-17197.

Dammak, A.; Quémener, B.; Bonnin, E.; Alvarado, C.; Bouchet, B.; Villares, A.; Moreau, C. I.; Cathala, B., Exploring architecture of xyloglucan cellulose nanocrystal complexes through enzyme susceptibility at different adsorption regimes. *Biomacromolecules* **2015**, *16* (2), 589-596.

Danino, D.; Bernheim-Groswasser, A.; Talmon, Y., Digital cryogenic transmission electron microscopy: an advanced tool for direct imaging of complex fluids. *Colloids and Surfaces A: Physicochemical and Engineering Aspects* **2001**, *183*, 113-122.

de Macedo, B. d. S.; Almeida, T. d.; Cruz, R. d. C.; Netto, A. D. P.; Silva, L. d.; Berret, J.-F.; Vitorazi, L., Effect of pH on the complex coacervation and on the formation of layers of sodium alginate and PDADMAC. *Langmuir* **2020**.

Decher, G.; Hong, J.; Schmitt, J., Buildup of ultrathin multilayer films by a self-assembly process: III. Consecutively alternating adsorption of anionic and cationic polyelectrolytes on charged surfaces. *Thin solid films* **1992**, *210*, 831-835.

Decher, G.; Schlenoff, J. B., *Multilayer thin films: sequential assembly of nanocomposite materials*. John Wiley & Sons: 2006.

Decher, G., Layer-by-layer assembly (putting molecules to work). *Multilayer thin films* **2012**, *1*, 1-21.

Dhar, N.; Au, D.; Berry, R. C.; Tam, K. C., Interactions of nanocrystalline cellulose with an oppositely charged surfactant in aqueous medium. *Colloids and Surfaces A: Physicochemical and Engineering Aspects* **2012**, *415*, 310-319.

Dick-Pérez, M.; Zhang, Y.; Hayes, J.; Salazar, A.; Zabolina, O. A.; Hong, M., Structure and interactions of plant cell-wall polysaccharides by two- and three-dimensional magic-angle-spinning solid-state NMR. *Biochemistry* **2011**, *50* (6), 989-1000.

Donath, E.; Sukhorukov, G. B.; Caruso, F.; Davis, S. A.; Möhwald, H., Novel hollow polymer shells by colloid-templated assembly of polyelectrolytes. *Angewandte Chemie International Edition* **1998**, *37* (16), 2201-2205.

- Dong, S.; Roman, M., Fluorescently labeled cellulose nanocrystals for bioimaging applications. *Journal of the American Chemical Society* **2007**, *129* (45), 13810-13811.
- Dong, X. M.; Revol, J.-F.; Gray, D. G., Effect of microcrystallite preparation conditions on the formation of colloid crystals of cellulose. *Cellulose* **1998**, *5* (1), 19-32.
- Eeman, M.; Deleu, M., From biological membranes to biomimetic model membranes. *Biotechnologie, Agronomie, Société et Environnement* **2010**, *14* (4), 719-736.
- Egerton, R. F., *Physical principles of electron microscopy*. Springer: 2005; Vol. 56.
- Ehmann, H. M.; Mohan, T.; Koshanskaya, M.; Scheicher, S.; Breitwieser, D.; Ribitsch, V.; Stana-Kleinschek, K.; Spirk, S., Design of anticoagulant surfaces based on cellulose nanocrystals. *Chemical Communications* **2014**, *50* (86), 13070-13072.
- Eisele, N. B.; Andersson, F. I.; Frey, S.; Richter, R. P., Viscoelasticity of thin biomolecular films: a case study on nucleoporin phenylalanine-glycine repeats grafted to a histidine-tag capturing QCM-D sensor. *Biomacromolecules* **2012**, *13* (8), 2322-2332.
- Elazzouzi-Hafraoui, S.; Nishiyama, Y.; Putaux, J.-L.; Heux, L.; Dubreuil, F.; Rochas, C., The shape and size distribution of crystalline nanoparticles prepared by acid hydrolysis of native cellulose. *Biomacromolecules* **2007**, *9* (1), 57-65.
- Faïk, A.; Chileshe, C.; Sterling, J.; Maclachlan, G., Xyloglucan galactosyl- and fucosyltransferase activities from pea epicotyl microsomes. *Plant Physiology* **1997**, *114* (1), 245-254.
- Favier, V.; Chanzy, H.; Cavallé, J., Polymer nanocomposites reinforced by cellulose whiskers. *Macromolecules* **1995**, *28* (18), 6365-6367.
- Fenz, S. F.; Sengupta, K., Giant vesicles as cell models. *Integrative Biology* **2012**, *4* (9), 982-995.
- Finnemore, A.; Cunha, P.; Shean, T.; Vignolini, S.; Guldin, S.; Oyen, M.; Steiner, U., Biomimetic layer-by-layer assembly of artificial nacre. *Nature communications* **2012**, *3*, 966.
- Foster, E. J.; Moon, R. J.; Agarwal, U. P.; Bortner, M. J.; Bras, J.; Camarero-Espinosa, S.; Chan, K. J.; Clift, M. J.; Cranston, E. D.; Eichhorn, S. J., Current characterization methods for cellulose nanomaterials. *Chemical Society Reviews* **2018**, *47* (8), 2609-2679.
- Fraeye, I.; Duvetter, T.; Doungla, E.; Van Loey, A.; Hendrickx, M., Fine-tuning the properties of pectin-calcium gels by control of pectin fine structure, gel composition and environmental conditions. *Trends in Food Science & Technology* **2010**, *21* (5), 219-228.
- Freyer, M. W.; Lewis, E. A., Isothermal titration calorimetry: experimental design, data analysis, and probing macromolecule/ligand binding and kinetic interactions. *Methods in cell biology* **2008**, *84*, 79-113.
- Fry, S. C., Cellulases, hemicelluloses and auxin-stimulated growth: a possible relationship. *Physiologia Plantarum* **1989**, *75* (4), 532-536.
- Fry, S. C., The structure and functions of xyloglucan. *Journal of Experimental Botany* **1989**, *40* (1), 1-11.
- Fry, S. C.; York, W. S.; Albersheim, P.; Darvill, A.; Hayashi, T.; Joseleau, J. P.; Kato, Y.; Lorences, E. P.; Maclachlan, G. A.; McNeil, M., An unambiguous nomenclature for xyloglucan-derived oligosaccharides. *Physiologia Plantarum* **1993**, *89* (1), 1-3.

Fultz, B.; Howe, J. M., *Transmission electron microscopy and diffractometry of materials*. Springer Science & Business Media: 2012.

Furt, F.; Simon-Plas, F.; Mongrand, S., Lipids of the plant plasma membrane. In *The plant plasma membrane*, Springer: 2011; pp 3-30.

Gao, C.; Donath, E.; Moya, S.; Dudnik, V.; Möhwald, H., Elasticity of hollow polyelectrolyte capsules prepared by the layer-by-layer technique. *The European Physical Journal E* **2001**, *5* (1), 21-27.

Geitmann, A., Experimental approaches used to quantify physical parameters at cellular and subcellular levels. *American Journal of Botany* **2006**, *93* (10), 1380-1390.

Giddings, T. H.; Brower, D. L.; Staehelin, L. A., Visualization of particle complexes in the plasma membrane of *Micrasterias denticulata* associated with the formation of cellulose fibrils in primary and secondary cell walls. *The Journal of cell biology* **1980**, *84* (2), 327-339.

Gilboa, B.; Gillo, D.; Farago, O.; Bernheim-Groswasser, A., Bidirectional cooperative motion of myosin-II motors on actin tracks with randomly alternating polarities. *Soft Matter* **2009**, *5* (11), 2223-2231.

Glinel, K.; Moussa, A.; Jonas, A. M.; Laschewsky, A., Influence of polyelectrolyte charge density on the formation of multilayers of strong polyelectrolytes at low ionic strength. *Langmuir* **2002**, *18* (4), 1408-1412.

Glinel, K.; Déjugnat, C.; Prevot, M.; Schöler, B.; Schönhoff, M.; Klitzing, R. v., Responsive polyelectrolyte multilayers. *Colloids and Surfaces A: Physicochemical and Engineering Aspects* **2007**, *303* (1-2), 3-13.

Grasdalen, H.; Bakøy, O. E.; Larsen, B., Determination of the degree of esterification and the distribution of methylated and free carboxyl groups in pectins by ¹H-NMR spectroscopy. *Carbohydrate research* **1988**, *184*, 183-191.

Gronnier, J.; Germain, V.; Gouguet, P.; Cacas, J.-L.; Mongrand, S., GIPC: Glycosyl Inositol Phospho Ceramides, the major sphingolipids on earth. *Plant signaling & behavior* **2016**, *11* (4), 1-6.

Grosjean, K.; Mongrand, S.; Beney, L.; Simon-Plas, F.; Gerbeau-Pissot, P., Differential effect of plant lipids on membrane organization specificities of phytosphingolipids and phytosterols. *Journal of Biological Chemistry* **2015**, *290* (9), 5810-5825.

Gu, J.; Catchmark, J. M., The impact of cellulose structure on binding interactions with hemicellulose and pectin. *Cellulose* **2013**, *20* (4), 1613-1627.

Hamant, O.; Mouliat, B., How do plants read their own shapes? *New Phytologist* **2016**, *212* (2), 333-337.

Hambardzumyan, A.; Molinari, M.; Dumelie, N.; Foulon, L.; Habrant, A.; Chabbert, B.; Aguié-Béghin, V., Structure and optical properties of plant cell wall bio-inspired materials: cellulose–lignin multilayer nanocomposites. *Comptes rendus biologiques* **2011**, *334* (11), 839-850.

Hanus, J.; Mazeau, K., The xyloglucan–cellulose assembly at the atomic scale. *Biopolymers: Original Research on Biomolecules* **2006**, *82* (1), 59-73.

Hayashi, T.; Maclachlan, G., Pea xyloglucan and cellulose: I. Macromolecular organization. *Plant Physiology* **1984**, *75* (3), 596-604.

Hayashi, T.; Marsden, M. P.; Delmer, D. P., Pea xyloglucan and cellulose: VI. Xyloglucan-cellulose interactions *in vitro* and *in vivo*. *Plant Physiology* **1987**, *83* (2), 384-389.

Hayashi, T., Xyloglucans in the primary cell wall. *Annual review of plant biology* **1989**, *40* (1), 139-168.

- Hayashi, T.; Takeda, T.; Ogawa, K.; Mitsuishi, Y., Effects of the degree of polymerization on the binding of xyloglucans to cellulose. *Plant and Cell Physiology* **1994**, *35* (6), 893-899.
- Hepler, P. K.; Winship, L. J., Calcium at the cell wall-cytoplasm interface. *Journal of integrative plant biology* **2010**, *52* (2), 147-160.
- Hesslink, F. T.; Vrij, A.; Overbeek, J. T. G., Theory of the stabilization of dispersions by adsorbed macromolecules. II. Interaction between two flat particles. *The Journal of Physical Chemistry* **1971**, *75* (14), 2094-2103.
- Hiemenz, P. C.; Rajagopalan, R., *Principles of Colloid and Surface Chemistry, revised and expanded*. CRC press: 2016.
- Hochmuth, R. M., Micropipette aspiration of living cells. *Journal of biomechanics* **2000**, *33* (1), 15-22.
- Hunter, R. J., *Zeta Potential in Colloid Science: Principles and Applications*. Academic Press: London, 2013; Vol. 2.
- Husemann, E., Übermikroskopische Untersuchungen an hydrolytisch abgebauten Fasern. Mitteilung über makromolekulare Verbindungen. *Journal für Praktische Chemie* **1943**, *1* (1-6), 16-27.
- Israelachvili, J. N.; Mitchell, D. J.; Ninham, B. W., Theory of self-assembly of lipid bilayers and vesicles. *Biochimica et Biophysica Acta (BBA)-Biomembranes* **1977**, *470* (2), 185-201.
- Israelachvili, J. N., *Intermolecular and Surface Forces*. Academic Press: New York, 2015.
- Itoh, T.; Brown, R. M., The assembly of cellulose microfibrils in *Valonia macrophysa* Kütz. *Planta* **1984**, *160* (4), 372-381.
- Iwamoto, S.; Kai, W.; Isogai, A.; Iwata, T., Elastic modulus of single cellulose microfibrils from tunicate measured by atomic force microscopy. *Biomacromolecules* **2009**, *10* (9), 2571-2576.
- Janiak, M. J.; Small, D. M.; Shipley, G. G., Temperature and compositional dependence of the structure of hydrated dimyristoyl lecithin. *Journal of Biological Chemistry* **1979**, *254* (13), 6068-6078.
- Jaqaman, K.; Loerke, D.; Mettlen, M.; Kuwata, H.; Grinstein, S.; Schmid, S. L.; Danuser, G., Robust single-particle tracking in live-cell time-lapse sequences. *Nature methods* **2008**, *5* (8), 695-702.
- Jean, B.; Dubreuil, F.; Heux, L.; Cousin, F., Structural details of cellulose nanocrystals/polyelectrolytes multilayers probed by neutron reflectivity and AFM. *Langmuir* **2008**, *24* (7), 3452-3458.
- Jean, B.; Heux, L.; Dubreuil, F.; Chambat, G.; Cousin, F., Non-electrostatic building of biomimetic cellulose–xyloglucan multilayers. *Langmuir* **2009**, *25* (7), 3920-3923.
- Johannsmann, D., Feature Article Viscoelastic analysis of organic thin films on quartz resonators. *Macromol. Chem. Phys* **1999**, *200*, 501-516.
- Johannsmann, D., Viscoelastic, mechanical, and dielectric measurements on complex samples with the quartz crystal microbalance. *Physical Chemistry Chemical Physics* **2008**, *10* (31), 4516-4534.
- JPK instruments, NanoWizard Handbook. JPK instruments AG: Berlin Germany, 2012; Vol. Version 2.2, pp 4-5.
- Kalashnikova, I.; Bizot, H.; Cathala, B.; Capron, I., New Pickering emulsions stabilized by bacterial cellulose nanocrystals. *Langmuir* **2011**, *27* (12), 7471-7479.

Kalashnikova, I.; Bizot, H.; Bertoncini, P.; Cathala, B.; Capron, I., Cellulosic nanorods of various aspect ratios for oil in water Pickering emulsions. *Soft Matter* **2013**, *9* (3), 952-959.

Kaushik, M.; Fraschini, C.; Chauve, G.; Putaux, J.-L.; Moores, A., Transmission electron microscopy for the characterization of cellulose nanocrystals. In *Transmission Electron Microscopy - Theory and Applications*, Maaz, K., Ed. InTech: Rijeka, Croatia, 2015; pp 130-156.

Keegstra, K.; Talmadge, K. W.; Bauer, W.; Albersheim, P., The structure of plant cell walls: III. A model of the walls of suspension-cultured sycamore cells based on the interconnections of the macromolecular components. *Plant Physiology* **1973**, *51* (1), 188-197.

Kishani, S.; Vilaplana, F.; Ruda, M.; Hansson, P.; Wågberg, L., The influence of solubility on the adsorption of different Xyloglucan fractions at Cellulose Water Interfaces. *Biomacromolecules* **2019**.

Kittle, J. D.; Du, X.; Jiang, F.; Qian, C.; Heinze, T.; Roman, M.; Esker, A. R., Equilibrium water contents of cellulose films determined via solvent exchange and quartz crystal microbalance with dissipation monitoring. *Biomacromolecules* **2011**, *12* (8), 2881-2887.

Kolakovic, R.; Peltonen, L.; Laukkanen, A.; Hellman, M.; Laaksonen, P.; Linder, M. B.; Hirvonen, J.; Laaksonen, T., Evaluation of drug interactions with nanofibrillar cellulose. *European journal of pharmaceuticals and biopharmaceutics* **2013**, *85* (3), 1238-1244.

Kummrow, M.; Helfrich, W., Collapse of giant phosphatidylcholine vesicles. *Chemistry and physics of lipids* **1996**, *79* (2), 147-156.

Kuntsche, J.; Horst, J. C.; Bunjes, H., Cryogenic transmission electron microscopy (cryo-TEM) for studying the morphology of colloidal drug delivery systems. *International journal of pharmaceuticals* **2011**, *417* (1-2), 120-137.

Lai-Kee-Him, J.; Chanzy, H.; Müller, M.; Putaux, J.-L.; Imai, T.; Bulone, V., In vitro versus in vivo cellulose microfibrils from plant primary wall synthases: Structural differences. *Journal of Biological Chemistry* **2002**, *277* (40), 36931-36939.

Lasic, D. D., The mechanism of vesicle formation. *Biochemical Journal* **1988**, *256* (1), 1-11.

Lasic, D. D.; Templeton, N., Liposomes in gene therapy. *Advanced Drug Delivery Reviews* **1996**, *20* (2-3), 221-266.

Levy, I.; Shani, Z.; Shoseyov, O., Modification of polysaccharides and plant cell wall by endo-1, 4- β -glucanase and cellulose-binding domains. *Biomolecular engineering* **2002**, *19* (1), 17-30.

Li, Y.; Wang, X.; Sun, J., Layer-by-layer assembly for rapid fabrication of thick polymeric films. *Chemical Society Reviews* **2012**, *41* (18), 5998-6009.

Lichtenberg, D.; Barenholz, Y., Liposomes: preparation, characterization, and preservation. *Methods Biochem. Anal* **1988**, *33*, 337-462.

Liu, Z.; Persson, S.; Sánchez-Rodríguez, C., At the border: the plasma membrane-cell wall continuum. *Journal of Experimental Botany* **2015**, *66* (6), 1553-1563.

Lombardo, S.; Eyley, S.; Schütz, C.; Van Gorp, H.; Rosenfeldt, S.; Van den Mooter, G.; Thielemans, W., Thermodynamic study of the interaction of bovine serum albumin and amino acids with cellulose nanocrystals. *Langmuir* **2017**, *33* (22), 5473-5481.

- Lombardo, S.; Thielemans, W., Thermodynamics of adsorption on nanocellulose surfaces. *Cellulose* **2018**, 1-31.
- Lopez, M.; Bizot, H.; Chambat, G.; Marais, M.-F.; Zykwinska, A.; Ralet, M.-C.; Driguez, H.; Buléon, A., Enthalpic studies of xyloglucan– cellulose interactions. *Biomacromolecules* **2010**, *11* (6), 1417-1428.
- Makino, K.; Yamada, T.; Kimura, M.; Oka, T.; Ohshima, H.; Kondo, T., Temperature-and ionic strength-induced conformational changes in the lipid head group region of liposomes as suggested by zeta potential data. *Biophysical chemistry* **1991**, *41* (2), 175-183.
- Marchessault, R. H.; Morehead, F.; Walter, N., Liquid crystal systems from fibrillar polysaccharides. *Nature* **1959**, *184* (4686), 632-633.
- Martin, C.; Jean, B., Nanocellulose/polymer multilayered thin films: tunable architectures towards tailored physical properties. *Nordic Pulp & Paper Research Journal* **2014**, *29* (1), 19-30.
- Martin, C.; Barker, R.; Watkins, E. B.; Dubreuil, F. d. r.; Cranston, E. D.; Heux, L.; Jean, B., Structural variations in hybrid all-nanoparticle gibbsite nanoplatelet/cellulose nanocrystal multilayered films. *Langmuir* **2017**, *33* (32), 7896-7907.
- Mathai, J. C.; Tristram-Nagle, S.; Nagle, J. F.; Zeidel, M. L., Structural determinants of water permeability through the lipid membrane. *The Journal of general physiology* **2008**, *131* (1), 69-76.
- Mazeau, K., On the external morphology of native cellulose microfibrils. *Carbohydrate Polymers* **2011**, *84* (1), 524-532.
- Mazeau, K.; Charlier, L., The molecular basis of the adsorption of xylans on cellulose surface. *Cellulose* **2012**, *19* (2), 337-349.
- McNamara, J. T.; Morgan, J. L.; Zimmer, J., A molecular description of cellulose biosynthesis. *Annual review of biochemistry* **2015**, *84*, 895-921.
- McQueen-Mason, S.; Durachko, D. M.; Cosgrove, D. J., Two endogenous proteins that induce cell wall extension in plants. *The Plant Cell* **1992**, *4* (11), 1425-1433.
- Mertins, O.; Dimova, R., Binding of chitosan to phospholipid vesicles studied with isothermal titration calorimetry. *Langmuir* **2011**, *27* (9), 5506-5515.
- MicroCal, ITC data analysis in Origin: Tutorial Guide. In *MicroCal, LLC, Northampton, MA*, 2004.
- Migliorini, E.; Thakar, D.; Sadir, R.; Pleiner, T.; Baleux, F.; Lortat-Jacob, H.; Coche-Guerente, L.; Richter, R. P., Well-defined biomimetic surfaces to characterize glycosaminoglycan-mediated interactions on the molecular, supramolecular and cellular levels. *Biomaterials* **2014**, *35* (32), 8903-8915.
- Milani, P.; Gholamirad, M.; Traas, J.; Arnéodo, A.; Boudaoud, A.; Argoul, F.; Hamant, O., In vivo analysis of local wall stiffness at the shoot apical meristem in Arabidopsis using atomic force microscopy. *The Plant Journal* **2011**, *67* (6), 1116-1123.
- Mohnen, D., Pectin structure and biosynthesis. *Current opinion in plant biology* **2008**, *11* (3), 266-277.
- Mølgaard, S. L.; Henriksson, M.; Cárdenas, M.; Svagan, A. J., Cellulose-nanofiber/polygalacturonic acid coatings with high oxygen barrier and targeted release properties. *Carbohydrate Polymers* **2014**, *114*, 179-182.

Moncelli, M. R.; Becucci, L.; Guidelli, R., The intrinsic pKa values for phosphatidylcholine, phosphatidylethanolamine, and phosphatidylserine in monolayers deposited on mercury electrodes. *Biophysical journal* **1994**, *66* (6), 1969-1980.

Montis, C.; Maiolo, D.; Alessandri, I.; Bergese, P.; Berti, D., Interaction of nanoparticles with lipid membranes: a multiscale perspective. *Nanoscale* **2014**, *6* (12), 6452-6457.

Montis, C.; Gerelli, Y.; Fragneto, G.; Nylander, T.; Baglioni, P.; Berti, D., Nucleolipid bilayers: A quartz crystal microbalance and neutron reflectometry study. *Colloids and Surfaces B: Biointerfaces* **2016**, *137*, 203-213.

Morgan, J. L. W.; Strumillo, J.; Zimmer, J., Crystallographic snapshot of cellulose synthesis and membrane translocation. *Nature* **2013**, *493* (7431), 181-186.

Morgan, J. L. W.; McNamara, J. T.; Fischer, M.; Rich, J.; Chen, H.-M.; Withers, S. G.; Zimmer, J., Observing cellulose biosynthesis and membrane translocation *in crystallo*. *Nature* **2016**, *531* (7594), 329-334.

Mornet, S.; Lambert, O.; Duguet, E.; Brisson, A., The formation of supported lipid bilayers on silica nanoparticles revealed by cryoelectron microscopy. *Nano letters* **2005**, *5* (2), 281-285.

Mousseau, F.; Berret, J.-F., The role of surface charge in the interaction of nanoparticles with model pulmonary surfactants. *Soft Matter* **2018**, *14* (28), 5764-5774.

Mousseau, F.; Oikonomou, E. K.; Baldim, V.; Mornet, S.; Berret, J.-F., Nanoparticle-lipid interaction: Job scattering plots to differentiate vesicle aggregation from supported lipid bilayer formation. *Colloids and Interfaces* **2018**, *2* (4), 50.

Mueller, S. C.; Brown, R. M., Evidence for an intramembrane component associated with a cellulose microfibril-synthesizing complex in higher plants. *The Journal of cell biology* **1980**, *84* (2), 315-326.

Mukherjee, S.; Woods, H., X-ray and electron microscope studies of the degradation of cellulose by sulphuric acid. *Biochimica et biophysica acta* **1953**, *10*, 499-511.

Muller, F. O.; Jean, B.; Perrin, P.; Heux, L.; Boué, F.; Cousin, F., Mechanism of associations of neutral semiflexible biopolymers in water: the xyloglucan case reveals inherent links. *Macromolecular Chemistry and Physics* **2013**, *214* (20), 2312-2323.

Muller, F. o. O.; Manet, S.; Jean, B.; Chambat, G.; Boué, F. o.; Heux, L.; Cousin, F., SANS measurements of semiflexible xyloglucan polysaccharide chains in water reveal their self-avoiding statistics. *Biomacromolecules* **2011**, *12* (9), 3330-3336.

Navon, Y.; Radavidson, H.; Putaux, J.-L.; Jean, B.; Heux, L., pH-Sensitive Interactions between Cellulose Nanocrystals and DOPC Liposomes. *Biomacromolecules* **2017**, *18* (9), 2918-2927.

Navon, Y.; Jean, B.; Coche-Guerente, L.; Dahlem, F.; Bernheim-Groswasser, A.; Heux, L., Deposition of cellulose nanocrystals onto biomimetic lipid membranes. *Langmuir* **2020**.

Nečas, D.; Klapetek, P., Gwyddion: an open-source software for SPM data analysis. *Open Physics* **2012**, *10* (1), 181-188.

Nielsen, L. J.; Eyley, S.; Thielemans, W.; Aylott, J. W., Dual fluorescent labelling of cellulose nanocrystals for pH sensing. *Chemical Communications* **2010**, *46* (47), 8929-8931.

Niinivaara, E.; Faustini, M.; Tammelin, T.; Kontturi, E., Water vapor uptake of ultrathin films of biologically derived nanocrystals: quantitative assessment with quartz crystal microbalance and spectroscopic ellipsometry. *Langmuir* **2015**, *31* (44), 12170-12176.

- Nishiyama, Y.; Kim, U.-J.; Kim, D.-Y.; Katsumata, K. S.; May, R. P.; Langan, P., Periodic disorder along ramie cellulose microfibrils. *Biomacromolecules* **2003**, *4* (4), 1013-1017.
- Nishiyama, Y., Structure and properties of the cellulose microfibril. *Journal of wood science* **2009**, *55* (4), 241-249.
- Nixon, B. T.; Mansouri, K.; Singh, A.; Du, J.; Davis, J. K.; Lee, J.-G.; Slabaugh, E.; Vandavasi, V. G.; O'Neill, H.; Roberts, E. M., Comparative structural and computational analysis supports eighteen cellulose synthases in the plant cellulose synthesis complex. *Scientific reports* **2016**, *6*, 28696.
- O'Neill, M.; Albersheim, P.; Darvill, A., The pectic polysaccharides of primary cell walls. In *Methods in plant biochemistry*, Elsevier: 1990; Vol. 2, pp 415-441.
- Ochoa-Villarreal, M.; Aispuro-Hernández, E.; Vargas-Arispuro, I.; Martínez-Téllez, M. Á., Plant cell wall polymers: function, structure and biological activity of their derivatives. In *Polymerization*, edit., A. D. S. G., Ed. Intech: Rijeka, Croatia 2012; pp 63-86.
- Oikonomou, E.; Mousseau, F.; Christov, N.; Cristobal, G.; Vacher, A.; Airiau, M.; Bourgaux, C.; Heux, L.; Berret, J.-F., Fabric Softener–Cellulose Nanocrystal Interaction: A Model for Assessing Surfactant Deposition on Cotton. *The Journal of Physical Chemistry B* **2017**, *121* (10), 2299-2307.
- Oikonomou, E.; Christov, N.; Cristobal, G.; Bourgaux, C.; Heux, L.; Boucenna, I.; Berret, J.-F., Design of eco-friendly fabric softeners: Structure, rheology and interaction with cellulose nanocrystals. *Journal of colloid and interface science* **2018**, *525*, 206-215.
- Park, I. H.; Choi, E.-J., Characterization of branched polyethyleneimine by laser light scattering and viscometry. *Polymer* **1996**, *37* (2), 313-319.
- Park, Y. B.; Cosgrove, D. J., Xyloglucan and its interactions with other components of the growing cell wall. *Plant and Cell Physiology* **2015**, *56* (2), 180-194.
- Paulraj, T.; Riazanova, A. V.; Yao, K.; Andersson, R. L.; Müllertz, A.; Svagan, A. J., Bioinspired layer-by-layer microcapsules based on cellulose nanofibers with switchable permeability. *Biomacromolecules* **2017**, *18* (4), 1401-1410.
- Paulraj, T.; Riazanova, A.; Svagan, A., Bioinspired capsules based on nanocellulose, xyloglucan and pectin–The influence of capsule wall composition on permeability properties. *Acta biomaterialia* **2018**, *69*, 196-205.
- Peaucelle, A.; Braybrook, S. A.; Le Guillou, L.; Bron, E.; Kuhlemeier, C.; Höfte, H., Pectin-induced changes in cell wall mechanics underlie organ initiation in Arabidopsis. *Current biology* **2011**, *21* (20), 1720-1726.
- Peaucelle, A.; Wightman, R.; Höfte, H., The control of growth symmetry breaking in the Arabidopsis hypocotyl. *Current biology* **2015**, *25* (13), 1746-1752.
- Peetla, C.; Stine, A.; Labhasetwar, V., Biophysical interactions with model lipid membranes: applications in drug discovery and drug delivery. *Molecular pharmaceutics* **2009**, *6* (5), 1264-1276.
- Pelloux, J.; Rusterucci, C.; Mellerowicz, E. J., New insights into pectin methylesterase structure and function. *Trends in plant science* **2007**, *12* (6), 267-277.
- Philipse, A. P., The random contact equation and its implications for (colloidal) rods in packings, suspensions, and anisotropic powders. *Langmuir* **1996**, *12* (5), 1127-1133.

- Pickering, S. U., Emulsions. *Journal of the Chemical Society, Transactions* **1907**, *91*, 2001-2021.
- Quemeneur, F.; Rinaudo, M.; Pépin-Donat, B., Influence of polyelectrolyte chemical structure on their interaction with lipid membrane of zwitterionic liposomes. *Biomacromolecules* **2008**, *9* (8), 2237-2243.
- Quemeneur, F. Relationship between mechanical parameters and behaviour under external stresses in lipid vesicles with modified membranes. University of Grenoble, Grenoble, 2010.
- Quemeneur, F.; Rinaudo, M.; Maret, G.; Pépin-Donat, B., Decoration of lipid vesicles by polyelectrolytes: mechanism and structure. *Soft Matter* **2010**, *6* (18), 4471-4481.
- Quemeneur, F.; Quilliet, C.; Faivre, M.; Viallat, A.; Pépin-Donat, B., Gel phase vesicles buckle into specific shapes. *Physical review letters* **2012**, *108* (10), 108303.
- Radavidson, H. Vésicules lipidiques biomimétiques décorées par un assemblage multicouche nanocristaux decellulose/xyloglucane : élaboration et caractérisation mécanique. University of Grenoble Alpes, 2016.
- Radotić, K.; Roduit, C.; Simonović, J.; Hornitschek, P.; Fankhauser, C.; Mutavdžić, D.; Steinbach, G.; Dietler, G.; Kasas, S., Atomic force microscopy stiffness tomography on living Arabidopsis thaliana cells reveals the mechanical properties of surface and deep cell-wall layers during growth. *Biophysical journal* **2012**, *103* (3), 386-394.
- Rånby, B. G., Aqueous colloidal solutions of cellulose micelles. *Acta Chemica Scandinavica* **1949**, *3* (5), 649-650.
- Rånby, B. G.; Ribi, E., Über den Feinbau der Zellulose. *Experientia* **1950**, *6* (1), 12-14.
- Reeves, J. P.; Dowben, R. M., Formation and properties of thin-walled phospholipid vesicles. *Journal of cellular physiology* **1969**, *73* (1), 49-60.
- Reid, M. S.; Villalobos, M.; Cranston, E. D., Cellulose nanocrystal interactions probed by thin film swelling to predict dispersibility. *Nanoscale* **2016**, *8* (24), 12247-12257.
- Reviakine, I.; Johannsmann, D.; Richter, R. P., Hearing What You Cannot See and Visualizing What You Hear: Interpreting Quartz Crystal Microbalance Data from Solvated Interfaces. *Analytical Chemistry* **2011**, *83* (23), 8838-8848.
- Revol, J.-F.; Bradford, H.; Giasson, J.; Marchessault, R. H.; Gray, D., Helicoidal self-ordering of cellulose microfibrils in aqueous suspension. *International journal of biological macromolecules* **1992**, *14* (3), 170-172.
- Richardson, J. J.; Björnmalm, M.; Caruso, F., Technology-driven layer-by-layer assembly of nanofilms. *Science* **2015**, *348* (6233), aaa2491.
- Richter, R.; Mukhopadhyay, A.; Brisson, A., Pathways of lipid vesicle deposition on solid surfaces: a combined QCM-D and AFM study. *Biophysical journal* **2003**, *85* (5), 3035-3047.
- Richter, R. P.; Brisson, A. R., Following the formation of supported lipid bilayers on mica: a study combining AFM, QCM-D, and ellipsometry. *Biophysical journal* **2005**, *88* (5), 3422-3433.
- Richter, R. P.; Bérat, R.; Brisson, A. R., Formation of solid-supported lipid bilayers: an integrated view. *Langmuir* **2006**, *22* (8), 3497-3505.
- Rodriguez, N.; Pincet, F.; Cribier, S., Giant vesicles formed by gentle hydration and electroformation: a comparison by fluorescence microscopy. *Colloids and Surfaces B: Biointerfaces* **2005**, *42* (2), 125-130.

- Routier-Kierzkowska, A.-L.; Smith, R. S., Measuring the mechanics of morphogenesis. *Current opinion in plant biology* **2013**, *16* (1), 25-32.
- Rubinger, C.; Moreira, R.; Cury, L.; Fontes, G.; Neves, B.; Meneguzzi, A.; Ferreira, C., Langmuir–Blodgett and Langmuir–Schaefer films of poly (5-amino-1-naphthol) conjugated polymer. *Applied Surface Science* **2006**, *253* (2), 543-548.
- Sandrin, L.; Coche-Guérente, L.; Bernstein, A.; Basit, H.; Labbé, P.; Dumy, P.; Boturyn, D., Cell adhesion through clustered ligand on fluid supported lipid bilayers. *Organic & biomolecular chemistry* **2010**, *8* (7), 1531-1534.
- Sapkota, J.; Shirole, A.; Foster, E. J.; Garcia, J. C. M.; Lattuada, M.; Weder, C., Polymer nanocomposites with nanorods having different length distributions. *Polymer* **2017**, *110*, 284-291.
- Scheller, H. V.; Ulvskov, P., Hemicelluloses. *Annual review of plant biology* **2010**, *61* (1), 263-289.
- Schneider, C. A.; Rasband, W. S.; Eliceiri, K. W., NIH Image to ImageJ: 25 years of image analysis. *Nature methods* **2012**, *9* (7), 671-675.
- Schoeler, B.; Delorme, N.; Doench, I.; Sukhorukov, G. B.; Fery, A.; Glinel, K., Polyelectrolyte films based on polysaccharides of different conformations: Effects on multilayer structure and mechanical properties. *Biomacromolecules* **2006**, *7* (6), 2065-2071.
- Sethaphong, L.; Haigler, C. H.; Kubicki, J. D.; Zimmer, J.; Bonetta, D.; DeBolt, S.; Yingling, Y. G., Tertiary model of a plant cellulose synthase. *Proceedings of the National Academy of Sciences* **2013**, *110* (18), 7512-7517.
- Sharma, B.; Naresh, L.; Dhuldhoya, N.; Merchant, S.; Merchant, U., An overview on pectins. *Times Food Processing Journal* **2006**, *23* (2), 44-51.
- Singh, A. V.; Rahman, A.; Kumar, N. S.; Aditi, A.; Galluzzi, M.; Bovio, S.; Barozzi, S.; Montani, E.; Parazzoli, D., Bio-inspired approaches to design smart fabrics. *Materials & Design (1980-2015)* **2012**, *36*, 829-839.
- Slama, J. S.; Rando, R. R., Lectin-mediated aggregation of liposomes containing glycolipids with variable hydrophilic spacer arms. *Biochemistry* **1980**, *19* (20), 4595-4600.
- Sneddon, I. N., The relation between load and penetration in the axisymmetric Boussinesq problem for a punch of arbitrary profile. *International journal of engineering science* **1965**, *3* (1), 47-57.
- Somerville, C.; Bauer, S.; Brininstool, G.; Facette, M.; Hamann, T.; Milne, J.; Osborne, E.; Paredez, A.; Persson, S.; Raab, T., Toward a systems approach to understanding plant cell walls. *Science* **2004**, *306* (5705), 2206-2211.
- Stana, K.; Pohar, C.; Ribitsch, V., Adsorption of whitening agents on cellulose fibers—Monitored by streaming potential measurements, calorimetry and fluorescence. *Colloid and Polymer Science* **1995**, *273* (12), 1174-1178.
- Svagan, A. J.; Musyanovych, A.; Kappl, M.; Bernhardt, M.; Glasser, G.; Wohnhaas, C.; Berglund, L. A.; Risbo, J.; Landfester, K., Cellulose nanofiber/nanocrystal reinforced capsules: A fast and facile approach toward assembly of liquid-core capsules with high mechanical stability. *Biomacromolecules* **2014**, *15* (5), 1852-1859.
- Szoka Jr, F.; Papahadjopoulos, D., Comparative properties and methods of preparation of lipid vesicles (liposomes). *Annual review of biophysics and bioengineering* **1980**, *9* (1), 467-508.

Tang, Z.; Wang, Y.; Podsiadlo, P.; Kotov, N. A., Biomedical applications of layer-by-layer assembly: from biomimetics to tissue engineering. *Advanced Materials* **2006**, *18*(24), 3203-3224.

Tashiro, K.; Kobayashi, M., Theoretical evaluation of three-dimensional elastic constants of native and regenerated celluloses: role of hydrogen bonds. *Polymer* **1991**, *32*(8), 1516-1526.

Taupin, C.; Dvolaitzky, M.; Sauterey, C., Osmotic pressure-induced pores in phospholipid vesicles. *Biochemistry* **1975**, *14*(21), 4771-4775.

Teeri, T. T.; Brumer III, H.; Daniel, G.; Gatenholm, P., Biomimetic engineering of cellulose-based materials. *Trends in Biotechnology* **2007**, *25*(7), 299-306.

Thakur, B. R.; Singh, R. K.; Handa, A. K.; Rao, M., Chemistry and uses of pectin—a review. *Critical Reviews in Food Science & Nutrition* **1997**, *37*(1), 47-73.

Thibault, J.-F.; Ralet, M.-C., Physico-chemical properties of pectins in the cell walls and after extraction. In *Advances in Pectin and Pectinase Research*, F. Voragen, H. S. a. R. V. E., Ed. Springer: Dordrecht, 2003; pp 91-105.

Thibault, J.; Rinaudo, M., Chain association of pectic molecules during calcium-induced gelation. *Biopolymers: Original Research on Biomolecules* **1986**, *25*(3), 455-468.

Toyotama, A.; Okuzono, T.; Yamanaka, J., Spontaneous formation of eutectic crystal structures in binary and ternary charged colloids due to depletion attraction. *Scientific reports* **2016**, *6*, 23292.

Valentin, R.; Cerclier, C.; Geneix, N.; Aguié-Béghin, V.; Gaillard, C.; Ralet, M.-C.; Cathala, B., Elaboration of extensin—pectin thin film model of primary plant cell wall. *Langmuir* **2010**, *26*(12), 9891-9898.

Vandoolaeghe, P.; Rennie, A. R.; Campbell, R. A.; Thomas, R. K.; Höök, F.; Fragneto, G.; Tiberg, F.; Nylander, T., Adsorption of cubic liquid crystalline nanoparticles on model membranes. *Soft Matter* **2008**, *4*(11), 2267-2277.

Villares, A.; Moreau, C.; Dammak, A.; Capron, I.; Cathala, B., Kinetic aspects of the adsorption of xyloglucan onto cellulose nanocrystals. *Soft Matter* **2015**, *11*(32), 6472-6481.

Villares, A.; Bizot, H.; Moreau, C.; Rolland-Sabaté, A.; Cathala, B., Effect of xyloglucan molar mass on its assembly onto the cellulose surface and its enzymatic susceptibility. *Carbohydrate Polymers* **2017**, *157*, 1105-1112.

Vinogradova, O. I., Mechanical properties of polyelectrolyte multilayer microcapsules. *Journal of Physics: Condensed Matter* **2004**, *16*(32), R1105.

Vitorazi, L.; Ould-Moussa, N.; Sekar, S.; Fresnais, J.; Loh, W.; Chapel, J.-P.; Berret, J.-F., Evidence of a two-step process and pathway dependency in the thermodynamics of poly (diallyldimethylammonium chloride)/poly (sodium acrylate) complexation. *Soft Matter* **2014**, *10*(47), 9496-9505.

Voinova, M. V.; Rodahl, M.; Jonson, M.; Kasemo, B., Viscoelastic acoustic response of layered polymer films at fluid-solid interfaces: continuum mechanics approach. *Physica Scripta* **1999**, *59*(5), 391.

Wacklin, H. P., Neutron reflection from supported lipid membranes. *Current Opinion in Colloid & Interface Science* **2010**, *15*(6), 445-454.

Walde, P.; Cosentino, K.; Engel, H.; Stano, P., Giant vesicles: preparations and applications. *ChemBioChem* **2010**, *11*(7), 848-865.

- Wang, B.; Zhang, L.; Bae, S. C.; Granick, S., Nanoparticle-induced surface reconstruction of phospholipid membranes. *Proceedings of the National Academy of Sciences* **2008**, *105* (47), 18171-18175.
- Wang, H.; Roman, M., Formation and properties of chitosan– cellulose nanocrystal polyelectrolyte–macroion complexes for drug delivery applications. *Biomacromolecules* **2011**, *12* (5), 1585-1593.
- Wang, T.; Zabolina, O.; Hong, M., Pectin–cellulose interactions in the Arabidopsis primary cell wall from two-dimensional magic-angle-spinning solid-state nuclear magnetic resonance. *Biochemistry* **2012**, *51* (49), 9846-9856.
- Wang, T.; Park, Y. B.; Cosgrove, D. J.; Hong, M., Cellulose-pectin spatial contacts are inherent to never-dried Arabidopsis primary cell walls: evidence from solid-state nuclear magnetic resonance. *Plant Physiology* **2015**, *168* (3), 871-884.
- Ward, M. D.; Buttry, D. A., In situ interfacial mass detection with piezoelectric transducers. *Science* **1990**, *249* (4972), 1000-1007.
- Wolf, S.; Mouille, G.; Pelloux, J., Homogalacturonan methyl-esterification and plant development. *Molecular plant* **2009**, *2* (5), 851-860.
- Wong, J. E.; Díez-Pascual, A. M.; Richtering, W., Layer-by-Layer assembly of polyelectrolyte multilayers on thermoresponsive P (NiPAM-co-MAA) microgel: Effect of ionic strength and molecular weight. *Macromolecules* **2009**, *42* (4), 1229-1238.
- Yakubov, G. E.; Bonilla, M. R.; Chen, H.; Doblin, M. S.; Bacic, A.; Gidley, M. J.; Stokes, J. R., Mapping nanoscale mechanical heterogeneity of primary plant cell walls. *Journal of Experimental Botany* **2016**, *67* (9), 2799-2816.
- Zdunek, A.; Kurenda, A., Determination of the elastic properties of tomato fruit cells with an atomic force microscope. *Sensors* **2013**, *13* (9), 12175-12191.
- Zhang, T.; Mahgoudy-Louyeh, S.; Tittmann, B.; Cosgrove, D. J., Visualization of the nanoscale pattern of recently-deposited cellulose microfibrils and matrix materials in never-dried primary walls of the onion epidermis. *Cellulose* **2014**, *21* (2), 853-862.
- Zhao, Z.; Crespi, V. H.; Kubicki, J. D.; Cosgrove, D. J.; Zhong, L., Molecular dynamics simulation study of xyloglucan adsorption on cellulose surfaces: effects of surface hydrophobicity and side-chain variation. *Cellulose* **2014**, *21* (2), 1025-1039.
- Zykwinska, A.; Thibault, J.-F.; Ralet, M.-C., Organization of pectic arabinan and galactan side chains in association with cellulose microfibrils in primary cell walls and related models envisaged. *Journal of Experimental Botany* **2007**, *58* (7), 1795-1802.
- Zykwinska, A.; Thibault, J.-F.; Ralet, M.-C., Competitive binding of pectin and xyloglucan with primary cell wall cellulose. *Carbohydrate Polymers* **2008**, *74* (4), 957-961.
- Zykwinska, A. W.; Ralet, M.-C. J.; Garnier, C. D.; Thibault, J.-F. J., Evidence for in vitro binding of pectin side chains to cellulose. *Plant Physiology* **2005**, *139* (1), 397-407.

ANNEX I



Article

pubs.acs.org/Biomac

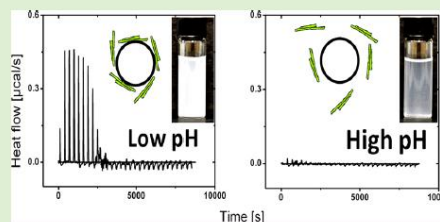
pH-Sensitive Interactions between Cellulose Nanocrystals and DOPC Liposomes

Yotam Navon, Harisoa Radavidson, Jean-Luc Putaux,¹ Bruno Jean,² and Laurent Heux^{1*}

Univ. Grenoble Alpes, Centre de Recherches sur les Macromolécules Végétales (CERMAV), F-38000 Grenoble, France
CNRS, CERMAV, F-38000 Grenoble, France

⁵ Supporting Information

ABSTRACT: The interaction of 1,2 dioleoyl-*sn*-glycero-3-phosphatidylcholine (DOPC) vesicles with cellulose nanocrystals (CNCs) using several complementary techniques. Dynamic light scattering, zeta-potential, cryo-transmission electron microscopy and isothermal titration calorimetry (ITC) analyses confirmed the formation of pH-dependent CNC–liposome complexes. ITC was used to characterize the thermodynamic properties of this interaction. Positive values of enthalpy were found at pH lower than 5 where the charge sign of the constituents was opposite. The association was more pronounced at lower pH, as indicated by the higher values of association constant. We suggest that the positive enthalpy is derived from the release of counterions from the particle hydration shell during the association and that the charge of the vesicles plays a significant role in this interaction.



LANGMUIR

pubs.acs.org/Langmuir

Article

Deposition of Cellulose Nanocrystals onto Supported Lipid Membranes

Yotam Navon, Bruno Jean, Liliane Coche-Guérénte, Franck Dahlem, Anne Bernheim-Groswasser,^{*} and Laurent Heux^{*}

Cite This: *Langmuir* 2020, 36, 1474–1483

Read Online

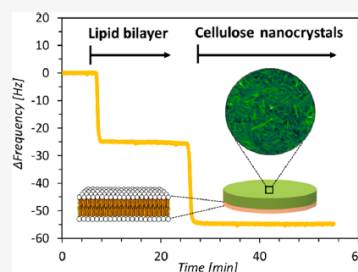
ACCESS |

Metrics & More

Article Recommendations

Supporting Information

ABSTRACT: The deposition of cellulose nanocrystals (CNCs) on a supported lipid bilayer (SLB) was investigated at different length scales. Quartz crystal microbalance with dissipation monitoring (QCM-D) was used to probe the bilayer formation and to show for the first time the CNC deposition onto the SLB. Specifically, classical QCM-D measurements gave estimation of the adsorbed hydrated mass and the corresponding film thickness, whereas complementary experiments using D₂O as the solvent allowed the quantitative determination of the hydration of the CNC layer, showing a high hydration value. Scanning force microscopy (SFM) and total internal reflection fluorescence microscopy (TIRF) were used to probe the homogeneity of the deposited layers, revealing the structural details at the particle and film length scales, respectively, thus giving information on the effect of CNC concentration on the surface coverage. The results showed that the adsorption of CNCs on the supported lipid membrane depended on lipid composition, CNC concentration, and pH conditions, and that the binding process was governed by electrostatic interactions. Under suitable conditions, a uniform film was formed, with thickness corresponding to a CNC monolayer, which provides the basis for a relevant 2D model of a primary plant cell wall.



ANNEX II

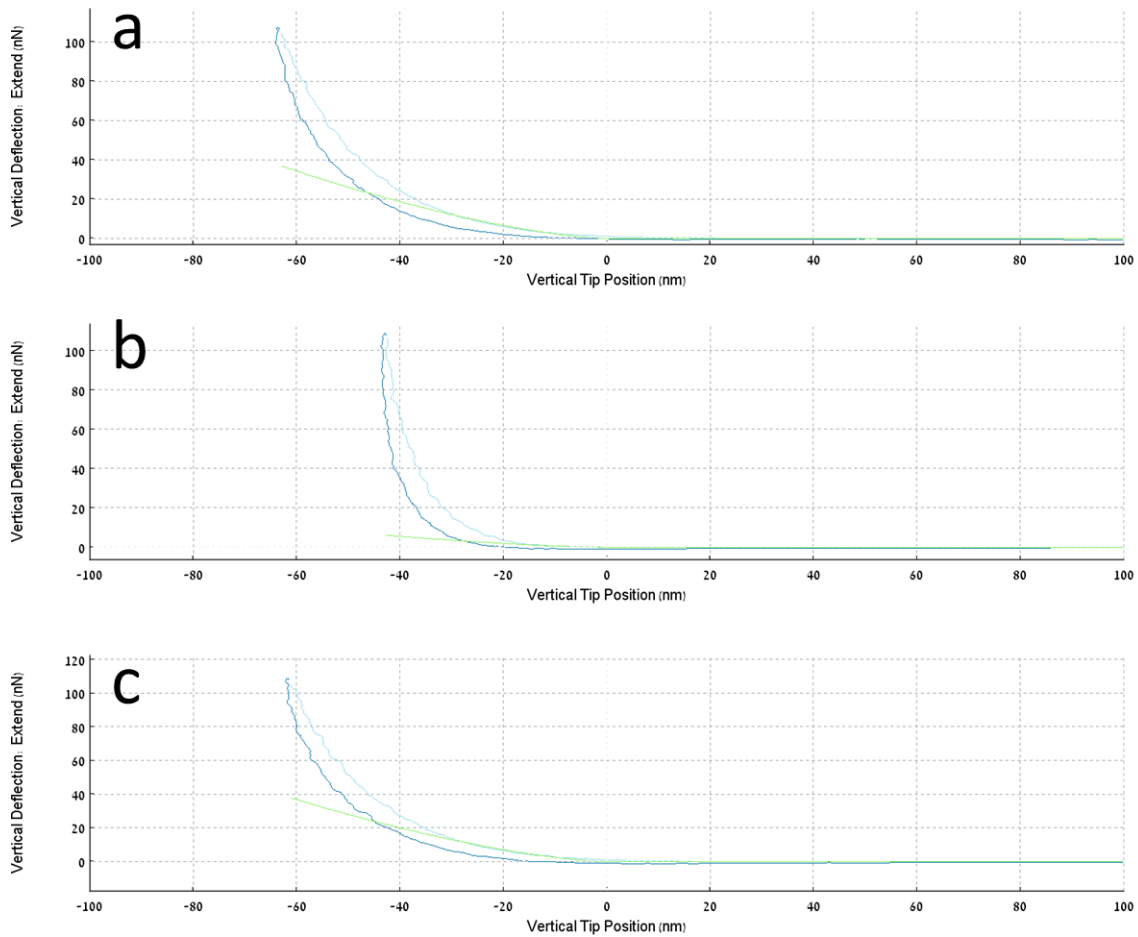


Figure 127. Force curves obtained with a colloidal probe on multilayered systems. Approach (light blue) and retract (dark blue) curves of (a) CNC/XG (b) CNC/Pectin (c) (CNC/XG/CNC/Pectin films with 20 deposition cycles). The green curve is a fit to the Hertz model. The limits are adjusted to fit the part of the curve corresponding to an indentation of 10% of the total film thickness as measured by AFM height profile on a scratched area. This is done in order to avoid contribution from the substrate.

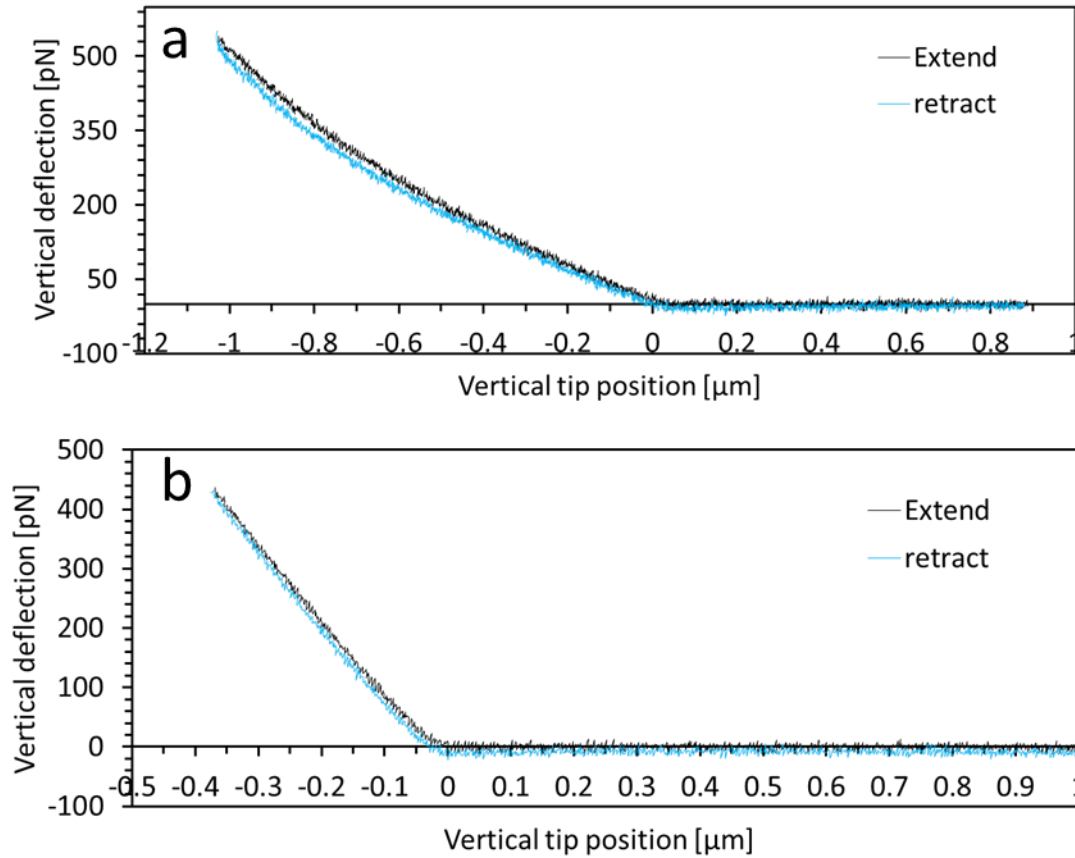


Figure 128. Force curves obtained for decorated vesicles. (a) soft type (b) stiff type.

Figure 128 shows two different profiles obtained from AFM indentation experiment on decorated vesicles (CNC/XG)_{10.5}. This reflects the difference in the mechanical behavior of the vesicles between measurements as previously explained in chapter 6.1.

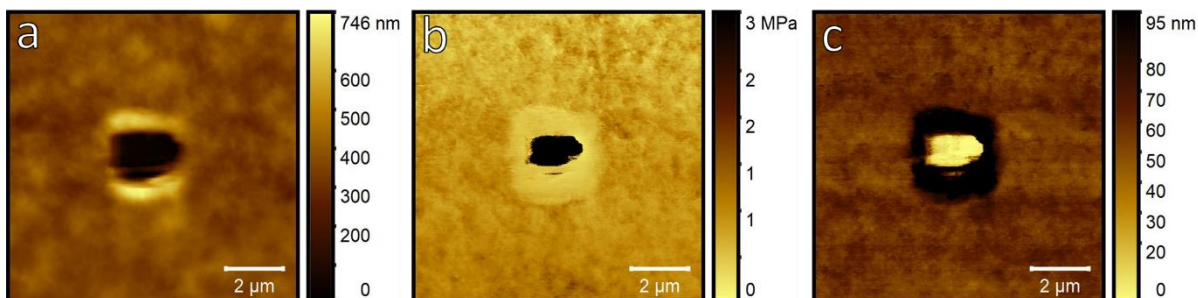


Figure 129. Peak force AFM profiles of (CNC/XG) 20.5 layers. (a) topography (b) Sneddon modulus (c) Indentation.

Figure 129 shows peak force AFM profiles obtained for $(\text{CNC}/\text{XG})_n$ multilayers with $n=20.5$. The topography, shown in figure 129a, is obtained with low resolution due to tip blunting following the nano shaving process. Figure 129b shows a force map based on the Sneddon modulus which is calculated from a fit to each force curve following tip approach. It can be clearly seen that the center of the image, which corresponds to the scratched region or the surface of the support, has significantly higher modulus than the rest of the image. Moreover, a lower modulus is obtained for the circumference of the square corresponding to unbound material removed from the center.

Figure 129c shows the indentation profile of the same region as in figure 129a and 129b. The average value of indentation, excluding the scratch and its circumference was 60 nm (minimum=40nm, maximum=90 nm) while the average value of indentation in the middle of the square was close to zero. In addition, closer inspection of the scratched surface yielded same height profile and roughness as the bare substrate.

These results thus reinforce the values obtained for the film thickness, by implying that the material was indeed removed from the surface.

Abstract

The goal of this work was to develop an in vitro model of the plant primary cell wall. A bottom up approach was chosen for the rational design of 2D and 3D constructs made of a lipid membrane, cellulose nano crystals (CNCs) and xyloglucan (XG). First, the interaction between the building blocks was probed using light scattering, isothermal titration calorimetry, quartz crystal microbalance and electron microscopy, revealing firstly the electrostatic nature of the interaction between CNCs and a lipidic membrane and secondly, specific interaction between CNCs and XG in a precise stoichiometric ratio. Then, the optimal parameters from the interaction studies were used to obtain 2D and 3D structures by depositing alternating layers of CNCs and XG on flat substrates (multilayered films) and giant unilamellar vesicles (GUVs). A linear growth of the films was revealed by atomic force microscopy (AFM) experiments while the response of decorated vesicles to osmotic shocks lead to their buckling due to the rigidification of the lipid membrane. Finally, the mechanical properties of the constructs were characterized using AFM indentation, revealing a Young's modulus of few hundred kPa, similarly to what is observed for real plant cell walls.

Key words: primary cell wall, lipid membranes, cellulose, interaction, biomimetics

L'objectif de ce travail était de développer un modèle in vitro de la paroi primaire des plantes. Une approche ascendante a été choisie pour la conception rationnelle de constructions 2D et 3D faites d'une membrane lipidique, de nanocristaux de cellulose (CNC) et de xyloglucane (XG). Tout d'abord, l'interaction entre les blocs de base a été examinée à l'aide de la diffusion de la lumière, la calorimétrie de titrage isotherme, la microbalance à quartz et la microscopie électronique, révélant tout d'abord la nature électrostatique de l'interaction entre les CNC et une membrane lipidique ainsi qu'une interaction spécifique entre les CNC et XG dans un rapport stœchiométrique précis. Par la suite, les paramètres optimisés des études d'interaction ont été utilisés pour obtenir des structures 2D et 3D en déposant des couches alternées de CNC et XG sur des substrats plats (films multicouches) et des vésicules unilamellaires géantes (GUV). Une croissance linéaire des films a été révélée par les expériences de microscopie à force atomique (AFM), tandis que la réponse des vésicules décorées aux chocs osmotiques conduit à leur flambage en raison de la rigidification de la membrane lipidique. Enfin, les propriétés mécaniques des constructions ont été caractérisées en utilisant l'AFM par indentation, révélant un module d'Young de quelques centaines de kPa, similaire à celui observé pour de vraies parois cellulaires végétales.

Mots-clés : paroi primaire, membranes lipidiques, cellulose, interaction, biomimétique

General bstract

Our increasing environmental awareness brought to light the importance of materials made from plants as a renewable ecological source. It is therefore essential to understand the structure and function of plant cell walls, from both fundamental and applicative aspects, in order to utilize them for the design of novel eco-friendly materials. However, since the living cell is a very complex system, a simple model can help to better understand the behavior of this material. The model systems existing up to date are lacking the basic elements and architecture of the plant cell wall, thus, it is necessary to develop a relevant model which will contain all the basic elements, organized in a manner that resembles the natural structure. Thus, this work was aimed to create and characterize a simple bioinspired model of the plant cell wall by studying the interactions between the basic elements composing this structure. Thanks to these studies, we were able to construct a simple model system which represents the plant cell wall in terms of structure and properties, paving the way for the design of a new class of bio-based materials.

Notre conscience environnementale croissante a mis en évidence l'importance des matériaux à base de plantes comme source écologique renouvelable. Il est donc essentiel de comprendre la structure et la fonction de la paroi cellulaire, à la fois ses aspects fondamentaux mais aussi applicatifs, afin de les utiliser pour la conception de nouveaux matériaux respectueux de l'environnement. Cependant, comme la cellule vivante est très complexe, un modèle simple peut aider à mieux comprendre le comportement de ce matériau. Les systèmes modèles existants ne disposent, pourtant, pas des éléments de base ni de l'architecture de la paroi cellulaire végétale. Il est donc nécessaire de développer un modèle pertinent qui contiendra tous les éléments de base, organisés d'une manière qui ressemble aux structures naturelles. Ainsi, ce travail visait à créer et caractériser un modèle simple de la paroi, en étudiant les interactions entre ses éléments constitutifs. Grâce à ces études, nous avons pu construire un système modèle bio inspiré de la paroi, reproduisant sa structure et ses propriétés, ouvrant la voie à la conception d'une nouvelle classe de matériaux biosourcés.